SIMULATION OF MANUFACTURING PROCESSES AND MANUFACTURING CHAINS USING FINITE ELEMENT TECHNIQUES

Shukri Afazov, BSc

Thesis submitted to the University of Nottingham for the degree of Doctor of Philosophy

June 2009

Тази дисертация е посветена на моите Родители, моя Брат и Елеонора

This thesis is dedicated to my Parents, my Brother and Eleonora

ABSTRACT

This thesis presents work on the simulation of manufacturing chains, simulation of manufacturing processes (casting, forging, shot-peening and heat treatment) and fatigue life prediction by using the finite element method (FEM). The objectives and the contributions of this thesis consist of development of mathematical algorithms and techniques for mapping and transferring FE data (stresses, strains, displacements, etc.) from macro-to-macro and micro-to-macro FE models among different FE solvers and meshes. All these features have been implemented into a new finite element data exchange system (FEDES). FEDES has been developed to simulate manufacturing chains by using FE techniques. Extensive research has been carried out on the simulation of investment casting processes of aero-engine parts under equiaxed and directional cooling. Methodologies for predicting the component life undergoing low cycle fatigue (LCF) and high cycle fatigue (HCF) have been developed. Life prediction based on the effect of the residual stresses obtained from micro machining and shot-peening processes has been investigated.

FEDES has been used to simulate two manufacturing chains where the residual stresses and the distortions after each manufacturing process have been passed to the next process of the chain. Manufacturing chain simulation including casting, forging and heat treatment has been carried out on a simple parallelepiped geometry. A second manufacturing chain simulation has been performed on an aero-engine vane component which includes the following manufacturing processes: metal deposition, welding, heat treatment, machining and shot-peening. An investment casting simulation under equiaxed cooling of the bottom core vane (BCV) component of the aero-engines vane has been performed. The gap formation and the gap conductance have been studied and implemented in the analyses. The main goal is to investigate the residual stresses in the BCV cast with Inconel 718 material. Two FE solvers (ABAQUS and ProCAST) have been used for validation purposes. An investment casting simulation under directional cooling in a Bridgman furnace of a high pressure turbine blade (HPTB) with CMSX-4 material has been carried out. The effect of the withdrawal velocity on the temperature and the residual stresses of the HPTB cast has been investigated.

ACKNOWLEDGEMENTS

First of all, I would like to express my sincere thanks to Professor A A Becker and Professor T H Hyde for giving me the opportunity to pursue a research degree at University of Nottingham. Their valuable knowledge and guidance at each stage of the project ensured that I was able to achieve my objectives successfully.

I would like to acknowledge the support of the EU-VERDI consortium and Rolls-Royce plc and the following companies and research organisations: AICIA-Spain, Avio-Italy, CENAERO-Belgium, CIMNE-Spain, EngineSoft-Italy, ITP-Spain, Luleå University of Technology-Sweden, MTU Aeroengines-Germany, Politecnico di Torino-Italy, Techspace Aero-Belgium, University of Trollhättan Uddevalla-Sweden, Universität Karlsruhe-Germany, Volvo Aero Corporation-Sweden and WZL Aachen University of Technology-Germany for their valuable contributions to the project.

Finally, none of this would have been possible if it had not been for the confidence my parents, my brother and Eleonora transmitted me. Hence, this thesis is directly dedicated to them.

CONTENTS

NOMENCLATURE

a	Accommodation coefficient
A	Cross sectional areas
A	Creep material constant
A	Empirical constant to account for a contact pressure
$\overrightarrow{AB}$	Direct vector between nodes A and B
$\overrightarrow{AC}$	Direct vector between nodes A and C
$\overrightarrow{AD}$	Direct vector between nodes A and D
$\overrightarrow{AO}$	Direct vector between nodes A and O
$\overrightarrow{AF}$	Direct vector between nodes A and F
$\overrightarrow{AP}$	Direct vector between nodes A and P
b	Fatigue strength coefficient
$\overrightarrow{BO}$	Direct vector between nodes B and O
d	Gap width
d	Distance
d_{AB}	Distance between nodes A and B
d_{AO}	Distance between nodes A and O
d_{BO}	Distance between nodes B and O
$d_{average}$	Average distance
$d_{initial}$	Initial distance
d_r	Roughness of two contacting surfaces
d_α	Distance from node to plane
D	Data
Det	Determinant
E	Elastic modulus
f	Radiation factor
g	Temperature jump distances
g,h,r	Local coordinates
H,h	Height

h	Gap conductance coefficient
h_0	Initial value of the heat transfer coefficient
h_{rad}	Radiative equivalent heat transfer coefficient
h_c	Cavity height
F	Force
F_{1-2}	View factor
$F_{\max}$	Maximum force
$F_{\min}$	Minimum force
F_n	Normal force
F_s	Sliding force
I^J	Internal force vector
J	Jacobian matrix
k	Proportional distance coefficient
k_a	Air conductance coefficient
k_g	Gas conductance coefficient
L_{num}	Layers number
m	Mapping tolerance coefficient
M^{NJ}	Mass matrix
n	Material constant of the Norton creep law
$\vec{n}$	Normal vector
$\vec{\hat{n}}$	Normal unit vector
$\overrightarrow{\hat{n}_{AB}}$	Unit vector for nodes A and B
$\overrightarrow{\hat{n}_{AF}}$	Unit vector for nodes A and F
N	Shape function
N, n	Number of nodes
N_f	Number of cycles
$\overrightarrow{OA}$	Direct vector between nodes O and A
$\overrightarrow{OB}$	Direct vector between nodes O and B
$\overrightarrow{OC}$	Direct vector between nodes O and C

$\overrightarrow{OD}$	Direct vector between nodes O and D
P	Contact pressure
P_g	Gas pressure
P^J	Applied load vector
q	Heat transfer
q_c	Gas conductance heat transfer
q_g	Gap heat transfer
q_r	Radiation heat transfer
R, r	Radius
R	Universal gas constant
S	Surface
S_{ABCD}	Surface area of the rectangular ABCD
S_{ABC}	Surface area of the triangular ABC
S_{AOB}	Surface area of the triangular AOB
S_{AOC}	Surface area of the triangular AOC
S_{BOC}	Surface area of the triangular BOC
S_{COD}	Surface area of the triangular COD
S_{DOA}	Surface area of the triangular DOA
t	Time
t_s	Step time
t_m	Mould filling time
T	Temperature
T_g	Gas temperature
th	Wall thickness
u^N	Degree of freedom
v	Velocity
w	Width
w_c	Cavity width
x, y, z	Coordinates
α	Thermal diffusivity

α	Plane
α	Angle
γ	Specific heat ratio
ε	Emissivity coefficient
ε_f'	Fatigue ductility coefficient
ε_{pl}	Plastic strain
$\varepsilon_{pl\max.pr}$	Maximum principal plastic strain
$\varepsilon^m{}_{pl\max.pr}$	Maximum principal plastic mean strain
$\varepsilon^m{}_{pl}$	Mean plastic strain
$\dot{\varepsilon}$	Strain rate
$\Delta\varepsilon$	Strain range
$\Delta\varepsilon_{pl}$	Plastic strain range
$\Delta\varepsilon_{pl\max.pr}$	Maximum principal plastic strain range
λ	Material dependent constant
μ	Friction coefficient
ρ	Density
σ	Stefan-Boltzmann constant
σ	Stress
$\sigma_{11}, \sigma_{22}, \sigma_{33}$	Direct stresses in the x, y and z directions
$\sigma_{12}, \sigma_{23}, \sigma_{13}$	Shear stresses in the x-y, y-z and x-z planes
σ_a	Stress amplitude
$\sigma_{average}$	Average stress
σ^m	Mean stress
$\sigma^m{}_{\max.pr}$	Maximum principal mean stress
$\sigma_{\max}$	Maximum stress
$\sigma_{\min}$	Minimum stress
σ_f'	Fatigue strength coefficient
σ_y	Yield strength
υ	Poisson's ratio

$[R_z]$	Rotation matrix about the z axis
$[T]$	Transformation matrix
$[T]^T$	Transpose transformation matrix
$[\sigma]$	Global Cartesian stress matrix
$[\sigma']$	Local Cartesian stress matrix

ABBREVIATIONS

BCV	Bottom core vane
BMG	Bulk metallic glass
CA-FD	Cellular automation-finite difference
BEM	Boundary element method
DMUE	Distance method using elements
DMUFP	Distance method using field of points
DC	Directional cooling
DS	Directional solidification/solidified
FDM	Finite difference method
FE	Finite element
FEA	Finite element analysis/analyses
FEDES	Finite element data exchange system
FEM	Finite element method
FEP	Finite element package
GUI	Graphic user interface
HCF	High cycle fatigue
HPTB	High pressure turbine blade
HTC	Heat transfer coefficient
LCF	Low cycle fatigue
MM	Meshless method
MUESF	Method using the element shape function
NN-FEM	Nearest nodes finite element method

NPM	Nearest point method
RAM	Random access memory
RP	Reference point
SC	Single crystal
SF	Scale factor
TCC	Thermal contact conductance
VCL	Visual component library
XML	Extensible markup language

CHAPTER 1

INTRODUCTION

1.1 General

The competition between industrial organizations for maintaining existent markets and enlarging to other markets requires producing components with high quality and low cost. This is achieved by continuous and accurate research. The research in this thesis aims to provide knowledge which can be used by industrial or research organizations. Nowadays, numerical methods for solving different engineering problems are widely used. The Finite Element Method (FEM) has been developed for the last three decades by many researchers. A lot of research into elasticity, plasticity, contact mechanics, fluid dynamics, creep etc. has been implemented in the FEM. Many commercial and non-commercial Finite Element (FE) codes have been developed for solving different linear and non-linear problems in engineering. Many of the FE codes are specialised in particular areas, which makes them a first option for simulating a particular manufacturing process. For example, for producing a final part from an aero engine, many manufacturing processes can be involved, such as casting, forming, forging, metal deposition, welding, macro and micro machining, shot-peening, etc. Each of these processes creates residual stresses which can be either beneficial and extend the life of the component, or create cracks and reduce the life. The research in this thesis is concentrated on the accurate simulation of manufacturing processes, creating methodologies and tools for accurate simulation of a chain of manufacturing processes by using the FEM.

1.2 Manufacturing process modelling

Producing a final component in industry requires the involvement of many manufacturing processes, such as casting, forming, forging, metal deposition, welding, macro and micro machining, shot-peening, etc. For improving the quality

of the component, the manufacturing processes can be improved by implementing better materials or changing the process parameters. Experimental and numerical methods can be used for optimizing the manufacturing processes. The disadvantage of experimental methods is that they are expensive. Numerical methods such as the FEM, boundary element method (BEM), finite deference method (FDM) and meshless method (MM) are available in a variety of software packages and have proved their accuracy during the last two decades. As a well-established powerful and widely used method, the FEM is chosen to carry out the research in this thesis. Four manufacturing processes (casting, forging, heat treatment and shot-peening) are investigated in this thesis by using the FEM. The main goal is to simulate these processes accurately in order to obtain accurate results. Investigation of the residual stresses and the distortions after each process is the main target. FE simulations with different process parameters and conditions are performed in order to provide knowledge for the corresponding manufacturing process.

1.3 Manufacturing chain simulation

As mentioned earlier, producing a final component requires the involvement of many manufacturing processes performed sequentially. Many manufacturing processes create residual stresses and distortions. The residual stresses can be beneficial and extend the life of the component, for example the residual compressive stresses after shot-peening, or can create cracks and decrease the life of the component. The residual stresses and the distortions created after each process affect the next process in the manufacturing chain. Therefore, the residual stresses and the distortions must be passed to the next FE simulation as an initial condition. Many commercial and non-commercial FE codes for solving linear and nonlinear structural analysis, fluid flow, solid-fluid interaction, heat conduction, flow through porous media, and coupled physical problems are available nowadays.

There are specialized FE codes for simulation of particular manufacturing processes which are preferred by the designers and analysts. Some manufacturing processes, such as shot-peening, roller-burnishing, machining, etc. are simulated on simple geometries. This requires transferring the results from the micro-scale into the

macro-scale FE models. A new finite element data exchange system (FEDES) is developed to allow the simulation of a manufacturing chain by using the FEM. FEDES links the FE results obtained with different FE solvers and different element types in order to allow the simulation of the manufacturing chain. FEDES allows designers and analysts to use the most suitable FE solver and element types for the corresponding process simulations.

1.4 Scope of the thesis

The main objective of the work in this thesis is to provide knowledge for accurate simulation of manufacturing processes and manufacturing chains by using the FEM. In order to achieve the objectives of this thesis the following innovations have been achieved:

- studying and implementing the gap conductance effect into casting simulation using FEM
- simulation of investment casting under equiaxed cooling of the BCV component and directional cooling of the HPTB component
- development of mathematical algorithms and techniques for mapping and transferring FE data (stresses, strains, displacements, etc.) from macro-to-macro and micro-to-macro FE models
- development of a new software (FEDES) which has the capability to simulate manufacturing chains by using the FEM
- development of life prediction methodologies by taking into account the micro stresses from processes such as micro machining and shot-peening

Chapter 2 reviews the literature related to primary processes such as casting and forging, thermal contact conductance, data mapping, data transfer and simulation of manufacturing chains between different FE meshes and solvers. The main goal is to identify the gaps in knowledge where innovative research can be performed. Thermal, thermo-mechanical and directional solidification aspects in casting, model design, thermo-mechanical and friction aspects in forging are reviewed. Thermal contact is identified as a potential research field which is required in both casting and forging processes. Gaps in the knowledge of the simulation of manufacturing

chains using the FEM are identified as potential areas of research development with potential applicability in industry.

Chapter 3 describes forging and casting simulations. In forging simulations, re-meshing algorithms are included for modelling the substantial plastic deformations. The elastic springback is investigated where the elastic strains are released and the residual stresses are generated. Casting simulation of a simple geometry is demonstrated. The gap formation and the gap conductance are studied and implemented in the FEA. The mould filling and the solidification criterion are investigated. Results of the residual stresses are shown and discussed.

Chapter 4 reviews an investment casting simulation of a complex aero-engine component (BCV) under equiaxed cooling. The simulation is carried out by using the FEM. Two FE solvers (ABAQUS and ProCAST) are used for performing the simulation and the results from both solvers are compared and reviewed. The main goal is to investigate the residual stresses in the BCV. Inconel 718 material is used for the ingot (BCV) and a ceramic material (sand silica) for the mould.

Chapter 5 reviews an investment casting simulation of a HPTB under directional cooling performed in vacuum in a Bridgeman furnace. The simulation is based on the single crystal (SC) and the directional solidification (DS) processes, and it is carried out by using the FEM in ABAQUS. The temperature and the residual stresses are investigated for different withdrawal velocities. The simulation is performed in a vacuum environment of the furnace where the heat transfer is achieved by cavity radiation where the view factor calculations are performed.

Chapter 6 reviews mathematical algorithms, methodologies and implementation for mapping residual stresses from micro-to-macro FE models. Residual stresses from a shot-peening simulation are mapped into a perforated parallelepiped, model with a complex surface and an industrial component of an aero-engine. The mathematical algorithms and techniques, the implementation and the results are presented in detail. The shot-peening process is simulated by performing a single shot in the middle of a parallelepiped. Different shot-peening velocities are investigated and the results are analyzed.

Chapter 7 reviews four interpolation techniques used for mapping FE data (stresses, strains, displacements, etc.) between different 2D and 3D meshes. The mathematical models and the algorithms for four different approaches; namely the nearest point method (NPM), the distance method using field of points (DMUFP), the distance method using elements (DMUE) and the method using the element shape function (MUESF) are described in detail. Comparison between all four interpolation techniques is performed and the results are reviewed and discussed.

Chapter 8 reviews the structure and the capabilities of FEDES for transferring FE data between different FE solvers. Six FE solvers are implemented in FEDES (ABAQUS, ANSYS, MARC, DEFORM, VULCAN and MORFEO). The four mapping techniques from Chapter 7 and the mapping technique from micro-to-macro FE models from Chapter 6 are incorporated in FEDES which allows data transfer between meshes with different element types, densities and scales. The design, structure and the capabilities of FEDES are described. Results from the data transfer and mapping between different FE simulations are shown. Two manufacturing chain simulations are performed by using FEDES. Manufacturing processes, such as casting, forging and heat treatment are used for the first chain simulation. The second manufacturing chain simulation consists of the following manufacturing processes: metal deposition, welding, heat treatment, machining and shot-peening.

Chapter 9 reviews the effects of the micro machining and the shot-peening residual stresses on the fatigue life. A broached specimen under three point bending is modelled using the FEM. Micro machining and shot-peening residual stresses are mapped around the notched area of the model and their influences on the low-cycle and high cycle fatigue life is investigated.

Chapter 10 contains a review of the main conclusions extracted from the previous chapters and a discussion. Finally, this chapter gives ideas of possible ways to extend the research field presented in this thesis.

CHAPTER 2

LITERATURE REVIEW

2.1 Introduction

Residual stress is a tension or compression which exists in the bulk of a material without the application of an external load (applied force, displacement or thermal gradient). Residual stresses are stresses that remain after the original cause of the stresses has been removed. They occur for a variety of reasons, including inelastic deformations, heat treatment, and cooling. Depending on the scale at which the problem is analyzed, different kinds of stresses are classically defined: macro over a few grains, stresses over one particular grain and stresses across sub-microscopic areas, say several atomic distances within a grain. Residual stress is produced by heterogeneous plastic deformations, non-uniform thermal contractions and phase transformations induced by manufacturing processes. Generally, compressive residual stress has a beneficial effect on the fatigue life and stress corrosion because it delays crack initiation and propagation. Tensile stress, on the contrary, adversely affects the mechanical performance of materials. In the elastic range, the residual stress can just be added to the applied stress as a static load.

For this reason, compression can reduce the stress level of the layers where the applied load is the high. This leads to an apparent increase of the fatigue limit. When the total stress exceeds the actual yield strength, the material is plastically deformed. This leads to a change in the residual stress field, and an adaptation of the structure to the applied load takes place. In the case of cyclic loading, cracks can initiate and propagate for a stress level much lower than the yield strength. This leads to redistribution (relaxation) of the residual stress. An accommodation of the structure to the applied load takes place. Compressive residual stress may lead to crack closure and therefore may delay crack propagation. Residual stress relaxation, due to fatigue

or annealing, and surface layer removal (machining) may produce dimensional changes of industrial components.

While uncontrolled residual stresses are undesirable, many designs rely on them. For example, toughened glass and pre stresses concrete rely on residual stress to prevent brittle failure. Similarly, a gradient in martensite formation leaves residual stress in components with particular hard and sharp edges, which can prevent the opening of edge cracks. In certain types of gun barrels made with two telescoping tubes forced together, the inner tube is compressed while the outer tube stretches, preventing cracks from opening in the rifling when the gun is fired.

2.2 Casting analyses

Casting is a process where the material is heated to its melting temperature, poured or injected into a mould with the required geometry and quenched to room temperature. As a widely used manufacturing process, a lot of research has been performed in the simulation of casting. The selection of papers presented in this section reviews a variety of thermal and thermo-mechanical FEA for obtaining the temperature field, distortions and residual stresses for different casting processes, different materials and geometries. The current research developments and trends in casting technologies and FEA are represented by a number of selected papers in this section.

2.2.1 Thermal analyses

Aydıner et al. [1] have analysed experimentally and theoretically the stress generation in bulk metallic glasses. By using a stainless steel tube as mould, thermal contact has been assured throughout casting and quenching to better define the boundary conditions of the problem. The resulting residual stresses have been measured using the crack compliance method. It has been observed that high stresses can be attained in metallic glasses due to thermal tempering: about 300 MPa compressions on the surface balanced by +150 MPa tension in the middle. The FEM has been then employed to deduce the convection heat transfer coefficient during quenching and to model the residual stress generation. The latter analysis has been performed with a

previously developed viscoelastic model. This model has been shown to be accurate within 15–30% of the experimental stress data.

Aydıner et al. [2] have studied the bulk metallic glasses (BMG) as new structural materials with impressive mechanical properties which can be cast into large dimensions. Due to the thermal tempering a significant residual stress can be generated. In this process, surface compression develops balanced with tension in the interior. To evaluate this phenomenon non-destructively, a model cylindrical stainless steel (SS)–BMG composite has been prepared and studied using neutron diffraction and FE modelling. The residual strain data from the SS obtained by diffraction have been used in modelling calculations to show that significant tempering could be achieved in the composite (about 200MPa surface compression in the SS). The strong bond between the SS and BMG allowed efficient load transfer and facilitated stress generation. The final values of the residual stresses have been seen to be relatively insensitive to the high temperature constitutive behaviour of the SS due to the physics of the thermal tempering in BMGs. The approach presented here constitutes an effective means to study non-destructively thermal tempering in BMGs.

Diószegi et al. [3] have studied the difficulties of thermal analysis induced by using one or several thermocouples, the shape of the analysed thermal field and the boundary conditions of the experimental set-up. The migration of the hot spot of a thermal field during solidification as well the migration of the thermocouples in complex shaped castings due to thermally induced stresses have been investigated. Simulation and thermal analysis have been performed on both idealized 1-D cylindrical test geometry and common industrially used 3-D thermal analysis to compare different interpretation methods.

He et al. [4] have examined the effects of thermal expansion mismatch on the residual stresses and flow response of microballoon-reinforced metal composites using the FE analyses of a unit cell model. The calculations indicated that residual tensile stresses can develop within some regions of the microballoons, despite the fact that the thermal expansion coefficient of the microballoon material is lower than that of the matrix. The magnitude of the residual tension increases as the microballoons are

brought closer together. The effects of the thermal expansion mismatch on yielding within the matrix both after cooling from the processing temperature and after mechanical loading have also been studied numerically. Preliminary comparisons have been made between the FE predictions and experimental measurements on two Ai/AI203 microballoon composites, with different microballoon wall thicknesses.

Sengupta et al. [5] have studied a comprehensive coupled thermal and stress-strain fields during the start-up of the direct chill casting process for AA5182 aluminium ingots. The heat transfer analysis incorporates the thermal boundary conditions that describe primary cooling via the mould, secondary cooling via the chill water, and ingot base cooling. To quantify the extent of secondary cooling, boiling curves that are a function of ingot surface temperature, water flow rate, impingement point temperature, and position relative to the point of water impingement have been used. Other complex heat transfer phenomena including water ejection on the vertical faces of the ingot, and water incursion into the gap at the base of the ingot have also been accounted for. The stress analysis employs a temperature dependent elastic rate-dependent plastic material constitutive behaviour to quantify the stress and strain fields inside the ingot. The model has been validated against temperature and displacement measurements obtained from two 711mm×1680mm AA5182 ingots, cast under different start-up conditions (non-typical “cold” practice and non-typical “hot” practice). The stress analysis has been further validated by residual stress data obtained from the cold cast ingot. Comparison of the model predictions with the industrial and laboratory data indicates that the model is capable of satisfactorily simulating aspects of the thermo-mechanical behaviour of the ingot during the start-up phase. The model has been applied in a preliminary way to analyze the problem of hot tearing in ingots during the start-up phase. The need for further refinement of the mesh has been identified.

2.2.2 Thermo-mechanical analyses

Kim et al. [6] have investigated and measured the thermal expansion coefficients of a 50 vol.% SiCp/Al composite prepared by a squeeze casting route from room temperature to 600◦C using thermo-mechanical analysis method, under the

conditions of as-cast, water-quenched, furnace-cooled and air-cooled. The influence of thermal processing on thermal expansion coefficient of the SiCp/Al composite has been studied in terms of thermal residual stresses generated upon cooling from the processing temperature. It has been found that the introduction of high volume fraction of SiC particles to Al matrix could notably reduce the thermal expansion coefficient of matrix, leading to the low thermal expansion coefficient values of the composite either at room temperature or at high temperature. The water-quenched and as-cast specimens present lower thermal expansion coefficients compared to the furnace cooled and air cooled ones, which is thought to be due to the difference in original thermal residual stresses within these specimens and their release during subsequent heating.

Liu et al. [7] have studied the development of thermal stresses and predicted the hot tearing and residual stresses in shaped casting. Two models have been used to carry out the stress analysis of the two stages of solidification. The rheological model has been used for the quasi-solid zone while the thermo-elasto-plastic model has been used for the period after solidification. Coupling the thermal analysis based on the FDM with the FE stress, a FDM/FEM integrated system of thermal stresses during the solidification process has been developed. The analysis result during the quasi-solid zone showed that the visco-plastic strain is an important factor for the occurrence of hot tearing. The hot tearing of a case steel casting and the residual stresses and deformation of a hydro-turbine blade steel casting have been analysed and predicted using the system.

The quality of castings is partly affected by the type and extent of residual stresses, which may lead to undesirable distortions and dimensional changes in critical parts and components. The effect of pouring temperature on residual stress in Ni-base superalloys, IN713C and U500 has been examined by Farhangi et al. [8].

Ragab et al. [9] have used a coupled thermo-mechanical FE model to simulate the die casting process. The simulation models the effect of thermal and mechanical interaction between the casting and the die. It also includes the temperature dependent material properties of the casting. Based on a design experiment, a sensitivity analysis has been conducted on the model to investigate the effects of key

factors. These factors include the casting material model, material properties and thermal interaction between the casting and the die.

Grigoriev et al. [10] have studied the effects of structure and residual stresses on the mechanical behaviour of the SiC/TiB2 multilayer composite ceramic materials. The multilayered ceramics have been obtained using the following scheme: a slip casting of thin films followed by a packet rolling and hot pressing. The use of b-SiC powders allowed SiC layers to be formed with porous structure reinforced by prismatic crystals. Such structures possess the relaxation ability of thermal strains that excludes formation of cracks during material production and provides enhanced strength of the SiC/TiB2 composite. Mechanical response of the laminated ceramic composites to static bending has been studied experimentally. A procedure for solving the inverse problem using experimental data on the deformation of a laminated ceramic composite specimen in the form of a beam has been developed. This approach allows the mechanical characteristics of the laminates to be predicted. The nonlinear stress–strain dependencies for the laminate as a quasi-homogeneous structure and for each of the two separate materials of the layers have been obtained. The modelling of the stress–strain state of the laminate was performed.

Metzget et al. [11] have studied a method to efficiently predict residual stress in foundry casting by FEM. Explicit modelling of the sand mould during stress analysis has been replaced by using locally applied boundary condition elements. Several constitutive models for the sand have been evaluated. It has been found that the plastic strain and displacements in the casting did not depend strongly on the sand constitutive model. The stress states produced, when using the new surface elements, have been in good agreement with those found using a full mould.

2.2.3 Directional solidification

Yang et al. [12] have investigated the stray grains from using a combined cellular automation-finite difference (CA-FD) model. The model has been first validated by a quantitative comparison of solute profiles and dendritic tip undercooling obtained from prior models. Then, the model has been applied to simulate dendritic growth in

the platform region of turbine blades. The influence of the withdrawal velocity and the thermal gradient on the formation of stray grains has been studied. The simulation results have shown that increasing either the withdrawal velocity or the inclination angle of isotherms increases the undercooling within the platform region, which allows the formation and growth of stray grains. The predicted dendritic microstructures using the CA-FD model offers the capability to understand the casting process for single crystal components of nickel-based superalloys at a microstructural level.

Kermanpur et al. [13] have improved the manufacturing process of a directionally solidified (DS) In738LC turbine blade, produced with the liquid metal cooling (LMC) process. The improvements have involved changing the system dimensions in the baffle area of the furnace and optimising the mould thickness, design and the withdrawal parameters. The grain structure of the DS blade shows well defined <001> crystallographic pole with few stray grains.

D'Souza el al. [14] have experimentally investigated the evolution of misorientation accompanying branching and growth of dendrite stems advancing into an increasingly undercooled liquid at a geometrical discontinuity in cross section (platform of a turbine blade) during solidification of a Ni-base supperalloy. It has been proposed that the misorientation arises from plastic deformation of the dendrite stems during growth. Low angle boundaries have been subsequently produced across impinging dendrite fronts.

Hofmann et al. [15] have investigated the grain structure for different withdrawal velocities of the directional casting in a Bridgman furnace. Results from a constant withdrawal velocity are compared to optimized withdrawal velocities as a function of the withdrawal position.

Esaka et al. [16] have developed 2D engineering model for grain selection under the condition of unidirectional solidification of alloy. The model has been applied to single crystal casting process. They have investigated the effect of the angle, width and length of pigtail to the yield rate which is defined as ratio between the number of well oriented products and the total number of trails.

Carter et al. [17] have described the process model for the grain selection occurring during the solidification of single crystal investment casting, which are used widely for a number of applications in gas turbine engines. The basis of the model has been a thermal analysis of the heat transfer in the vicinity of the chill region onto which the molten metal is poured. The competitive growth of grains during directional solidification has been simulated via a cellular-automaton technique. The thermal cycles set up around the vicinity of the grain selector have been measured. The evolution of grain structure during competitive growth have been characterised by using orientation imaging microscopy. The model has been used to study the geometrical factors influencing competitive growth and the efficacy of two designs of grain selector.

Saari et al. [18] have studied the directional solidification of gamma titanium aluminides. Aligned columnar microstructures with varying lamellar orientations within the individuals grains are produced using two gamma titanium aluminide compositions under varying process conditions. Numerical simulation of the directional solidification casting process has been employed. The orientation of the columnar grains is shown to be a function of the shape of the solidification interface while the final lamellar orientation seems to depend on the temperature gradient.

Li et al. [19] have used bottom filling principles in order to minimize turbulence in casting. X-ray radiographic video has been used to observe and compare the filling of both bottom- and top- filled moulds. Ni-based alloy investment-cast blades melted and cast in vacuum clearly have validated the bottom filling design. Compared to conventional filling in vacuum, dye penetrant indications have been reduced by approximately by factor of 10, and the hot cracking appeared to be eliminated.

2.3 Forging analyses

A metal forging process is characterized by various process parameters such as the forming sequence, shapes of the pre-form, product, and dies, friction, initial temperature distributions in the workpiece and in the dies, forming speed, die stroke, and thermal and mechanical properties of the workpiece and those of the dies. The

selection of papers presented in this section reviews a variety of thermo-mechanical FEA and process parameter investigations, such as model design and contact with friction. The selected papers reflect the current trends in research in forging simulations.

2.3.1 Model design analyses

Model design has a significant effect on the residual stresses in the components. Well thought initial design strategy for creating the required geometry plays an important role in minimising the residual stresses. During the plastic deformation in forging, elastic and plastic strains occur in the component. After relieving the load the billet springbacks and relieves the elastic strains. The magnitude of the springback depends on the component's material properties. If the springback is not taken into account during the design process, it can cause unrequited geometry and further assembly problems. Wang et al. [20] have investigated the creep and non-linear behaviour in the springback of aluminium alloys. A previous draw-bend test has revealed that the specimen shapes for aluminium alloys can continue to change for a long period following forming and unloading. The FE method has been used for simulating the creep-based time-dependent springback and experiments for non-linear deformations.

Gašper et al. [21] have aimed to improve the ventilator design in order to develop a quality product. For the selected product it has been necessary to study the residual stresses after forming and the stress state caused during the operation. Different FE software packages have been used in order to gain all the necessary information on the properties of the product.

Mungi et al. [22] have forged a simple plate from the top and the bottom side. It has been observed that by increasing the height/width ratio, the loading stress distribution becomes more inhomogeneous at the core of the workpiece and the residual stresses increase their values in this region.

2.3.2 Thermo-mechanical analyses

Precipitation-hardened aluminium alloys gain their high strength through heat treatment involving a severe quenching operation, which can have the adverse effect of introducing residual stresses. Tanner et al. [23] have used the FE method for simulating the quenching of aluminium alloy 7010 in an attempt to predict the residual stress distribution that develops in simple shapes. The rate of heat transfer from the material has been determined using the FE method to predict the heat transfer coefficient from surface cooling curves achieved experimentally. The flow stress of the material has been assumed to be strain rate dependent and to behave in a perfectly plastic manner. The predicted residual stress magnitudes and directions are compared to the values determined using the hole-drilling strain gage method and the X-ray diffraction technique.

Giuliani et al. [24] have investigated the residual macro and micro stresses in AA6061 + 22% Al_2O_3. A neutron diffraction test has been submitted to several loading/uploading conditions at different temperatures. The aim of the measurements was to establish the optimal temperature for the AA6061 + 22% Al_2O_3 workpiece during the pre-heating, before forging. A huge variation of macro stresses was not observed in the considered temperature range and 500ºC for pre-heating and 460º±20ºC for forging were chosen.

Lee et al. [25] have investigated the properties of hardness, hardening depth and residual stress of low carbon 12Cr steel after the flame hardening modification. The temperature has been controlled precisely as a function of the surface temperature and the cooling rate. The rapid cooling rate has increased the hardening depth and the surface hardness. The properties of the residual stress generated by flame hardening have been discussed in terms of contributions of both the thermal and transformation stress components. By increasing the maximum surface temperature and maximum cooling rate, decreasing of the compressive stresses occurs or tensile stresses develop with the enhanced contribution of the transformation stress component.

Robinson et al. [26] have measured the residual stresses using the X-ray diffraction technique and longitudinal split sawcat method to determine the magnitude of the residual stress that develops in aluminium alloy 7010 specimens sectioned from large open die forgings as a result of (a) quenching these specimens into water at different temperatures, and (b) cold water quenching from different furnace temperatures. Residual stress reductions as a result of retrogression, reaging and standard thermal treatments have been investigated.

The quenching of aluminium alloys by immersion or spraying using cold water produces large thermal gradients in thick components such as forgings. Whilst the rapid cooling ensures good mechanical properties, the thermal gradients can be large enough to produce high levels of residual stress. Reducing the cooling rates during the quench can reduce the magnitude of the residual stresses; however it can also be detrimental to the mechanical properties, particularly for quench sensitive alloys. By generating time temperature property C-curves for each alloy and using quench factor analysis, it is possible to slowly cool the alloy from the solution heat treatment temperature to an intermediate temperature, above the critical temperature region of the C-curve, and then quench to room temperature. The result of this is a reduction in the residual stresses generated during the quench due to a reduced thermal gradient combined with a negligible effect on the mechanical properties of the alloys.

Dolan et al. [27] has generated the C-curves for the Vickers hardness for 7175-T73, 6061-T6 and 2017A-T4. The residual stresses have been quantified for this alternative quenching route for each alloy and the Vickers hardness results have been presented. The observations have shown a reduction in the residual stress during the slow cooling period for each alloy.

Serajzadeh [28] has developed a mathematical method for evaluating temperature and strain fields as well as dynamic and static microstructure changes during the non-isothermal forging process. FE and micro-structural analyses have been coupled for predicting temperature history, velocity and strain field as well as phase transformations within the metal during and after hot forging.

Hsieh et al. [29] have performed an experimental and FE investigation on the buckling mechanism of a thin metal tube during a laser forming processes. Metal tubes made of 304 stainless steel have been heated by a CO_2 Gaussian laser beam, which has induced the buckling phenomenon on the tube surface due to elastic-plastic deformation. Due to the elastic-plastic deformation, transient angle and residual stresses of the thin metal tube under specific operation conditions have been studied.

Gao et al. [30] has used the FE method to simulate a super-plastic forming process. The distribution of residual stress and distortion within the tool were investigated in order to evaluate the damage effect of thermo-mechanical loading. The following procedures have been followed for investigating the super-plastic process.

a) The mould has been heated up to 900ºC for Ti-6Al-4V alloy
b) Clamping pressure has been applied on the boundary of the sheet in order to be clamped with the mould whose surface forms the cavity of the required shape
c) Gas pressure has been applied to the opposite surface of the sheet
d) The mould has been pulled out from the heating press for removing the formed component, and than pushed into the heating press again to form a new sheet component
e) The processes from b to d have been repeated as many times as needed for producing the required amount of components in one manufacturing campaign
f) After the forming work, the mould has been taken out exposed to ambient air so that the temperature decreases gradually down to room temperature

Giuliani et al. [31] have investigated the residual stresses in wheel hubs made of AA6061 + 22% Al_2O_{3p} and studied the effect of thermal treatment in the component. Measurements have been carried out on two identical simple shape demonstrators in order to evaluate the stress conditions after forging and T6 treatment and without taking into account the final design of the wheel hub. A general decrease of macro-stress has been observed in the points close to the surface both in the border and the central region. The hub was subjected to tensile stresses in the hoop and radial direction during its service life. The T6 treatment has induced an opposite initial residual stresses.

As a result of rapid quenching, residual stresses can develop and leave the material in an unsuitable condition for further operations and services. The quenching creates severe thermal gradients acting as a source of inelastic strains leading to compressive residual stresses near the surface and tensile stresses in the core. Tanner et al. [32] have investigated the stretching and cold compression techniques for relieving the residual stresses caused by the quenching. A model of each of the stress relieving techniques has been compared by observing stress magnitudes and by using the FE model to predict the results from the layer removal technique.

Prime et al. [33] have used the cold-compression stress relief process and measured the residual stresses. The following sequences have been simulated by using the FE method. First, a thermal analysis simulated the quenching using appropriate thermal boundary conditions and temperature dependent material properties. Second, a structural analysis used the thermal history and a temperature and strain-rate dependent constitutive model to predict the stresses after quenching. Third, the structural analysis have been continued to simulate the multiple cold compressions of the stress relief process. Experimentally, the residual stresses have been mapped using the contour method, which involves cutting the forgings using a wire and then measuring the contours of the cut surface.

2.3.3 Contact analyses

Friction between the workpiece and the die plays an important role in the forming force and strain distribution in the forged parts. By increasing the friction coefficient, the loading stress distribution becomes more inhomogeneous and the value of the residual stress increases everywhere in the workpiece. Mungi et al. [22] have forged a simple 2D plate and observed that the highest residual stresses have been located around the edges of the specimen. Further, at higher friction coefficient, the residual stress pattern approaches the sticking friction condition. Lubricants have been applied between the billet and the punch for decreasing the friction and respectively the residual stress [34].

Jang et al. [35] investigated a radial forging in hollow shafts assuming that the workpiece undergoes elastic-plastic behaviour during the cold forging process. The FE method has been used for defining the residual stresses in axial, radial and hoop direction. Coulomb friction law has been applied in the contact area between the workpiece and the die as follows:

$$F_s \leq \pm \mu F_n \tag{2.1}$$

where F_s is the sliding force, F_n is the normal force and μ is the coefficient of friction. Tensile residual stresses were observed in the outer surface of the forged hollow shaft and compressive residual stresses in the inner surface. The highest tensile stress of the surface has been located in axial direction.

Quach et al. [36, 37] have used the FE method and laboratory measurements for predicting the residual stresses in press-braked thin-walled sections. The effects of coiling and uncoiling have been accounted for analytically, with the resulting residual stresses specified as the initial stresses in a subsequent FE simulation of cold bending. The method has provided residual stress distribution over the cross-section as well as across the thickness. The maximum residual stresses have occurred in the corner region and away from the surfaces, and their values have been higher than those at the surfaces.

Fogarassy et al. [38] have performed Neutron and X-ray diffraction measurements in near-net shape formed conical specimens of yttria partial stabilised zirconia in order to evaluate the level of residual stress induced by the manufacturing process. A preliminary FE analysis has been also carried out. In all three analysed specimens it has been observed that compressive stresses form in the axial direction, tensile stresses in the tangential direction and negligible stresses in radial direction.

Cho et al. [39] have simulated a powder forging process for cup-shaped Al 6061 aluminium products using the FEM. The mechanical behaviour of the powder has been assumed to obey the isotropic compressible viscoplasticity, while the thermal behaviour of the powder has been effectively modelled by a non-linear transient heat transfer problem. Through the numerical simulation, the distribution of the stresses has been determined. The highest values have been located in the web-rib corner of the simulated piston.

2.4 Thermal contact conductance

All engineering surfaces exhibit some level of microscopic roughness. The resistance to heat flow through a contact interface occurs because only a small portion (usually 1-2%) of the nominal surface area is actually in contact [40]. Heat may pass through the interface via three paths: conduction through the contact spots, conduction through the gas present in the gap between the surfaces, and radiation across the gap [41]. Convection may be neglected due to the small length scales involved. Also, radiation does not play a significant role at temperatures below 500°C [42].

Cooper et al. [43] have studied the resistance to the heat flow between two thick solid bodies in contact in a vacuum. Existing analyses of single idealized contacts have been summarized and compared, and then applied, together with results of recent electrolytic analogue tests, to predict the conductance of multiple contacts. Reconsideration of the theory of interaction between randomly rough surfaces shows how the parameters required for predicting the heat transfer can be determined in principle by simple manipulation of typical profiles of the mating surface, together with an approximation from deformation theory. It has been also shown that this process depends more crucially than had been realized upon the distribution of the few high peaks of the surfaces, where the assumption of Gaussian distribution of heights has been suspect. In place of that assumption, the use of describing functions is suggested. The few experimental data relevant to these theories have been examined and compared with predictions of theory.

Madhusudana [44] has investigated the heat flow across a joint formed by two concentric cylinders which depends not only on the geometrical, thermo-physical and surface properties of the cylinders but on the heat flux and maximum operating temperatures. An analysis has been presented in which it was shown that, depending on the heat flow direction, the contact may be reinforced or completely relaxed during operation. These results were consistent with previous experimental observations of other workers in this area.

Fuller et al. [45] have developed an analytical model for prediction of thermal joint conductance for both thermo-plastic and electrometric polymers placed between metallic solids. The assumption included nominally flat contacting surfaces, uniform pressure distribution at the interface, elastic deformation of the polymer layer and asperities, and vacuum environment.

Lee et al. [46] have investigated an indirect squeeze casting process applied to a wrought 5083 Al alloy (Al_ 4.7Mg_ 0.7Mn) experimentally and numerically. A two-dimensional FE analysis for fully coupled heat transfer and deformation analysis, using ABAQUS has been used to simulate the cooling curves obtained from the experiments. Thermal contraction of the material during solidification creates an air gap between the mould and the cooling material. The formation of this air gap was explained using the calculated results. The experimental and predicted results are discussed in conjunction with the relationships between the cooling rate, microstructure, die geometry and applied pressure.

Wahid et al. [47] have carried out an experimental investigation of the effects on joint conductance of progressive loading and unloading, cyclic loading and overloading to a predetermined value. In all cases a hysteresis loop has been seen to exist for the loading unloading cycle and has been seen to decrease with increasing number of cycles. The conductance values eventually appeared to settle down to values higher than those obtained during first loading. Enhancement of contact conductance by cyclic loading has been found to be rather small. On the other hand, overloading the test pairs to a predetermined contact pressure has been found to be promising.

The heat transfer across a joint depends on surface finish, surface flatness, thermal conductivity of the contacting metals, contact pressure at the interface and the hardness of the softer of the two solids forming the joint. Again Wahid et al. [48] have studied the effects of surface topography and mean interfacial temperature on the thermal contact conductance (TCC) of stainless steel pairs at a low contact pressure of 0.43 MPa. Data for solid spot conductance has been generated by conducting tests in a vacuum environment. The vacuum level has been maintained at 300 mbar. There has been no significant change in TCC over the range of mean

interface temperatures 40–100 ºC. The experimental results have been compared with the experimental results from [43] and the prediction of the authors deduced from the deformation analysis. It is demonstrated that the ratio of surface roughness to slope and not roughness alone is the appropriate parameter to be taken into account in evaluating contact heat transfer.

Singhal et al. [49] have developed a predictive model for estimating thermal contact conductance between two nominally flat metallic rough surfaces, which has been experimentally validated. The predictive model consists of two complementary parts, the first of which is a surface deformation analysis to calculate the actual area of contact for each contact spot, while the second accounts for the effects of constriction resistance and gas gap conductance between the contacting surfaces. The constriction resistance values for all the contacting asperities have been used to calculate the total thermal contact conductance. An experimental facility has also been constructed to measure thermal contact conductance of interfaces to verify the results of the predictive model.

Xu et al. [50] have studied experimentally the thermal contact conductance with pressed pairs of aluminium alloy 5052 and stainless steel 304 over the low temperature range from -118 to -63 ºC, with nominal contact pressure from 1 to 7 MPa. The contact surfaces have been prepared through bead blasting. From the measured results, thermal contact conductance over this temperature range (-118 to -63 ºC) was less than that near or above room temperature. The load sensitivity at low temperature was less than that at room temperature.

2.5 Manufacturing chain simulation. FE data mapping and transfer

Fernandes et al. [51] have developed an algorithm for automatic generation of all-hexahedral meshes, which represent the deformed geometry of a workpiece during updated Lagrangian FE calculations without losing geometrical and mechanical consistency. The addressed topics include the extraction of the basic geometrical features, contraction of the core mesh, generation of a boundary mesh linking the

core with the surface of the workpiece, applications of smoothing procedures to edges and transfer of field variables from the old to the new mesh. The transfer of the field variables is made in the following sequence. (a) The field variables from the Gauss points are extrapolated to the nodal values by using a least square fitting. (b) Identifying for each nodal point of the new mesh the element of the old mesh in which the nodal point falls. (c) Performing the mapping form the old to the new mesh by using the shape function of the elements.

Dureisseix et al. [52] have transferred information between non-matching FE meshes. The work concerns a transfer of FE variables defined at the integration points of the meshes by using only local element-by-element matrices.

Luo [53] has proposed nearest-nodes finite element method (NN-FEM) where the finite elements have been used only for numerical integration while the shape functions are constructed in a similar way as in meshless methods, i.e. by using a set of nodes that are the nearest to a concerned quadrature point. A local multivariate Lagrange interpolation method has been used to construct the shape function. This method has the following attractive features: (a) It can be used to interpolate irregularly distributed data points; (b) It does not need to solve local problems;

Hyun et al. [54] have demonstrated different meshing capabilities when simulating a chain of manufacturing processes by using an in-house FE code. A billet made of stainless steel SS316L has been forged, heat treated and cut. The billet is modelled as an axisymmetric model and meshed with 2D 4 or 8 node quadrilateral elements. The forging process has been performed by pressing an upper tool towards a billet and having a fixed lower tool. The process has been simulated as a quasi-static analysis where the inertia and the elastic springback have been ignored. Remeshing has been used by creating a new mesh and transferring the nodal and integration point data from the old to the new mesh. The heat treatment starts by removing the tools from the forging simulation. The elements around the surface are created to prepare the model for the cutting process. The cutting has been performed by automatically removing elements from the model. Thus elements with residual stresses are removed but the cutting has not been simulated.

Pietrzyk et al. [55] have performed a manufacturing chain simulation of the M14 bolt which involves heat treatment, drawing, multi step forging, machining and rolling. Forge 2005 FE code has been used to carry out the manufacturing chain simulation. Heat treatment of the material to obtain uniform grain size has been the first step in the manufacturing chain. It has been followed by drawing, which is a typical sizing operation to obtain proper dimensions of the piece. The piece has been further used for forging in two steps. Crop of the allowance material has been performed in the next stage of the production chain. Finally the obtained part has been subjected to rolling operation.

Jahansson et al. [56] have developed a system to manage the simulation information of manufacturing processes, such as mesh information, boundary conditions and process parameters. The system has been used to predict simulation of cutting process using mesh information and process parameters from the database which is embedded in the system that uses a conceptual EXPRESS scheme. EXPRESS is an information modelling language. The system has functions for importing and exporting data in ASCII based STEP Part 21 files defined by the step standard and represented as an EXPRESS scheme. Data import is managed through input files based on the universal file format while data export in a format suited for input for MARC FE commercial code using user defined FORTRAN subroutines. For development of the input routines for data based on the universal file format, a commercial parser (a program that breaks large units of data into smaller units) has been used to parse the EXPRESS data model into C++ classes. Those classes have been used as the basis for the universal file import routines. Two examples have been demonstrated. The first example shows how mesh information can be extracted from the database and visualized. The second uses the system to produce error estimation concerning the cutting path in the method of element deactivation used to simulate cutting. 2D data has been used for both examples.

The papers reviewed in this section represent the main body of research into the simulation of manufacturing chains using FE software.

2.6 Aims of research

The primary manufacturing processes such as forging and casting are well-described in the literature as reviewed in the previous sections. The thermal contact conductance is also well-studied by many researchers. Research for precise simulation of investment casting by implementing the thermal gap conductance into the FEA of complex industrial components subjected to equiaxed cooling is identified as a potential research field.

As reviewed, most of the research carried out in single crystal and directional solidification castings is focused on investigating the dendrite growth and the microstructure. Previous work on the residual stress prediction of castings under directional cooling by using the FEM is limited. Creating the methodology and performing FE simulation of a high pressure turbine blade casting under directional cooling to obtain the residual stresses is identified as a potential research field. The influence of the withdrawal velocity of the Bridgman furnace on the temperature and the residual stresses is the main parameter to be investigated in this work.

Very little has been found in the literature on the simulation of manufacturing chains using numerical methods. Some researchers have performed a simulation of a manufacturing chain by using identical meshes in the same FE code. This can lead to some restrictions if there is a process in the chain which cannot be simulated with the corresponding FE code or the element type is not suitable for one part of the chain simulation. Some research in FE data mapping and data transfer between non-matching meshes has been performed for simple benchmarks. Very little has been found for data transfer between different FE codes. To the best of the author's knowledge, there has been no previous research on mapping micro FE data to macro FE models, for example mapping residual stresses from a shot-peening process to macro FE models. The simulation of manufacturing chains with different FE codes, different meshes and element types is identified as a major gap in the literature where new research can be dedicated.

The simulation of manufacturing chains requires development of tools and mathematical algorithms for performing the mapping between non-matching meshes and FE codes. There is a need of developing mathematical algorithms for mapping micro FE data to macro FE models in order to include the processes simulated on micro scale geometries, such as shot-peening, roller-burnishing, micro-machining, etc. All these mentioned issues need to be embedded in a user friendly and robust system. Creating such a system can be beneficial to simulate any manufacturing chain in industry, create a final residual stress state and distortions of the simulated components where the components life can be predicted more accurately.

CHAPTER 3

RESIDUAL STRESS INVESTIGATION IN CASTING AND FORGING ANALYSES

Forging simulation is performed in static and dynamic analyses where the inertia is taken into account. Re-meshing algorithms are included for overcoming large plastic deformations. The elastic springback is investigated in a static analysis where the elastic strains are released and the residual stresses are obtained. Casting simulation of a parallelepiped is demonstrated. The gap formation and the gap conductance between the ingot and the mould are studied and implemented in the FEA. The mould filling and the solidification criterion are investigated. Results of the residual stresses are discussed.

3.1 Introduction

The primary manufacturing processes, such as forging and casting, are widely used in industry. The numerical simulation of these processes is beneficial in terms of saving time and cost for obtaining the optimum results. The FEM is used for investigating the residual stresses after forging and casting. The commercial FE package ABAQUS [57] is used to carry out the simulations.

Investigations of the elastic springback, the re-meshing and the inertia are taken into account in the forging simulation. The elastic springback occurs when the load is removed and the component releases its elastic strains. The re-meshing technique is used when substantial plastic deformations are expected. The inertia is taken into account by using a dynamic analysis using an explicit code in ABAQUS.

The explicit dynamic analysis is based on the implementation of an explicit integration rule together with the use of diagonal element mass matrices. The

equations of motion for the body are integrated using the explicit central-difference integration rule [58].

$$\dot{u}^N_{\left(i+\frac{1}{2}\right)} = \dot{u}^N_{\left(i-\frac{1}{2}\right)} + \frac{\Delta t_{(i+1)} + \Delta t_{(i)}}{2} \ddot{u}^N_{(i)} \tag{3.1}$$

$$u^N_{(i+1)} = u^N_{(i)} + \Delta t_{(i+1)} \dot{u}^N_{\left(i+\frac{1}{2}\right)} \tag{3.2}$$

where u^N is a degree of freedom (a displacement or rotation component) and the subscript *i* refers to the increment number in the explicit dynamic step. The central-difference integration operator is explicit in the sense that the kinematic state is advanced using known values of $\dot{u}^N_{\left(i-\frac{1}{2}\right)}$ and $\ddot{u}^N_{(i)}$ from the previous increment.

The key to the computational efficiency of the explicit procedure is the use of diagonal element mass matrices because the accelerations at the beginning of the increment are computed by [58].

$$\ddot{u}^N_{(i)} = \left(M^{NJ}\right)^{-1} \left(P^J_{(i)} - I^J_{(i)}\right) \tag{3.3}$$

where M^{NJ} is the mass matrix, P^J is the applied load vector, and I^J is the internal force vector.

The effect of the gap conductance and the mould filling are investigated in the casting simulation. The gap conductance is implemented in ABAQUS by the user-defined GAPCON subroutine. The residual stresses are obtained by air cooling where the gap conductance and the mould filling are taken into account.

3.2 Forging simulation

3.2.1 Geometry and FE model

The forging model is generated by using ABAQUS/CAE [59]. Two assembled parts (billet and punch) define the FE model. Figure 3.1 shows the overall dimensions of the model. The billet is a quarter of a cylinder with radius of 25 mm and a height of 10 mm. The punch is a half sphere with radius of 20 mm. The punch is generated

as a rigid body with reference point RP. The reference point represents the punch where the boundary conditions and the loads are applied. Eight node linear hexahedron elements with reduced integration and hourglass control, C3D8R from the ABAQUS library [57], are used for the billet mesh. The number of the elements is 40,000.

3.2.2 Boundary and contact conditions

Figure 3.1 shows the boundary and the contact conditions applied to the model. A reference point RP which presents the punch is located in the centre of the sphere. In order to move the punch only in the y direction, the following boundary conditions are applied to the reference point RP:

- Zero displacements in the x and the z directions
- Zero rotations in the x-y, y-z and x-z planes
- A velocity of 200 mm/s is applied to the reference point in the y direction

The following symmetry boundary conditions are applied to the billet:

- Zero displacements in the x direction to all nodes belonging to surface S_1
- Zero displacements in the y direction to all nodes belonging to surface S_3
- Zero displacements in the z direction to all nodes belonging to surface S_2

In order to move the punch by 5 mm, in the negative y direction, having a velocity of 200 mm/s, a step time of 0.0025 seconds is chosen for the analysis. Contact is defined between surfaces S_4 and S_5. A friction coefficient of 0.2 is used in the contact area.

3.2.3 Material properties

Table 3.1 shows the material properties of the billet used in the forging analysis. The billet material model is an elastic-plastic with linear isotropic hardening. The punch is modelled as an analytical rigid body.

3.2.4 Loading sequence of the simulation

The simulation is carried out in two steps. In the first step, the punch is moved by 5 mm in the negative y direction which deforms the billet. This step is simulated by using a static analysis in ABAQUS/Standard and a dynamic analysis in ABAQUS/Explicit for compression purposes. The purpose of using both FE codes is to examine the effect of the inertia due to the punch velocity by comparing the results from the static and the dynamic analyses. Also, the effect of the re-meshing is investigated in ABAQUS/Explicit. The second step is run as a static analysis in ABAQUS/Standard. In this step the punch is removed which allows the billet to springback and release the elastic strains which creates the residual stresses.

3.2.5 Results and discussion

The results are presented in two sections. Results determined due to the plastic deformation when the punch in moved into the billet and due to the springback when the punch is removed.

Plastic deformation

Figure 3.2 shows the Von Mises stresses in the billet obtained in ABAQUS/Standard and ABAQUS/Explicit. It can be seen that a similar stress distribution obtained in both codes. The peak stresses determined in ABAQUS/Explicit have slightly higher values, less than 0.5%. This is because ABAQUS/Explicit takes into account the mass calculations and respectively the inertia.

Elastic springback

The springback analysis is simulated in ABAQUS/Standard. The saved results from the step where the punch is moved into the billet are imported as an initial condition into a static step for analysing the elastic spring-back. Figure 3.3 shows the residual Von Mises stresses after the spring-back. The peak Von Mises stresses decrease from around 266 MPa to 175-181 MPa. It is worth mentioning that the dynamic analysis using explicit integration is many times faster and shows better convergence than the static analyses using implicit integration. The inertia did not

influence the residual stresses for this FE model and material properties. Using a re-meshing did not change the results significantly which means that the mapping algorithms during re-meshing are reliable. Therefore re-meshing can be used for models with large plastic deformations. Based on the performed analyses, it can be concluded that the forging analysis can be performed in a dynamic explicit analysis using re-meshing in the case of large plastic deformations and performing the elastic springback in a static analysis.

3.3 Thermal contact

For accurate simulation of the casting, hot and warm forging processes, attention must be paid to the thermal contact conductance. The thermal contact can be treated as either contact between two surfaces touching each other (perfect contact) or surfaces with a gap between them. In the FE modelling, the contact is defined between two nodes or a node from the slave surface and a projection of this node to the nearest element face from the master surface. Using the FEM the gap conductance coefficient must be specified for achieving the heat transfer between two interfaces in a contact.

3.3.1 Theoretical background of gap conductance

Figure 3.4 shows contact between two interfaces represented by nodes 1 and 2 with temperatures T_1 and T_2 with distance d between them. A gap between two solids exists when d > 0. This gap is typically filled with air or another gas. The gap heat transfer is defined by the summation of the gas conductance heat transfer and the radiation heat transfer between two solids or nodes 1 and 2 in this case.

$$q_g = q_c + q_r \tag{3.4}$$

where q_g is the gap heat transfer, q_c is the gas conductance heat transfer and q_r is the radiation heat transfer.

The gas conductance heat transfer can be given by [41].

$$q_c = \frac{k_g (T_1 - T_2)}{d} \tag{3.5}$$

where: k_g is the conductance coefficient of the gas, T_1 and T_2 are the temperatures at nodes 1 and 2, and d is the gap clearance.

If the roughness of the surfaces and the temperature jump distances from the kinetic theory are taken into account then Equation (3.5) can be given by:

$$q_c = \frac{k_g (T_1 - T_2)}{d + d_r + g_1 + g_2} \tag{3.6}$$

where: d_r is related to the roughness of the two contacting surfaces and g_1 and g_2 are the temperature jump distances for nodes 1 and 2 of the contacting pair which are given by Kennard [60]:

$$g_1 = \frac{k_g}{P_g} \frac{(2-a)}{a} \left(\frac{2\pi T_1}{R} \right)^{1/2} \left(\frac{\gamma - 1}{\gamma + 1} \right) \tag{3.7}$$

$$g_2 = \frac{k_g}{P_g} \frac{(2-a)}{a} \left(\frac{2\pi T_2}{R} \right)^{1/2} \left(\frac{\gamma - 1}{\gamma + 1} \right) \tag{3.8}$$

where: k_g is the conductance coefficient of the gas, P_g is the gas pressure, R = 8.3144 kJ is the universal gas constant, a is the accommodation coefficient (fraction of heat transferred between the surface and the molecule), γ is the specific heat ratio, T_1 and T_2 are the temperatures in nodes 1 and 2.

The radiation heat transfer between two nodes in contact is given by [41]:

$$q_r = f\sigma(T_1^4 - T_2^4) \tag{3.9}$$

where: f is the radiation factor, $\sigma = 5.6697 \times 10^{-8}$ W/(m^{2}K^4) is the Stefan-Boltzmann constant, T_1 and T_2 are the temperatures in nodes 1 and 2 and they must have units in Kelvin.

The radiation factor in a bisurface system is given by [41].

$$f = \left(\frac{\rho_1}{\alpha_1} + \frac{1}{F_{1-2}} + \frac{A_1}{A_2} \frac{\rho_2}{\alpha_2} \right)^{-1} \tag{3.10}$$

where: ρ_1 and ρ_2 are the density, α_1 and α_2 are the thermal diffusivities, A_1 and A_2 are the cross sectional areas for surfaces 1 and 2 and F_{1-2} is the view factor.

The view factor F_{1-2} between parallel plates is equal to one [41]. The two cross section areas are equal ($A_1 = A_2$) for FE contact modelling between two nodes and the radiation factor can be given by:

$$f = \left(\frac{\rho_1}{\alpha 1} + 1 + \frac{\rho_2}{\alpha_2} \right)^{-1} \tag{3.11}$$

The radiation factor can be given as a function of the emissivity [41]:

$$f = \left(\frac{1}{\varepsilon_1} + \frac{1}{\varepsilon_2} - 1 \right)^{-1} \tag{3.12}$$

where ε_1 and ε_2 are the emissivity coefficients for surfaces 1 and 2.

3.3.2 Implementing the gap conductance in FE models

The theory behind the gap conductance is implemented in ABAQUS by using the user defined GAPCON subroutine. The heat transfer between contacting interfaces in ABAQUS is defined as:

$$q = h(T_1 - T_2) \tag{3.13}$$

where q is the heat transfer between corresponding nodes 1 and 2, h is the gap conductance.

The heat transfer equilibrium equation according to the ABAQUS definition and the theoretical definition can be given by:

$$q = q_g = q_c + q_r \tag{3.14}$$

or

$$h(T_1 - T_2) = \frac{k_g (T_1 - T_2)}{d + d_r + g_1 + g_2} + \left(\frac{1}{\varepsilon_1} + \frac{1}{\varepsilon_2} - 1 \right)^{-1} \sigma (T_1^4 - T_2^4) \tag{3.15}$$

The following assumptions are made in Equation (3.15):

- During pouring, in casting, the contact is between solid and liquid, which means that the liquid will be in full contact with the mould surface and both surfaces will have the same roughness, where $d_r = 0$

- In macro scale simulations the surface jump distances can be neglected because their influence is insignificant, where $g_1 = 0$ and $g_2 = 0$. This conclusion is based on the following example.

Example:

The temperature jump distance from Equation (3.7) is calculated using air properties for a temperature of 1000 ºC [41]. The accommodation coefficient can vary from 0 to 1, where an average value of 0.5 is used.

- Surface temperature T = 1000 ºC
- Accommodation coefficient $(0 \leq a \leq 1)$ $a = 0.5$
- Air specific heat ratio $\gamma = 1.321$
- Air gas pressure (atmospheric) $P_g = 0.1$ MPa
- Air conductance coefficient $k_g = 0.083$ W/mºC
- Universal gas constant R = 8.3144 kJ

$$g = \frac{0.083}{0.1\times10^{6}}\frac{(2-0.5)}{0.5}\left(\frac{2\pi 1000}{8.3144\times10^{3}}\right)^{1/2}\left(\frac{1.321-1}{1.321+1}\right) = 0.31\times10^{-6}\,m$$

The conclusion from this example is that the temperature jump distance is smaller than 1 μm and can be neglected for the macro scale models. However, it can have a more significant influence for thermal contacts in micro scale models.

The gap conductance coefficient from Equation (3.15) after the applied assumptions can be given by.

$$h = \frac{k_g}{d} + \left(\frac{1}{\varepsilon_1} + \frac{1}{\varepsilon_2} - 1\right)^{-1} \sigma\left(\frac{(T_1^{\,4} - T_2^{\,4})}{T_1 - T_2}\right) \tag{3.16}$$

The gap conductance coefficient from Equation (3.16) is implemented into the user defined GAPCON subroutine. This subroutine is called in each time increment of the coupled temperature-displacement analyses in ABAQUS. Contact in ABAQUS can be defined between a node from the slave surface and the nearest node to it from the master surface, when node to node contact is selected, or between a node from the slave surface and the projection of this node to the nearest element face of the

master surface, when node to surface contact is applied. When the GAPCON subroutine is called, it provides the following variables for solving Equation (3.16):

- Distance clearance d
- Temperatures T_1 and T_2 of the contacting nodes 1 and 2

The known and the unknown variables from Equation (3.16) for defining the gap conductance coefficient can be given by:

Known variables:

- Distance clearance d
- Temperatures T_1 and T_2 for nodes 1 and 2.
- Stefan-Boltzmann constant $\sigma = 5.6697\times10^{-8}$ W(m^2K^4)

Unknown variables:

- Emissivity for surface 1 ε_1
- Emissivity for surface 2 ε_2
- Gas conductance coefficient k_g

Variables to be defined:

- Gap conductance coefficient h

The gas temperature T_g is calculated as an average value of the temperatures T_1 and T_2 for the corresponding nodes 1 and 2.

$$T_g = \frac{T_1 + T_2}{2} \tag{3.17}$$

Data for temperature dependant gas conductance coefficient is included in the GAPCON subroutine. After linear interpolation for the corresponding gas temperature, the gas conductance coefficient is obtained. The following example clarifies the problem by using air as the gas in the gap. When the gas temperature (air in this example) is calculated from Equation (3.17) then the gas conductance coefficient is obtained by linear interpolation (see Figure 3.5). For clarification of the linear interpolation, the area A is enlarged and the two nodes between which the linear interpolation is performed are named as node M and N. After performing the linear interpolation the conductance coefficient of the air is calculated for the

corresponding temperature at node X. For defining the emissivity coefficients ε_1 and ε_2 for surfaces 1 and 2, a linear interpolation is used as well. Equations 3.18 and 3.19 show the emissivity as a function of the temperature.

$$\varepsilon_1 = f(T_1) \tag{3.18}$$

$$\varepsilon_2 = f(T_2) \tag{3.19}$$

In perfect thermal contact ($d = 0$) Equation (3.16) becomes indefinite i.e.

$$h = \infty \tag{3.20}$$

This means that a very large value must be assigned for h. It must be taken into account that very large values for h can cause numerical problems in the FE solver. In high pressure die casting, for pressure applied to the liquid metal is in range 10 – 100 MPa the h is known to be 50 – 100 kW/m^{2}C^o [61]. Therefore the maximum value of 50 kW/m^{2}C^o is applied for h, where the contact pressure is caused mainly by the gravity. This value is applicable in perfect contact and when the gap separation is very small.

3.4 Casting simulation

The main goal of the casting analysis is to obtain accurate residual stresses. The simulation is performed in two stages. First, thermal analysis is performed where the mould filling and the ingot solidification criteria are taken into account. The temperature distribution of the mould and the ingot, when the solidification of the ingot has begun, is passed as an initial condition to the coupled temperature-displacement analysis. The coupled temperature-displacement analysis takes into account the initial temperature coming from the thermal analysis and the gap conductance for calculating the residual stresses and the distortions of the model.

3.4.1 Geometry and FE model

The model has been generated using ABAQUS/CAE. Two assembled parts define the final geometry of the model. The part which represents the mould has a parallelepiped form with an extruded cavity in the middle (see Figure 3.6). The overall dimensions are:

- width (w) = 200 mm

- height (h) = 140 mm
- cavity width (w_c) = 160 mm
- cavity height (h_c) = 120 mm
- wall thickness (th) = 20 mm

The wall thickness can be given by:

$$th = \frac{w - w_c}{2} \quad \text{or} \quad th = h - h_c \tag{3.21}$$

The second part which represents the ingot has a parallelepiped geometry with dimensions:

- width (w_c) = 160 mm
- height (h_c) = 120 mm

For both, the thermal and the coupled temperature-displacement analyses, hexahedron elements with eight nodes are used (see Figure 3.7). Heat transfer linear elements DC3D8 are used for the thermal analysis and trilinear temperature-displacement elements with reduced integration and hourglass control C3D8RT are used for the temperature-displacement analysis from the ABAQUS library. The ingot has 18,816 hexahedron elements, while the mould has 12,396 hexahedron elements.

3.4.2 Material properties

Temperature dependant material properties are used for both thermal and coupled temperature-displacement analyses. The mould is modelled with steel P91 material obtained elsewhere [62]. The ingot is modelled with Inconel 718 nickel based alloy. Thermo-physical temperature dependent material properties are used for the Inconel 718 alloy, such as thermal conductivity [63], specific heat capacity [63] and density [64, 65]. A latent heat of 145 kJ/kg, melting temperature of 1336 ºC and solidus temperature of 1260 ºC are used [66]. The expansion coefficient, elastic modulus, Poison's ratio and the yield strength material data are obtained elsewhere [67-73]. The yield and the ultimate stresses at room temperature are respectively 890 MPa and 1252 MPa.

3.4.3 Boundary and initial conditions

The boundary and the initial conditions are described separately for the thermal and for the coupled temperature-displacement analyses. Figure 3.8 shows the surfaces on which the boundary and the initial conditions are prescribed for both simulations.

It can be seen from Figure 3.8 that the ingot is defined by six surfaces S_1, S_2, S_3, S_4, S_5 and S_6. Points P_5, P_6, P_7 and P_8 are located in the middle of the corresponding edges. The mould is defined by eleven surfaces, six external and five internal. The external surfaces are defined in Figure 3.8 by S_7, S_8, S_9, S_{10}, S_{11} and S_{12}. The internal surfaces are defined by names S_{7in}, S_{8in}, S_{9in}, S_{10in} and S_{12in} where each of them is located parallel to the corresponding external surface. For example, the internal surface S_{7in} is parallel to the external S_7, S_{8in} to S_8, S_{9in} to S_9, S_{10in} to S_{10} and S_{12in} to S_{12}. Points P_1, P_2, P_3 and P_4 are located in the middle of the corresponding edges of the mould.

Thermal analysis

The following thermal conditions are applied to the model:

- Initial temperature of the ingot (poring temperature) = 1475 ºC
- Initial temperature of the mould (mould preheating) = 1050 ºC
- Contact defined between surfaces S_1-S_{7in}, S_2-S_{8in}, S_3-S_{9in}, S_4-S_{10in} and S_6-S_{12in} is applied as inactive (contact activation is performed during mould filling)
- Gap conductance coefficient of 50 000 W/m2ºC is applied between the contacting surfaces. This means that the contact is considered to be perfect
- Convection is applied to surfaces S_5, S_7, S_8, S_9, S_{10}, S_{11} and S_{12} where the convection is inactive on surface S_5 (activation is performed in the end of the mould filling process)

Coupled temperature-displacement analysis

The following thermo-mechanical conditions are applied:

- The mould and the ingot initial temperatures are imported from the thermal analysis after performing the mould filling and the solidification criterion.
- The contact defined between surfaces S_1-S_{7in}, S_2-S_{8in}, S_3-S_{9in}, S_4-S_{10in} and S_6-S_{12in} is applied as active
- The gap conductance coefficient from Equation (3.16) is implemented into the user defined GAPCON subroutine
- The convection is applied to surfaces S_5, S_7, S_8, S_9, S_{10}, S_{11} and S_{12}
- Zero displacements in the x direction are applied at points P_2, P_4, P_6 and P_8
- Zero displacements in the y direction are applied at points P_1, P_3, P_5 and P_7
- Zero displacements in the z direction are applied at all nodes of surface S_{12}
- A gravity of 9.81 m/s^2 is applied to the ingot which keeps the bottom surface in contact with the mould

3.4.4 Simulation sequence and results

The casting modelling is carried out in two consecutive simulations, thermal and coupled temperature-displacements analyses. Figure 3.9 illustrates the sequence of the simulations.

Thermal analysis

The thermal analysis is performed in ABAQUS/Standard. The main goals in this analysis are:

- Modelling of the mould filling
- Performing a solidification criterion where the temperature history is imported into the coupled temperature-displacement analysis as an initial temperature
- Quenching to room temperature

The mould filling is considered in the thermal analysis. The mould filling process lasts three seconds. An initial temperature of 1475 ºC is applied to the ingot and contact is defined between the ingot and the mould which is initially inactive. The ingot is split in twelve layers as shown in Figure 3.10. The contact between the

mould and the ingot layers is activated in separate steps. The time for each step is defined by proportion between the mould filling time and the number of steps as follows:

$$t_s = \frac{t_m}{L_{num}} \tag{3.22}$$

where t_s is the step time, t_m is the mould filling time and L_{num} is the number of the layers. The step time can be calculated for this case as:

$$t_s = \frac{3}{12} = 0.25s \tag{3.23}$$

Table 3.2 shows the sequence of the contact pair activation of all surfaces belonging to the corresponding layer with the mould. The convection is activated on surface S5 (see Figure 3.8) in step 12. The quenching to room temperature is achieved in step 13. The solidification criterion is performed during the quenching process. This criterion is based on observation of the temperature variation of the ingot. Figure 3.11 shows the temperature distribution for half of the model for each step during the contact activation between the mould and the ingot layers for the corresponding step. The contact activation allows a heat transfer between the ingot and the mould. As it can be seen from Figure 3.11, the ingot and the mould temperatures remain unchanged in the places where the contact between the mould and the layers of the ingot are inactive.

Knowing the solidus temperature for the ingot material (Inconel 318) which is equal to 1260 ºC and the temperature distribution contour, it can be used as an activation criterion for indicating the beginning of forming a thin solid layer of the ingot. The main idea of performing a solidification criterion is to define when the ingot starts solidifying and separating from the mould. When this moment is detected then the temperature distribution for the thermal model is transferred to the coupled temperature-displacement analysis where the gap formation, the gap conductance, the ingot shrinkage, the mould expansion and shrinkage and the residual stresses are investigated. Figure 3.13 shows the temperature along the path AB (see Figure 3.12) for different quenching times in step 13. It can be seen that the ingot in the down side and the middle side of the path AB is solid in step 13. The temperature in the upper side of the path remains solid for times greater that 0.25s. This means that solid thin frame formation has begun in the ingot and a gap formation starts between

the mould and the ingot. The temperature distribution is saved and transferred as an initial temperature condition into the coupled temperature-displacement analysis for a time of 5.2 seconds of the quenching process (see Figure 3.12).

Coupled temperature-displacement analysis

A coupled temperature-displacement analysis is performed in ABAQUS/Standard. The main goals in this analysis are:

- Transferring the temperature distribution from the thermal analysis, where the solidification criterion is applied, as an initial condition into the coupled temperature-displacement analysis
- Implementing the gap conductance by the user defined GAPCON subroutine
- Quenching to room temperature

After transferring the temperature distribution from the thermal analysis, a quenching to room temperature is performed. During the gap formation air fills the gap. Figure 3.14 shows the temperature distribution for times 0, 10, 50, 100, 1000 and 1×10^{7} seconds of the quenching. It can be noticed that the gap grows as the temperature decreases. The final ingot shrinkage can be noticed in the last stage of the quenching when the model is cooled to room temperature. Two areas, A and B from Figure 3.14 are enlarged in order to analyse the gap conductance influence on the temperature distribution. Figure 3.15 shows the gap clearance between the ingot and the mould and the temperature contours of the enlarged area A from Figure 3.14. Based on the temperature contours, it can be seen that a temperature difference of around 100 ºC exists between the mould and the ingot. This temperature difference is due to the gap conductance coefficient implemented by Equation (3.16). The area B from Figure 3.14 is enlarged and showed in Figure 3.16. This is the area where a perfect contact exists. It can be seen that the temperature of the contacting surfaces of the mould and the ingot have the same magnitude in a perfect contact. The residual stresses and the ingot shrinkage are obtained after considering the mould filling, solidification criterion, transferring temperature distribution from thermal to coupled temperature-displacement analyses and gap conductance influence during quenching. The residual stress distribution and the gap formation

for the model are shown in Figures 3.17. Figure 3.18 shows the Von Mises stresses in the mould and the ingot. The peak Von Mises stresses of 830.6 MPa for the ingot and 416.5 for the mould are located in the centre of the edges.

3.5 Conclusions

A forging simulation was performed in static and dynamic analyses when the punch was moved into the billet. The inertia calculations were investigated in a dynamic analysis. Re-meshing was activated for the model. The elastic spring-back was performed in a static analysis by importing the results from the static and the dynamic analyses where the punch was moved into the billet. It can be concluded for the forging model that the inertia did not have an influence on the final results for the material properties used and the applied velocity of the punch. The model using re-meshing showed similar results as the models without re-meshing. It can be concluded that the re-meshing algorithm in ABAQUS is reliable and can be used for models where very large plastic deformations are expected. Therefore, for simulating a forging process when the punch is moved into the billet, it is recommended to use dynamic analyses with explicit code and re-meshing when very large plastic deformations are expected. The elastic spring-back was calculated in a static analysis where the residual stress state was obtained after releasing the elastic strains from the model.

A casting process was simulated using the FEM. The main goal was to obtain the residual stresses and implement the gap conductance into the FEA. A parallelepiped geometry surrounded by the mould was used for the simulation. The gap conductance was studied and implemented in ABAQUS by using the user defined GAPCON subroutine. A mould filling technique was implemented in a thermal analysis by activating contact pairs between the mould and the ingot. A solidification criterion was performed based on the temperature variation of the ingot. After the initiation of the solidification, the temperature from the thermal analysis was imported into the coupled temperature-displacement analysis where the final gap formation and the residual stresses were obtained.

Table 3.1: Material properties of the billet in the forging simulation

Elastic Modulus (GPa)	200
Poisson's ratio (-)	0.3
Density (kg/m^3)	7800
Yield Strength (MPa)	100
Ultimate Strength (MPa)	300
Elongation (%)	100

Table 3.2: Sequence of activating contact pairs between the mould and the surfaces of the corresponding ingot layer

Step Time	**Step Number**	Active contact pairs between the mould internal surfaces and the surfaces of the ingot layers within the steps											
sec	**-**	**L_1**	**L_2**	**L_3**	**L_4**	**L_5**	**L_6**	**L_7**	**L_8**	**L_9**	**L_{10}**	**L_{11}**	**L_{12}**
0	0	no	no	no	no	no	no	no	no	no	no	no	no
0.25	1	**yes**	no	no	no	no	no	no	no	no	no	no	no
0.50	2	**yes**	**yes**	no	no	no	no	no	no	no	no	no	no
0.75	3	**yes**	**yes**	**yes**	no	no	no	no	no	no	no	no	no
1.00	4	**yes**	**yes**	**yes**	**yes**	no	no	no	no	no	no	no	no
1.25	5	**yes**	**yes**	**yes**	**yes**	**yes**	no	no	no	no	no	no	no
1.50	6	**yes**	**yes**	**yes**	**yes**	**yes**	**yes**	no	no	no	no	no	no
1.75	7	**yes**	**yes**	**yes**	**yes**	**yes**	**yes**	**yes**	no	no	no	no	no
2.00	8	**yes**	**yes**	**yes**	**yes**	**yes**	**yes**	**yes**	**yes**	no	no	no	no
2.25	9	**yes**	**yes**	**yes**	**yes**	**yes**	**yes**	**yes**	**yes**	**yes**	no	no	no
2.50	10	**yes**	**yes**	**yes**	**yes**	**yes**	**yes**	**yes**	**yes**	**yes**	**yes**	no	no
2.75	11	**yes**	**yes**	**yes**	**yes**	**yes**	**yes**	**yes**	**yes**	**yes**	**yes**	**yes**	no
3.00	12	**yes**	**yes**	**yes**	**yes**	**yes**	**yes**	**yes**	**yes**	**yes**	**yes**	**yes**	**yes**
1×10^8	13	**yes**	**yes**	**yes**	**yes**	**yes**	**yes**	**yes**	**yes**	**yes**	**yes**	**yes**	**yes**

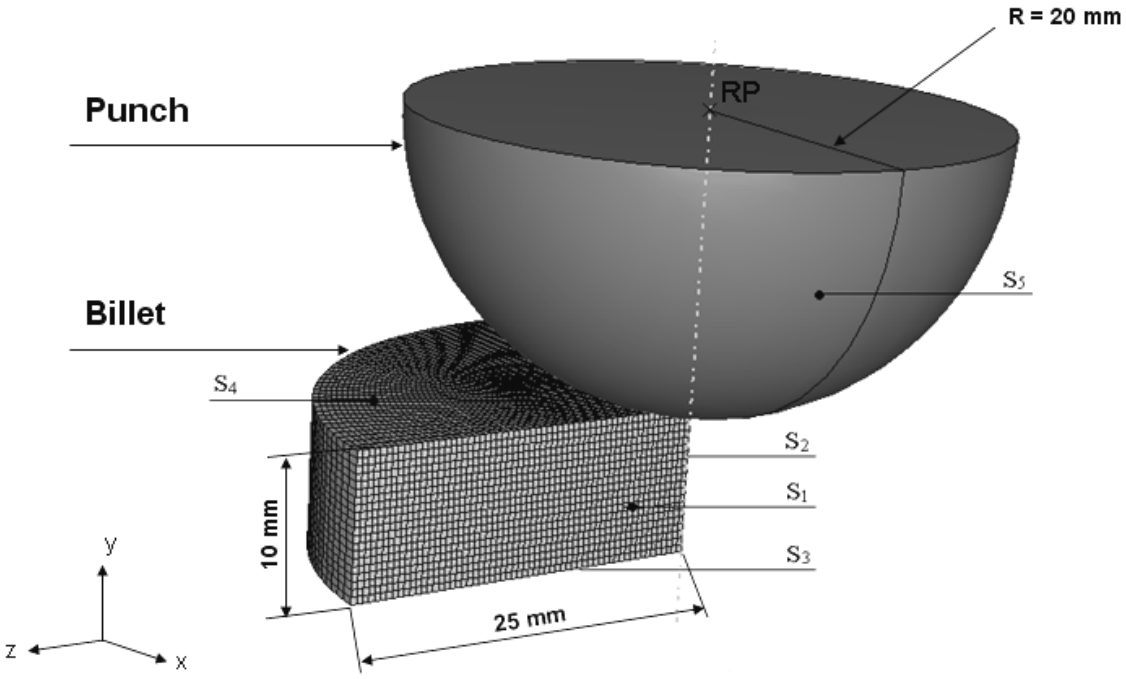

Figure 3.1: Geometry of the punch and the billet of a forging FE model.

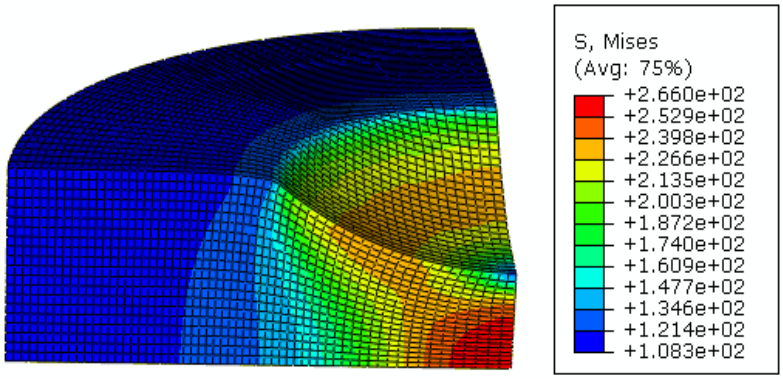

(a)

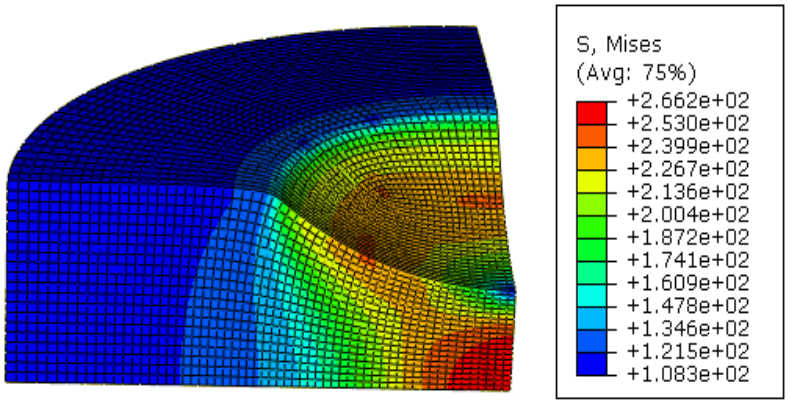

(b)

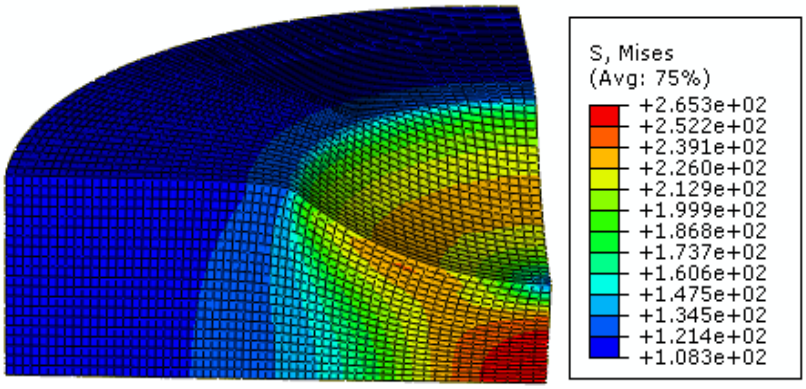

(c)

Figure 3.2: Von Mises stresses in the billet obtained in: **(a)** ABAQUS/Explicit by using dynamic analysis; **(b)** ABAQUS/Explicit by using dynamic analysis and re-meshing; **(c)** ABAQUS/Standard by using static analysis

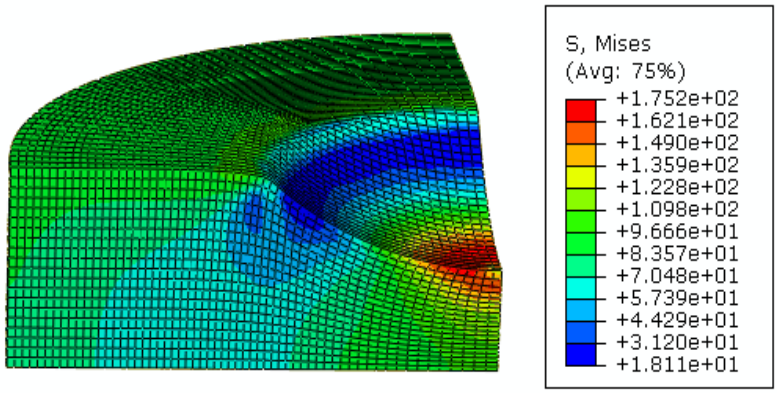

(a)

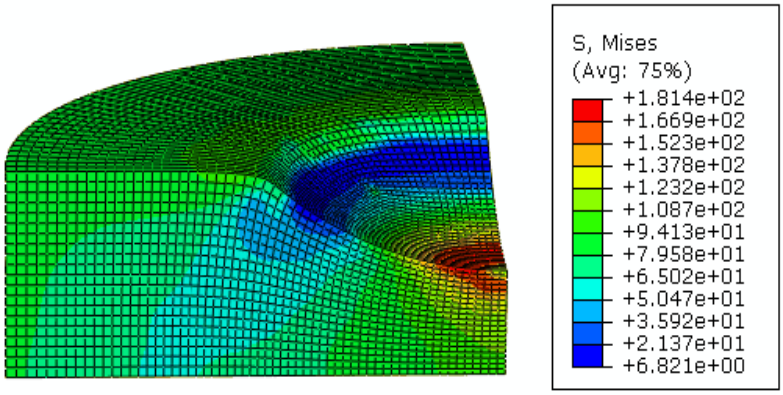

(b)

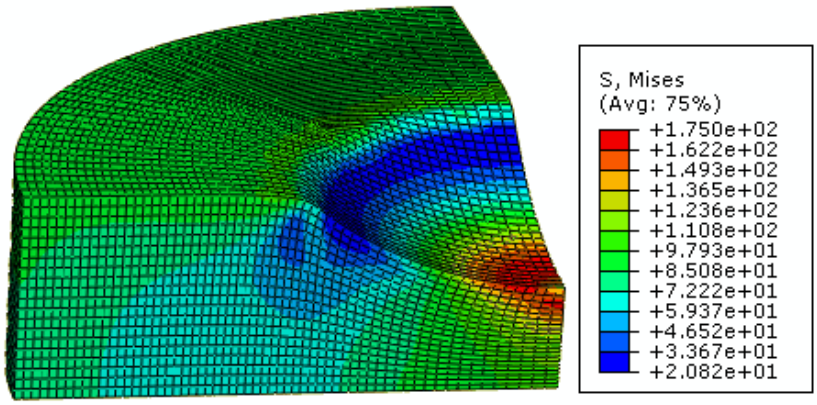

(c)

Figure 3.3: Von Mises stresses in the billet after performing the springback process obtained in ABAQUS/Standard analysis using the results from Figure 3.2 determined by: **(a)** ABAQUS/Explicit; **(b)** ABAQUS/Explicit with re-meshing; **(c)** ABAQUS/Standard

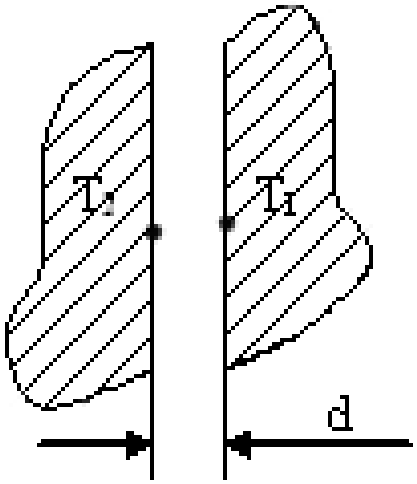

Figure 3.4: Thermal contact between two interfaces represented by two nodes with temperatures T_1 and T_2 and distance d

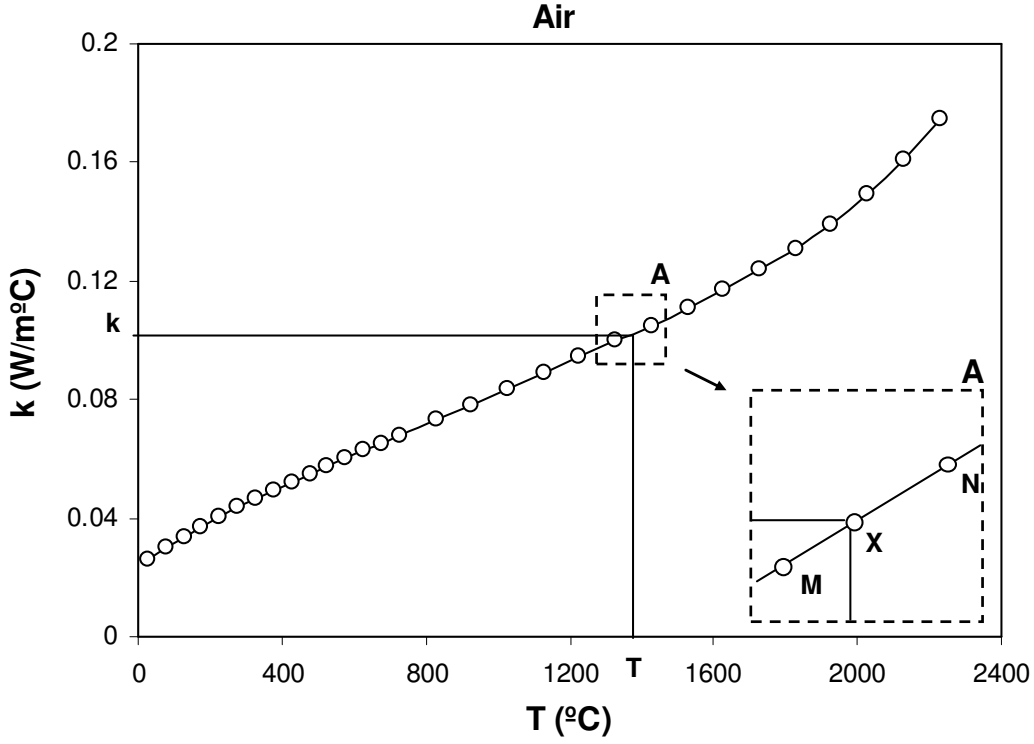

Figure 3.5: Air conductance coefficient versus temperature [41].

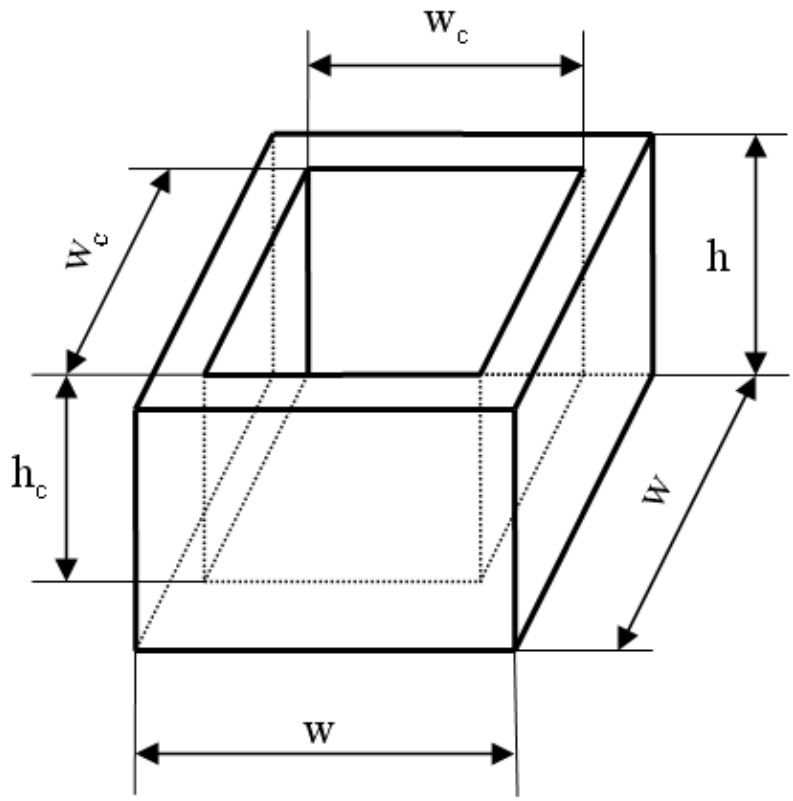

Figure 3.6: The overall dimensions of the mould used in a casting simulation of a model with parallelepiped geometry

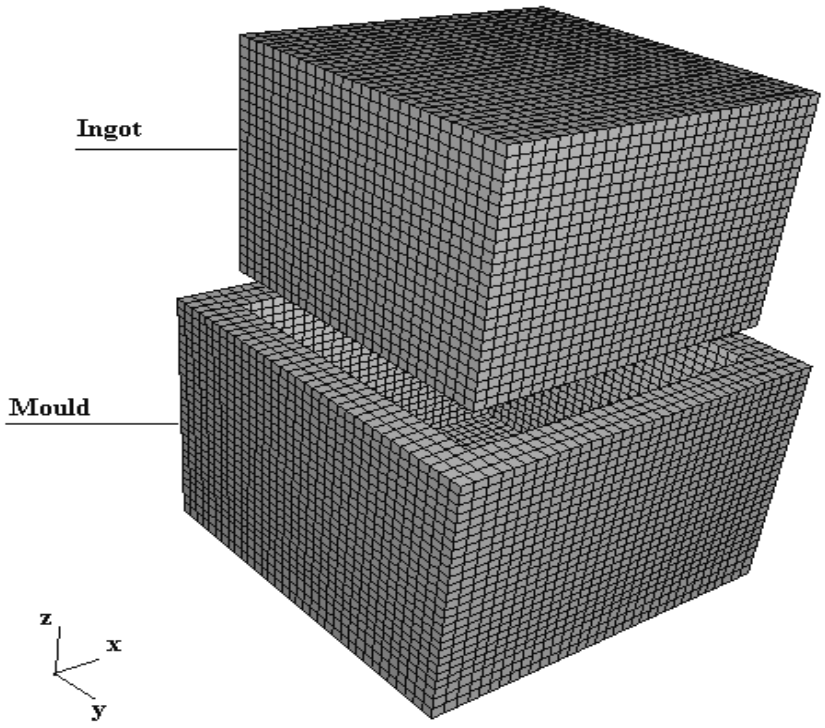

Figure 3.7: Ingot and mould meshes with eight node hexahedron elements with reduced integration

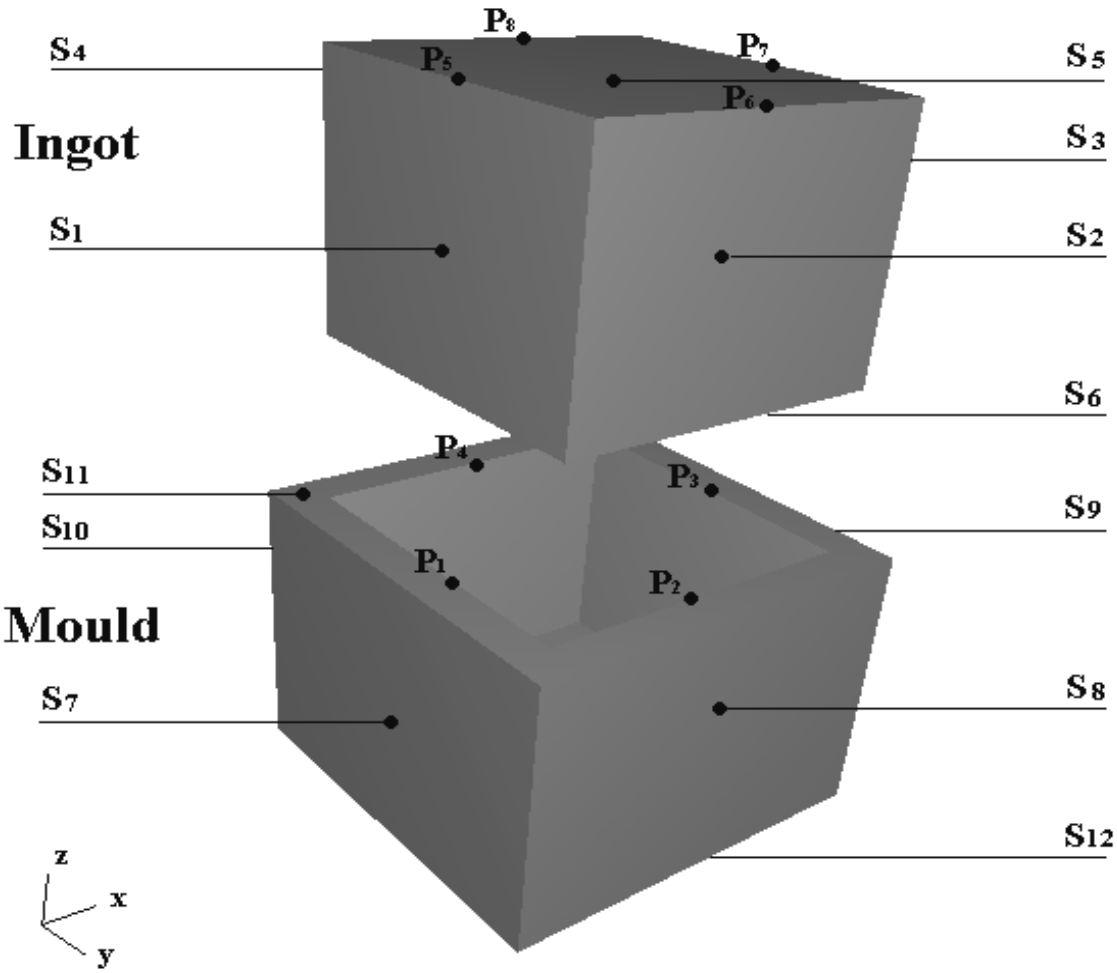

Figure 3.8: Boundary conditions for the casting model

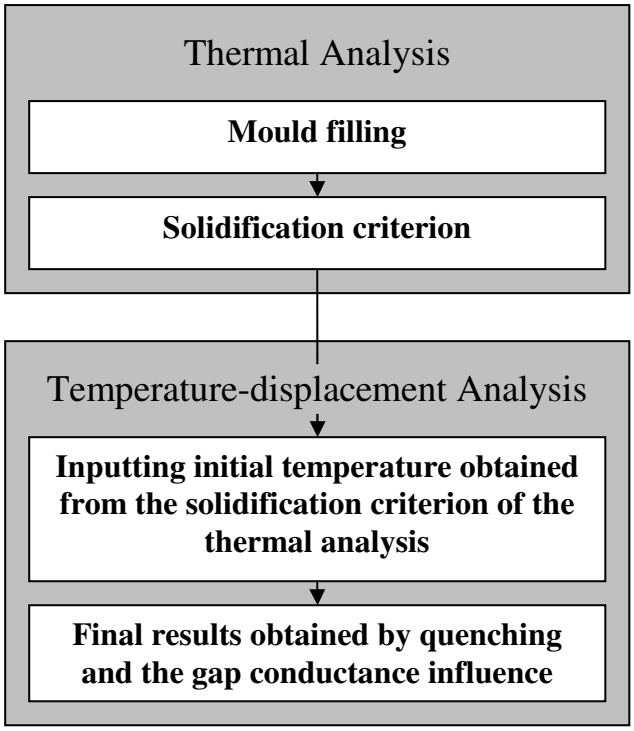

Figure 3.9: Casting simulation sequence

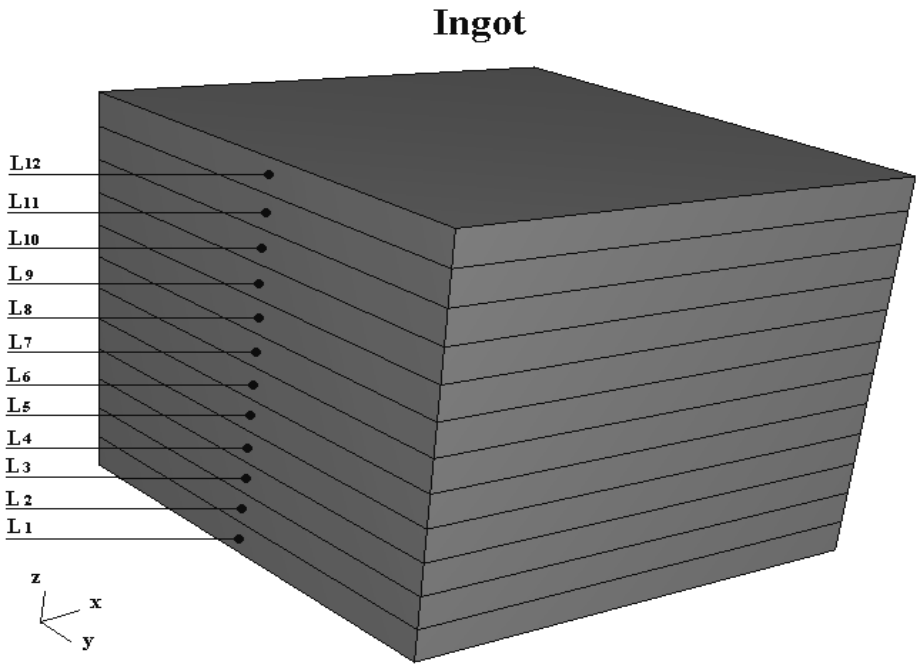

Figure 3.10: The ingot presented in twelve layers

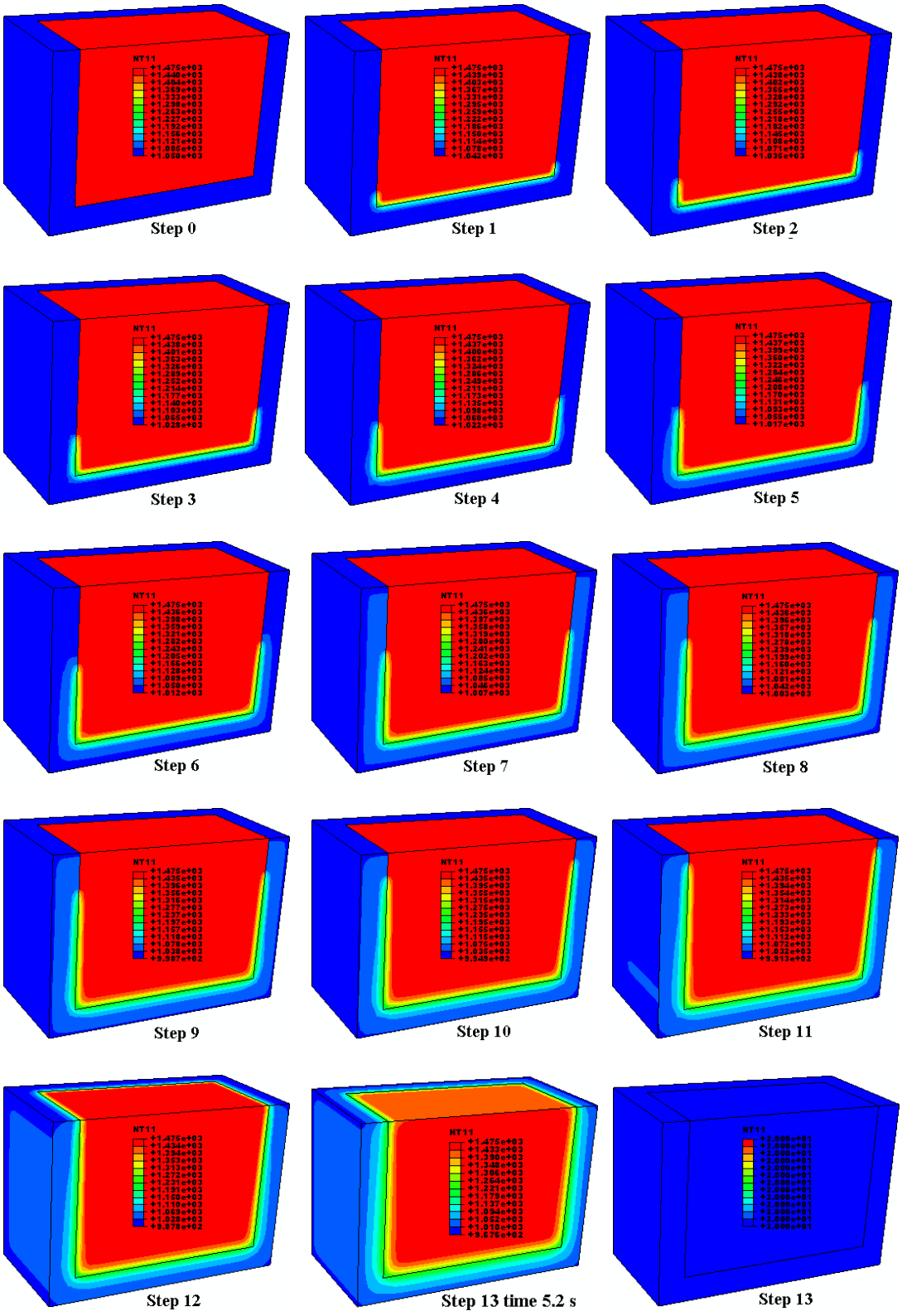

Figure 3.11: Temperature distributions during mould filling in twelve steps, and quenching to room temperature presented as a half model

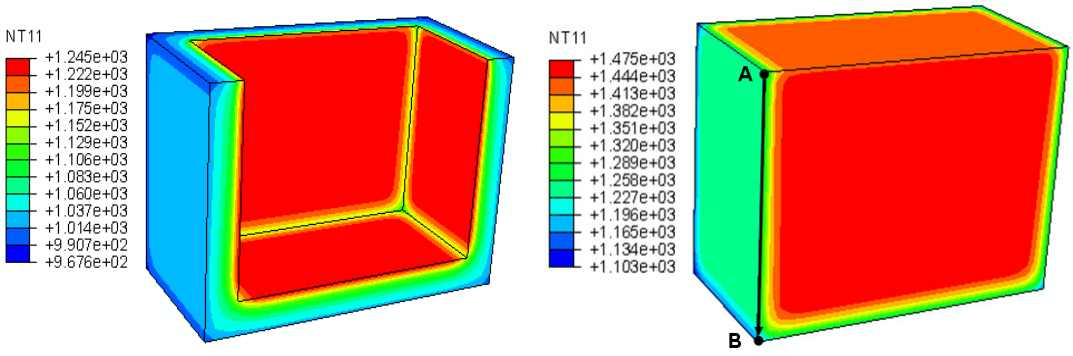

(a) (b)

Figure 3.12: Temperature distributions for the half of the model in step 13 and time of 5.2 seconds of the quenching process for the: **(a)** Mould; **(b)** Ingot;

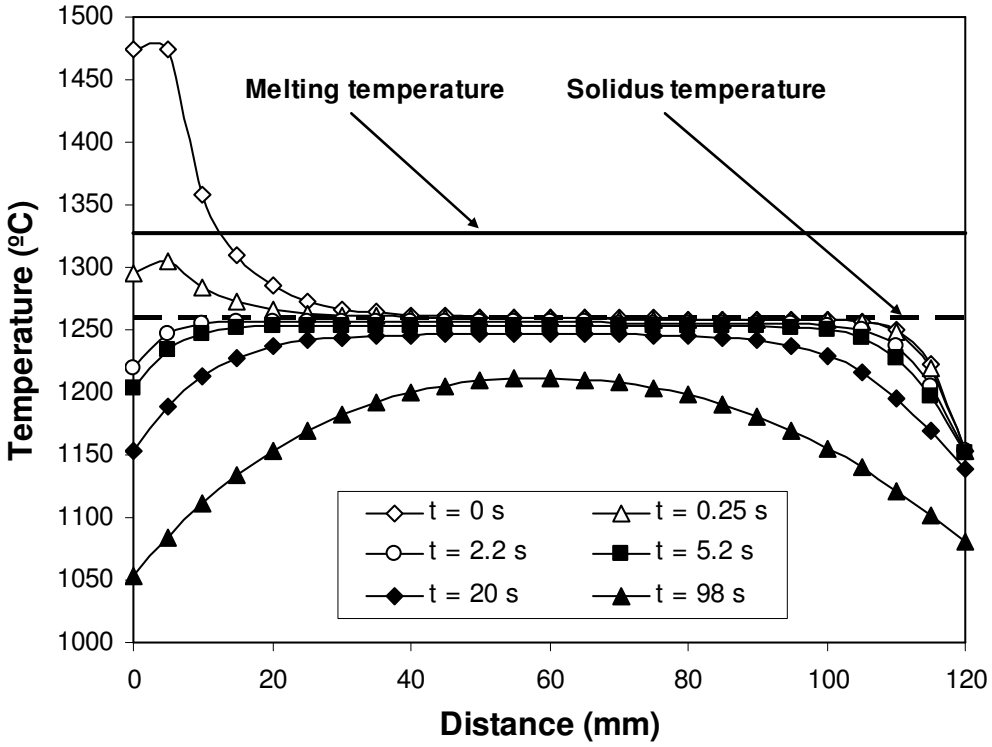

Figure 3.13: Temperature along the path AB from point A (see Figure 3.12(b)) for different times during the quenching process in step 13.

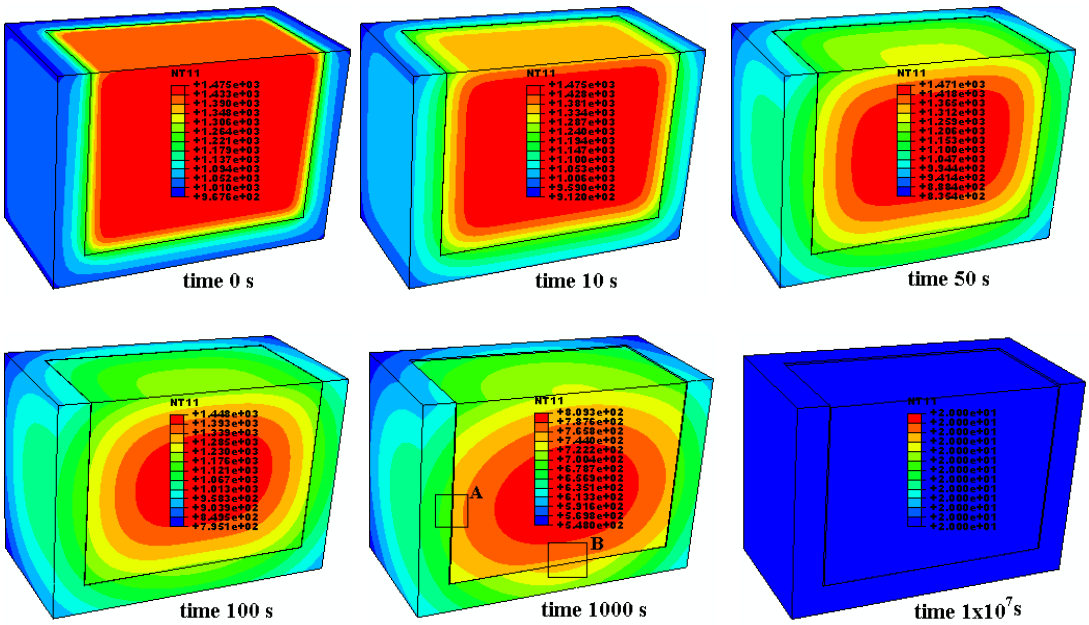

Figure 3.14: Temperature distributions during quenching at different times in the coupled temperature-displacement analysis

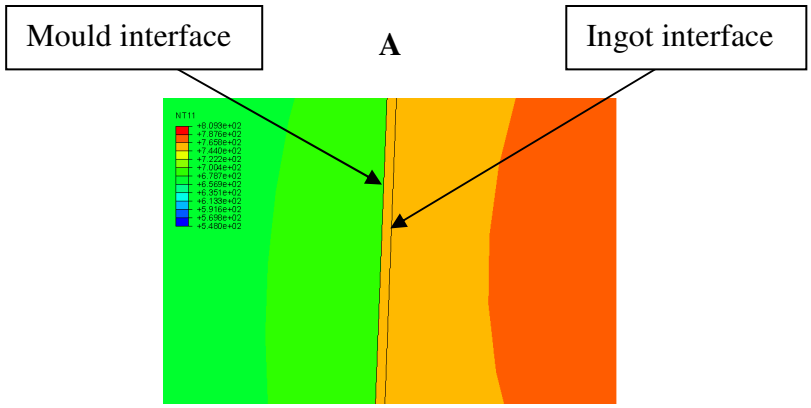

Figure 3.15: Enlarged area A for cooling time of 1000s from Figure 3.14

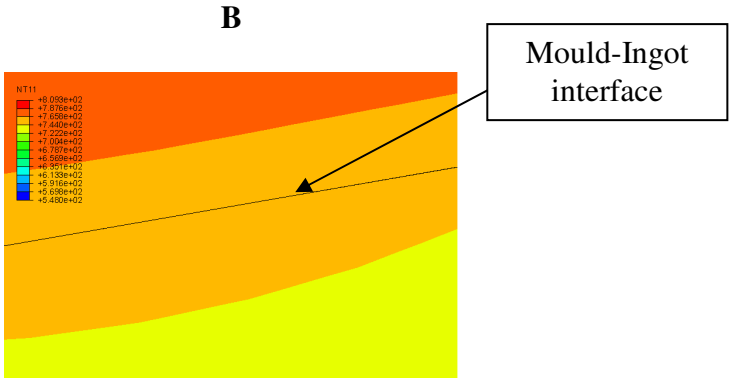

Figure 3.16: Enlarged area B for cooling time of 1000s from Figure 3.14

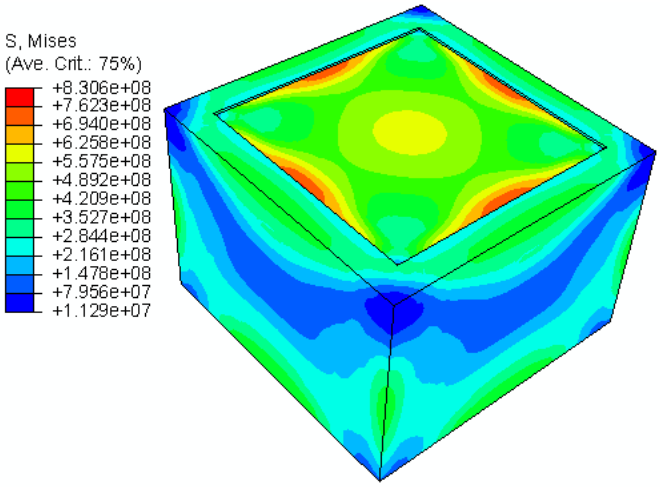

Figure 3.17: Von Mises stresses at the end of the quenching for the model

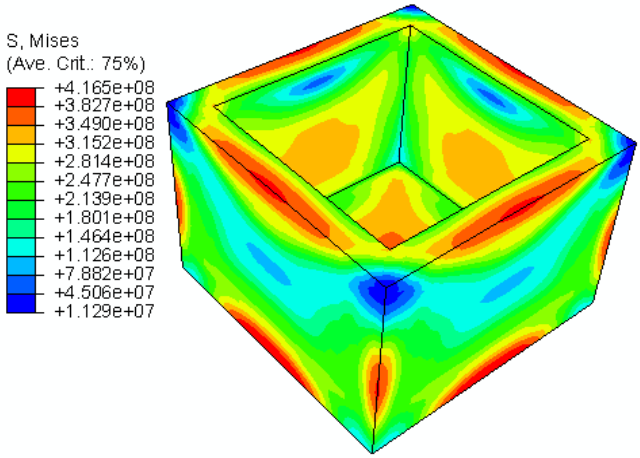

(a)

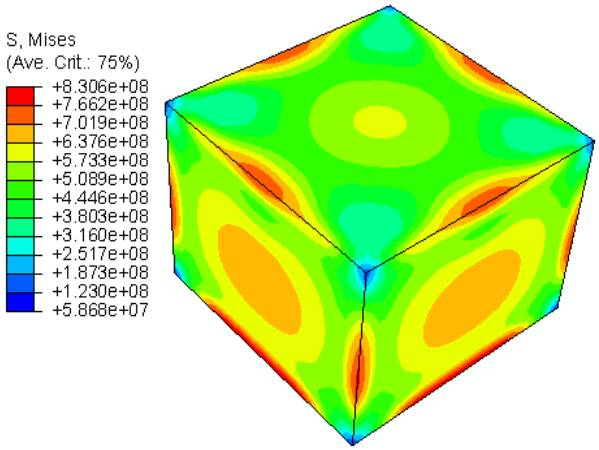

(b)

Figure 3.18: Von Mises stresses at the end of the quenching for the model, shown separately for the: **(a)** mould; **(b)** ingot

CHAPTER 4

FE PREDICTION OF RESIDUAL STRESSES OF INVESTMENT CASTING IN A BOTTOM CORE VANE (BCV) UNDER EQUIAXED COOLING

This chapter reviews an investment casting simulation of the BCV component of an aero engine subjected to equiaxed cooling. The simulation is carried out by using the FEM. Two FE codes (ABAQUS and ProCAST) are used for performing the simulation and the results from both codes are compared and reviewed. The main goal is to predict the residual stresses in the BCV in a casting simulation. Inconel 718 material is used for the ingot (BCV) and a ceramic material (Sand Silica) for the mould. The gap formation and the gap conductance models, between the ingot and the mould are implemented into the FEA.

4.1 Introduction

The BCV is a part of the tail bearing housing of the aero engine located in the rear part of the engine. The prevalent failure mechanisms in the tail bearing housing are creep and fatigue.

The investment casting process involves the following steps. First, a wax model of the casting is prepared by injecting molten wax into a metallic 'master' mould. Next, the wax model is dipped into ceramic slurries. This operation is repeated three or four times until the shell thickness is adequate. Finally, the mould is baked to build up its strength. The first step involves a temperature just sufficient to melt out the wax. Further steps in high temperature are employed to fire the ceramic mould [73]. The equiaxed casting is performed by the 'power-down' method. This method involves the switching off of the furnace after pouring the metal, which allows equal cooling in all axes. A lot of research has been carried out in modelling the equiaxed dendritic solidification in casting [74-78].

The casting simulation using the FEM depends on many parameters involved in this process. For example, accurate material properties have a significant influence on the accuracy of the results. Different FE solvers possess different algorithms and use different convergence tolerances for solving a variety of mathematical models. Choosing an appropriate FE solver for casting simulation can have an influence on the final results. The BCV is cast in a ceramic mould and the simulation is performed in ABAQUS [57] and ProCAST [79]. A mechanical analysis is carried out in ABAQUS by using the temperature history from ProCAST for validation purposes. The effect of the mould filling on the residual stresses is investigated.

4.2 Thermal analyses – parallelepiped benchmark

A simple thermal analysis is performed in ABAQUS and ProCAST before simulating the complex geometry of the BCV. The aim of this simulation is to investigate whether both FE solvers arrive at similar solutions for the thermal analyses.

4.2.1 Geometry and FE model

Figure 4.1 shows the parallelepiped geometry used for the FE simulation. The overall dimensions are:

- width (w) = 160 mm
- height (h) = 120 mm

Four node linear tetrahedron elements are used for the mesh as shown in Figure 4.2. The mesh has 24,055 elements and 4,767 nodes.

4.2.2 Boundary conditions, loading and material properties

Initial temperature of 1475 ºC is applied to the model. The parallelepiped is cooled to room temperature in air with a convection coefficient of 10 W/m^{2}ºC applied to all six surfaces of the parallelepiped. The ambient (sink) temperature of the surrounding air is 20 ºC.

Inconel 718 material is used for the cube simulation. The thermo-physical material properties from Section 3.4.2 are used.

4.2.3 Results and discussion

The temperature history for two nodes (node A and node B), calculated in ABAQUS and ProCAST with and without latent heat inclusion, are shown in Figures 4.3 and 4.4. Node A is located on one of the corners of the parallelepiped and Node B is located in the core of the parallelepiped (see Figure 4.2). Three analyses are performed:

- Thermal analysis with latent heat inclusion in ABAQUS
- Thermal analysis with latent heat inclusion in ProCAST
- Thermal analysis without latent heat inclusion in ABAQUS

It can be seen from Figures 4.3 and 4.4 that when the latent heat is included within the calculation, the cooling in the mushy zone (this is the range between the liquid and the solid temperature of the material) is slower than when the latent heat is neglected. The curves obtained in ABAQUS and ProCAST with latent heat inclusion show very good agreement with slight difference in the mushy zone where the results from ABAQUS show linear behaviour while the results from ProCAST show non-linear behaviour during the cooling process. The temperature history curves for both nodes have the same trend. There is an obvious difference in the temperature history when the latent heat is not included within the calculations, which shows that the latent heat has some influence on the temperature history. This means that when the material re-crystallises the latent heat should be included in the analyses to obtain accurate temperature history and consequently accurate residual stresses.

Both solvers showed good agreement in the thermal analyses. The only small difference is the temperature in the mushy zone due to the different calculations in both solvers. This slight difference will have a very small influence to the residual stresses because the material is not solidified at that stage. This simple benchmark

showed that the thermal calculations in ABAQUS and ProCAST arrive at similar results in the thermal analyses for the parallelepiped benchmark.

4.3 Coupled thermo-mechanical analyses of the BCV

Thermo-mechanical analyses of the BCV are performed in this section. The aim of these simulations is to predict accurately the residual stresses in the BCV. Therefore, both ABAQUS and ProCAST are used to carry out the simulation and the results are compared for validation purposes.

4.3.1 Geometry and FE model

The overall dimensions are shown in Figure 4.5. The BCV is wrapped in a shell of thickness of 3 mm. This shell represents the mould where the liquid is poured. Figure 4.6(a) shows the mesh of the ingot and Figure 4.6(b) the mesh of the mould. Therefore, linear tetrahedron elements with four nodes are used for the ingot mesh and linear wedge elements with six nodes for the mould mesh. The ingot has 18,920 tetrahedron elements, while the mould has 6,917 elements.

4.3.2 Material properties

The same material properties and material models with isotropic hardening are used in the ABAQUS and the ProCAST models. Inconel 718 material properties are used for the ingot. The thermo-physical and the mechanical properties from Section 3.4.2 are used for the simulations in both solvers. Sand Silica material is used for the mould. The thermal conductivity, specific heat capacity and density are given in Table 4.1.

4.3.3 Contact conditions

Figure 3.4 shows two interfaces separated by a gap. The gap conductance coefficient has to be determined to allow the heat transfer between the two interfaces. In the FE

analyses, the heat transfer is achieved between two nodes on either face of the contacting interfaces.

ABAQUS model

Equation (3.16) is used for implementing the gap conductance coefficient in ABAQUS by using the user defined GAPCON subroutine. Contact is achieved between a node from the slave surface (ingot surface) and the projection of this node to the nearest element surface of the master surface (mould surface). The GAPCON subroutine provides the temperature of the two contacting nodes and the width of the gap separation. The gas temperature is calculated by Equation (3.17). The emissivities (ε_1 and ε_2) and the gas conductance coefficient k_g are temperature dependent. The coupled temperature-displacement analysis is based on incremental calculations. Therefore, for each increment the temperature of both interfaces and respectively the gas temperature change. Figure 4.7 shows the emissivity for the Inconel 718 [81] and the imported emissivity with the GAPCON subroutine in each increment. A linear interpolation is performed for obtaining the emissivity for the corresponding temperature of the ingot interface. Figure 4.8 shows the emissivity for the Sand Silica and the imported emissivity with the GAPCON subroutine for the corresponding temperature of the mould interface. Figure 4.9 shows the air conductance [41] and the imported air conductance with the GAPCON subroutine for the corresponding temperature of gas at each increment.

ProCAST model

There are three options for defining contact in ProCAST. The first option is when node 1 and node 2 (see Figure 3.4) are joined and there is no contact interface. This is the case used for welding simulations. The second option is when the two nodes on either sides of the contact face coincide. The third option is when both nodes do not coincide. In this case, a node from the slave surface and the nearest node of the master surface define the contact. ProCAST can include the gap conductance calculations according to the gap separation. The formulations are given by [79]. For perfect contact, when $d = 0$ (see Figure 3.4):

$$h = h_0\left(1+\frac{P}{A}\right) \tag{4.1}$$

In contact when $d \geq 0$

$$h = \frac{1}{\frac{1}{h_0} + R_{gap}} \tag{4.2}$$

$$R_{gap} = \frac{1}{\frac{k_a}{d} + h_{rad}} \tag{4.3}$$

where:

h_0	initial value of the heat transfer coefficient
h_{rad}	radiative equivalent heat transfer coefficient
d	gap width
k_a	Air conductance coefficient
A	empirical constant to account for contact pressure
P	contact pressure

4.3.4 Boundary conditions and loading

The ingot and the mould are shown in Figure 4.10, where the ingot is placed inside the mould. The following conditions are applied:

- Zero displacements in the x, y and z directions on all nodes of the mould
- Heat transfer coefficient is applied in the ingot-mould contact area (see Section 4.3.3)
- Air cooling by convection of 10 W/m^{2}ºC is applied to all surfaces which are in touch with the surrounding air
- The mould is preheated by applying an initial temperature of 1050 ºC
- The mould filling is not taken into account at this stage and an initial temperature of 1475 ºC is applied to the ingot

4.3.5 Results and discussion

The simulation is run in ABAQUS and ProCAST and the residual stress contours are shown in Figures 4.11 and 4.12 which show similar stress distribution in the upper part and different stress distribution in the lower part of the BCV obtained in ABAQUS and ProCAST. The peak Von Mises stresses, calculated in both solvers, have nodal stress values of 1252 MPa and occur at the same location at node A. Three nodes (B, C and D) from both models are chosen for investigating the calculated residual stresses in both FE codes. Figure 4.13 shows the residual Von Mises stresses versus time for nodes B, C and D calculated in ABAQUS and ProCAST. It can be seen that for node B the stresses obtained in ABAQUS and ProCAST have the same trend during cooling. ABAQUS calculations show 4.2 % higher stresses than the ProCAST at the end of the cooling. The stresses for nodes C and D, in the end of the cooling, are higher for the model calculated by ABAQUS. Differences of 53.5 % for node C and 40.4 % for node D are observed at the end of the cooling.

Temperatures for nodes B, C and D versus the time are plotted in Figure 4.14 in order to investigate the temperature at these nodes. It can be seen that the temperatures for the three nodes calculated in both FE codes show the same trend. It can be seen that the ProCAST model cools faster than the ABAQUS model. This is due to the different gap conductance models and the different mechanical calculations between both FE codes. The mechanical calculations can influence the gap conductance by changing the contacting gap width. In order to investigate further the mechanical stress calculations in both FE codes, the temperature history calculated in the coupled temperature-displacement analysis in ProCAST is used for performing mechanical calculations in ABAQUS. This is described in detail in Section 4.4.1.

Most of the constitutive equations for creep and fatigue life prediction involve the use of the maximum principal stresses component. The maximum principal residuals stresses of the BCV, calculated in ABAQUS, are shown in Figure 4.15.

4.4 Parameter sensitivity of the casting simulation

Three analyses are performed to investigate the sensitivity of the casting simulation in this section. A mechanical analysis is performed in ABAQUS by using the temperature history from the coupled temperature-displacement analysis in ProCAST. The aim of this analysis is to investigate the mechanical calculations of ABAQUS and ProCAST for validation purposes. The mesh sensitivity is investigated by refining the mesh from Section 4.3.1 and running a coupled temperature-displacement analysis in ProCAST. The influence of the mould filling is investigated as well.

4.4.1 Mechanical analysis in ABAQUS

A mechanical analysis is performed in ABAQUS by using the temperature history obtained in ProCast for the model described in Section 4.3. The temperature for each node is imported in ABAQUS by using the user defined UTEMP subroutine. This subroutine is called for each node of the model in each increment of the analysis step. The following sequence is performed:

- Exporting temperature history for all nodes from ProCAST in a file with ASCII format
- Creating an algorithm for reading the output data from the ProCAST output file
- Creating UTEMP subroutine for reading the temperature history and performing a linear interpolation within the time-temperature curves for each node

Figure 4.16 shows the temperature versus the time, calculated in ProCast and imported in ABAQUS by UTEMP subroutine for node A (see Figure 4.17). Figure 4.17 shows the Von Mises residual stresses obtained in ABAQUS from the temperature history calculated from the coupled temperature-displacement analysis in ProCAST. By comparing Figures 4.11 and 4.12 with Figure 4.17, it can be seen that the calculated residual stresses in ABAQUS using the calculated temperature history from ProCAST are similar as the stresses calculated in the coupled

temperature-displacement analysis in ABAQUS. The peak stresses have the same magnitude of 1252 MPa and occur at same location at node A. Figure 4.18 shows the residual Von Mises residual stresses for nodes B, C and D versus time for the coupled temperature-displacement analyses in ABAQUS and ProCAST and mechanical analysis in ABAQUS based on the temperature history from the coupled temperature-displacement analysis in ProCAST. It can be seen that the residual stresses calculated in ABAQUS based on the temperature history from ProCAST for nodes B, C and D show similar trends and magnitudes as the stresses calculated in the coupled temperature-displacement analysis in ABAQUS.

4.4.2 Mould filling sensitivity

ProCAST has three built-in algorithms for filling a mould. The mould filling convergence depends on the mesh, gravity, fluid velocity, etc. The mould filling in ABAQUS can be achieved by activating elements or contact pairs as demonstrated in Section 3.4. The fluid flow needs to be known in order to activate the relevant contact pairs or elements at the corresponding time. The aim of this section is to show whether the mould filling influences the residual stresses. The following sequence is performed:

- The mould filling is performed in ProCAST for the model from section 4.3.1
- The temperature for all nodes is saved at the end of the filling process from ProCAST
- The saved temperatures for all nodes are imported in ABAQUS as initial conditions.
- Coupled temperature-displacement analysis is performed in ABAQUS

The model from section 4.3.1 is used for performing the mould filling. The filling is completed after 1.63 seconds. The filling velocity of the fluid is 100 mm/s and a gravity of 9.81 m/s^2 is applied. Figure 4.19 shows the temperature and the fluid flow for the ingot at different filling times. Figure 4.20 shows the residual Von Mises stresses obtained in ABAQUS by including the initial temperature condition obtained in the end of the filling process in ProCAST at time 1.63s. Comparing

Figure 4.11 with Figure 4.20, it can be seen that the residual stresses have similar distribution and magnitudes. Figure 4.21 shows the residual Von Mises stresses for nodes B, C and D versus the time with and without taking into account the mould filling as an initial condition for the coupled temperature-displacement analyses performed in ABAQUS. It can be seen that the stresses during cooling have similar values. The stresses at nodes B and D has identical values in the end of the cooling in both analyses and a difference of 4 % is observed at node C. Based on this analysis, it can be concluded that the mould filling for time of 1.63s has not significantly influenced the residual stresses for the used material properties. The mould filling can be performed separately to investigate whether the mould can be filled without forming voids or gaps.

4.4.3 Mesh sensitivity

The aim of this section is to check the residual stress results by performing the casting simulation with a refined mesh. The geometry, the boundary and contact conditions, the material properties and the loading are the same as the model in section 4.3. The only difference is the number of elements in the model. Figure 4.22 shows the refined mesh of the ingot and the mould. Linear tetrahedron elements with four nodes are used for the ingot mesh and linear wedge elements with six nodes are used for the mould mesh. The ingot has 379,440 tetrahedron elements, while the mould has 209,730 wedge elements. A coupled temperature-displacement analysis is performed in ProCAST. Figure 4.23 shows the residual Von Mises stresses obtained in ProCAST. By comparing the results from Figures 4.11 and 4.12 with Figure 4.23, it can be seen that the residual stresses obtained with the refined mesh have slightly different stress distribution in the lower part of the BCV. However, the peak stresses have similar magnitude and location.

4.5 Conclusions

Residual stresses for the casting simulation of the BCV have been obtained using two commercial FE codes (ABAQUS and ProCAST). The temperature and the residual stresses have been compared in both FE codes. The results showed that both

codes are suitable for carrying out casting simulation. Some differences were observed in the residual stress calculations between both codes. However, the calculated peak stresses have the same location and magnitude in both codes.

The mould filling effect on the residual stresses has been investigated. The results has shown that for a filling time of 1.63 seconds, the mould filling effect has not significantly affected the residual stresses.

Table 4.1: Material Properties of Sand Silica [80]

Thermal conductivity (W/m ºC)	2.09
Specific heat (J/kg ºC)	1074
Density (kg/m^3)	2400

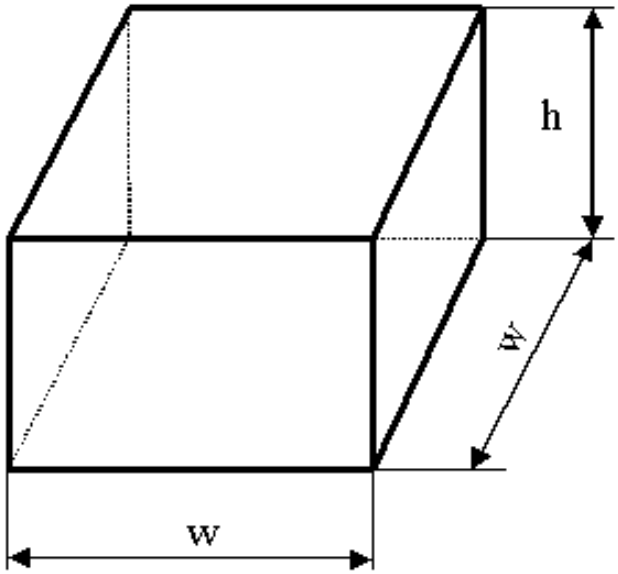

Figure 4.1: The overall dimensions of a parallelepiped used for the thermal analyses in ABAQUS and ProCAST

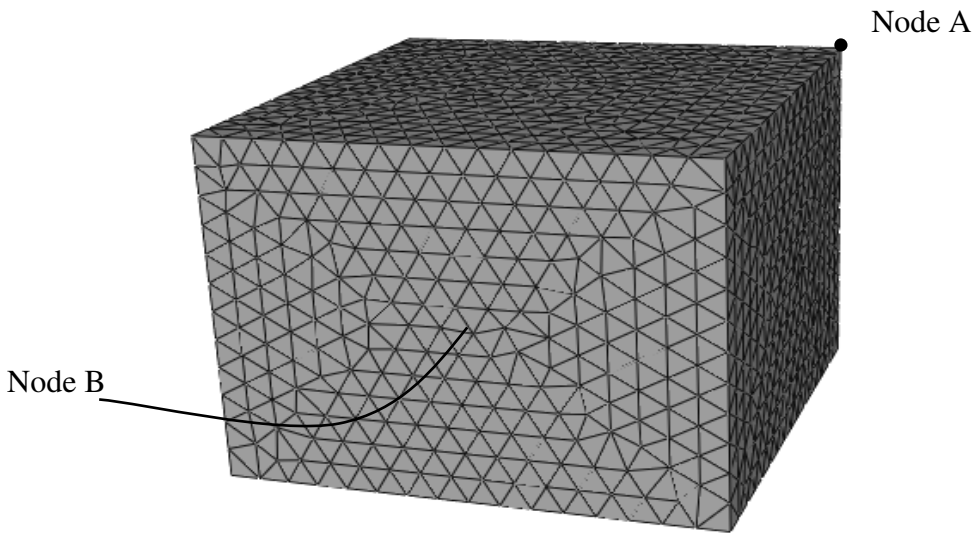

Figure 4.2: Parallelepiped mesh with 24,055 four node linear tetrahedron elements

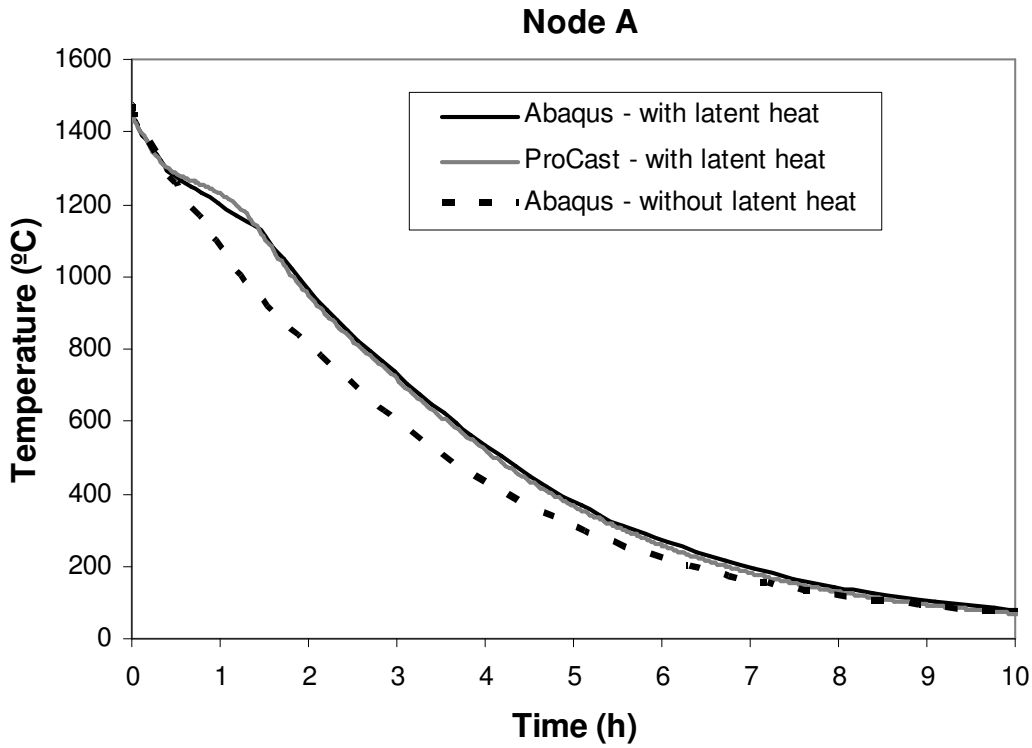

Figure 4.3: Temperature history for Node A obtained in ABAQUS and ProCAST

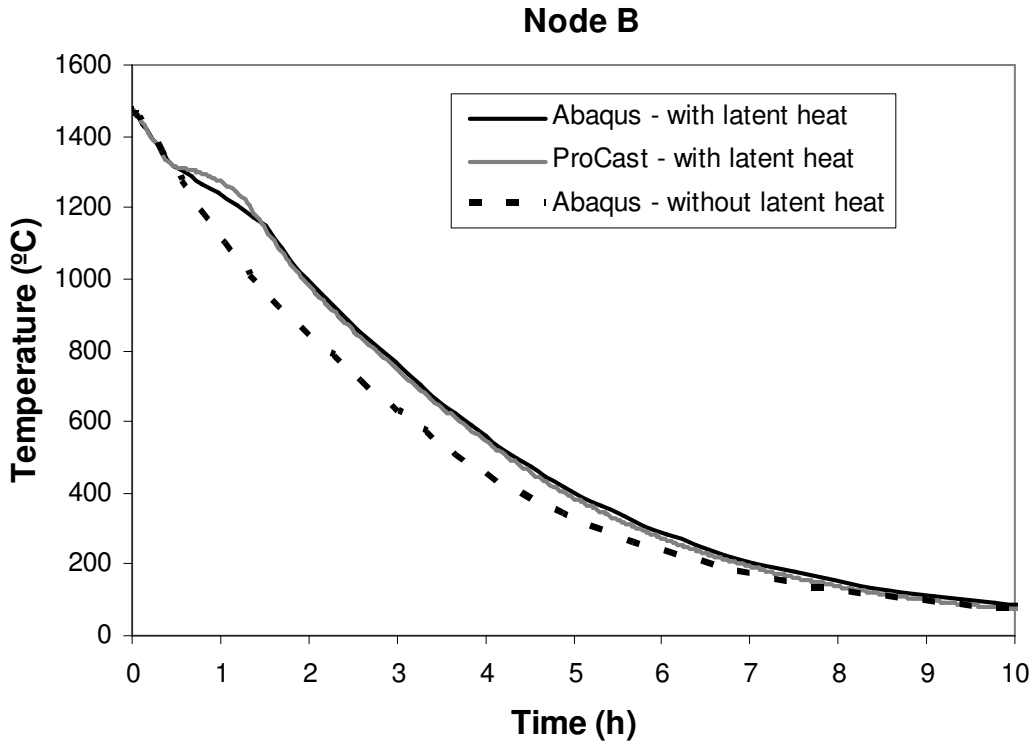

Figure 4.4: Temperature history for Node B obtained in ABAQUS and ProCAST

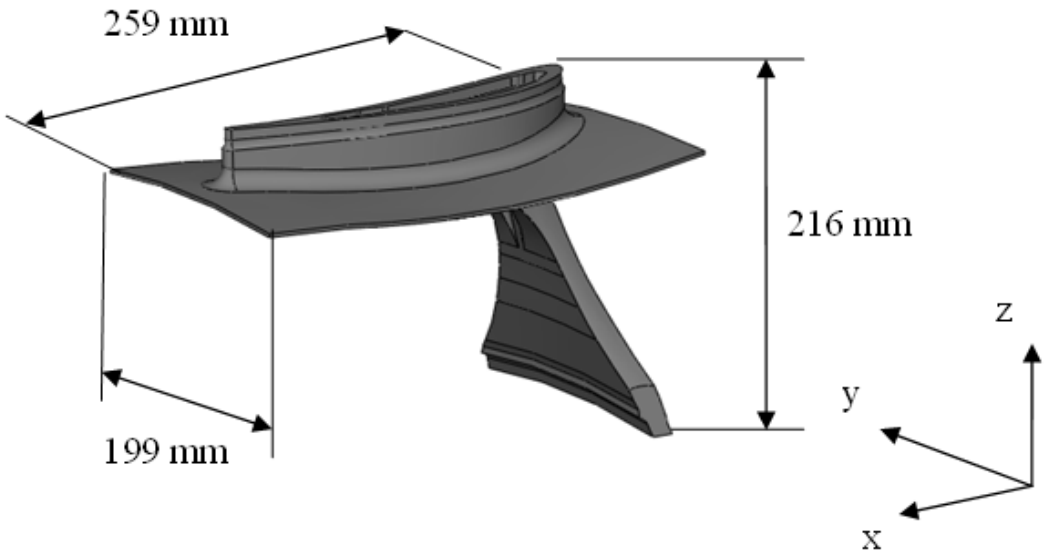

Figure 4.5: Geometry and overall dimensions of the BCV

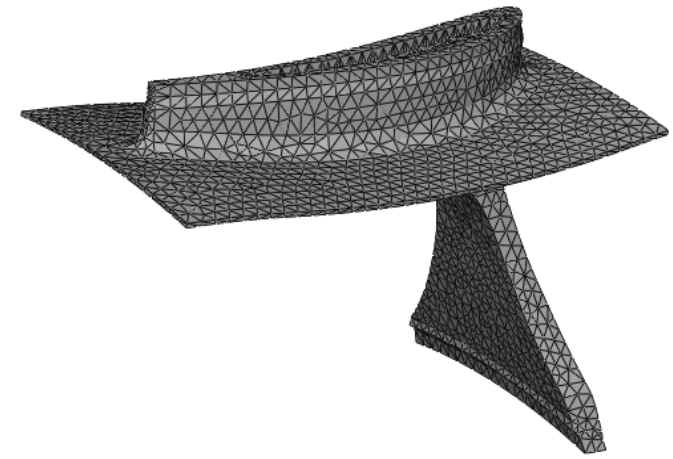

(a)

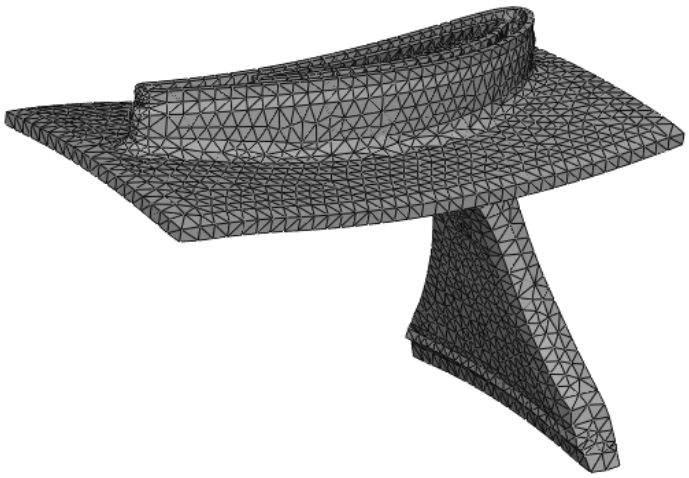

(b)

Figure 4.6: FE meshes for the: **(a)** ingot mesh with 18,920 four node tetrahedron elements; **(b)** mould mesh with 6,917 six node wedge elements

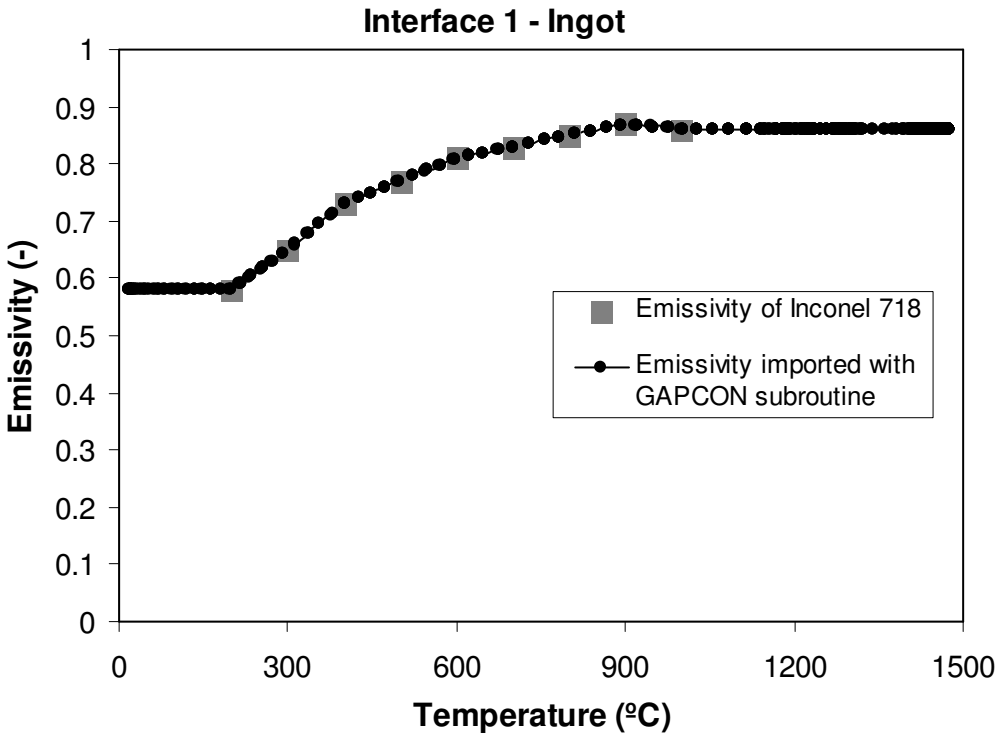

Figure 4.7: Inconel 718 emissivity [81] and the imported emissivity with the GAPCON subroutine

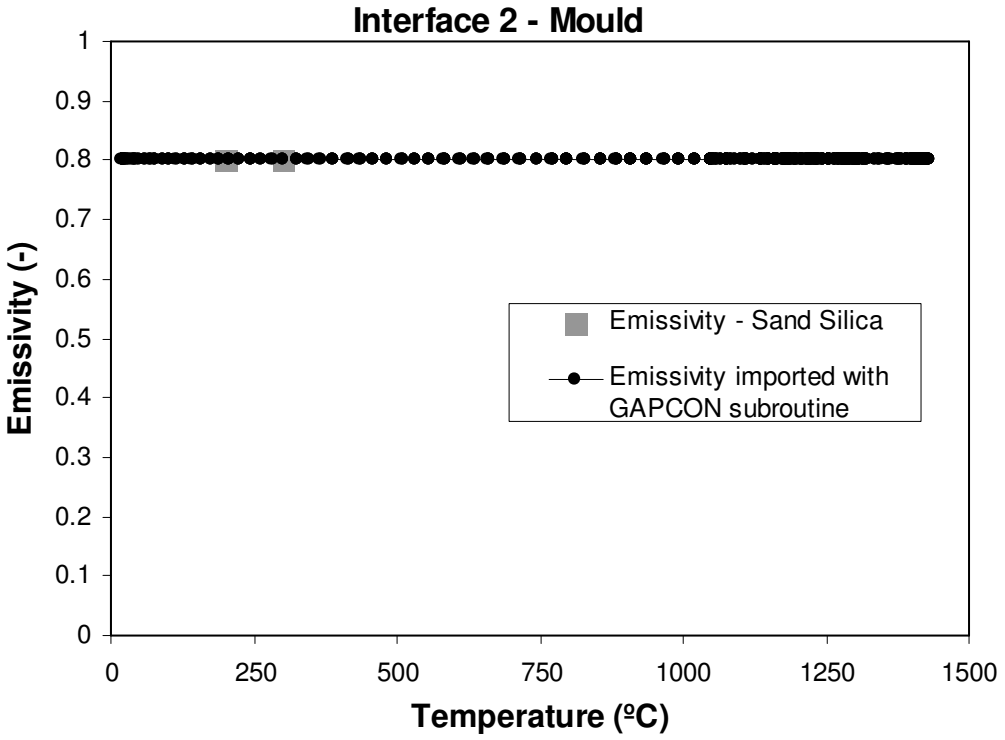

Figure 4.8: Sand Silica emissivity and the imported emissivity with the GAPCON subroutine

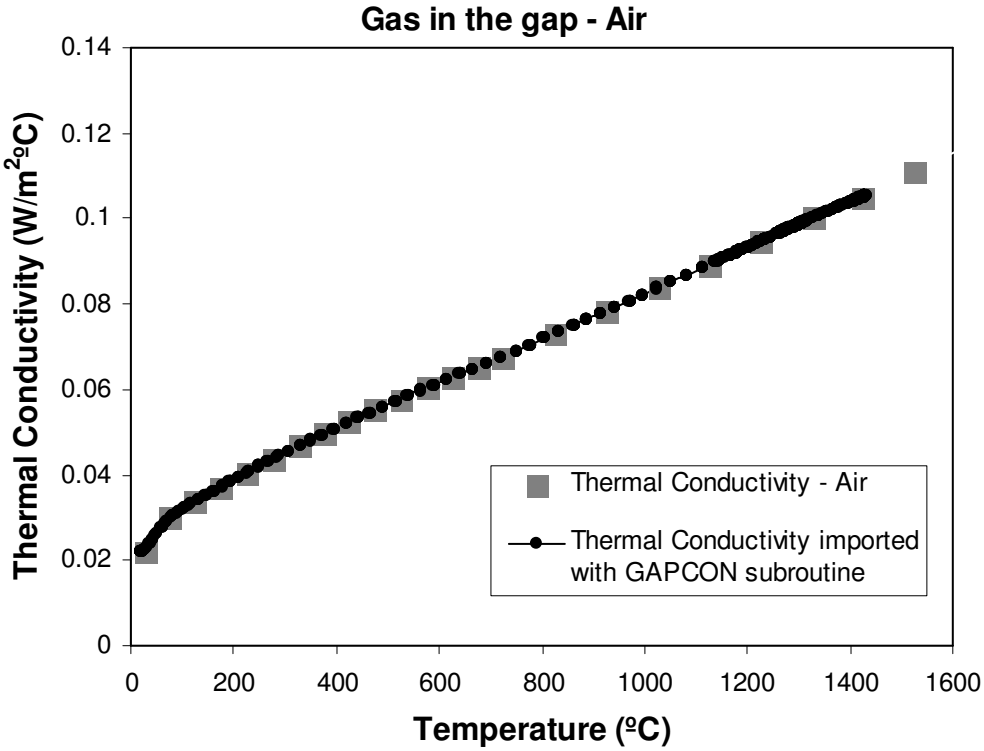

Figure 4.9: Air thermal conductivity [41] and the imported air conductivity with the GAPCON subroutine

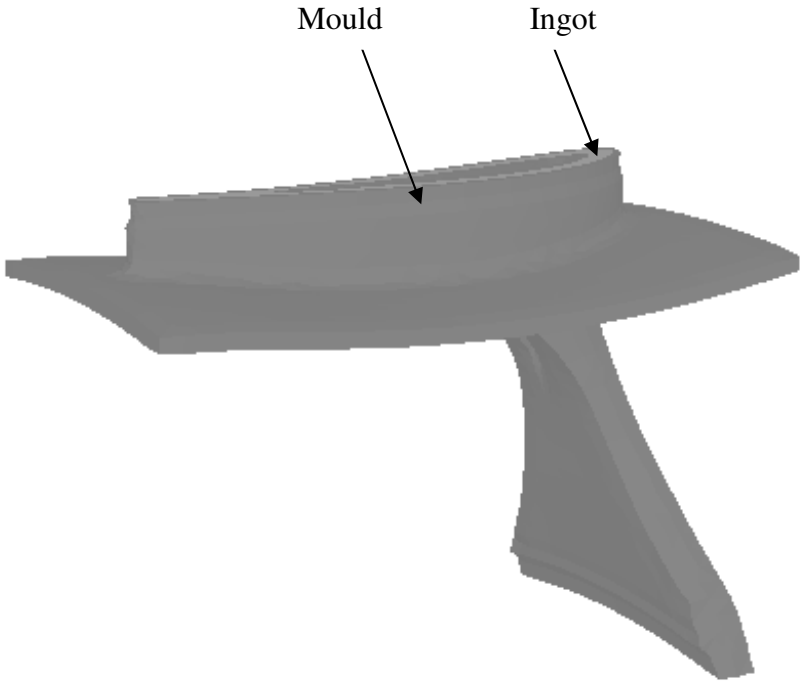

Figure 4.10: BCV (ingot) wrapped in a shell mould

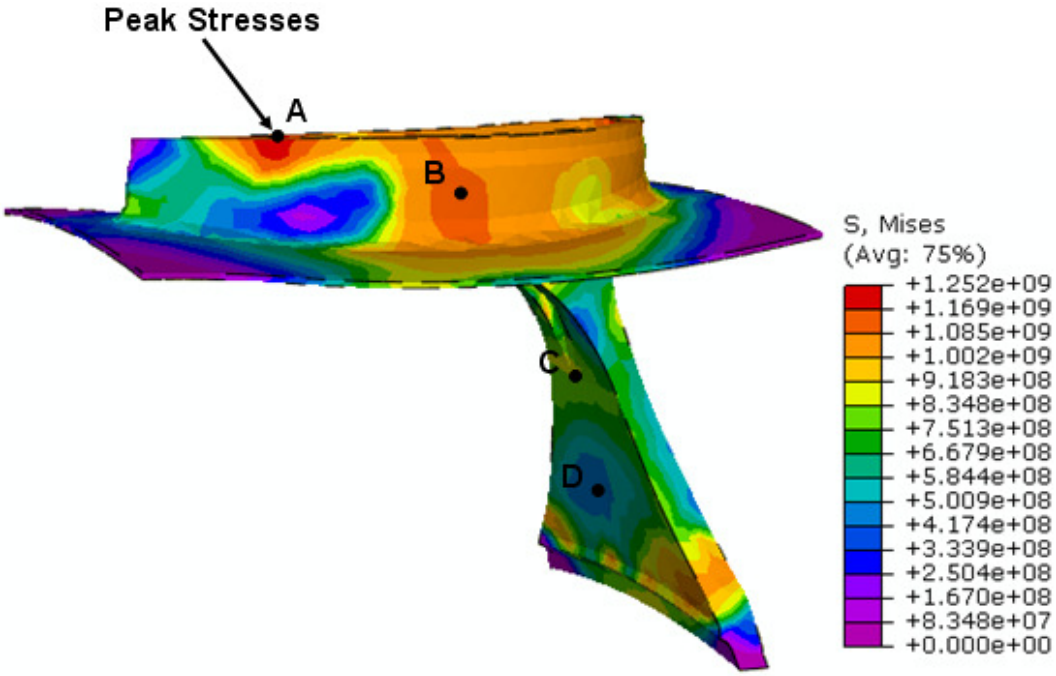

Figure 4.11: Von Mises residual stresses in Pa obtained in ABAQUS

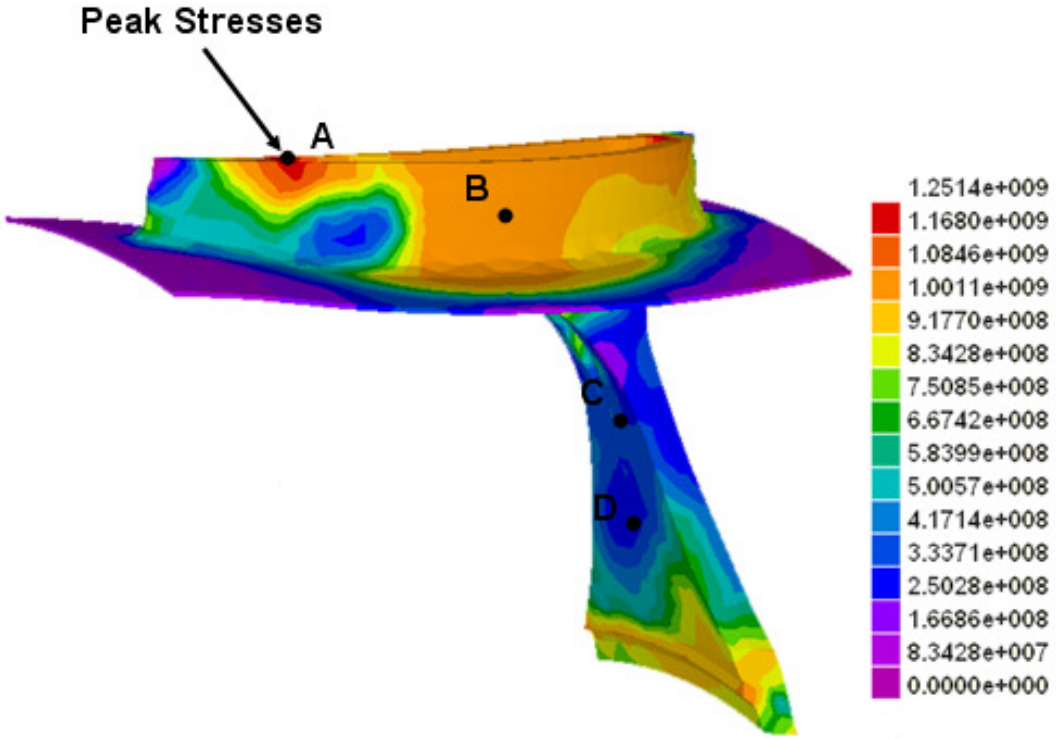

Figure 4.12: Von Mises residual stresses in Pa obtained in ProCAST

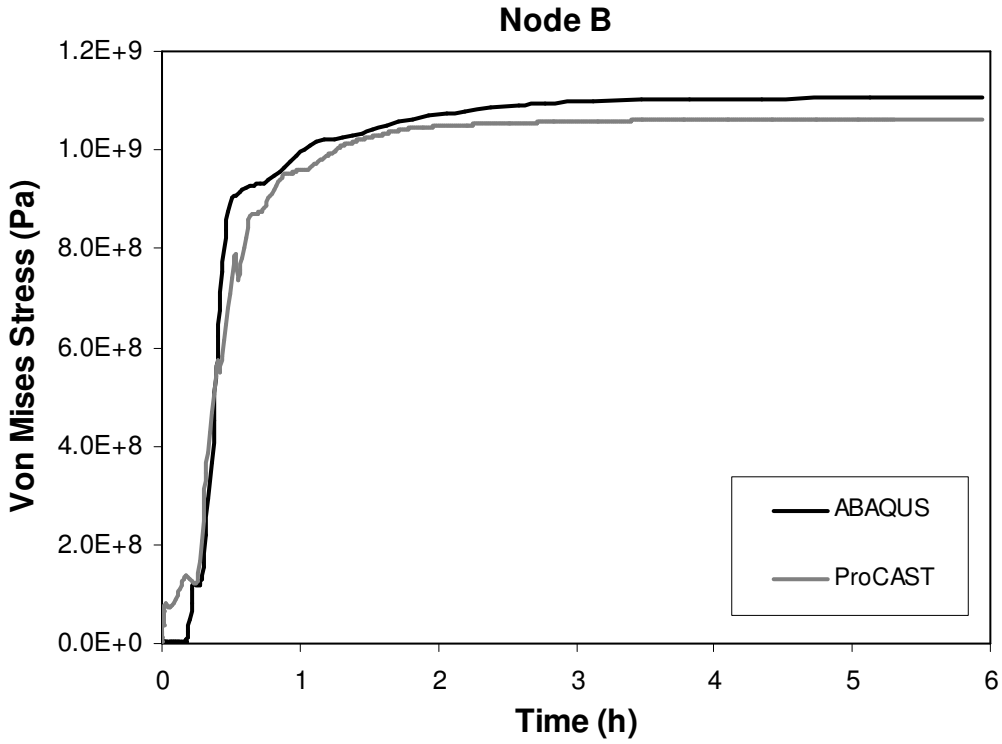

(a)

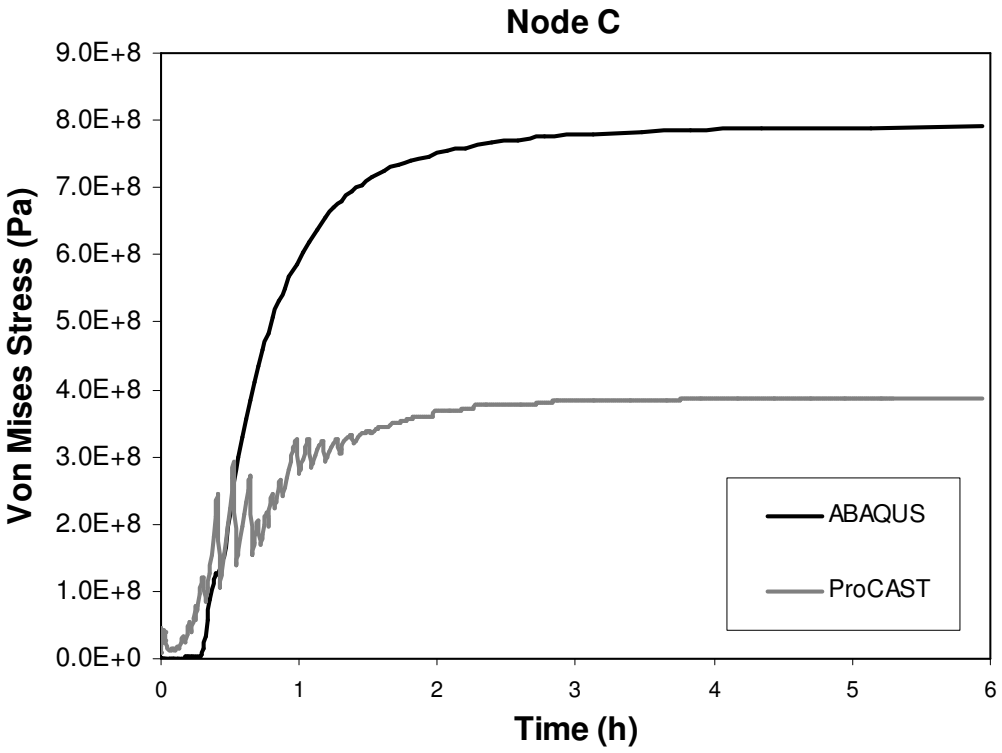

Figure 4.13: (b)

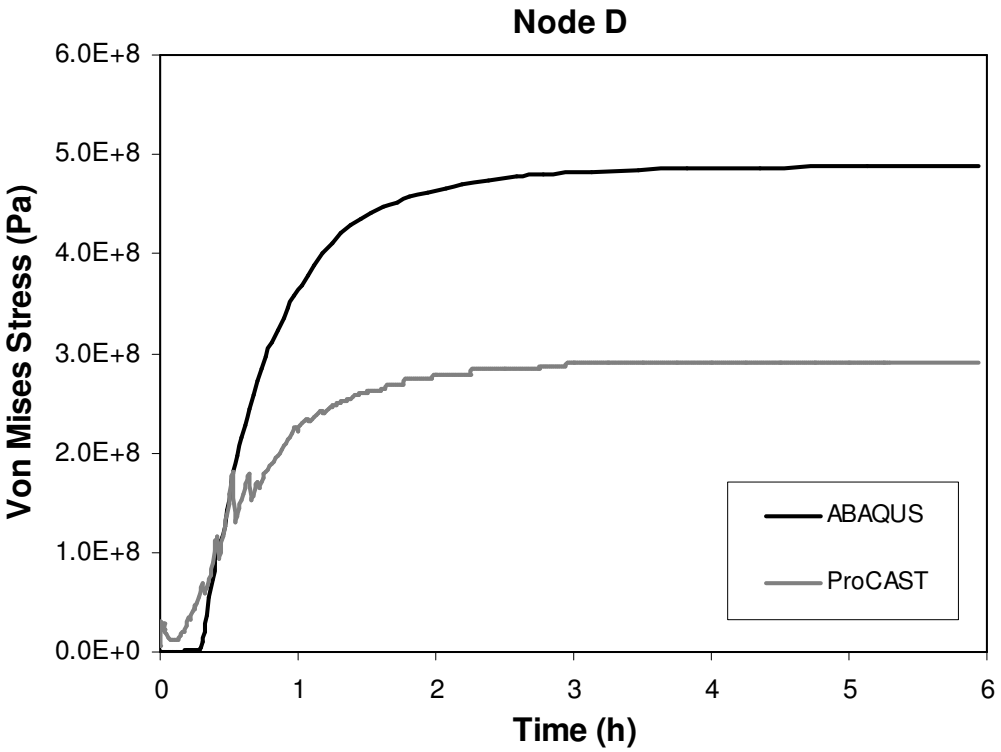

(c)

Figure 4.13: Von Mises residual stresses versus the time obtained in ABAQUS and ProCAST for: **(a)** Node B; **(b)** Node C; **(c)** Node D; (see Figures 4.11 and 4.12)

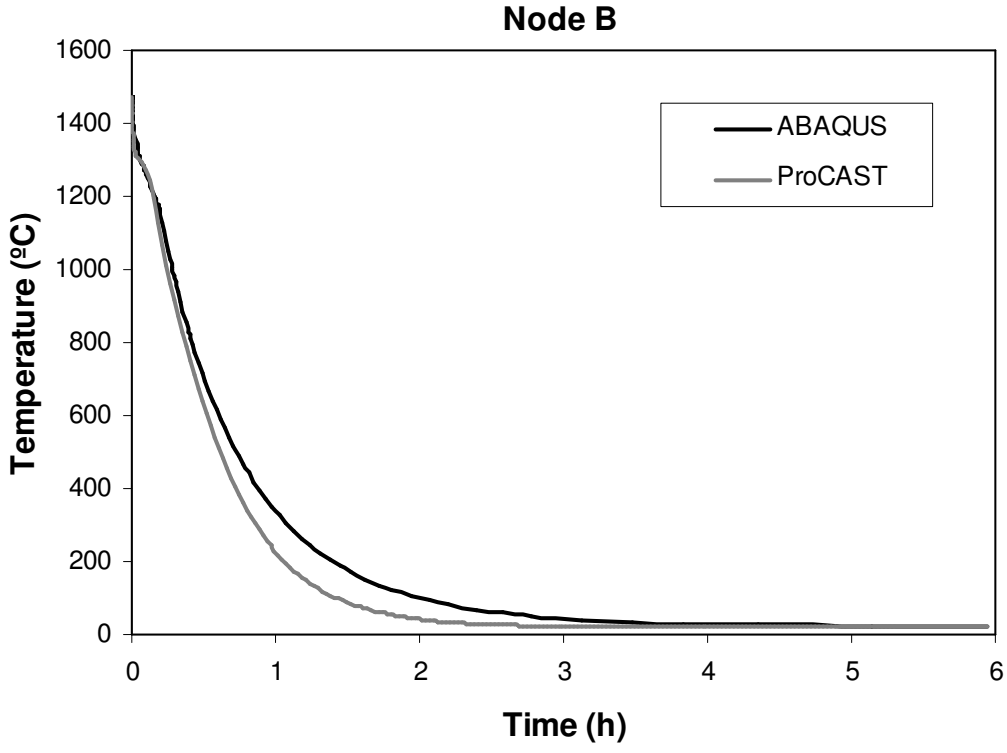

Figure 4.14: (a)

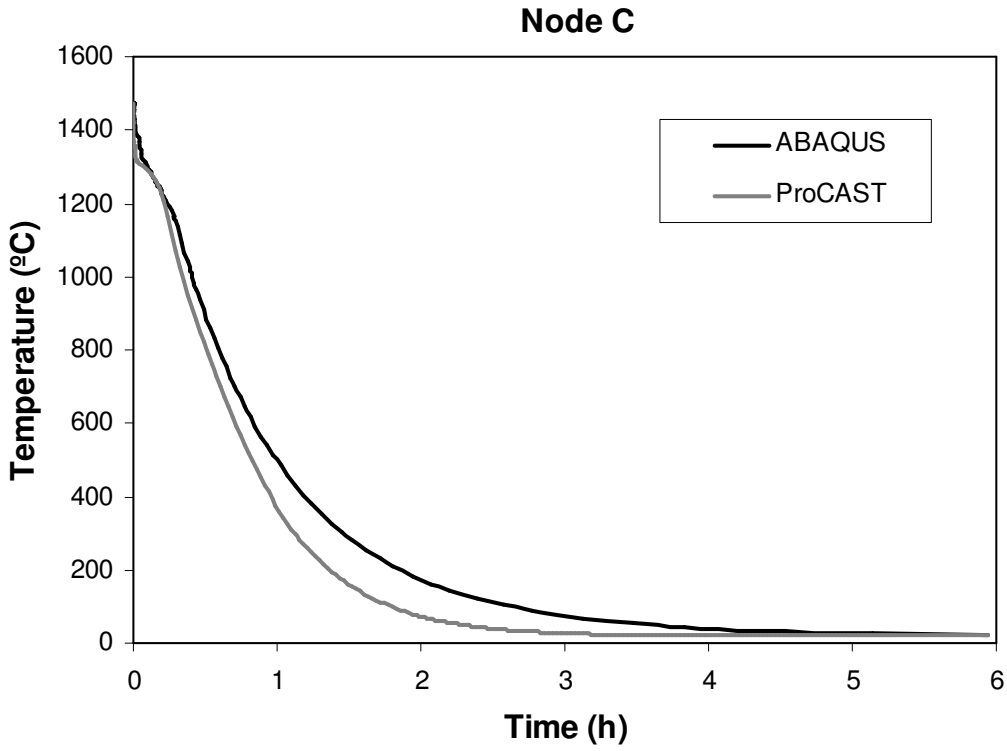

(b)

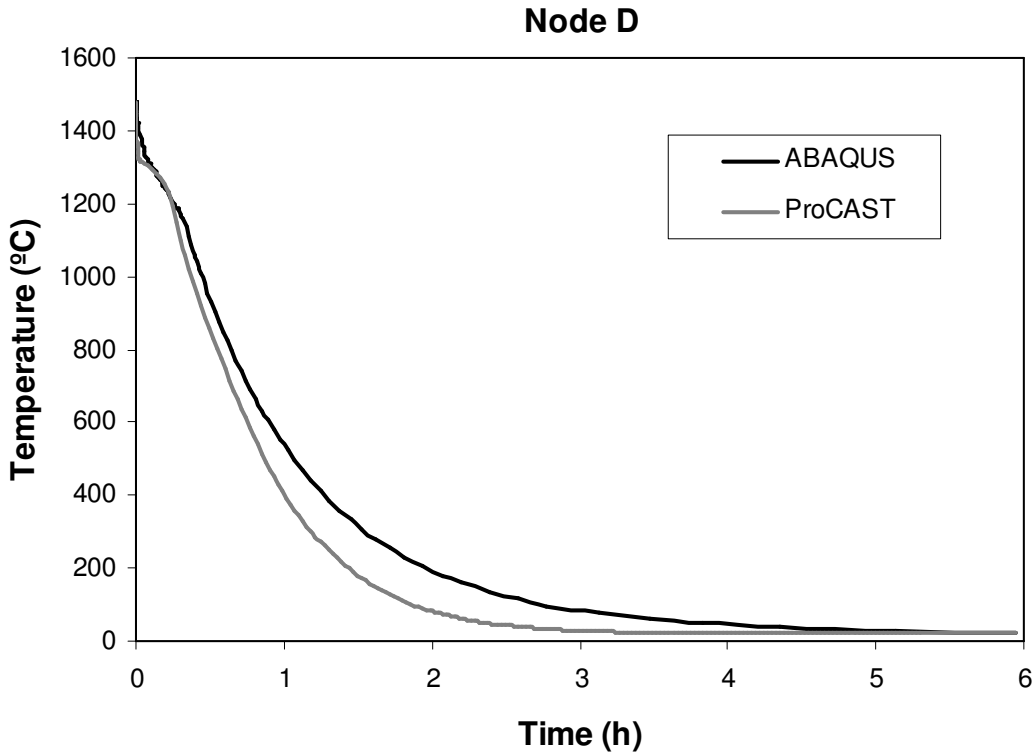

(c)

Figure 4.14: Temperature versus the time obtained in ABAQUS and ProCAST for: **(a)** Node B; **(b)** Node C; **(c)** Node D; (see Figures 4.11 and 4.12)

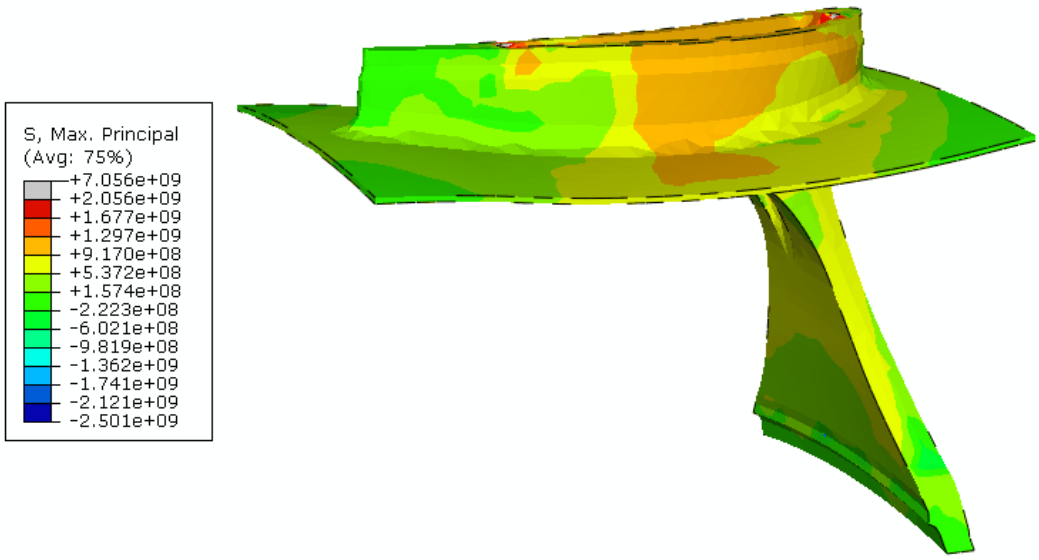

Figure 4.15: Maximum principal residual stresses of the BCV in Pa calculated in ABAQUS

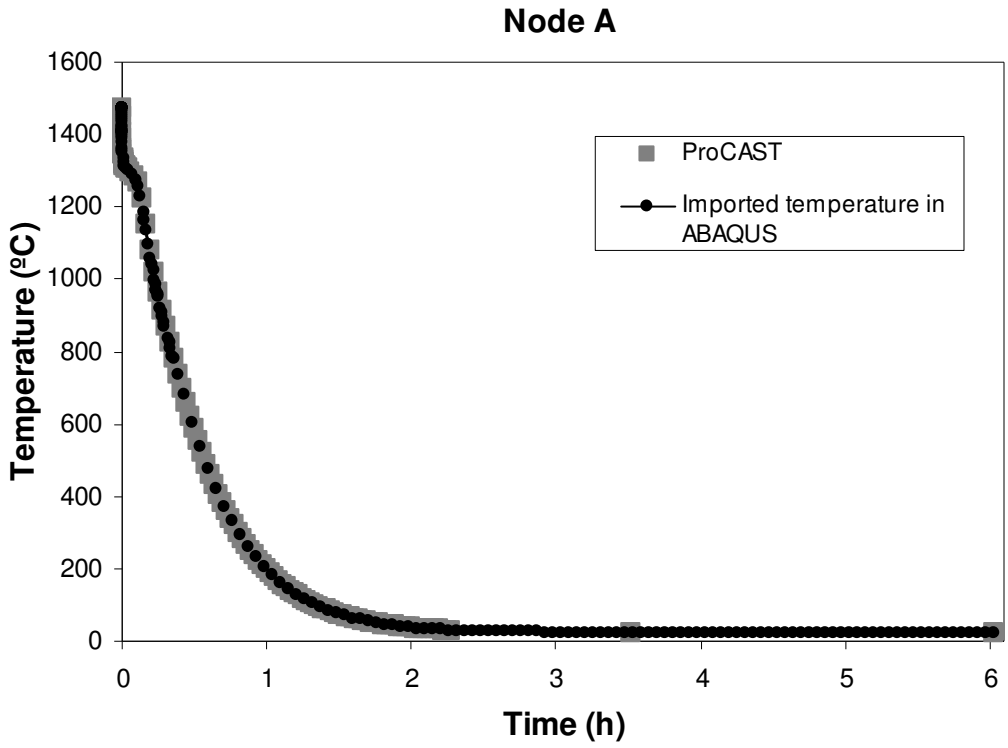

Figure 4.16: Temperature versus the time at point A calculated in ProCAST and imported in ABAQUS by using the UTEMP subroutine

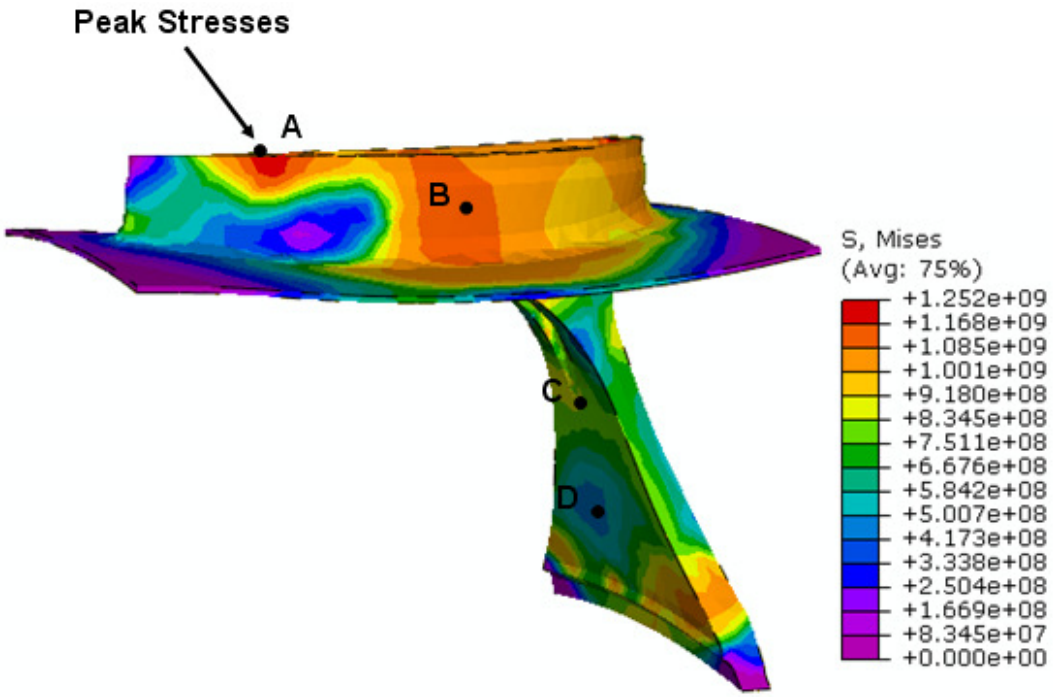

Figure 4.17: Von Mises in Pa calculated in ABAQUS based on the thermal history from ProCAST

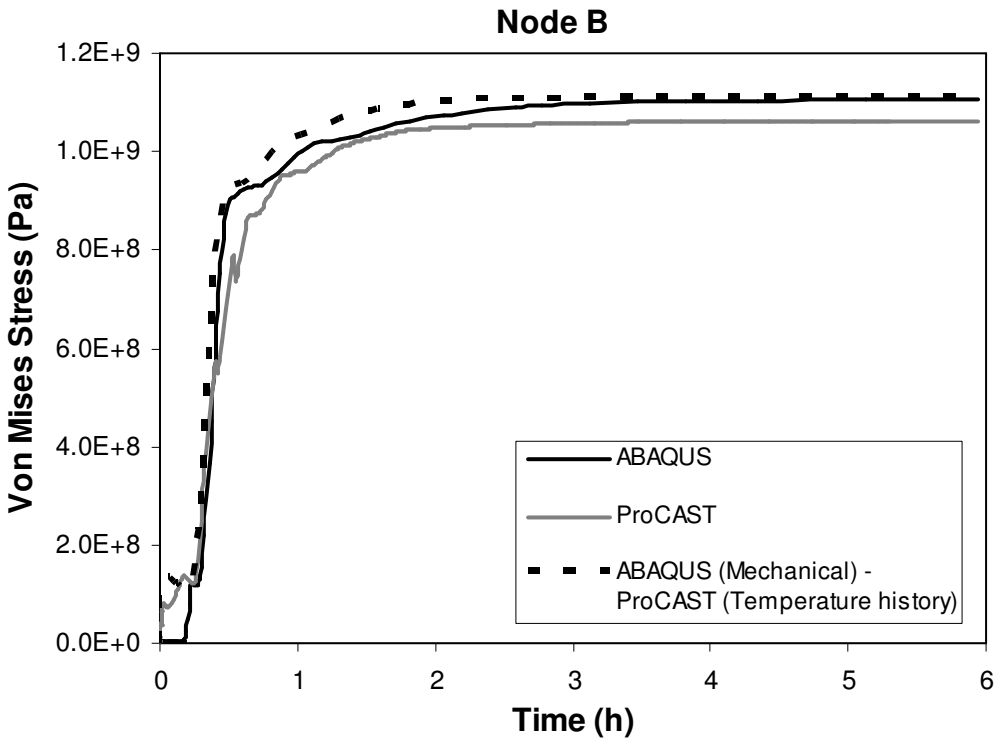

Figure 4.18: (a)

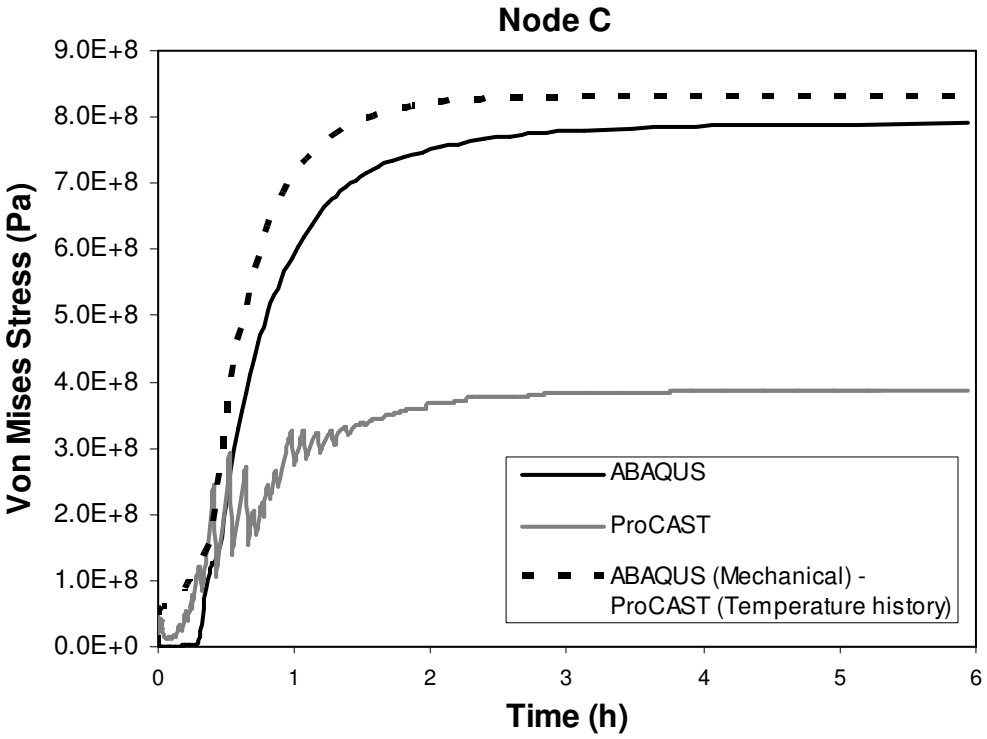

(b)

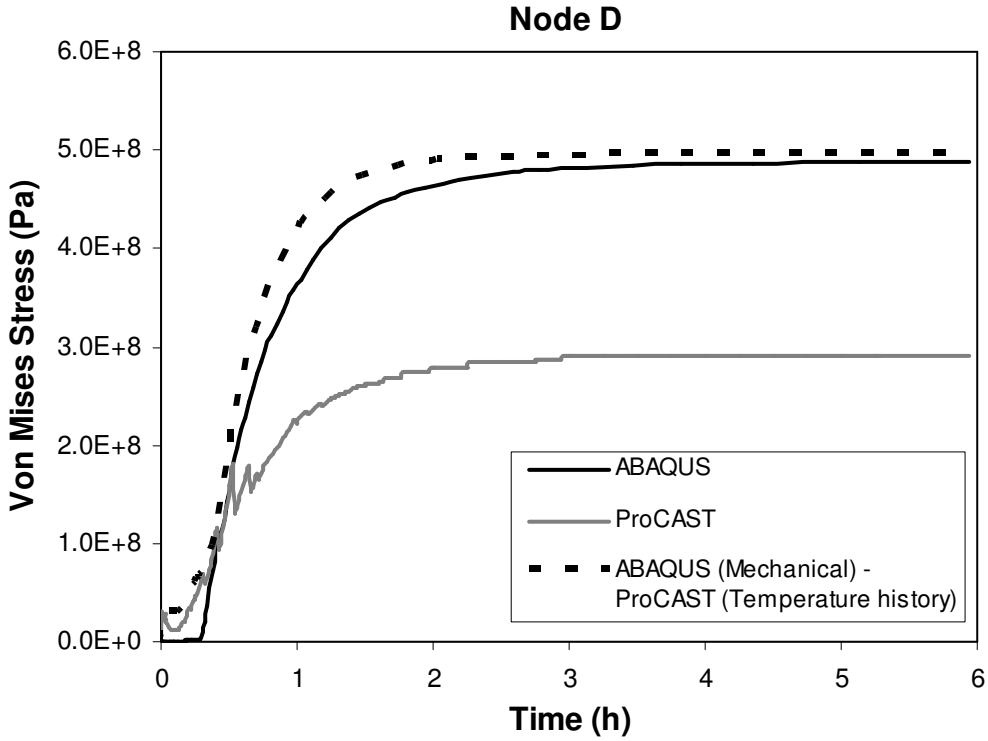

(c)

Figure 4.18: Von Mises residual stresses versus the time obtained in ABAQUS and ProCAST for: **(a)** Node B; **(b)** Node C; **(c)** Node D; (see Figure 4.17)

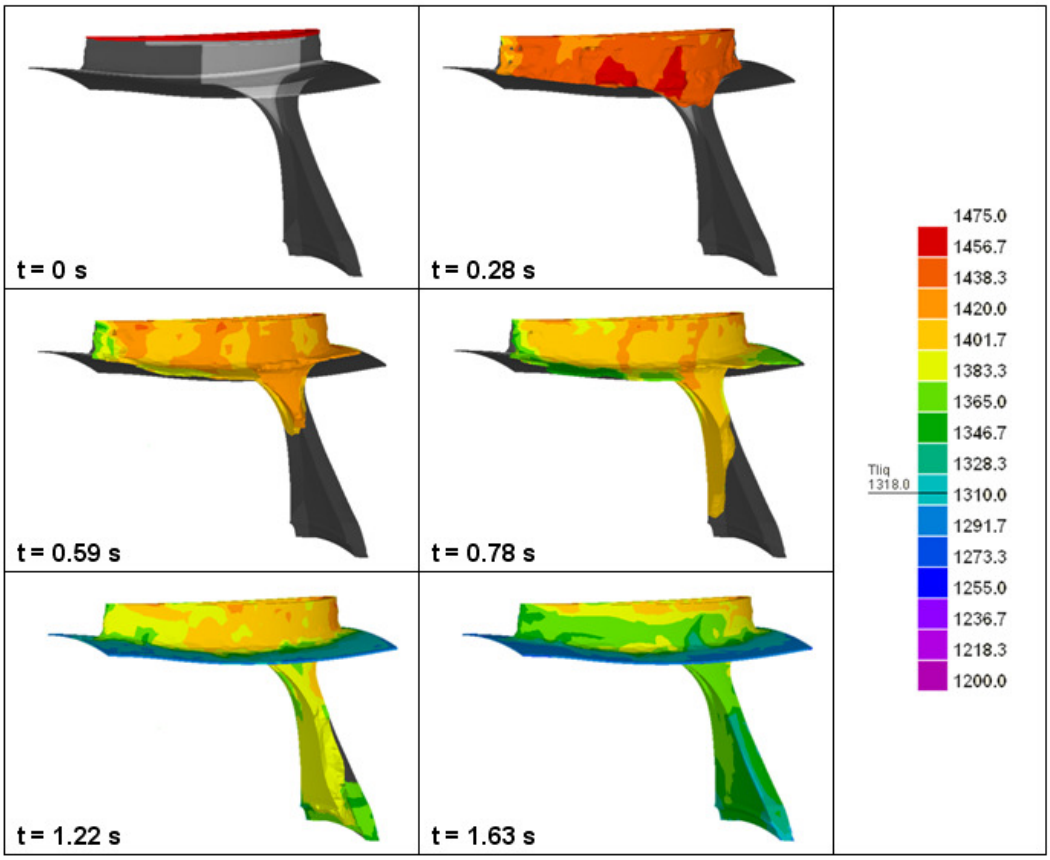

Figure 4.19: Temperature and fluid flows during the mould filling at different filling times

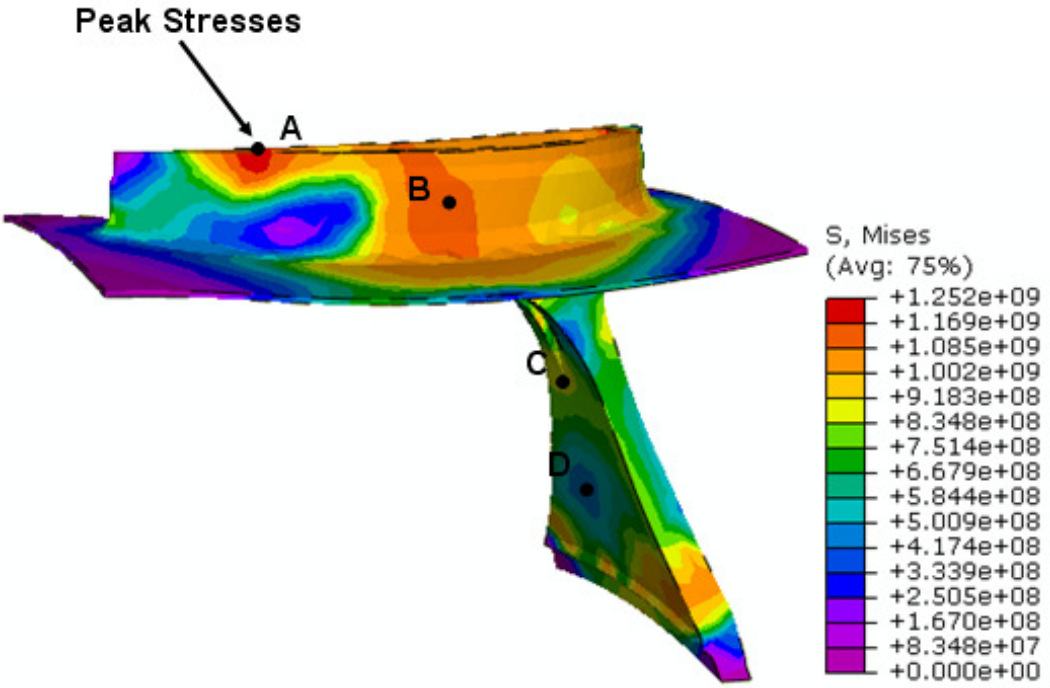

Figure 4.20: Residual Von Mises stresses in Pa obtained in ABAQUS by taking into account the mould filling effect

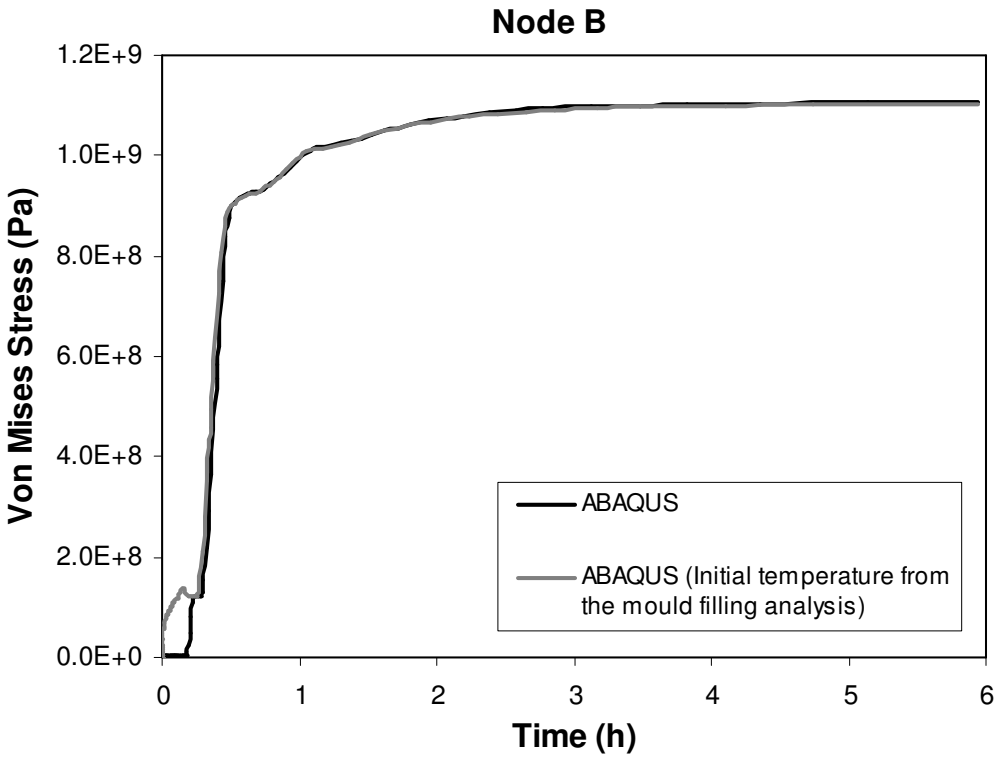

(a)

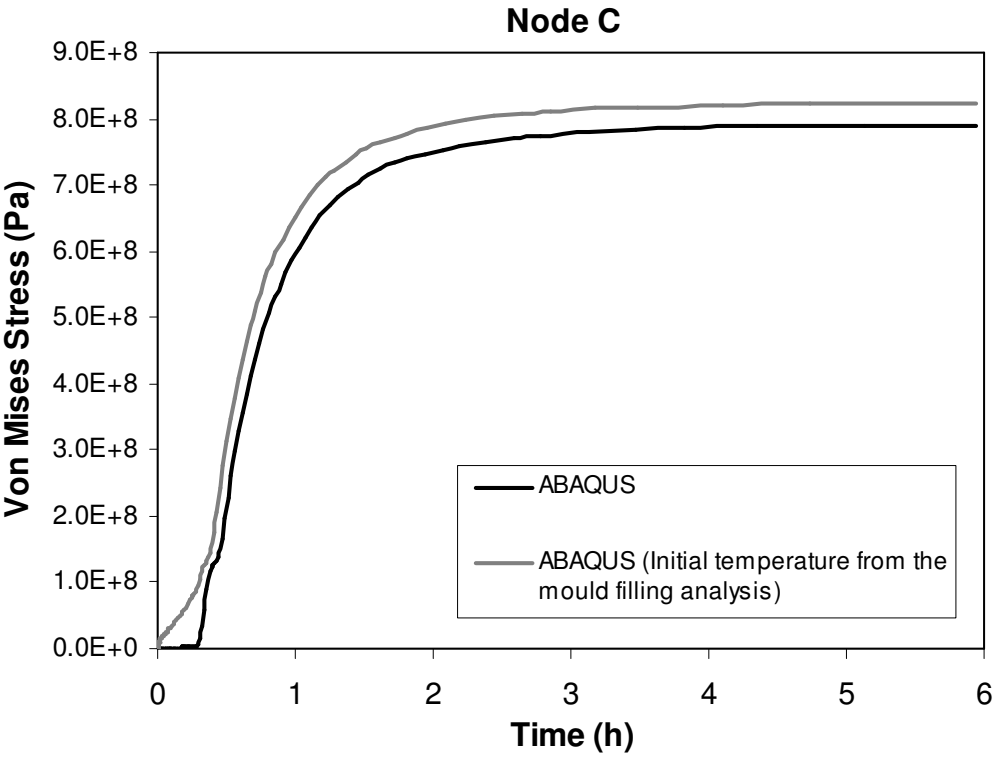

Figure 4.21: (b)

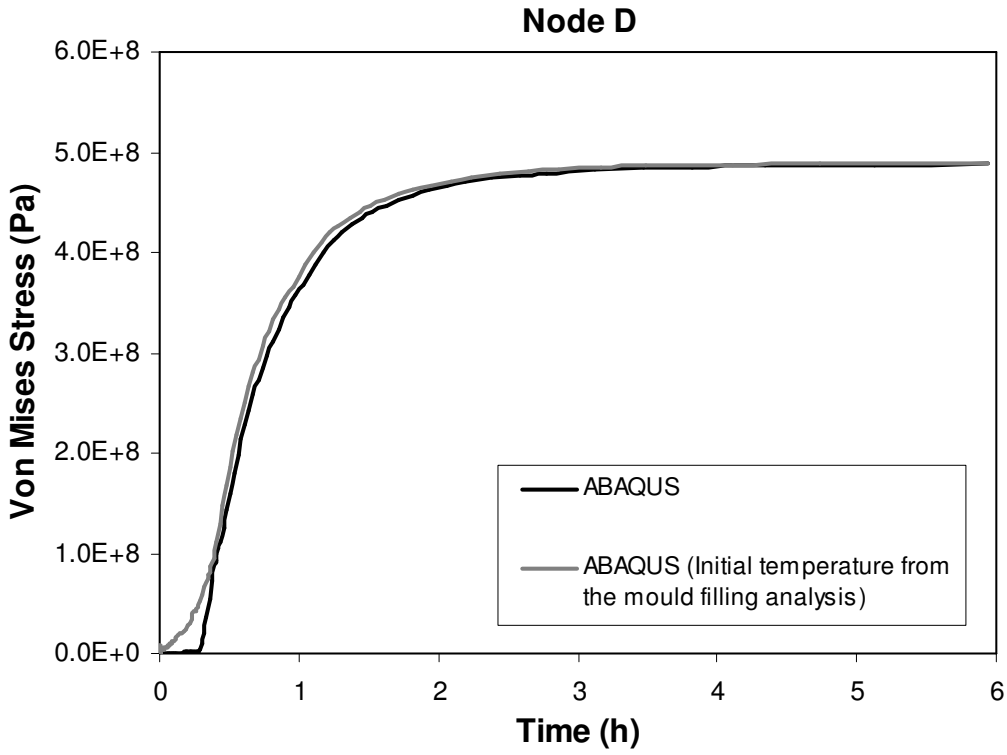

(c)

Figure 4.21: Von Mises residual stresses versus the time with and without taking into account the mould filling as an initial condition for the coupled temperature-displacement analyses in ABAQUS for: **(a)** Node B; **(b)** Node C; **(c)** Node D; (see Figure 4.20)

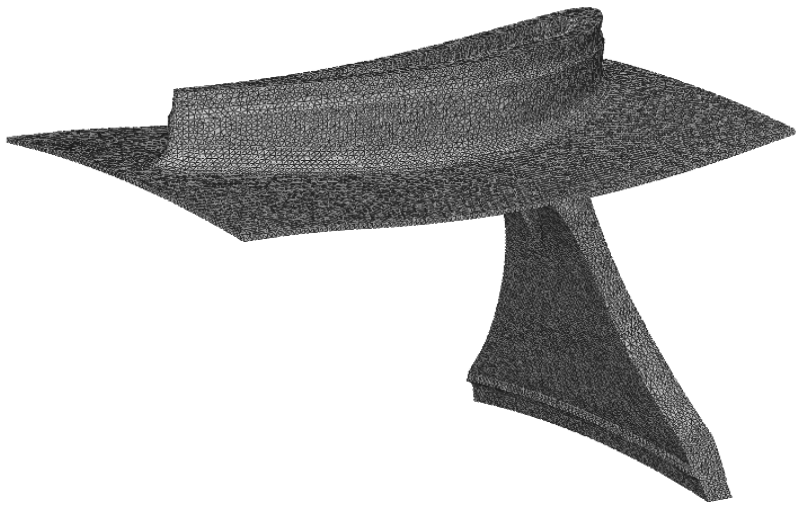

Figure 4.22: (a)

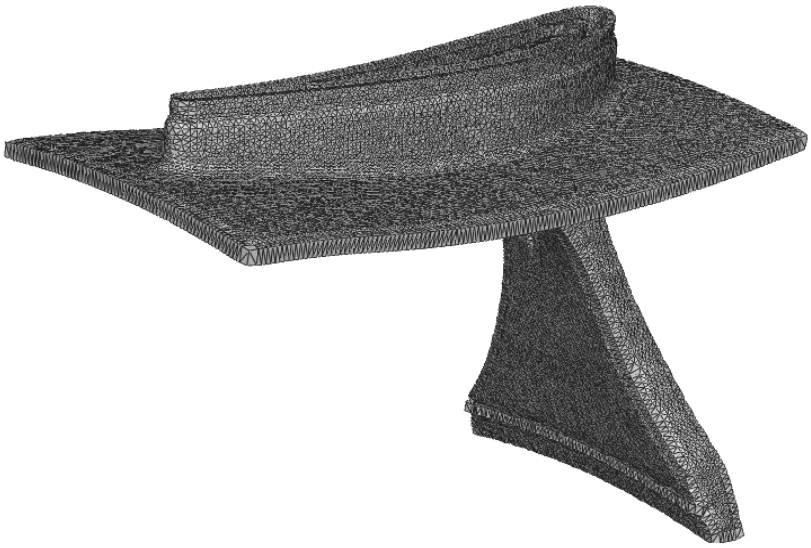

(b)

Figure 4.22: Refined mesh: **(a)** ingot with 379,440 four node tetrahedron elements; **(b)** mould with 209,730 six node wedge elements

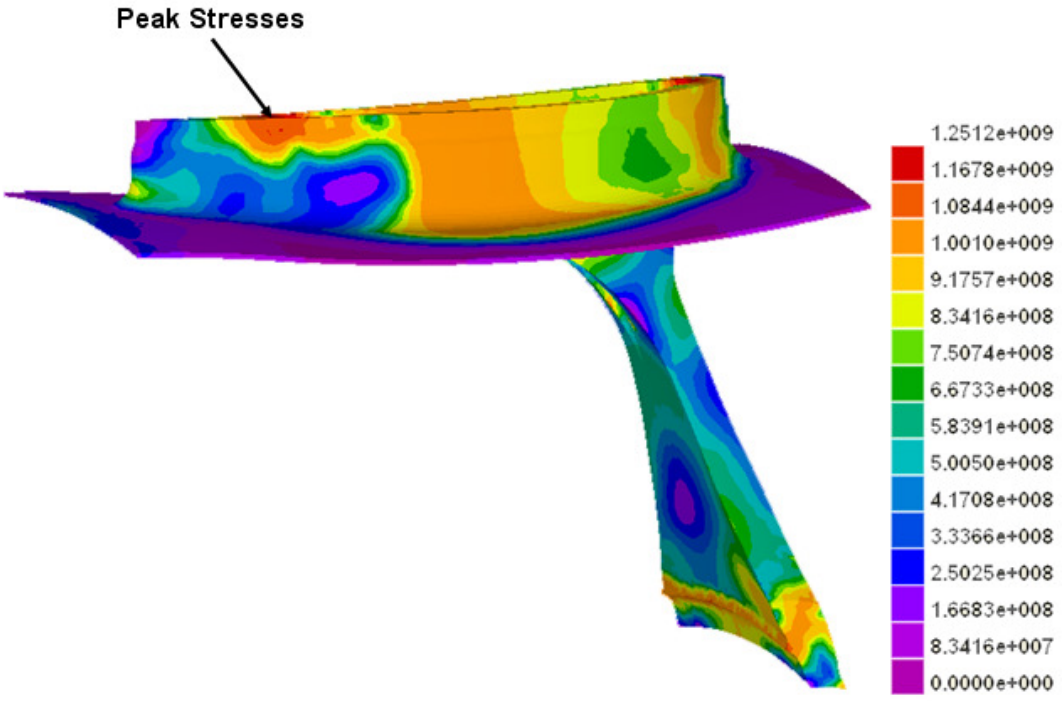

Figure 4.23: Residual Von Mises stresses in Pa obtained in ProCAST by using a refined mesh

CHAPTER 5

FE PREDICTION OF RESIDUAL STRESSES IN INVESTMENT CASTING OF A HIGH PRESSURE TURBINE BLADE UNDER DIRECTIONAL COOLING IN A BRIDGEMAN FURNACE

This chapter reviews an investment casting simulation of a high pressure turbine blade (HPTB) under directional cooling (DC) performed in vacuum in a Bridgeman furnace. The simulation is based on the single crystal (SC) and the directional solidification (DS) processes, and it is carried out by using the FEM in ABAQUS. The temperature and the residual stresses are investigated for withdrawal velocities of 0.6 and 0.06 mm/s. The simulation is performed in a vacuum environment of the furnace where the heat transfer is achieved by cavity radiation where the view factor calculations are performed.

5.1 Introduction

The investment casting process for HPTB involves the following steps. First, a wax model of the casting is prepared by injecting molten wax into a metallic 'master' mould, if necessary (for hollow blades) by allowing wax to set around a ceramic core, which is a replica of the cooling passages required. These are arranged in clusters connected by wax replicas of runners and risers which enable several blades to be produced in a single casting, as shown in Figure 5.1. Next, the investment shell is produced by dipping the model into ceramic slurries. This operation is repeated three or four times until the shell thickness is adequate. Finally, the mould is baked to build up its strength. The first step involves a temperature just sufficient to melt out the wax. Further steps at high temperature are employed to fire the ceramic mould [73].

The blading for the very first gas turbine engines was produced by extrusion and forging operations. However, in the 1970s it became apparent that there were severe

limitations with this approach. First, the blades tended to be heavy, since they are made in hollow form, without subsequent machining operation. Second, they were prone to cracking and incipient melting, since high working temperatures were required, particularly for alloys with high yield stress. Thus, nowadays, superalloy turbine blading is always produced by investment casting. When investment casting was first applied to the production of turbine blading, equiaxed castings were produced by the 'power-down' method, which involves the switching off of the furnace after pouring the molten metal, which allows equal cooling in all axes.

However, it has been found that the creep properties are improved markedly if directional solidification is used. After pouring, the casting is withdrawn at a controlled rate from the furnace. A speed of a few inches per hour is typical so that the solid/liquid interface progresses gradually along the casting, beginning at its base. This has the effect of producing large columnar grains which are elongated in the direction of withdrawal, so that transverse grain boundaries are absent. In a variant of this process, the grain boundaries are removed entirely. Most typically, this is achieved by adding a 'grain selector', typically in the form of a pig-tail-shaped spiral. Since this is not significantly larger in cross-section than the grain size, only a single grain enters the cavity of the casting, which is then in monocrystalinne form [73]. Figure 5.2 shows the Rolls-Royce Trent 800 HPTB casting after removal of the investment shell, while Figure 5.3 shows the final HPTB after machining and other applied manufacturing processes, such as applying thermal barrier coatings.

5.2 Process definition

As mentioned, the SC and the DS are widely used in the aero industry for casting HPTB with nickel based alloys. These processes increase the durability of the blades by improving the creep resistance due to the dendrite growth in direction of withdrawal. The SC and the DS processes are achieved in a Bridgman furnace in the following sequence:

- The mould is placed on a water-cooled copper chill

- The mould is placed into an induction heated vacuum Bridgman furnace. It is heated by radiation above the liquidus temperature of the alloy
- The liquid is poured into the mould. During mould filling the liquid cools around the selector (pig tail) due to the water-cooled copper chill and the grains start growing. The selector is used to allow passing only single crystals in the mould
- After the mould filling has finished, the mould and the ingot are left for some time in the furnace to equalise the temperature of the mould and the ingot
- The mould with the liquid inside is withdrawn from the hot to the cold chamber of the furnace where the DS is achieved and the dendrites start growing in direction of the withdrawal

Figure 5.4 shows a schematic figure of Bridgman furnace used at Carleton University, Canada [18]. The dimensions, maximum temperature, the travelling length, etc. of Bridgman furnaces are designed according to the casting geometry and the casting material. The furnaces can be ordered by specifying the furnace conditions and dimensions from the producers. For example, copper chill plate of the casting furnace at Rolls-Royce plc, Derby, UK has diameter of 140 mm [73]. This size is sufficient for five HPTB for a civil jet engine to be produced simultaneously.

5.3 FE model

A sequential thermo-mechanical analysis is carried out. First, the thermal analysis is performed to obtain the temperature history for all nodes of the model. Next, a mechanical analysis is carried out to predict the residual stresses based on the temperature history from the thermal analysis.

5.3.1 Geometry and mesh

The height of the HPTB is 115 mm, as shown in Figure 5.3 and the geometry of the HPTB is approximated based on Figure 5.2. The investment shell has a thickness of

0.75 mm thickness. It is assumed that the shell thickness can be simulated by decreasing the coefficient of thermal conductivity for the mould material, because the shell thickness of the mould is constant for the entire mould and the heat transfer is linear through the thickness due to the constant coefficient of thermal conductivity of the mould material as shown in Section 5.4. Based on this assumption, the shell thickness of 5 mm is simulated by decreasing the coefficient of thermal conductivity by 6.667 times. The water-cooled chill plate diameter is chosen to be 140 mm, where the shell cluster assembly of five blades is placed on it [73]. The furnace geometry is approximated based on the shell cluster assembly dimensions and the design of the Bridgman furnace from Figure 5.4. Due to cyclic symmetry, only one fifth of the furnace and the cluster assembly are modeled, as shown in Figure 5.5.

Four node linear tetrahedron elements are used for the mesh of the ingot, the mould and the copper chill. The furnace and the holder are meshed with eight node linear hexahedron elements. Figure 5.6 shows the two meshes used for the thermal and the mechanical analyses. The mesh used for the thermal analysis has 22,164 elements, while the mesh for the mechanical analysis has 42,946 elements. A more refined mesh is created for the ingot in the mechanical analysis in order to predict more accurately the residual stresses while the element number for the mesh in the thermal analysis is kept smaller due to the complexity of the thermal model which requires a huge amount of computational time.

5.3.2 Boundary conditions

The thermal analysis is simulated by applying the following boundary conditions. A constant temperature of 1500 ºC is applied to the heating elements of the furnace, which represents the heat generation in the hot chamber of the furnace. A constant temperature of 20 ºC is applied to the cold water-cooled chamber of the furnace, which represents the circulated water in the water-cooled cold chamber. An initial temperature of 1500 ºC is applied to the mould, ingot, baffles, hot water-cooled chamber and the copper-chill. These temperatures are considered with the poring temperature of the CMSX-4 alloy of 1500 ºC [17]. Air convection is applied to the outsides of the furnace by using a convection coefficient of 20 W/m^2K. Forced

convection of 2500 W/m^{2}K is applied to represent the water circulation inside the copper chill plate. Thermal contacts are defined between the following surfaces: (a) water-cooled chill plate and mould; (b) ingot and mould; (c) ingot and water-cooled chill plate. Heat transfer coefficient (HTC) of 20 W/m^{2}K is applied between contact surfaces (a), 200 W/m^{2}K between surfaces (b) and temperature deepened HTC between surfaces (c) [17]. Figure 5.7 shows the HTC between the contact surfaces (c). The heat transfer inside the furnace is achieved in vacuum, where the radiation is the dominant factor. Cavity radiation is defined between the internal furnace surfaces and the external surfaces of the mould and the holder. View factor calculations, with reflections in the cavity, are included. Withdrawal velocities of 0.6 and 0.06 mm/s are applied.

The mechanical analysis is simulated by applying the following boundary conditions. All components of the model, except the ingot, are modelled as constrained by applying zero displacements in all directions. The ingot is constrained by applying zero displacements in the z direction on one of the surfaces of the ingot feeder and zero displacements in the x and z direction on the edge of the ingot feeder. Gravity is applied to the ingot. Frictionless contact is applied between contact surfaces (a), (b) and (c).

5.3.3 Simulation sequence

A thermal analysis followed by mechanical analysis is carried out in the simulation. The thermal analysis is performed in two steps. In the first step, the mould and the ingot are withdrawn from the hot to the cold chamber. In the second step, when the mould and the ingot are located entirely in the cold chamber, the furnace is switched off. This is achieved by deactivating the constant temperature of the heating elements. The mechanical analysis is performed in three steps. The first two steps use the temperature history of the thermal analysis. Due to the two different meshes of the ingot used in the thermal and the mechanical analysis, a temperature interpolation is performed from the thermal to the mechanical mesh of the ingot by using the built-in algorithms in ABAQUS. A third step is applied to release the ingot from the mould where the contact between the mould and the ingot is deactivated.

5.4 Material properties

The ingot material is CMSX-4 single crystal nickel-based alloy. The mould material is Sand Silica. The furnace (see Figure 5.4) consists of the following materials: water cooled chill plate – copper; heating element – molybdenum, insulation and baffle – zirconia; water-cooled chamber and holder – stainless steel.

CMSX-4

CMSX-4 alloy is an ultra high strength second-generation nickel-base single-crystal superalloy. The solidus and the liquidus temperatures of the CMSX-4 alloy are respectively 1329 ºC and 1381ºC, and the latent heat is 304 kJ/kg [83]. Temperature dependent thermo-physical and mechanical material properties are summarised in Tables 5.1-5.5. It can be seen that the elastic modulus is obtained for temperatures up to 1100 ºC and the yield stress up to 1090 ºC. Elastic modulus of 250 MPa and a yield stress of 7.5 MPa are applied at the mushy zone of the alloy, as recommended in [79]. As described, in the DS the dendrites grow in one direction and the material exhibits an anisotropic behaviour. It is assumed that the CMSX-4 alloy exhibits isotropic behaviour. Therefore, a material model with isotropic hardening is used for the current FE model.

Sand Silica

Sand Silica material is hard, porous and brittle with low thermal conductivity. The thermo-physical material properties are given in Table 4.1.

Copper

Copper is a ductile metal with an excellent thermal and electrical conductivity. Temperature dependent thermo-physical properties are given in Tables 5.6 and 5.7.

Zirconia

Zirconia is a white crystalline oxide of zirconium. Temperature dependent thermo-physical material properties are summarised in Tables 5.8 and 5.9.

Molybdenum

Molybdenum is a transition metal with atomic mass of 95.9 g/mole and very high melting temperature. Temperature dependent thermo-physical material properties are given in Tables 5.10 and 5.11.

Stainless Steel

In metallurgy, stainless steel is defined as a steel alloy with a minimum of 10% chromium content by mass. It has high resistance to corrosion and staining. Temperature dependent thermo-physical material properties are given in Table 5.12. The density at room temperature of 7900 kg/m^3 is used [41].

5.5 Results and discussion

As mentioned before, two withdrawal velocities are investigated. A withdrawal motion of 240 mm is used for both withdrawal velocities. This means that for applied velocities of 0.6 and 0.06 mm/s, the directional cooling step lasts respectively 6.6 minutes and 66 minutes. Figure 5.8(a) shows the temperature contour of the ingot at a withdrawal motion of 144 mm for a withdrawal velocity of 0.6 mm/s. It can be seen that the temperature is different in the cross sections of the ingot, except the bottom part where the cooling is dominant by the water circulation in the copper chill plate. This temperature difference in the cross sections allows the dendrites to grow in direction different of the withdrawal. This creates stray grains in the blade which is not desirable as investigated somewhere else [12]. Figure 5.8(b) shows the temperature versus the time for the two steps of the thermal analysis at six points on the ingot (see Figure 5.8(a)). It can be seen that all nodes are in the mushy zone after the directional cooling step except node F. This means that the ingot arrives in the cold chamber as non-solid. This allows the formation of equiaxed grains during the entire cooling of the ingot at step two when the furnace is switched off.

Figure 5.9(a) shows the temperature contour of the ingot at motion of 144 mm for a withdrawal velocity of 0.06 mm/s. It can be seen that the temperature is similar in the cross sections of the ingot which avoids the formation of stray grains in the

blade. Figure 5.9(b) shows the temperature versus the time at the same six points from the ingot as at 0.6 mm/s (see Figure 5.9(a)). It can be seen that at the end of the directional solidification step, all six nodes are below the solidus temperature.

The dendrite growth starts at the baffle of the furnace as shown in Figure 5.4 except the bottom part where the cooling is mainly achieved by the water circulation in the water-cooled chill plate. Figure 5.10 shows the temperature as a function of the motion for withdrawal velocities of 0.6 and 0.06 mm/s at six nodes (see Figures 5.8-5.9). The baffle level is illustrated in Figure 5.10 when each of the six nodes reaches it for the corresponding motion. The requirement is that each node of the ingot has a temperature lower than the solidus temperature of the alloy when the baffle level is reached. It can be seen that for a withdrawal velocity of 0.6 mm/s all six nodes are in a liquid stage when the baffle level is reached. For a withdrawal velocity of 0.06 mm/s, nodes A, B, C and F are in a solid stage at the baffle level. Nodes D and E are in the mushy stage. This is because the HPTB is thick in that area and the cooling is slower. This indicates that a lower withdrawal velocity is required in that area in order to assure that the dendrites growth is in the direction of withdrawal.

Figure 5.11 shows the Von Mises residual stress contour of the ingot obtained for withdrawal velocities of 0.6 and 0.06 mm/s. The peak stresses of 917 MPa are observed around the sharp corners for both models. It can be seen that the stresses in the lower part of the HPTB are higher at a velocity of 0.6 mm/s compared to 0.06 mm/s. Figure 5.12 shows the Von Mises stresses obtained in the three steps of the mechanical analysis for both withdrawal velocities at six nodes (see Figure 5.11). As mentioned before, the cluster is withdrawn from the hot to the cold chamber in step one, the furnace is switched off and the cluster is cooled to room temperature in step two, and finally the ingot is released from the mould in step three. Node A shows Von Mises stresses around 100-130 MPa at step 3 for both withdrawal velocities. At the end of the cooling at step two the Von Mises stresses reach values of 900 MPa. High values are observed for nodes B, C and D at step two as well. The final Von Mises stresses at step three for nodes B, C and D are slightly different. Higher Von Mises stresses (more that 8 times) are obtained for Nodes E and F at the withdrawal velocity of 0.6 mm/s compared to 0.06 mm/s when the ingot is released from the mould.

Most of the constitutive equations for creep and fatigue life prediction involve the use of the maximum principal stresses component. Figure 5.13 shows the maximum principal residuals stresses of the HPTB at 0.6 and 0.06 mm/s.

5.6 Conclusions

Thermal and mechanical FEAs of a HPTB have been performed where the temperature and the residual stresses at the withdrawal velocities of 0.6 and 0.06 mm/s have been obtained.

It has been observed that for the withdrawal velocity of 0.6 mm/s, the temperature of the ingot in the baffle zone of the Bridgman furnace was in a liquid stage which is undesirable. Also, temperature differences in the cross sections have been observed which leads to the creation of stray grains. The temperature at six nodes of the ingot for the withdrawal velocity of 0.06 mm/s has been investigated. It has been observed that the temperature of the ingot in the baffle zone of the Bridgman furnace is in a solid stage which indicates the dendrites growth in the direction of withdrawal. Some nodes in the lower (thick) part of the HPTB have been found in the mushy stage. This indicates that a lower withdrawal velocity needs to be applied in that area. Also, an equal temperature for the withdrawal velocity of 0.06 mm/s in the cross sections has been observed which avoids the creation of stray grains.

Higher residual stresses have been determined in the lower (thick) part of the HPTB for the withdrawal velocity of 0.6 compared to 0.06 mm/s. The residual stresses in the rest of the HPTB have been found to be similar for both withdrawal velocities. The peak stresses have been observed in the sharp corners of the HPTB.

Table 5.1: Elastic modulus [84,85] and Poisson's ratio [84] of CMSX-4

Temperature (ºC)	Elastic modulus (GPa)	Poisson's ratio (-)
25	128	0.389
200	121	0.393
300	128	0.394
400	125	0.395
500	110	0.395
600	105.5	0.397
700	101	0.399
800	95.5	0.4025
900	90	0.409
1000	87.5	0.41
1100	78.5	

Table 5.2: Mechanical material properties of CMSX-4 [86]

Temperature (ºC)	Yield Stress (MPa)	Ultimate Stress (MPa)	Elongation (%)
25	910	960	12
390	945	1075	12
490	930	1010	9.6
690	980	1200	9.5
890	790	935	17
990	610	835	19.5
1090	360	465	22

Table 5.3: Emissivity of CMSX-4 [81]

Temperature (ºC)	Emissivity (-)
650	0.84
750	0.82
850	0.795
950	0.79
1000	0.789

Table 5.4: Density of CMSX-4 [83]

Temperature (ºC)	Density (kg/m^3)
23	8500
660	8310
1060	8130
1150	8036
1300	7921
1360	7863
1365	7736
1500	7532

Table 5.5: Thermo-physical material properties of CMSX-4 [87]

Temperature (ºC)	Expansion (1/K)	Conductivity (W/mK)	Heat capacity (J/kgK)
25	1.00×10^{-5}	10	420
100	1.07×10^{-5}	10.5	430
200	1.16×10^{-5}	11.7	440
300	1.23×10^{-5}	12.5	450
400	1.28×10^{-5}	14	460
500	1.32×10^{-5}	15.5	470
600	1.35×10^{-5}	17.5	490
700	1.38×10^{-5}	20	540
800	1.42×10^{-5}	22.5	580
900	1.46×10^{-5}	25	640
1000	1.55×10^{-5}	28	710
1100	1.64×10^{-5}	31	850
1200		35	1150
1300			1000
1400			680
1500			680

Table 5.6: Thermal conductivity and heat capacity of copper [41]

Temperature (ºC)	Conductivity (W/mK)	Heat capacity (J/kgK)
20	386	383
127	379	395
327	370	415
527	359	430
727	345	450
927	331	480

Table 5.7: Density and emissivity of copper [41]

Temperature (ºC)	Density (kg/m^3)	Emissivity (-)
20	8950	0.3
327		0.4
727		0.4

Table 5.8: Heat capacity and emissivity of Zirconia [88]

Temperature (ºC)	Heat capacity (J/kgK)	Emissivity (-)
400	520	0.7
500	550	0.72
560		0.72
630		0.71
700	590	0.705
750		0.7
800	610	0.69

Table 5.9: Density and thermal conductivity of Zirconia [41]

Density (kg/m^3)	3600
Thermal conductivity (W/mK)	2.44

Table 5.10: Thermo-physical material properties of Molybdenum [89,90]

Temperature (ºC)	Density (kg/m^3)	Conductivity (W/mK)	Heat capacity (J/kgK)
27	1024	138	251
127	1021	134	261
327	1016	126	275
427	1013	122.5	279
527	1011	118	285
627	1009	115	291
727	1006	112	295
927	1001	105	308
1227	994	98	330
1327	991.6	96.1	338
1627	984.3	91	367
1727	982	90	380
1827	979.6	88.6	393
2227	970	86	459
2327	967.6	85.9	480

Table 5.11: Emissivity of Molybdenum [41]

Temperature (ºC)	Emissivity (-)
527	0.06
727	0.1
1227	0.15
1727	0.21

Table 5.12: Thermo-physical material properties of stainless steel [41]

Temperature (ºC)	Conductivity (W/mK)	Heat capacity (J/kgK)	Emissivity (-)
20	14.9	477	0.17
127	16.6	515	
327	19.8	557	0.19
527	22.6	582	
727	25.4	611	0.3
927	28	640	

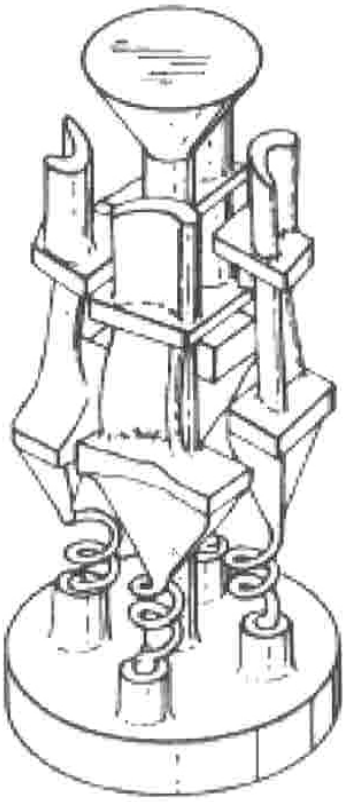

Figure 5.1: Wax cluster model for producing HPTB

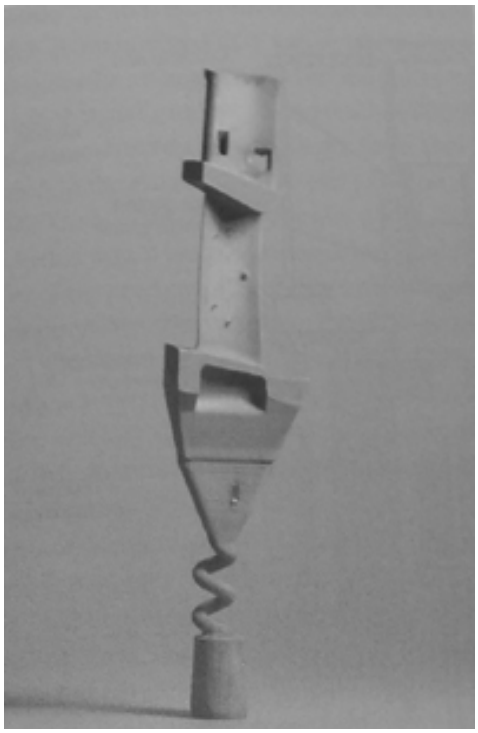

Figure 5.2: Rolls-Royce Trent 800 HPTB after removal of the investment shell [73].

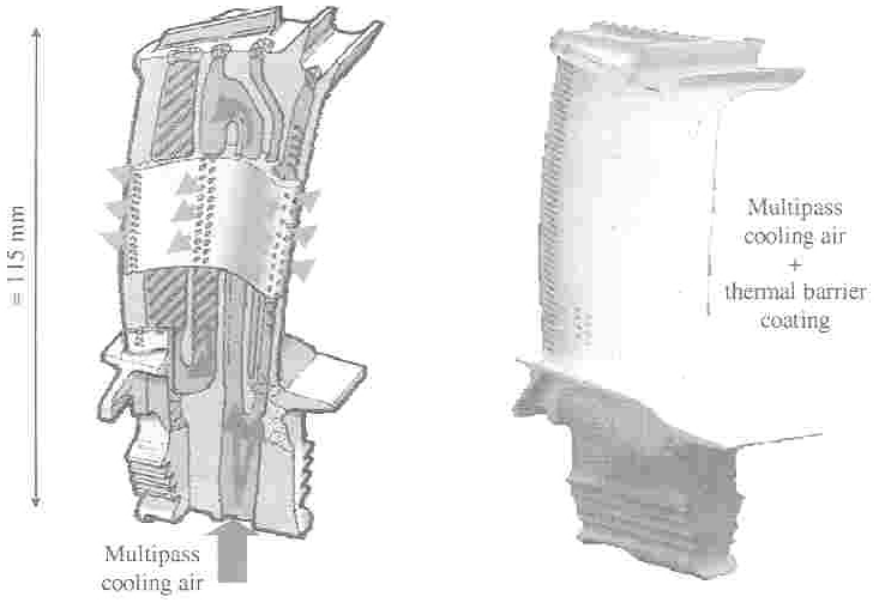

(a) (b)

Figure 5.3: Rolls-Royce Trent 800 HPTB: **(a)** Multipass cooling air where the turbine entry temperature is 1420 ºC; **(b)** Multipass cooling air plus thermal barrier coatings where the turbine entry temperature is more than 1550 ºC [82]

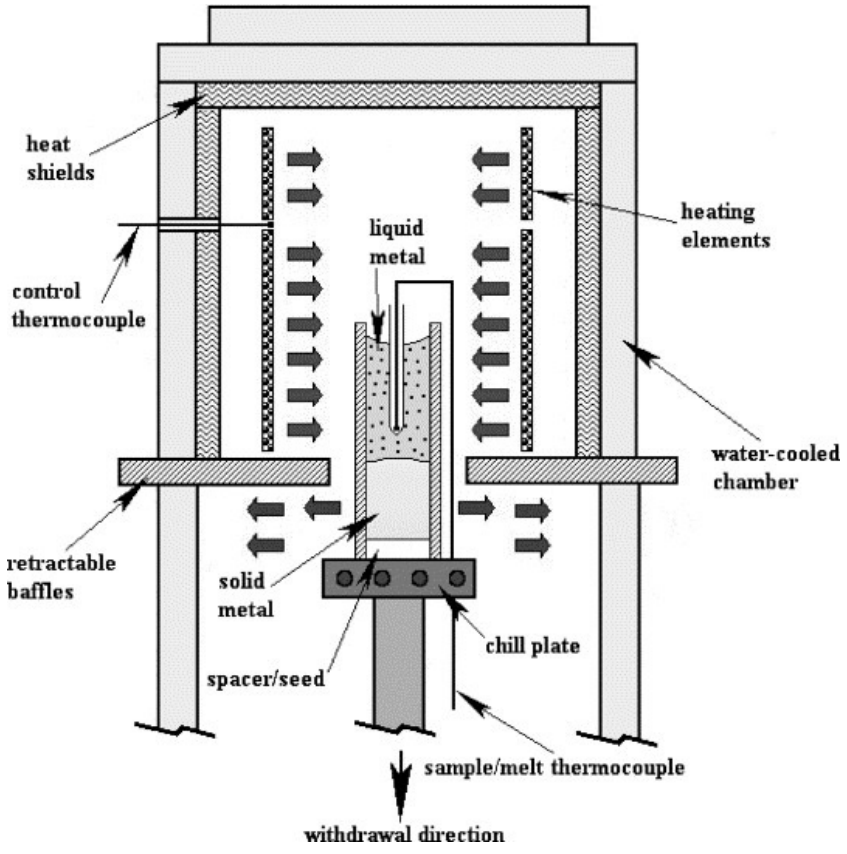

Figure 5.4: Schematic of a Bridgman casting furnace [18]

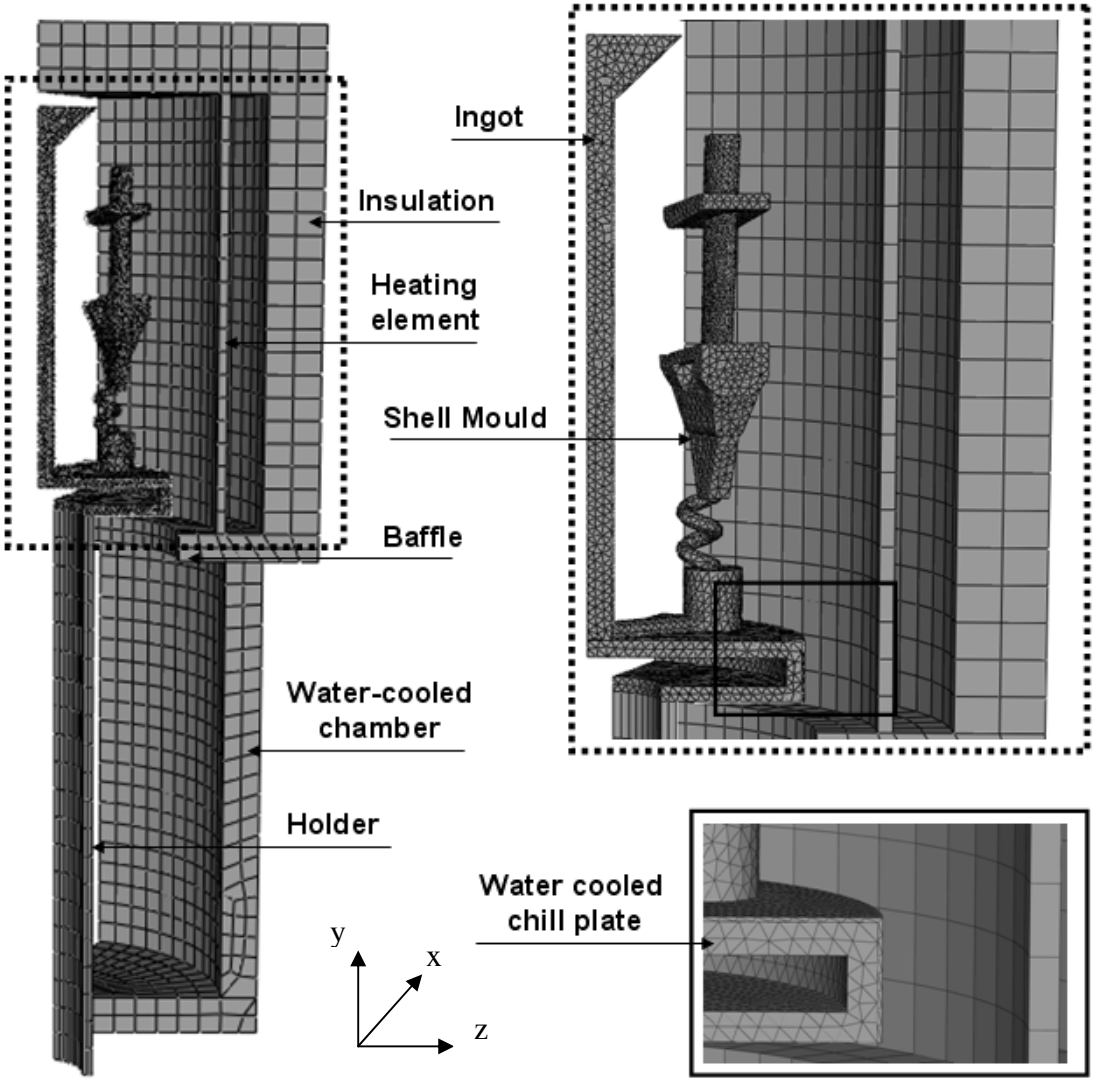

Figure 5.5: FE model of the mould, ingot and furnace. Enlarged figures of the hot chamber and the water cooled chill plate

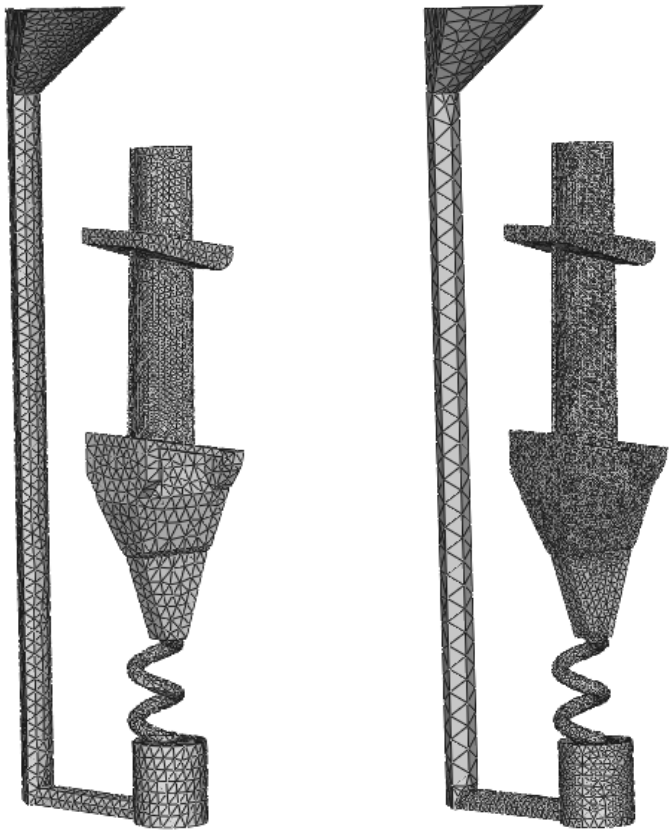

(a) (b)

Figure 5.6: Meshes used for the: **(a)** thermal analysis; **(b)** mechanical analysis

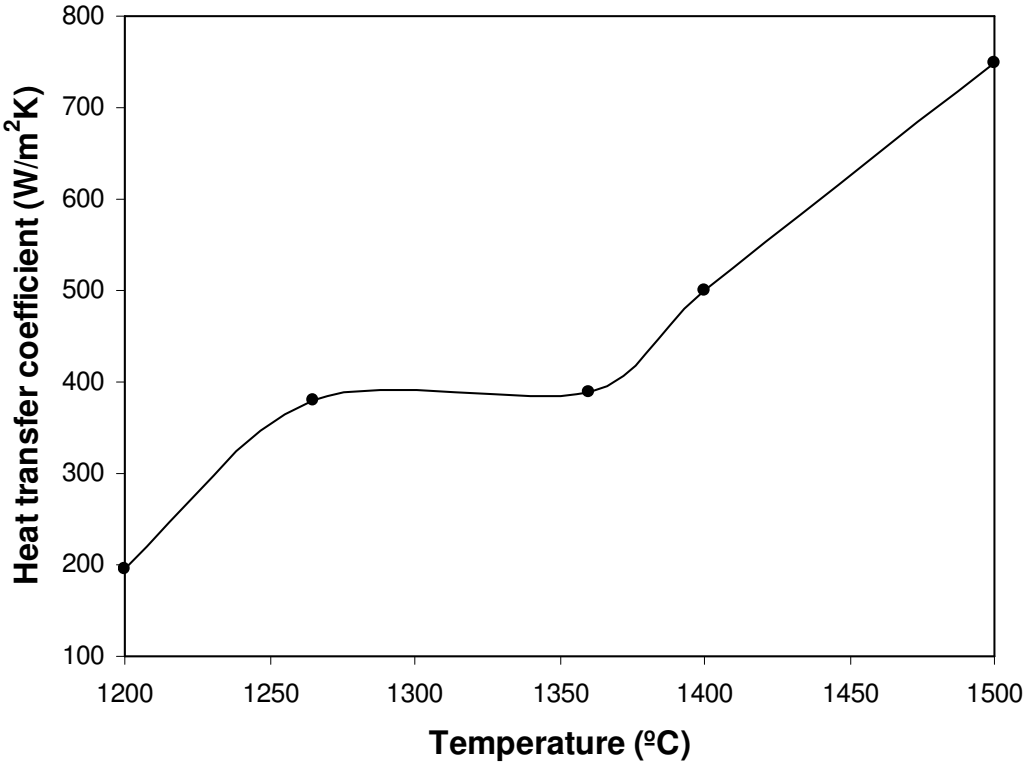

Figure 5.7: Optimised heat transfer coefficient between CMSX-4 alloy and copper [17]

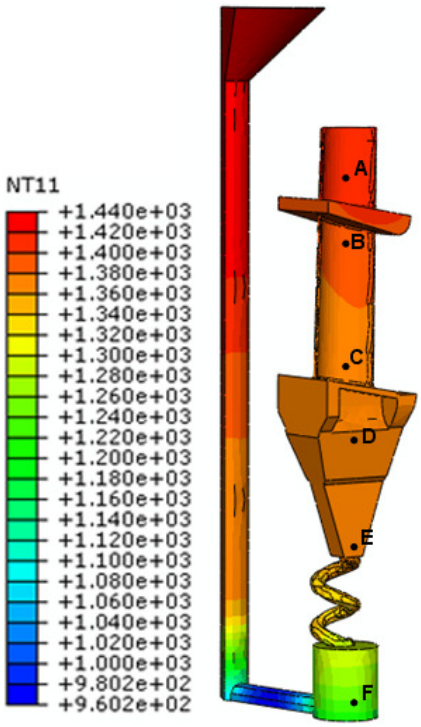

(a)

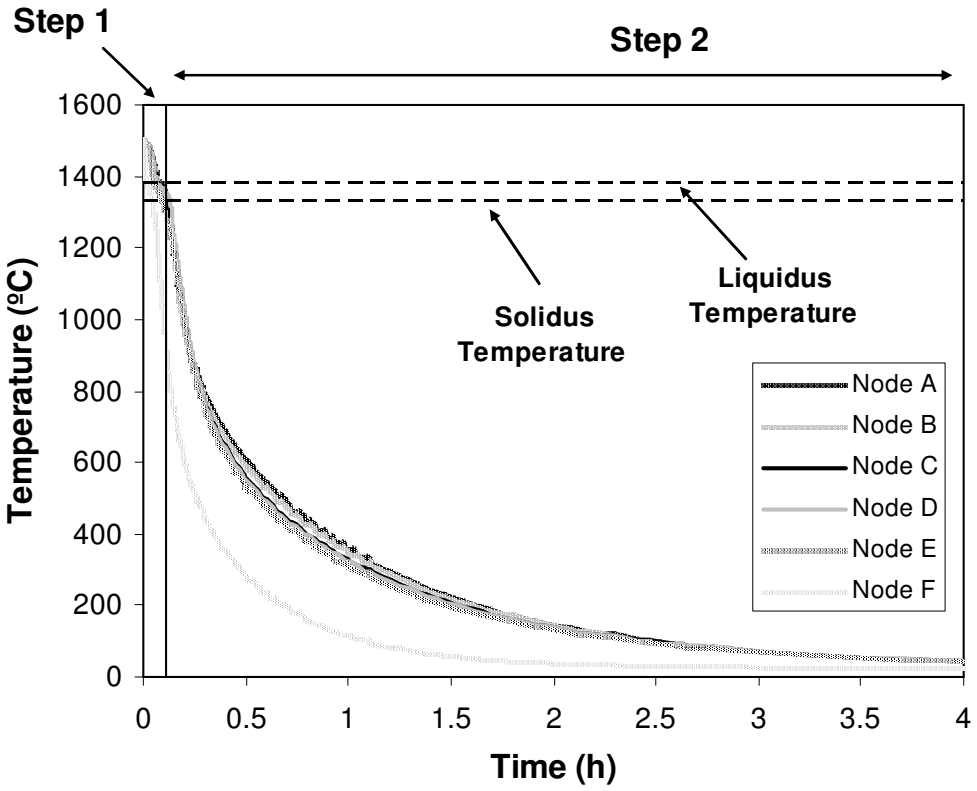

(b)

Figure 5.8: (a) Temperature contour of the ingot at motion of 144 mm for withdrawal velocity of 0.6 mm/s; **(b)** Temperature variation at nodes A, B, C, D, E and F versus the time for Step 1 (the model is withdrawn from the hot to the could chamber of the furnace) and Step 2 (the model is located in the could chamber of the furnace)

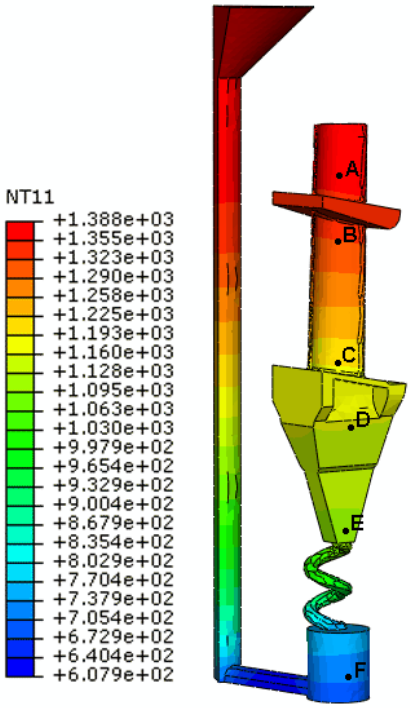

(a)

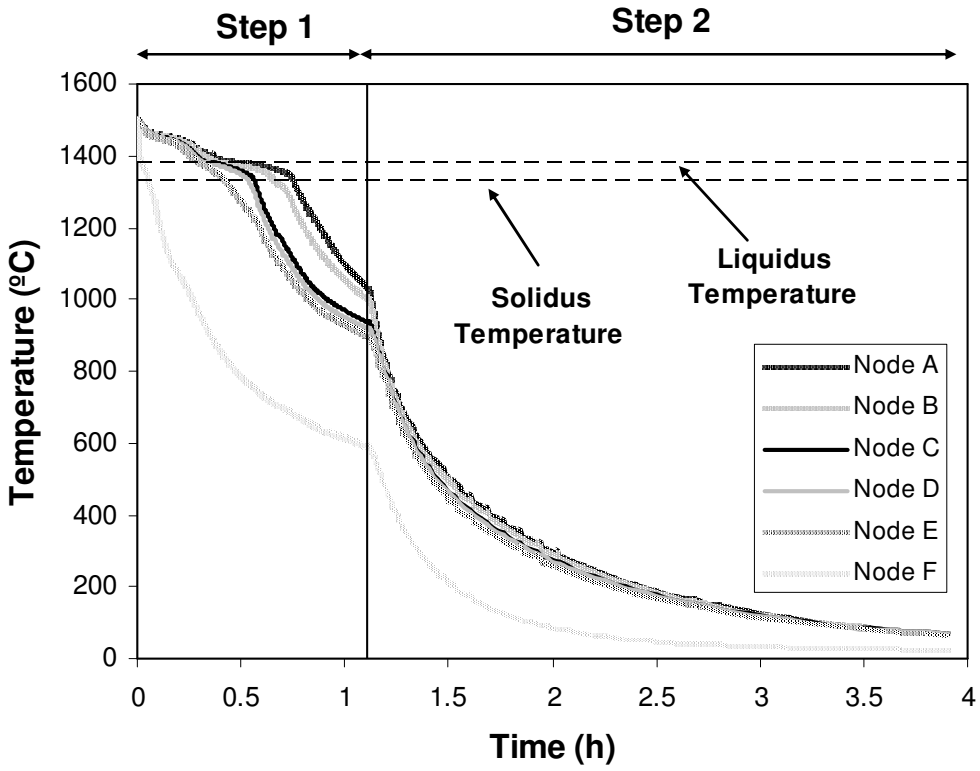

(b)

Figure 5.9: (a) Temperature contour of the ingot at motion of 144 mm for withdrawal velocity of 0.06 mm/s; **(b)** Temperature variation at nodes A, B, C, D, E and F versus the time for Step 1 (the model is withdrawn from the hot to the could chamber of the furnace) and Step 2 (the model is located in the could chamber of the furnace)

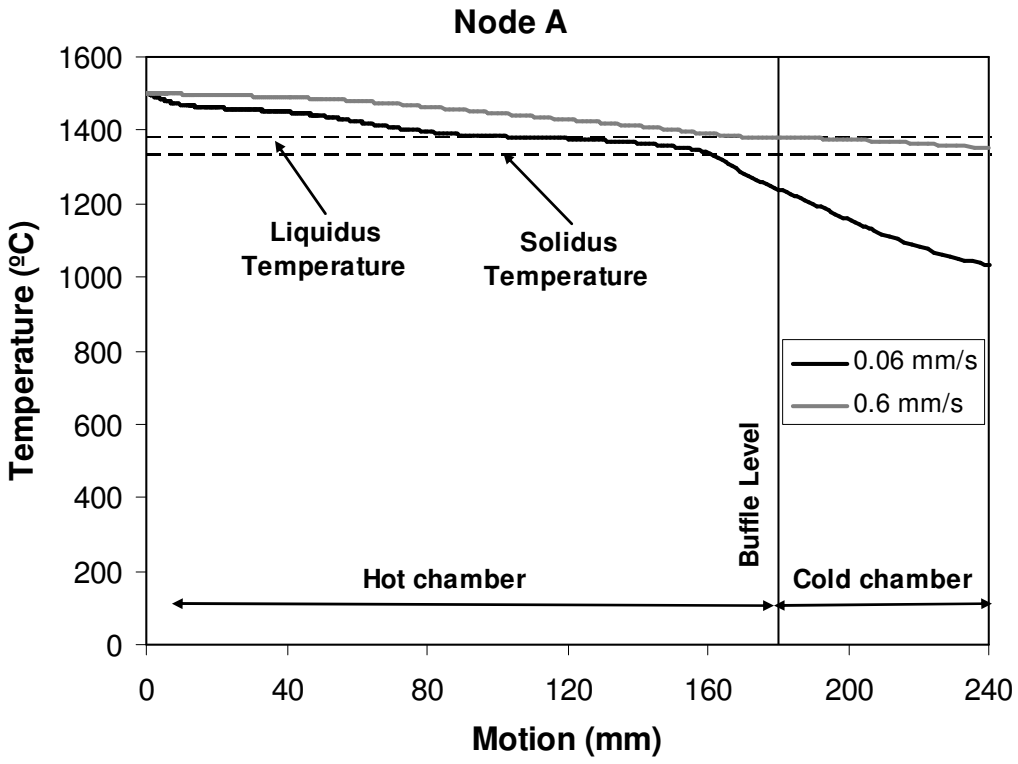

(a)

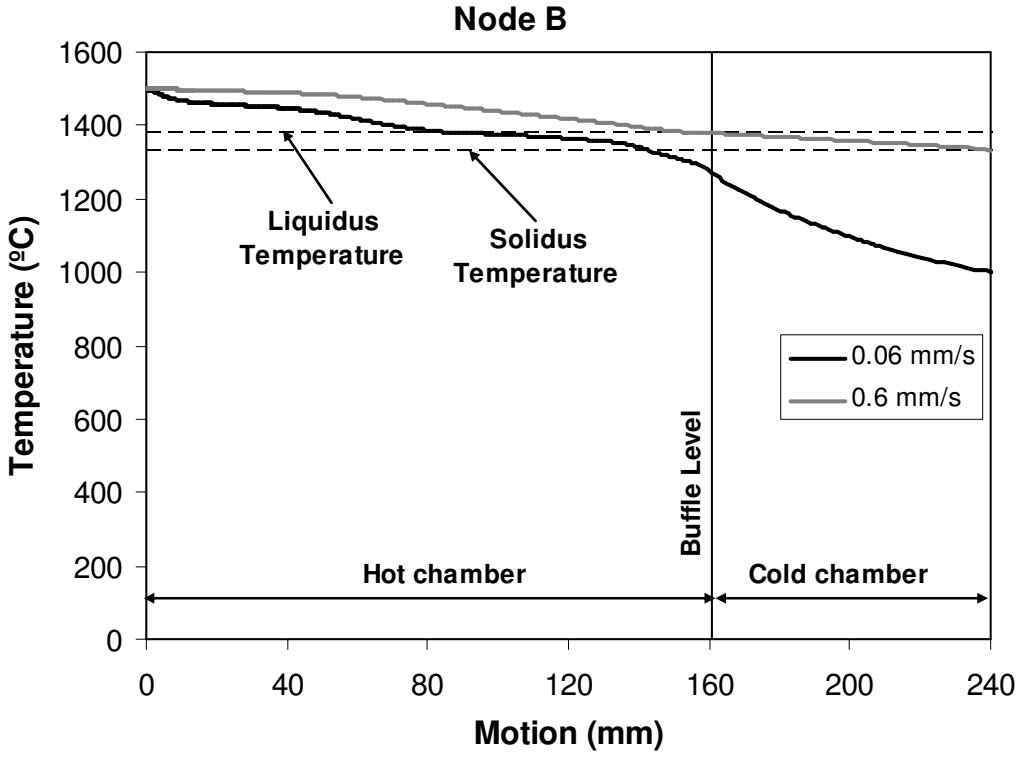

Figure 5.10: (b)

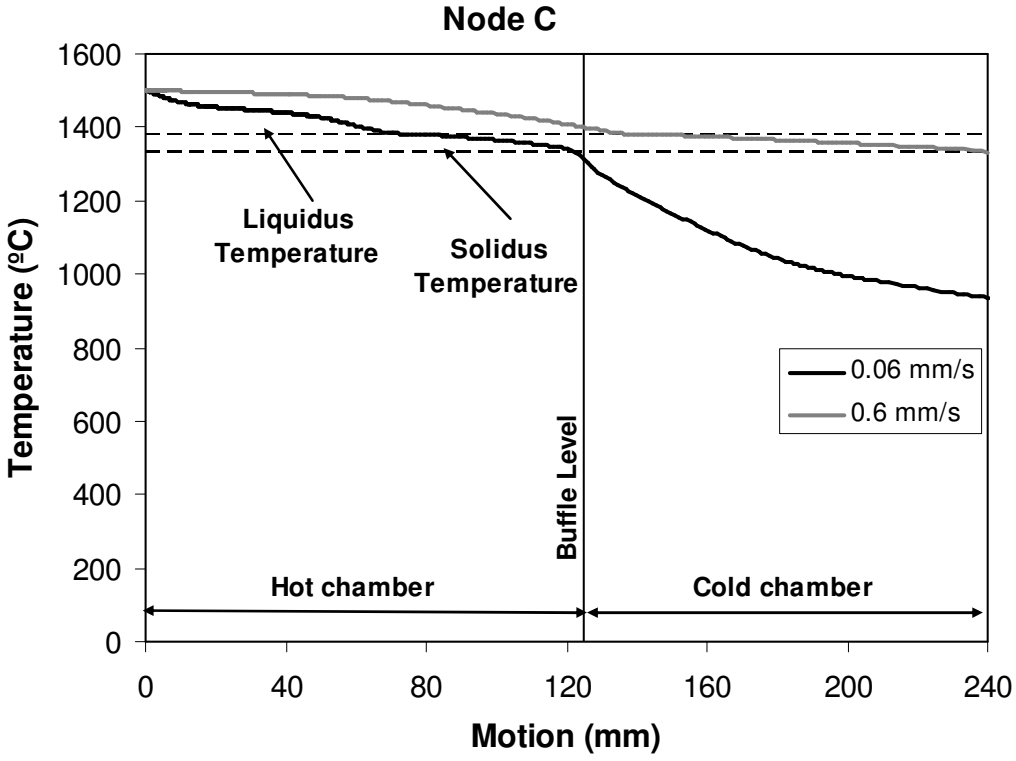

(c)

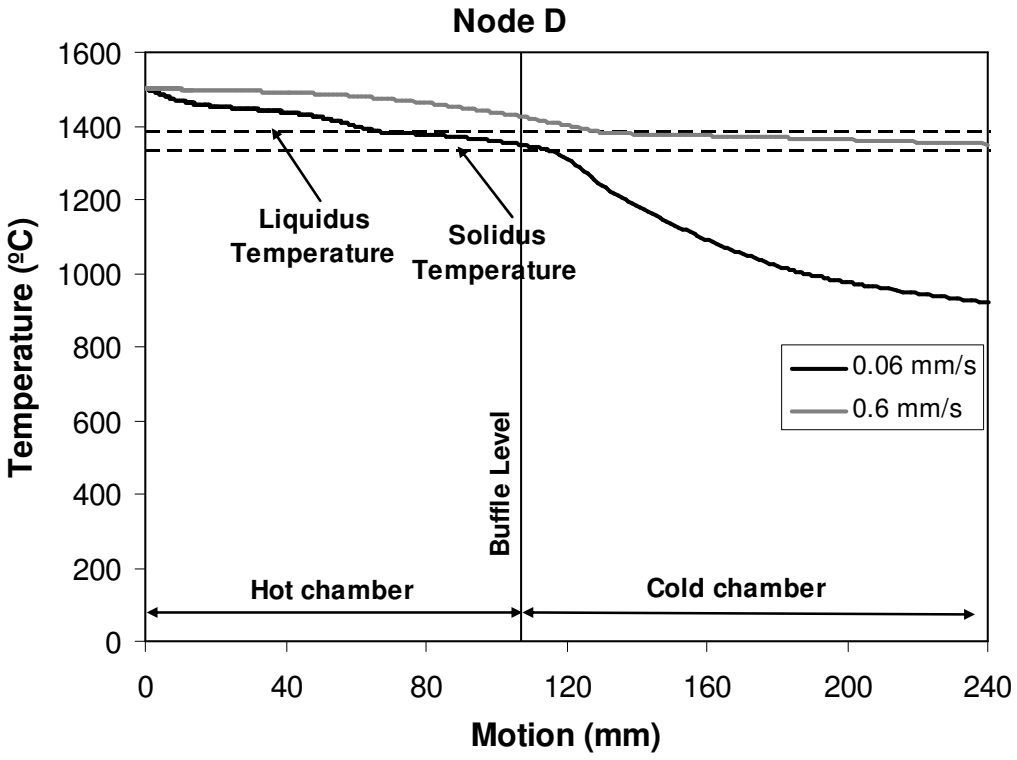

Figure 5.10: (d)

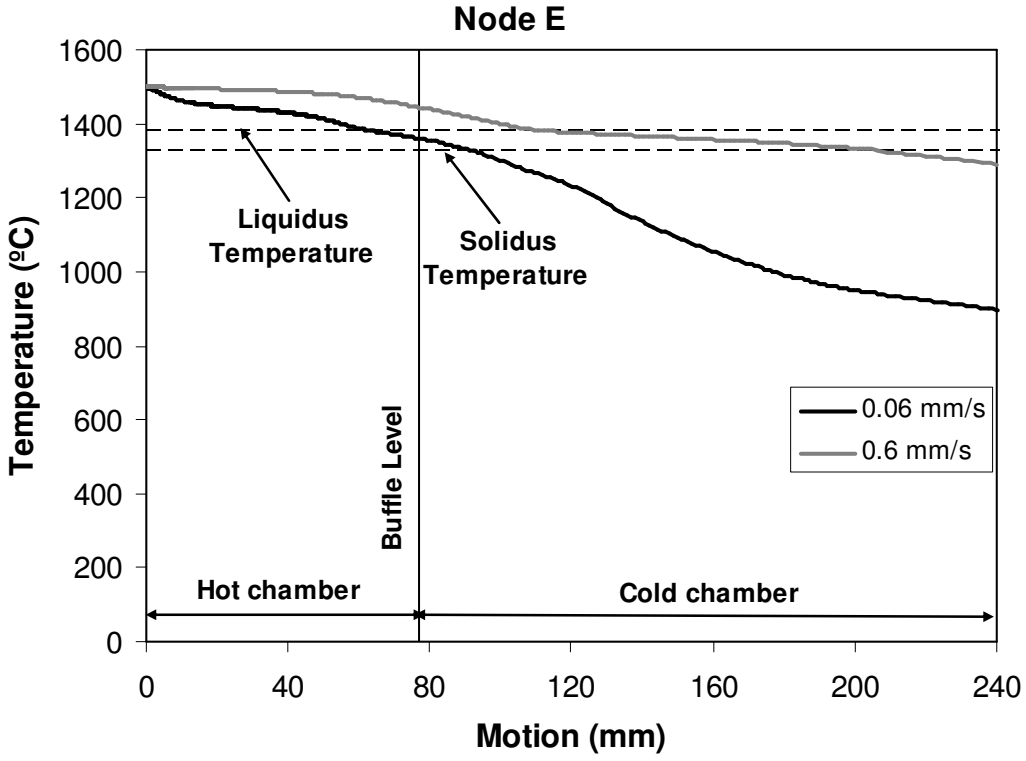

(e)

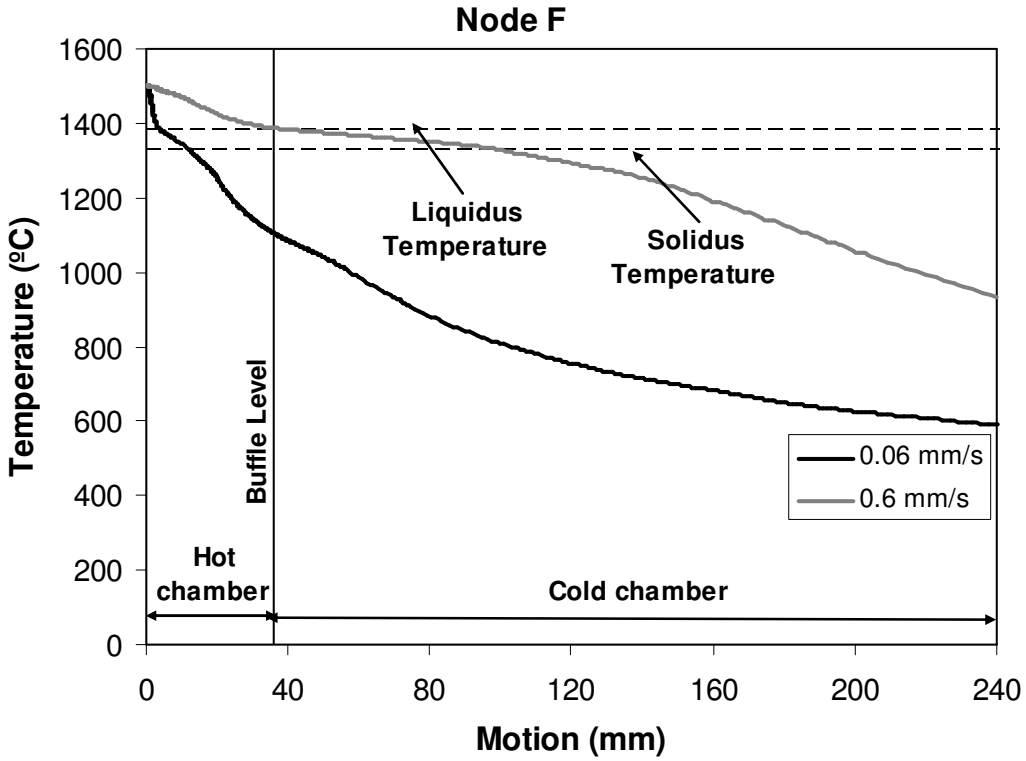

(f)

Figure 5.10: Temperature variation for the motion of the moving part at withdrawal velocities of 0.6 and 0.06 and mm/s for: **(a)** Nodes A; **(b)** Node B; **(c)** Node C; **(d)** Node D; **(e)** Node E; **(f)** Node F

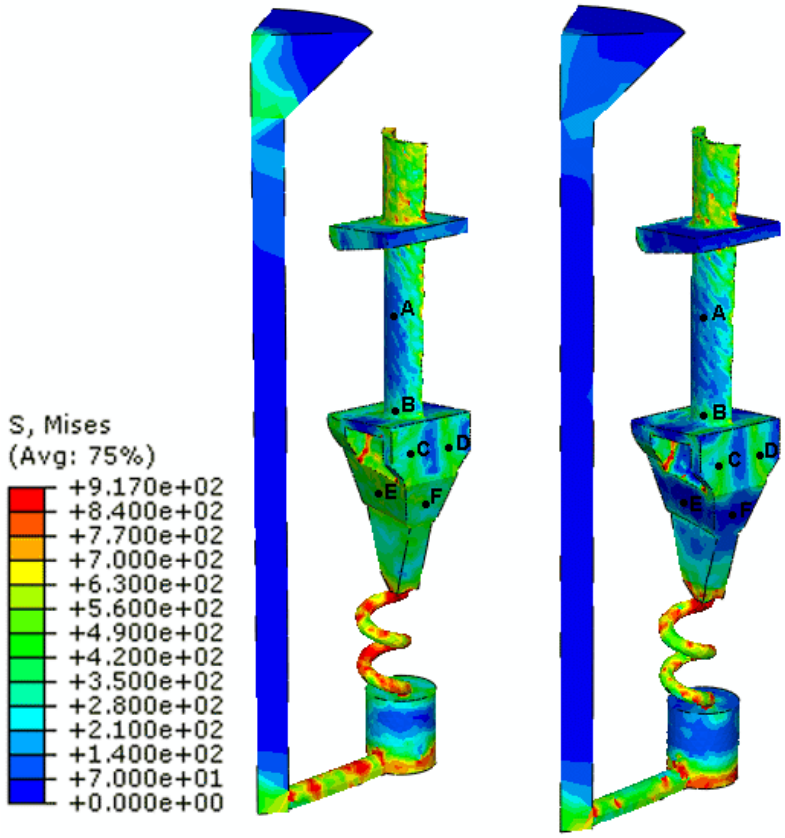

(a) (b)

Figure 5.11: Residual Von Mises stresses obtained at velocities of: **(a)** 0.6 mm/s; **(b)** 0.06 mm/s

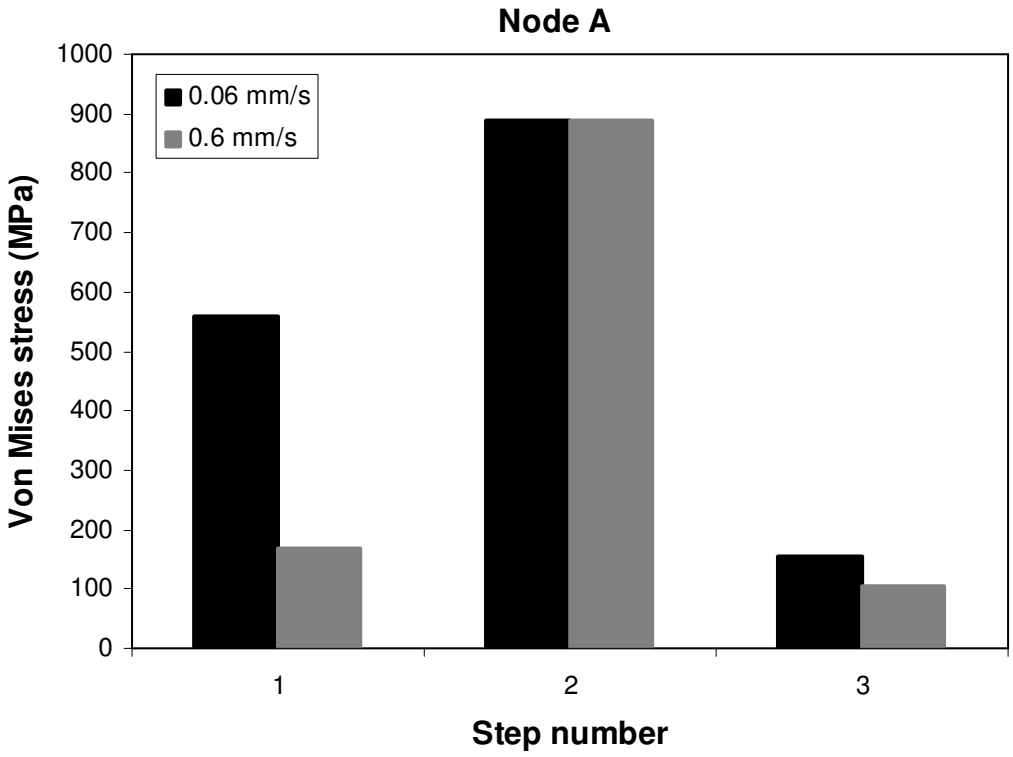

Figure 5.12: (a)

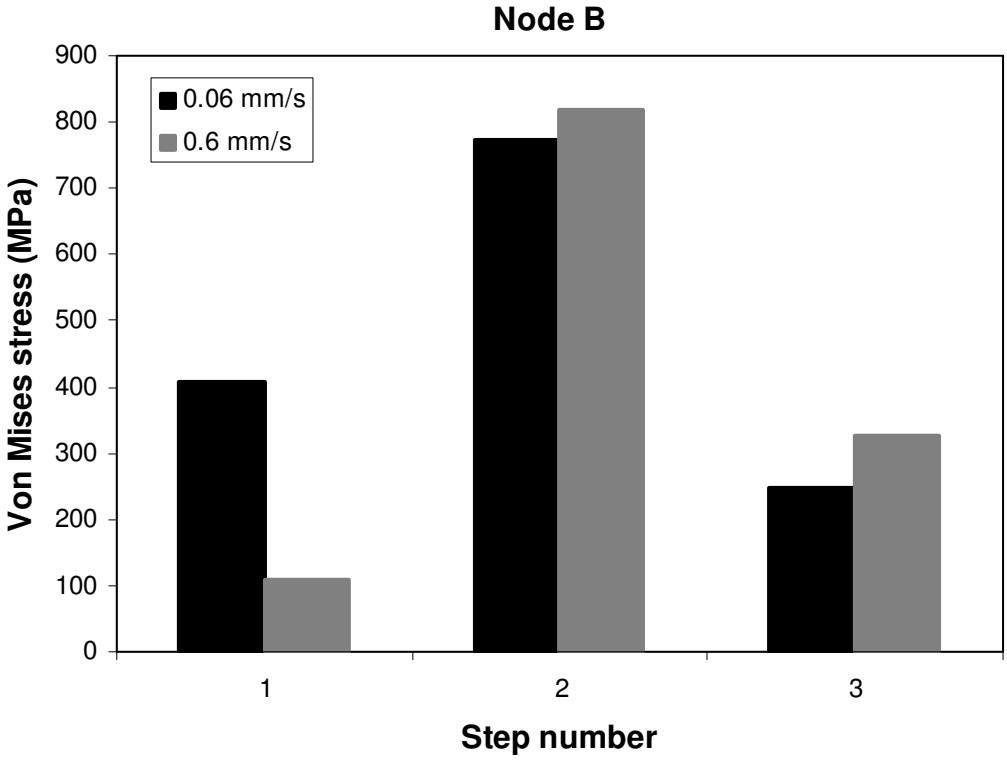

(b)

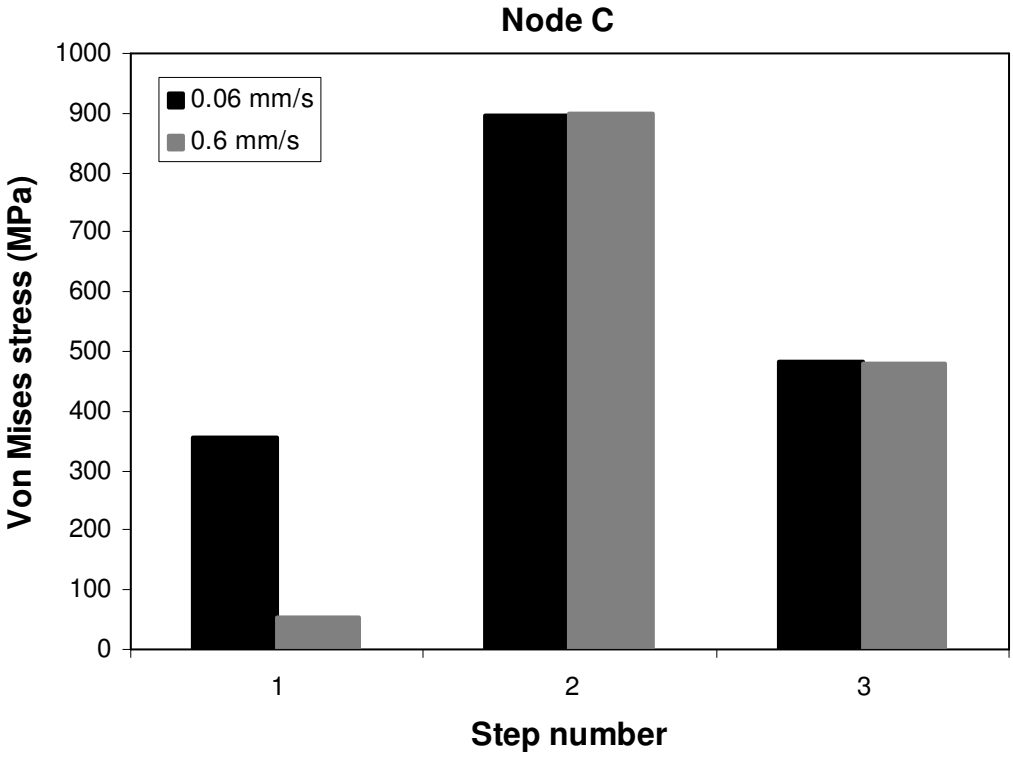

Figure 5.12: (c)

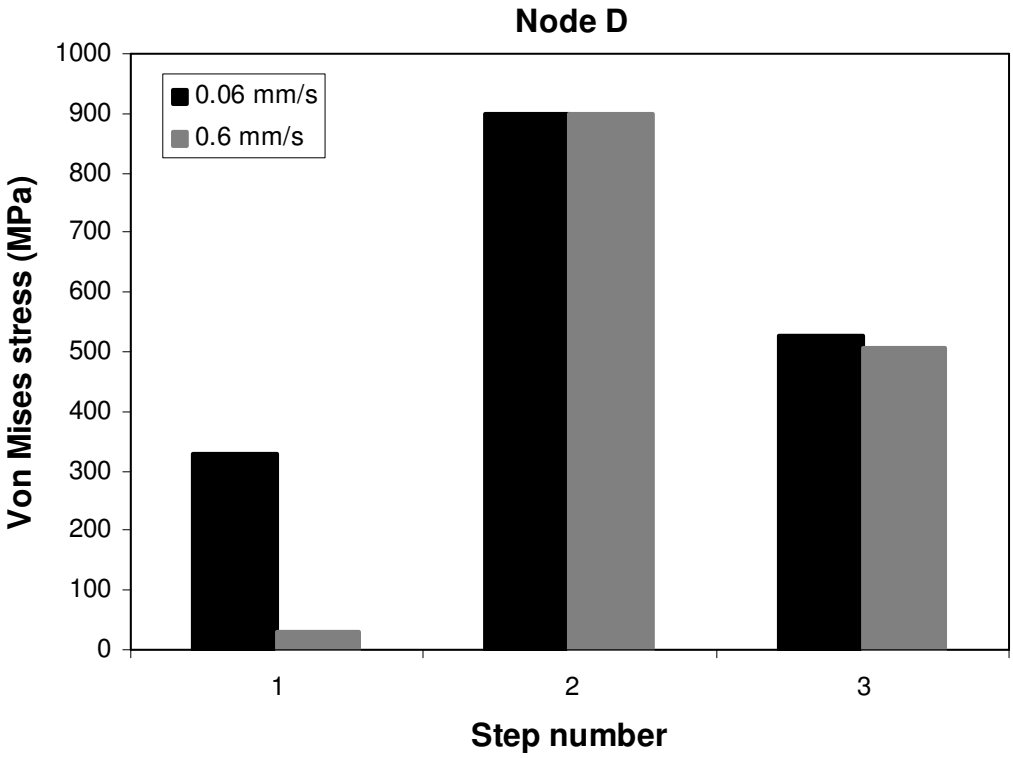

(d)

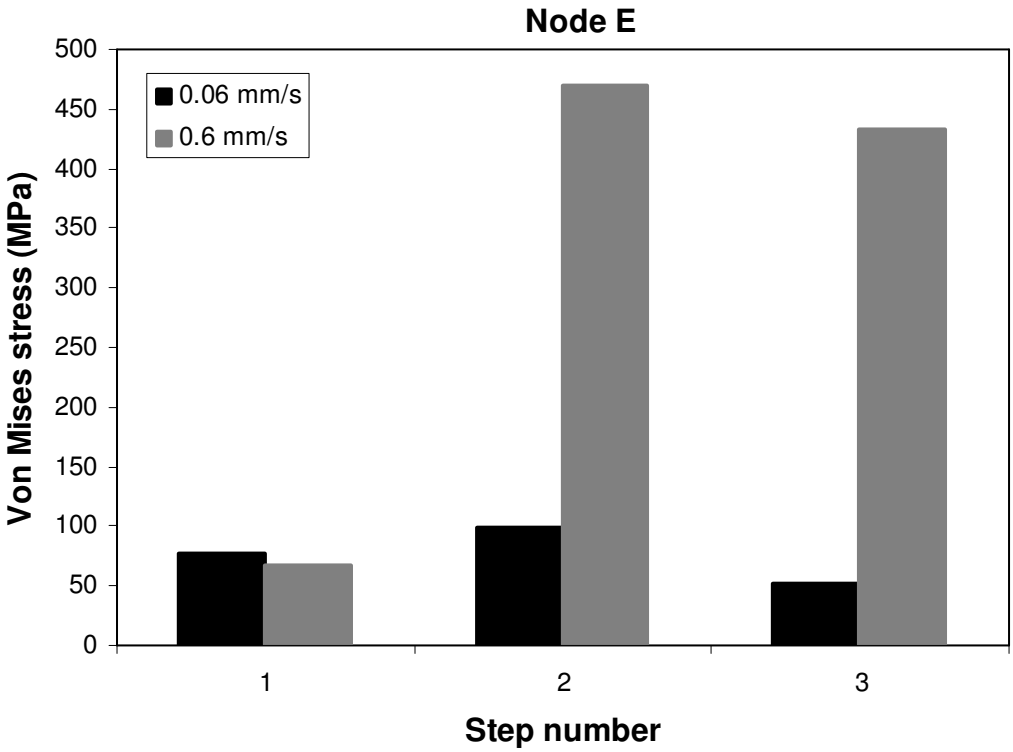

Figure 5.12: (e)

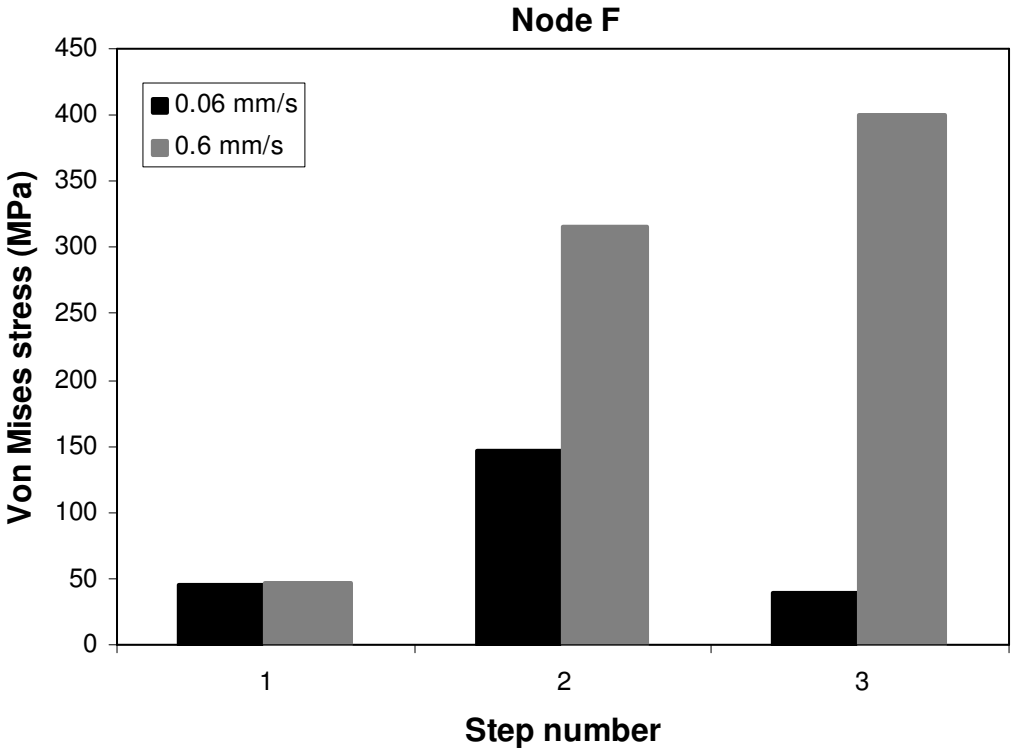

(f)

Figure 5.12: Von Mises stresses obtained in three steps of the mechanical analysis for withdrawal velocities of 0.6 and 0.06 and mm/s for: **(a)** Nodes A; **(b)** Node B; **(c)** Node C; **(d)** Node D; **(e)** Node E; **(f)** Node F (see Figure 5.11)

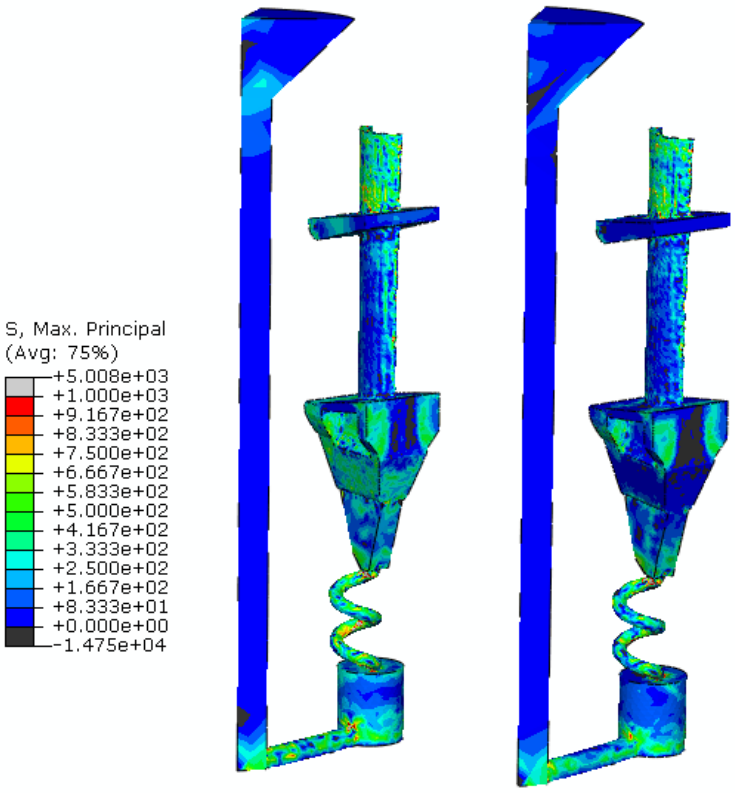

(a) (b)

Figure 5.13: Residual maximum principal stresses obtained at velocities of: **(a)** 0.6 mm/s; **(b)** 0.06 mm/s

CHAPTER 6

MATHEMATICAL ALGORITHMS AND IMPLEMENTATION OF RESIDUAL STRESS MAPPING FROM MICRO TO MACRO SCALE FE MODELS

This chapter reviews mathematical algorithms and implementation of residual stress mapping from micro to macro FE scale models. A shot-peening simulation of Inconel 718 is performed by using FEM for different shot velocities in order to obtain a stress field which is used for mapping purposes. The residual stresses from the shot-peening simulation are mapped into different complex FE models, such as a perforated parallelepiped, a model with a complex surface and an aero-engine vane. The mathematical mapping algorithms and formulations are developed for 2D and 3D models. The implementation and the results for the mapping techniques are presented and discussed in detail.

6.1 Introduction

Many manufacturing processes, such as shot-peening [91-97], are simulated on micro scale models. These processes are usually simulated using a simple FE geometry or the results are determined by experimental measurements. The obtained stresses are usually given from the surface to some depth in the normal direction. The aim is to take the through thickness stresses and map them to new FE models with complex surfaces. The requirement of the new model is to have a defined surface, beneath which the stresses can be mapped. A shot-peening simulation is performed in order to obtain the stresses beneath the shot-peened surface and map them to the new models.

Shot-peening is a process used to produce compressive residual stresses and modify the mechanical behaviour of the material. It entails impacting a surface with a shot

(round metallic, glass or ceramic particles) with a force sufficient to create plastic deformation. It is used for replacing the tensile stresses, created for example after grinding processes, with beneficial compressive stresses. Shot-peening can increase the fatigue life depending on the geometry, material properties, shot velocity, shot coverage, shot intensity, etc.

6.2 Shot-peening simulation

Shot-peening simulation with a single shot is performed in two steps. The first step is performed as a dynamic step in ABAQUS/Explicit which takes into account the inertia effect as explained in section 3.2. In this step the punch impacts the surface and causes plastic deformations. The second step is performed as a static analysis in ABAQUS/Standard where the elastic strains are released by the spring-back effect. The aim of this simulation is to obtain stresses beneath the shot-peened surface which are mapped to new models with complex surfaces.

6.2.1 Geometry and FE model

Figure 6.1 shows the overall dimensions of the punch and the billet. The billet is a parallelepiped with width W = 4 mm and height H = 2 mm. The punch is a half sphere with radios R = 1 mm and reference point RP. The reference point represents the punch where the boundary conditions are applied. It is located in the centre of the sphere.

Eight node linear hexahedron elements with reduced integration (C3D8R from the ABAQUS library) are used for the billet as shown in Figure 6.2. The number of the elements is 84,640. The punch is created as an analytical rigid surface.

6.2.2 Material properties

Inconel 718 material properties at room temperature are used for the billet. The material properties are shown in Table 6.1. Linear isotropic hardening is applied to the dynamic and the static analyses.

6.2.3 Boundary and contact conditions

Figure 6.3 shows the model to which boundary conditions are applied. Zero displacements are applied to surface S_1 in the x, y and z directions. Frictionless contact is applied between surfaces S_2 and S_3. In order to move the punch only in the y direction, zero displacements in the x and z directions and zero rotations in the x-y, y-z and z-x planes are applied to the reference point RP. Velocities v = 5, 10, 20, 40, 75 and 100 m/s are applied to the reference point RP in the y direction. The step time is calculated for the different velocities in order to move the punch to 0.025 mm depth into the billet.

6.2.4 Results and discussion

Figure 6.4 shows the two typical shapes created by the punch. The first shape is created when the punch is moved into the billet to a depth of 0.025 mm. This process is simulated in a dynamic analysis in ABAQUS/Explicit. The second (final) shape is obtained due to the spring-back effect when the punch is removed from the billet. This process is performed in a static analysis in ABAQUS/Standard. The proportion in percentages between the distances H_{SB} and H_P is called the spring-back recovery.

Figure 6.5 shows the spring-back recovery for shot velocities between 5 and 100 m/s. It can be seen that by increasing the shot velocity the spring-back recovery increases. For a velocity of 100 m/s the spring-back recovery is around 95 %. This means that for high velocities, the springback recovery is larger.

Figure 6.6 shows the residual stresses obtained beneath the shot-peened surface for velocities of 5, 10, 20, 40, 75 and 100 m/s in the tangential and normal directions. The shear stresses are zero for all shot velocities. The stresses in the normal direction σ'_{22} are lower than the stresses in the tangential directions σ'_{11} and σ'_{33}. As expected, the stresses on the surface in the normal direction are zero. Figure 6.6(a) shows the stresses in the tangential directions (σ'_{11} and σ'_{33}) versus the depth from the shot-peened surface for different velocities of the punch. It can be seen that by

increasing the shot velocity the maximum compressive stresses go up and their penetration through the thickness in the normal direction decreases, while the peak tensile stresses increase by increasing the shot velocity until 20 m/s and afterwards they start decreasing slowly. Figure 6.6(b) shows the stresses in the normal direction (σ'_{22}). It can be noticed that by increasing the shot velocity, the compressive stresses decrease while the tensile stresses increase up to a velocity of 20 m/s and then start to slightly decrease.

6.3 Problem definition of stress mapping

The aim of this section is to show the mathematical algorithms and the implementation of stress mapping obtained from the shot-peening simulation into new FE models. A perforated parallelepiped is selected as an example for illustration and validation purposes.

6.3.1 Geometry and FE model

Figure 6.7 shows a parallelepiped, with width and height of 8 mm, thickness of 4 mm, perforated in the middle by a cylinder with a radius of 2 mm. The mapping area is defined from surface S in depth d in the normal direction. The direct and the shear stresses, obtained for a shot velocity of 5 m/s in depth $d = 1\,\text{mm}$ (see Figure 6.6), are mapped into the mapping area. The perforated parallelepiped is meshed with four node linear tetrahedron elements as shown in Figure 6.8. The number of the elements is 134,138. A refined mesh around the hole is used in order to provide more elements in the mapping area and more accurate results.

6.3.2 Surface definition

Surface S (see Figure 6.7) is defined by element faces. The faces for linear and quadratic 3D elements are shown in Figure 6.9. Knowing the element numbering and the element faces which form surface S, the coordinates of the nodes belonging to the corresponding face can be identified by following the face and the node sequence shown in Figure 6.9. The faces of the linear tetrahedron elements are

defined by three nodes, the linear hexahedron by four nodes and the linear wedge elements have two faces defined by three nodes and three faces by four nodes. The quadratic elements are treated in the same manner as the linear elements.

The faces for the 2D elements are shown in Figure 6.10. The faces of the linear triangular and quadrilateral elements are defined by two nodes. As in the 3D elements, only the corner nodes of the quadratic elements are needed for defining the element faces.

6.4 Defining the nodes located in the mapping area

Figures 6.11-6.13 show the nodes from an element face defined by three nodes (A, B and C in Figure 6.11), four nodes (A, B, C, and D in Figure 6.12) and two nodes (A and B in Figure 6.13), which belong to surface S and node P which is any other node (integration point) from the FE model.

Two criteria are used for determining whether node P belongs to the mapping area:

i. Distance criterion, where:

$$d_{\alpha} \leq d \tag{6.1}$$

where d is the depth distance defined from the shot-peening analysis (see Figure 6.7)

ii. Area criterion, where node O is required to be inside the triangular ABC (see Figure 6.11) for faces defined by three points, or rectangular ABDC (see Figure 6.12) for faces defined by four nodes, or inside the line AB (see Figure 6.13) for faces defined by two nodes

The position of node P is checked relative to all element faces of surface S. If node P obeys both criteria for some of the element faces, it means that it belongs to the mapping area. All nodes of the FE model are checked to determine whether they belong to the mapping area.

6.4.1 Distance criterion

This section presents two cases for a 3D model where the element faces are defined by three and four nodes and a case for a 2D model where the element faces are defined by two nodes.

(a) Faces defined by three nodes – 3D models

The mathematical model for defining the distance from a point to a plane is determined by following Figure 6.11. Knowing the coordinates of nodes A, B, C and P, the direction vectors $\overrightarrow{AB}$, $\overrightarrow{AC}$ and $\overrightarrow{AP}$ can be given by:

$$\overrightarrow{AB} = \big(B(x) - A(x)\big)i + \big(B(y) - A(y)\big)j + \big(B(z) - A(z)\big)k \tag{6.2}$$

$$\overrightarrow{AC} = \big(C(x) - A(x)\big)i + \big(C(y) - A(y)\big)j + \big(C(z) - A(z)\big)k \tag{6.3}$$

$$\overrightarrow{AP} = \big(P(x) - A(x)\big)i + \big(P(y) - A(y)\big)j + \big(P(z) - A(z)\big)k \tag{6.4}$$

or in abbreviated forms:

$$\overrightarrow{AB} = a_1 i + a_2 j + a_3 k \tag{6.5}$$

$$\overrightarrow{AC} = b_1 i + b_2 j + b_3 k \tag{6.6}$$

$$\overrightarrow{AP} = p_1 i + p_2 j + p_3 k \tag{6.7}$$

The normal vector to the plane α can be defined as a scalar product of vectors $\overrightarrow{AB}$ and $\overrightarrow{AC}$:

$$\vec{n} = \overrightarrow{AB} \times \overrightarrow{AC} = \big(a_2 b_3 - a_3 b_2\big)i + \big(a_3 b_1 - a_1 b_3\big)j + \big(a_1 b_2 - a_2 b_1\big)k \tag{6.8}$$

or in abbreviated form:

$$\vec{n} = n_1 i + n_2 j + n_3 k \tag{6.9}$$

The unit normal vector to the plane α can be given by:

$$\vec{\hat{n}} = \frac{\vec{n}}{\left|\vec{n}\right|} = \frac{n_1}{\left|\vec{n}\right|} i + \frac{n_2}{\left|\vec{n}\right|} j + \frac{n_3}{\left|\vec{n}\right|} k \tag{6.10}$$

where $\left|\vec{n}\right|$ is the magnitude of the normal vector and is defined as:

$$\left|\vec{n}\right| = \sqrt{{n_1}^2 + {n_2}^2 + {n_3}^2} \tag{6.11}$$

The abbreviated form of Equation (6.10) is given by:

$$\vec{\hat{n}} = \hat{n}_1 i + \hat{n}_2 j + \hat{n}_3 k \tag{6.12}$$

The distance d_α is defined as a dot product of the unit normal vector $\vec{\hat{n}}$ and vector $\overrightarrow{AP}$.

$$d_\alpha = \overrightarrow{AP}.\hat{n} = p_1\hat{n}_1 + p_2\hat{n}_2 + p_3\hat{n}_3 \tag{6.13}$$

When the distance d_α is negative, it means that node P is located on the opposite side of the plane α.

(b) Faces defined by four nodes – 3D models

The distance from a point to a plane is determined by following Figure 6.12. Knowing the coordinates of nodes A, B, C, D and P, the direction vectors $\overrightarrow{AB}$ and $\overrightarrow{AP}$ can be respectively defined by Equation (6.2) and Equation (6.4) and the $\overrightarrow{AD}$ can be given by:

$$\overrightarrow{AD} = \big(D(x) - A(x)\big)i + \big(D(y) - A(y)\big)j + \big(D(z) - A(z)\big)k \tag{6.14}$$

or in abbreviated forms:

$$\overrightarrow{AD} = c_1 i + c_2 j + c_3 k \tag{6.15}$$

The normal vector to the plane α can be defined as a scalar product of vectors $\overrightarrow{AB}$ and $\overrightarrow{AD}$:

$$\vec{n} = \overrightarrow{AB} \times \overrightarrow{AD} = \begin{vmatrix} i & j & k \\ a_1 & a_2 & a_3 \\ c_1 & c_2 & c_3 \end{vmatrix} \tag{6.16}$$

The unit normal vector to the plane α can be defined by Equation (6.10) and the minimum distance d_α can be defined by Equation (6.13)

(c) Faces defined by two nodes – 2D models

The distance from a point to a line is determined by following Figure 6.13. Knowing the coordinates of nodes A, B and P, the projection of node P to line AB (node O) can be given by the equation of a line defined through two points:

$$O(x) = A(x) + u(B(x) - A(x))$$
$$O(y) = A(y) + u(B(y) - A(y)) \tag{6.17}$$

where:

$$u = \frac{(P(x) - A(x))(B(x) - A(x)) + (P(y) - A(y))(B(y) - A(y))}{(B(x) - A(x))^2 + (B(y) - A(y))^2} \tag{6.18}$$

The normal vector to line AB can be given:

$$\vec{n} = (P(x) - O(x))i + (P(y) - O(y))j \tag{6.19}$$

or in abbreviated form:

$$\vec{n} = n_1 i + n_2 j \tag{6.20}$$

The unit normal vector to line AB can be given by:

$$\vec{\hat{n}} = \frac{\vec{n}}{\left|\vec{n}\right|} = \frac{n_1}{\left|\vec{n}\right|} i + \frac{n_2}{\left|\vec{n}\right|} j \tag{6.21}$$

where the magnitude of the normal vector $\left|\vec{n}\right|$ is defined as:

$$\left|\vec{n}\right| = \sqrt{n_1^{\ 2} + n_2^{\ 2}} \tag{6.22}$$

The abbreviated form of Equation (6.21) is given by:

$$\vec{\hat{n}} = \hat{n}_1 i + \hat{n}_2 j \tag{6.23}$$

The minimum distance d_α is equal to the magnitude of the normal vector.

$$d_\alpha = \left|\vec{n}\right| \tag{6.24}$$

6.4.2 Area criterion

This section presents two cases for 3D model where the element faces are defined by three and four nodes and a case for 2D model where the element faces are defined by two nodes, as in Section 6.4.1.

(a) Faces defined by three nodes – 3D models

The projection of node P to the plane α is node O (see Figure 6.11). The criterion used to decide whether node O is inside the triangle ABC can be given by the

summation of the areas of triangles AOB, AOC and BOC equal to the area of triangle ABC.

$$S_{ABC} = S_{AOB} + S_{AOC} + S_{BOC} \tag{6.25}$$

In order to calculate the areas of the triangles AOC, AOB and BOC, the coordinates of node O are required. The coordinates of node O can be defined as the intersection between the plane α and the line PO.

The equation of the plane α can be given by:

$$n_1 x + n_2 y + n_3 z + d = 0 \tag{6.26}$$

where

$$d = -\left(n_1 A(x) + n_2 A(y) + n_3 A(z)\right) \tag{6.27}$$

Equation of the line PO can be given by:

$$\begin{aligned} x &= P(x) + n_1 t \\ y &= P(y) + n_2 t \\ z &= P(z) + n_3 t \end{aligned} \tag{6.28}$$

The intersection between the plane α and the line PO can be determined by substituting Equation (6.28) into Equation (6.26).

$$n_1(P(x) + n_1 t) + n_2(P(y) + n_2 t) + n_3(P(z) + n_3 t) + d = 0 \tag{6.29}$$

where the parameter t can be expressed as:

$$t = -\frac{n_1 P(x) + n_2 P(y) + n_3 P(z) + d}{n_1^{\,2} + n_2^{\,2} + n_3^{\,2}} \tag{6.30}$$

The coordinates of node O can be obtained by substituting Equation (6.30) into Equation (6.28)

$$\begin{aligned} O(x) &= P(x) + n_1 t \\ O(y) &= P(y) + n_2 t \\ O(z) &= P(z) + n_3 t \end{aligned} \tag{6.31}$$

A triangular area can be defined as a half of the scalar product magnitude of two direction vectors. The area of the triangle ABC is given by:

$$S_{ABC} = \frac{1}{2}\left|\overrightarrow{AB} \times \overrightarrow{AC}\right| = \frac{1}{2}\sqrt{\left(a_2 b_3 - a_3 b_2\right)^2 + \left(a_3 b_1 - a_1 b_3\right)^2 + \left(a_1 b_2 - a_2 b_1\right)^2} \tag{6.32}$$

The areas of triangles AOB, AOC and BOC can be given by:

$$S_{AOB} = \frac{1}{2}\left|\overrightarrow{OA} \times \overrightarrow{OB}\right| \tag{6.33}$$

$$S_{AOC} = \frac{1}{2}\left|\overrightarrow{OA} \times \overrightarrow{OC}\right| \tag{6.34}$$

$$S_{BOC} = \frac{1}{2}\left|\overrightarrow{OB} \times \overrightarrow{OC}\right| \tag{6.35}$$

(b) Faces defined by four nodes – 3D models

The projection of node P to the plane α is node O (see Figure 6.12). The criterion used to decide whether node O is inside the triangular ABC can be given by the summation of the areas of triangles AOB, BOC, COD and DOA equal to the area of rectangle ABCD.

$$S_{ABCD} = S_{AOB} + S_{BOC} + S_{COD} + S_{DOA} \tag{6.36}$$

The coordinates of node O can be defined by Equation (6.31). A rectangular area can be defined as a scalar product magnitude of two direction vectors. The area of the rectangle ABCD is given by:

$$S_{ABCD} = \left|\overrightarrow{AB} \times \overrightarrow{AD}\right| = \sqrt{(a_2c_3 - a_3c_2)^2 + (a_3c_1 - a_1c_3)^2 + (a_1c_2 - a_2c_1)^2} \tag{6.37}$$

The areas of triangles AOB, BOC, COD and DOA can be given by:

$$S_{AOB} = \frac{1}{2}\left|\overrightarrow{OA} \times \overrightarrow{OB}\right| \tag{6.38}$$

$$S_{BOC} = \frac{1}{2}\left|\overrightarrow{OB} \times \overrightarrow{OC}\right| \tag{6.39}$$

$$S_{COD} = \frac{1}{2}\left|\overrightarrow{OC} \times \overrightarrow{OD}\right| \tag{6.40}$$

$$S_{DOA} = \frac{1}{2}\left|\overrightarrow{OD} \times \overrightarrow{OA}\right| \tag{6.41}$$

(c) Faces defined by two nodes – 2D models

The projection of node P to the line AB is node O (see Figure 6.13). The criterion used to decide whether node O lies on the line AB can be given by:

$$d_{AB} = d_{AO} + d_{BO} \tag{6.42}$$

where: d_{AB}, d_{AO} and d_{BO} are distances, respectively between nodes A and B, A and O, B and O.

The coordinates of node O can be defined by Equation (6.17). A distance between two nodes can be given as the magnitude of a directional vector. The distances d_{AB}, d_{AO} and d_{BO} can be given by:

$$d_{AB} = \left|\overrightarrow{AB}\right| \tag{6.43}$$

$$d_{AO} = \left|\overrightarrow{AO}\right| \tag{6.44}$$

$$d_{BO} = \left|\overrightarrow{BO}\right| \tag{6.45}$$

6.4.3 Exceptional conditions

Figure 6.14 shows an exception when nodes from the mapping area are not detected as nodes belonging to the mapping area. This happens because the circular curve is not exactly fitted by straight line segments. Assuming that surface S is created by small number of elements as shown in Figure 6.14, then the nodes in the gray areas are not detected as nodes belonging to the mapping area. This happens because the projection of these nodes to the plane α, are outside the triangle ABC from Figure 6.11, rectangle ABCD from Figure 6.12 or the line AB from Figure 6.13. This exception can be avoided by creating a refined mesh around surface S and by changing the area criterion from Equation (6.25) to:

$$mS_{ABC} \geq S_{AOC} + S_{AOB} + S_{BOC} \tag{6.46}$$

Equation (6.36) to:

$$mS_{ABCD} = S_{AOB} + S_{BOC} + S_{COD} + S_{DOA} \tag{6.47}$$

and Equation (6.42) to:

$$md_{AB} = d_{AO} + d_{BO} \tag{6.48}$$

where m is a mapping tolerance coefficient

The value of the tolerance coefficient depends on the element density forming the corresponding surface. A small mapping tolerance coefficient is used for surfaces defined with refined meshes. A typical tolerance coefficient of 1.1 is considered to

be reasonable for a 2D model with a circle surface with a radius of 2 mm defined by 320 element faces and mapping depth of 1 mm.

6.5 Transferring stresses from local to global Cartesian coordinate systems

The aim of this section is to demonstrate the stress transformation from local to global Cartesian coordinate systems. After locating the nodes belonging to the mapping area and their distances to surface S, the direct and the shear stresses for the corresponding node are used from the shot-peening simulation for a shot velocity of 5 m/s from Figure 6.6. As an example, by assuming that node P (see Figures 6.11-6.13) is located in the mapping area (see Figure 6.7), then knowing the distance d_α, the stresses for node P can be determined by linear interpolation from the results from Figure 6.6. The interpolated direct and the shear stresses from Figure 6.6 for the corresponding node are referred to as local stresses. It is worth mentioning that elastic and inelastic strain tensors can be transferred from local to global Cartesian coordinate system by using the same formulations as the stress tensors.

(a) 3D models

The local stresses can be given in matrix form as follows:

$$[\sigma'] = \begin{bmatrix} \sigma'_{11} & \sigma'_{12} & \sigma'_{13} \\ \sigma'_{21} & \sigma'_{22} & \sigma'_{23} \\ \sigma'_{31} & \sigma'_{32} & \sigma'_{33} \end{bmatrix} \tag{6.49}$$

Considering that the direct stresses σ'_{22} from the shot-peening simulation are in the normal direction (in the y direction) and following the left hand rotation rule, the Cartesian axes change to the order y-x-z. The local stress matrix for the direct and the shear stresses can be given by:

$$[\sigma'] = \begin{bmatrix} \sigma'_{22} & \sigma'_{21} & \sigma'_{23} \\ \sigma'_{12} & \sigma'_{11} & \sigma'_{13} \\ \sigma'_{31} & \sigma'_{32} & \sigma'_{33} \end{bmatrix} \tag{6.50}$$

The stresses in the global Cartesian coordinate system can be given by:

$$[\sigma] = [T]^T [\sigma'][T] \tag{6.51}$$

where:

$[\sigma]$ is the global Cartesian stress matrix

$[T]$ is the transformation matrix

$[\sigma']$ is the local stress matrix

$[T]^T$ is the transpose transformation matrix

Equation (6.51) for 3D models can be given explicitly by:

$$\begin{bmatrix} \sigma_{11} & \sigma_{12} & \sigma_{13} \\ \sigma_{21} & \sigma_{22} & \sigma_{23} \\ \sigma_{31} & \sigma_{32} & \sigma_{33} \end{bmatrix} = \begin{bmatrix} T_{11} & T_{21} & T_{31} \\ T_{12} & T_{22} & T_{32} \\ T_{13} & T_{23} & T_{33} \end{bmatrix} \begin{bmatrix} \sigma'_{22} & \sigma'_{21} & \sigma'_{23} \\ \sigma'_{12} & \sigma'_{11} & \sigma'_{13} \\ \sigma'_{31} & \sigma'_{32} & \sigma'_{33} \end{bmatrix} \begin{bmatrix} T_{11} & T_{12} & T_{13} \\ T_{21} & T_{22} & T_{23} \\ T_{31} & T_{32} & T_{33} \end{bmatrix} \tag{6.52}$$

The transformation matrix can be defined by the direction cosines between the axis of the local and the global Cartesian systems. Figure 6.15 shows the global $x - y - z$ and the local $x' - y' - z'$ Cartesian coordinate systems with reference point A. Point A is a node from any element face forming surface S (see Figures 6.11-6.12). Three direction vectors from the local coordinate system are needed in order to define the direction cosines between the local and the global coordinate systems. The normal vector $\vec{n}$ to the plane α can be used as the x' axis for the local coordinate system. The direction cosines between the x' axis and the x, y and the z axis can be given by:

- Direction cosine between the x' and the x axis

$$\cos\alpha_1 = \hat{n}_1 \tag{6.53}$$

- Direction cosine between the x' and the y axis

$$\cos\beta_1 = \hat{n}_2 \tag{6.54}$$

- Direction cosine between the x' and the z axis

$$\cos\gamma_1 = \hat{n}_3 \tag{6.55}$$

For biaxial models, such as the shot-peening simulation, the direct stresses acting on plane α have the same magnitudes. Therefore any vector from the plane can be used for the y' axis of the local coordinate system. Vector $\overrightarrow{AB}$ is selected as the y'

axis. The direction cosine between the y' axis and the x, y and the z axis can be defined by the unit vector of $\overrightarrow{AB}$.

$$\overrightarrow{\hat{n}_{AB}} = \frac{\overrightarrow{AB}}{\left|\overrightarrow{AB}\right|} = \frac{a_1}{\left|\overrightarrow{AB}\right|} i + \frac{a_2}{\left|\overrightarrow{AB}\right|} j + \frac{a_3}{\left|\overrightarrow{AB}\right|} k \tag{6.56}$$

or in abbreviated form:

$$\overrightarrow{\hat{n}_{AB}} = \hat{n}_{AB_1} i + \hat{n}_{AB_2} j + \hat{n}_{AB_3} k \tag{6.57}$$

The direction cosines between y' axis and the x, y and the z axis can be given by:

- Direction cosine between the y' and the x axis

$$\cos\alpha_2 = \hat{n}_{AB_1} \tag{6.58}$$

- Direction cosine between the y' and the y axis

$$\cos\beta_2 = \hat{n}_{AB_2} \tag{6.59}$$

- Direction cosine between the y' and the z axis

$$\cos\gamma_2 = \hat{n}_{AB_3} \tag{6.60}$$

The scalar product of the normal $\vec{n}$ and the $\overrightarrow{AB}$ vector gives the direction vector $\overrightarrow{AF}$, which is perpendicular to the normal $\vec{n}$ and the $\overrightarrow{AB}$ vector and lies on the plane α. The direction vector $\overrightarrow{AF}$ is used for the z' axis of the local coordinate system.

$$\overrightarrow{AF} = \vec{n} \times \overrightarrow{AB} = f_1 i + f_2 j + f_3 k \tag{6.61}$$

The unit $\overrightarrow{AF}$ vector can be given by:

$$\hat{n}_{AF} = \frac{\overrightarrow{AF}}{\left|\overrightarrow{AF}\right|} = \frac{f_1}{\left|\overrightarrow{AF}\right|} i + \frac{f_2}{\left|\overrightarrow{AF}\right|} j + \frac{f_3}{\left|\overrightarrow{AF}\right|} k \tag{6.62}$$

or in abbreviated form:

$$\hat{n}_{AF} = \hat{n}_{AF_1} i + \hat{n}_{AF_2} j + \hat{n}_{AF_3} k \tag{6.63}$$

The direction cosines between the z' axis and the x, y and the z axis can be given by:

- Direction cosine between the z' and the x axis

$$\cos\alpha_3 = \hat{n}_{AF_1} \tag{6.64}$$

- Direction cosine between the z' and the y axis

$$\cos\beta_3 = \hat{n}_{AF_2} \tag{6.65}$$

- Direction cosine between the z' and the z axis

$$\cos\gamma_3 = \hat{n}_{AF_3} \tag{6.66}$$

The transformation matrix can be written as follows:

$$[T] = \begin{bmatrix} \cos\alpha_1 & \cos\beta_1 & \cos\gamma_1 \\ \cos\alpha_2 & \cos\beta_2 & \cos\gamma_2 \\ \cos\alpha_3 & \cos\beta_3 & \cos\gamma_3 \end{bmatrix} \tag{6.67}$$

When the z' and the z axis coincide, then the transformation matrix is equal to the rotation matrix about the z axis.

$$[T] = [R_z] = \begin{bmatrix} \cos\alpha_1 & -\sin\alpha_1 & 0 \\ \sin\alpha_1 & \cos\alpha_1 & 0 \\ 0 & 0 & 1 \end{bmatrix} \tag{6.68}$$

where:

$$\sin\alpha_1 = \sqrt{1-\cos^2\alpha_1} \tag{6.69}$$

(b) 2D models

Figure 6.16 shows the global and the local 2D Cartesian coordinate systems with reference point A. Equation (6.51) for 2D models can be given explicitly by:

$$\begin{bmatrix} \sigma_{11} & \sigma_{12} \\ \sigma_{21} & \sigma_{22} \end{bmatrix} = \begin{bmatrix} T_{11} & T_{21} \\ T_{12} & T_{22} \end{bmatrix} \begin{bmatrix} \sigma'_{11} & \sigma'_{12} \\ \sigma'_{21} & \sigma'_{22} \end{bmatrix} \begin{bmatrix} T_{11} & T_{12} \\ T_{21} & T_{22} \end{bmatrix} \tag{6.70}$$

The transformation matrix for 2D models can be given by:

$$T = \begin{bmatrix} \cos\alpha_1 & -\sin\alpha_1 \\ \sin\alpha_1 & \cos\alpha_1 \end{bmatrix} \tag{6.71}$$

The direction cosine between the x' and the x axis and y' and the y axis can be given by:

$$\cos\alpha_1 = \hat{n}_1 \tag{6.72}$$

$\sin\alpha_1$ can be defined by Equation (6.69).

It is worth mentioning that the axisymmetric and the plane strain 2D models provide stresses in the z direction (σ'_{33}). These stresses are not transferred from local to the global Cartesian coordinate systems. Only interpolation from the stress-depth curves is used (see Figure 6.6).

6.6 Results and discussion

Results using two methods, the method using the rotation matrix from Equation (6.68) (referred to as method A) and the method using the transformation matrix from Equation (6.67) (referred to as method B), are obtained and compared. The results from method A must be identical to method B in order to conclude that the transformation matrix using Equation (6.67) can be used for any 3D model. Figures 6.17-6.19 show the stress contours for the direct stresses where it can be seen that the results obtained by using method A and method B are identical, which means that the transformation matrix from Equation (6.67) is properly defined and can be used for any geometry. The mapping technique is implemented in ABAQUS, as shown in Figure 6.20, by mapping the residual stresses at the integration points of the elements.

6.7 Application to complex geometries

A geometry with a complex surface and a simplified aero-engine vane are used to show the capability of the mapping techniques.

6.7.1 Geometry with complex surface

A geometry with a complex surface is created in order to check the applicability of the mapping technique to a non-uniform surface. Figure 6.21 shows the geometry with a surface created by a revolved spline curve to 90 degrees. It is assumed that the selected surface from Figure 6.21 is shot-peened and the stresses are mapped through the thickness. Figure 6.22 shows the mesh of the model. Four node linear tetrahedron elements are used for the model. Figure 6.23 shows the contour of the mapped stresses in the x, y and z directions.

6.7.2 Aero-engine vane

Shot-peening is applied to a simplified aero-engine vane component. The mesh and the shot-peening surface are shown in Figure 6.24. Four node linear tetrahedron elements are used for the mesh. A refined mesh is used around the shot-peening area in order to obtain more accurate results after mapping. Shot-peening stresses obtained at a shot velocity of 40 m/s (see Figure 6.6) are used for the mapping.

Figure 6.25 shows the contours of the mapped stresses beneath the shot-peening surface of the vane. The stress mapping is implemented into the commercial FE package ABAQUS at the integration points of the elements. It can be seen that the Von Mises stresses are uniform along the shot-peening surface subjected to mapping, which verifies the developed algorithms and formulations.

6.8 Conclusions

Shot-peening was simulated using the FEM by performing a single shot with velocities in the range 5 – 100 m/s. The residual stresses and the spring-back recovery were investigated. It was shown that by increasing the shot velocity the springback recovery increases.

Mapping techniques were developed in order to map stresses obtained from processes simulated on a micro scale, such as shot-peening, machining, roller-burnishing, etc into new macro 2D and 3D FE models.

The mapping techniques were applied to a perforated parallelepiped, a geometry with a complex surface and a simplified aero-engine vane by using the residual stresses obtained from the shot-peening simulation. The mapping techniques were implemented in ABAQUS where the stresses from the shot-peening were mapped.

Table 6.1: Material Properties of Inconel 718 [68, 69, 98]

Elastic Modulus (GPa)	208
Poisson's ratio (-)	0.29
Density (kg/m^3)	8190
Yield Strength (MPa)	980
Ultimate Strength (MPa)	1320
Elongation (%)	20.5

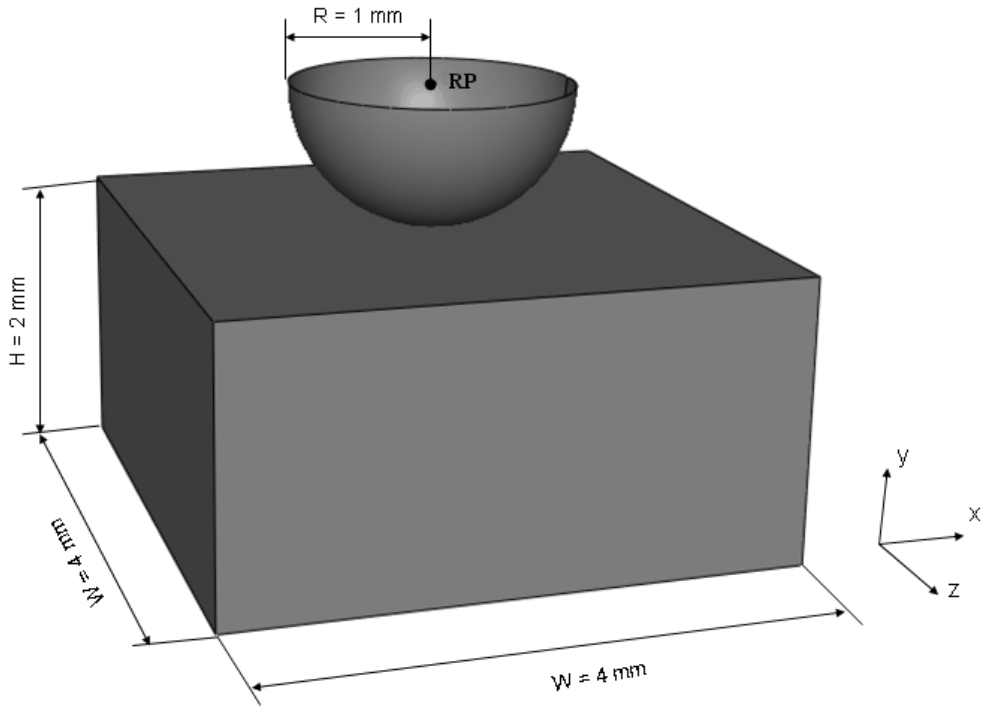

Figure 6.1: Geometry of the billet and the punch used for the shot-peening simulation

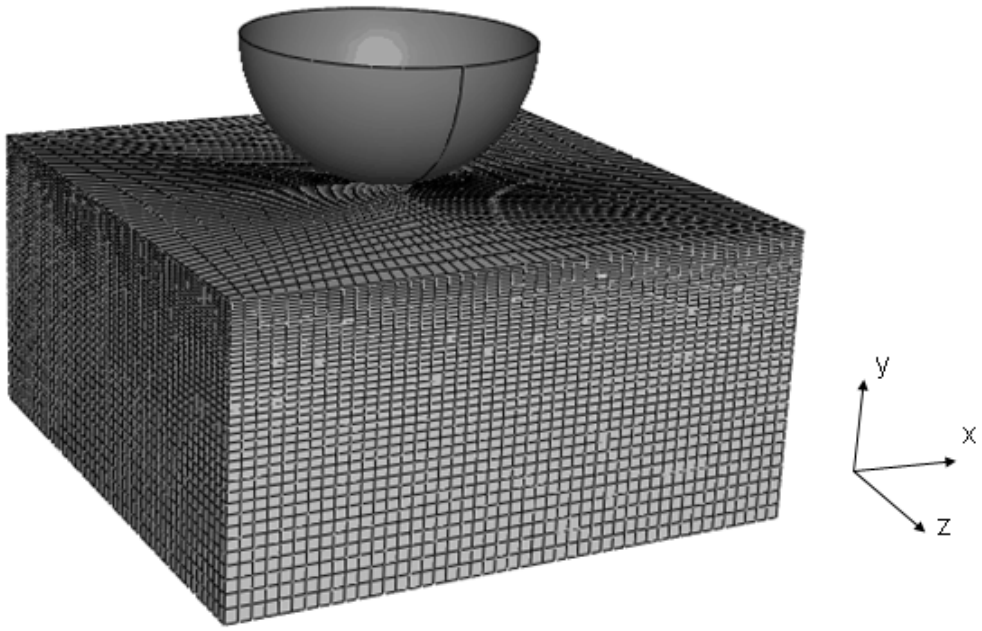

Figure 6.2: Billet mesh with 84,640 eight node linear hexahedron elements with reduced integration

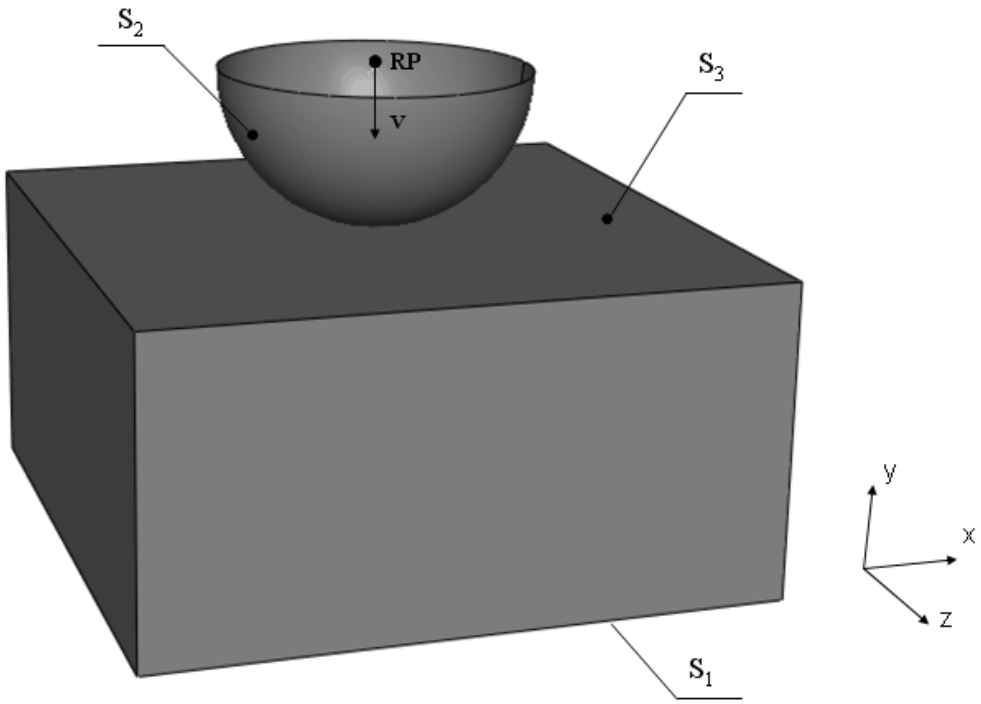

Figure 6.3: Boundary conditions of the shot-peening model

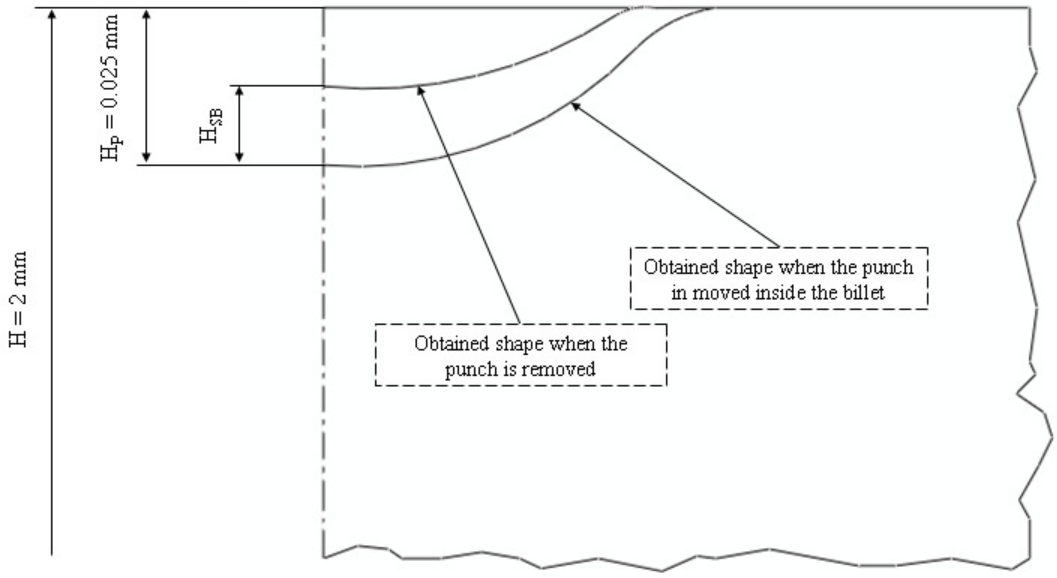

Figure 6.4: Shapes obtained when the punch is moved into the billet and when it is taken away

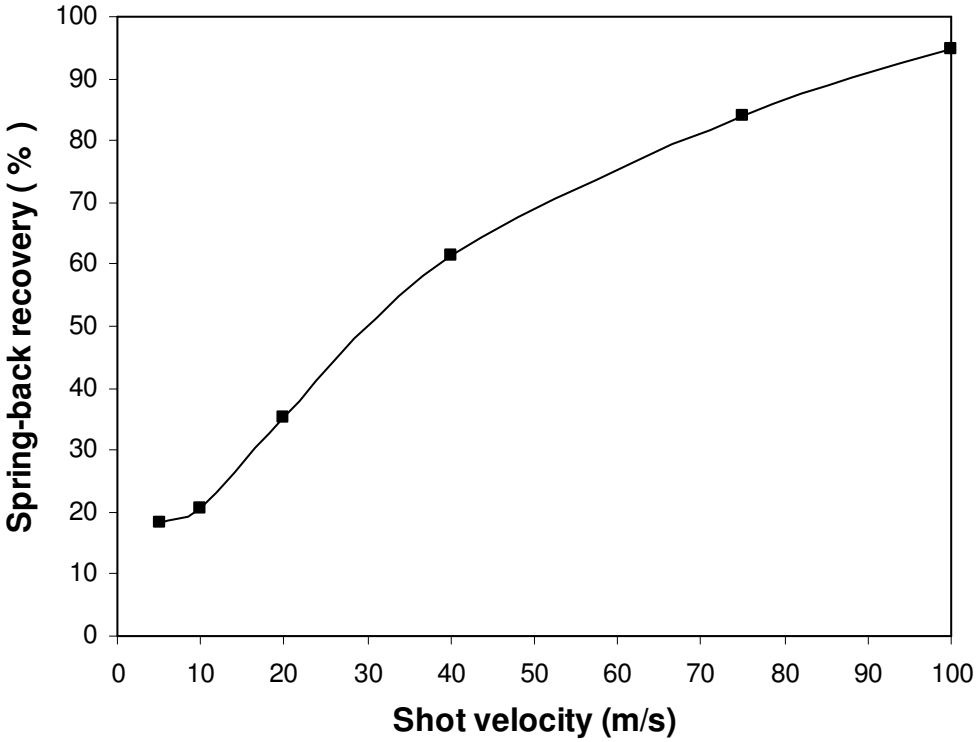

Figure 6.5: Spring-back recovery versus the shot velocity

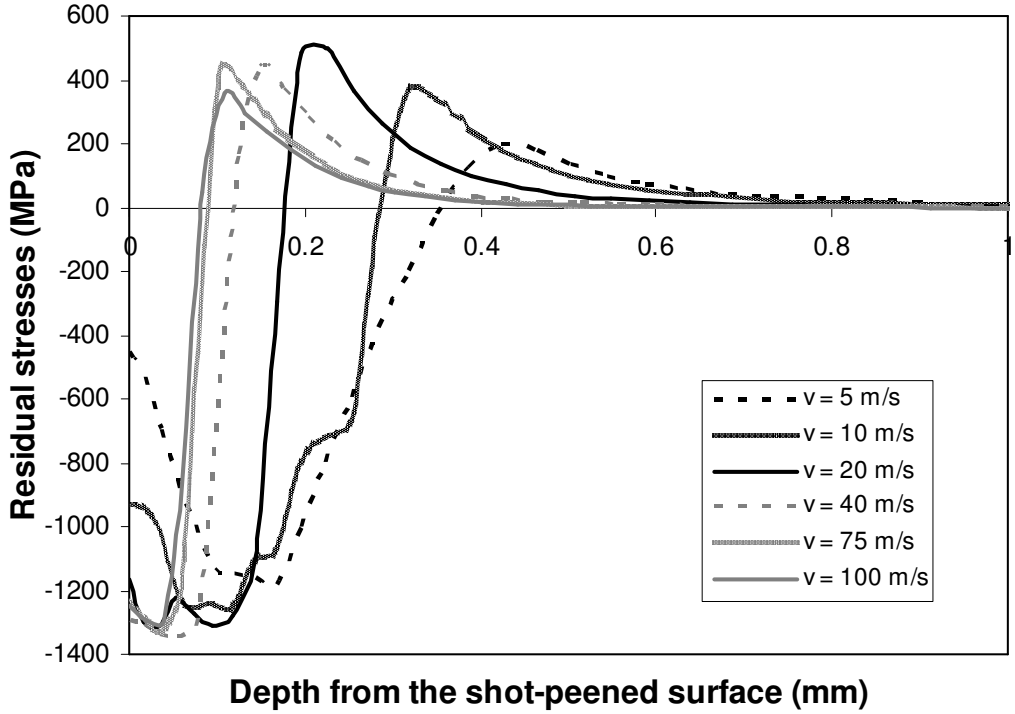

(a)

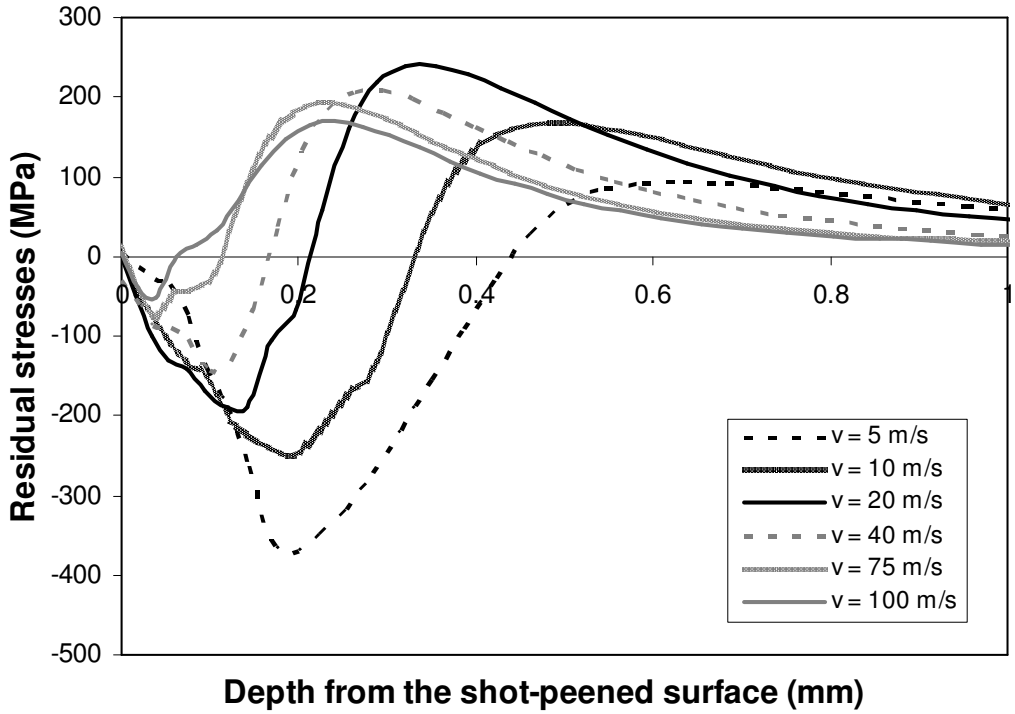

(b)

Figure 6.6: Residual stresses obtained beneath the shot-peened surface for velocities 5, 10, 20, 40, 75 and 100 m/s: (a) residual stresses in the tangential directions ($\sigma'_{11} = \sigma'_{33}$); (b) residual stresses in the normal direction (σ'_{22})

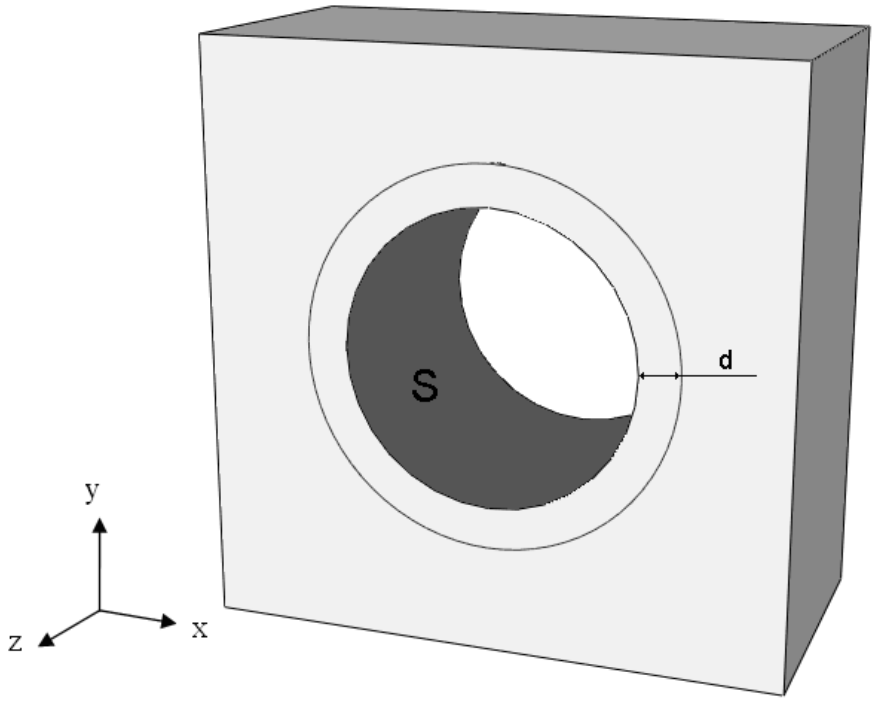

Figure 6.7: Perforated parallelepiped with width and height of 8 mm, thickness of 4 mm, perforated in the middle by a cylinder with radios of 2 mm

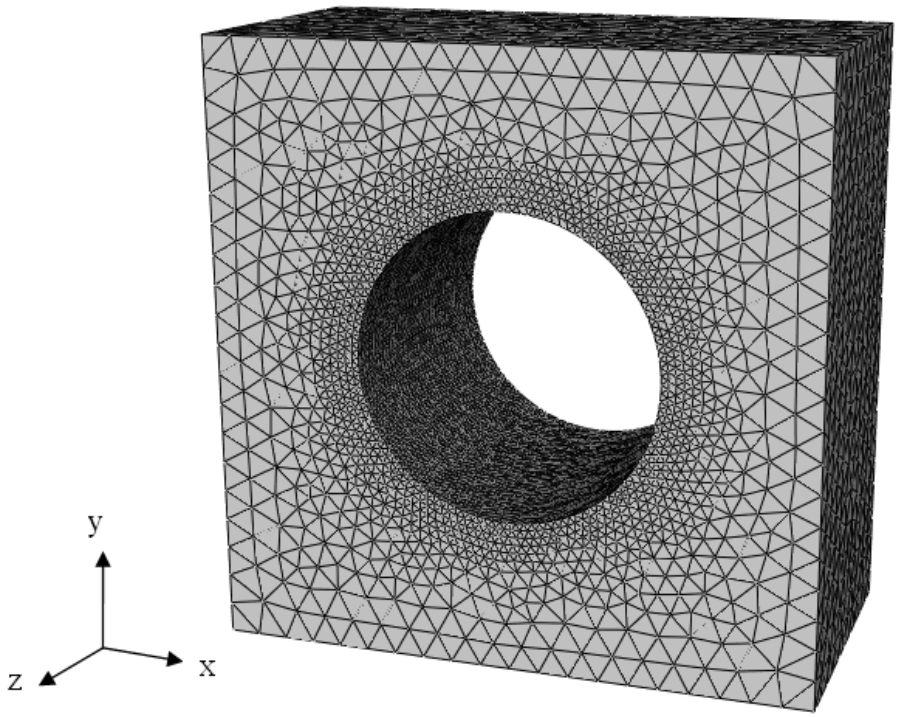

Figure 6.8: Perforated parallelepiped mesh with 134,138 four node linear tetrahedron elements

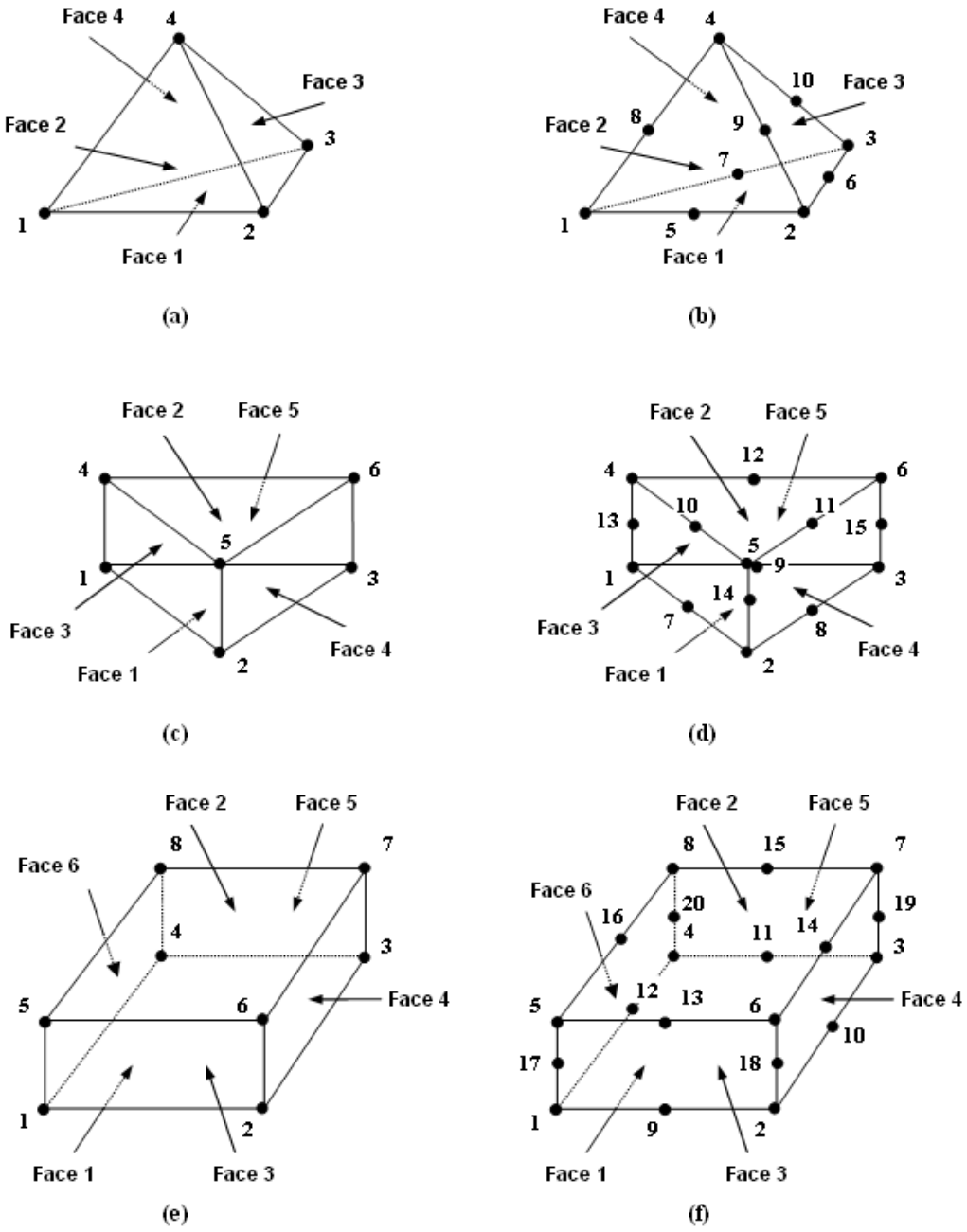

Figure 6.9: Element faces and node sequence for 3D elements; **(a)** four node linear tetrahedron element; **(b)** ten node quadratic tetrahedron element; **(c)** six node linear wedge element; **(d)** fifteen node quadratic wedge element; **(e)** eight node linear hexahedron element; **(f)** twenty node quadratic hexahedron element

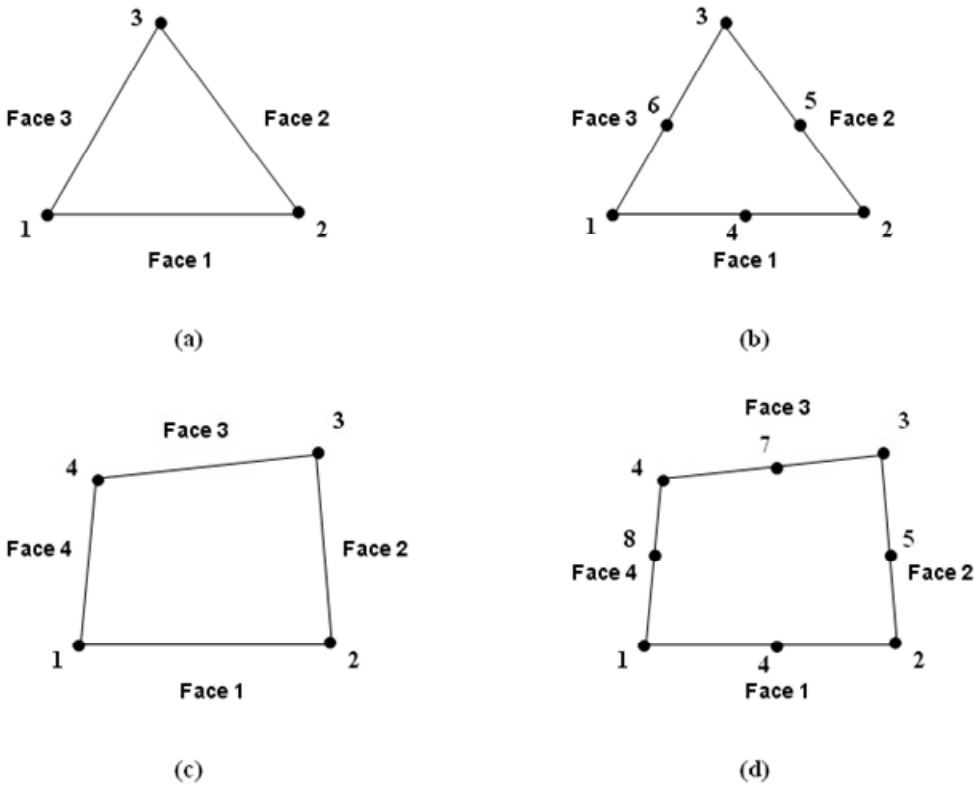

Figure 6.10: Element faces and node sequence for 2D elements; **(a)** three node linear triangular element; **(b)** six node quadratic triangular element; **(c)** four node linear quadrilateral element; **(d)** eight node quadratic quadrilateral element

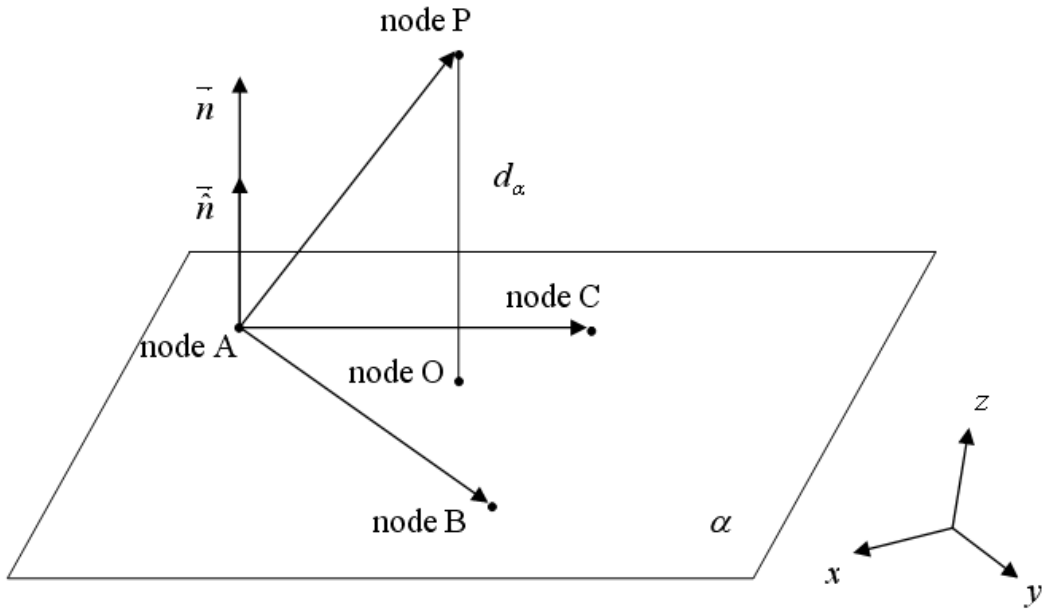

Figure 6.11: Minimum distance d_α from the node P to the plane α, the projection of a node P to plane α (node O), Node O inside the triangular ABC

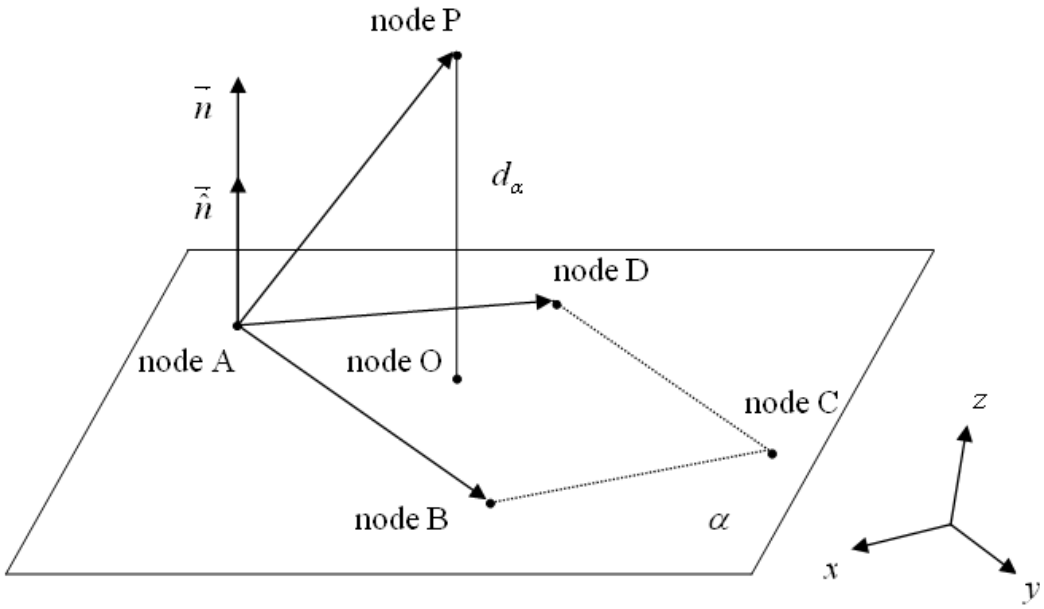

Figure 6.12: Minimum distance d_α from the node P to the plane α, the projection of a node P to plane α (node O), Node O inside the rectangular ABCD

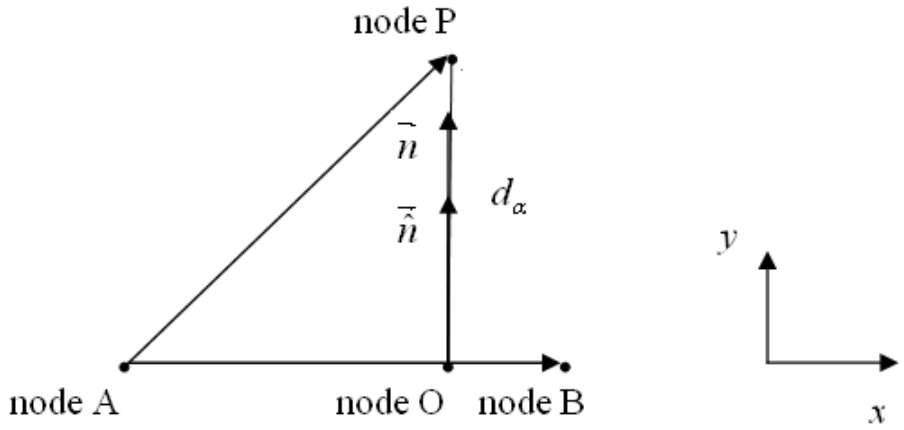

Figure 6.13: Minimum distance d_α from the node P to the line AB, the projection of a node P to line AB, Node O lies on line AB

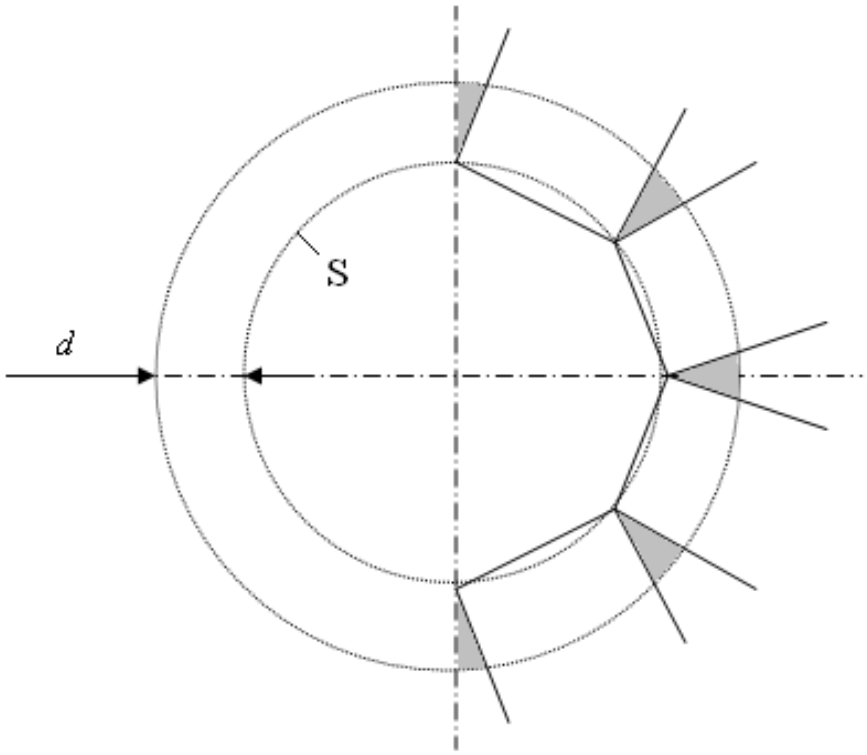

Figure 6.14: Exceptional condition when nodes from the mapping area are not detected

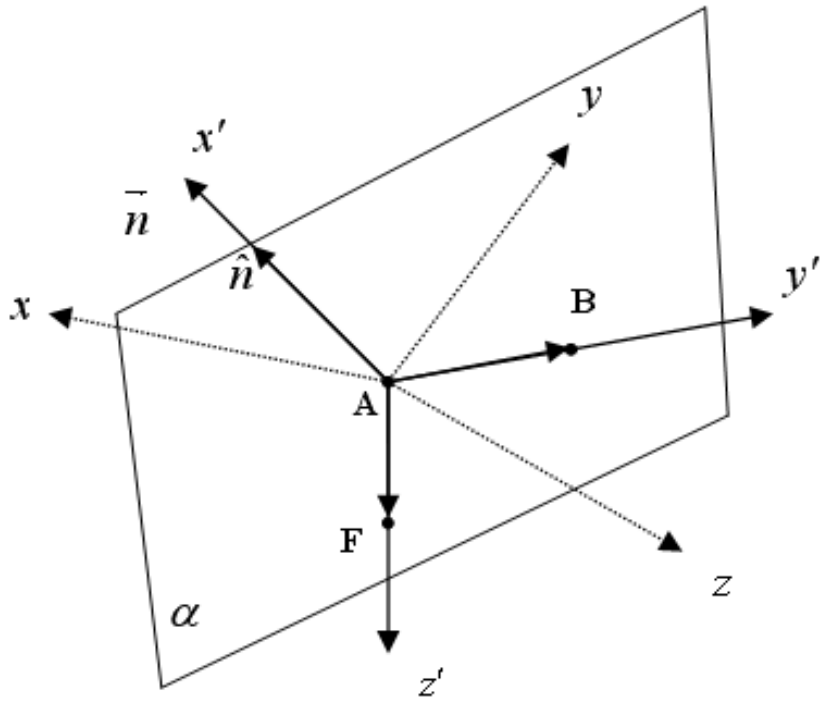

Figure 6.15: Global and local 3D Cartesian coordinate systems with reference point A

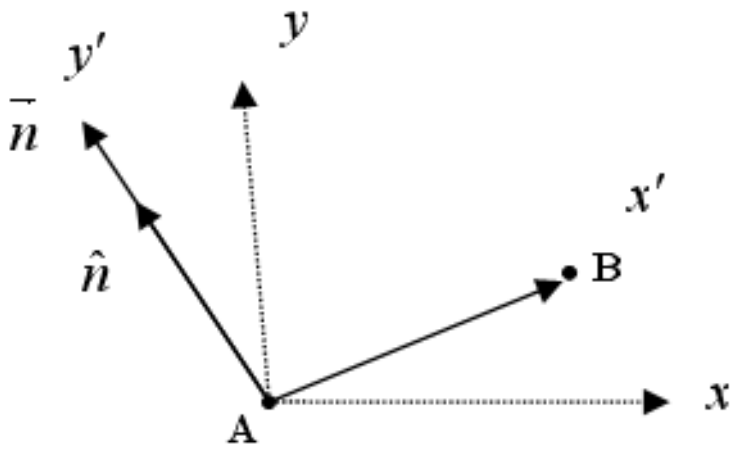

Figure 6.16: Global and local 2D Cartesian coordinate systems with reference point A

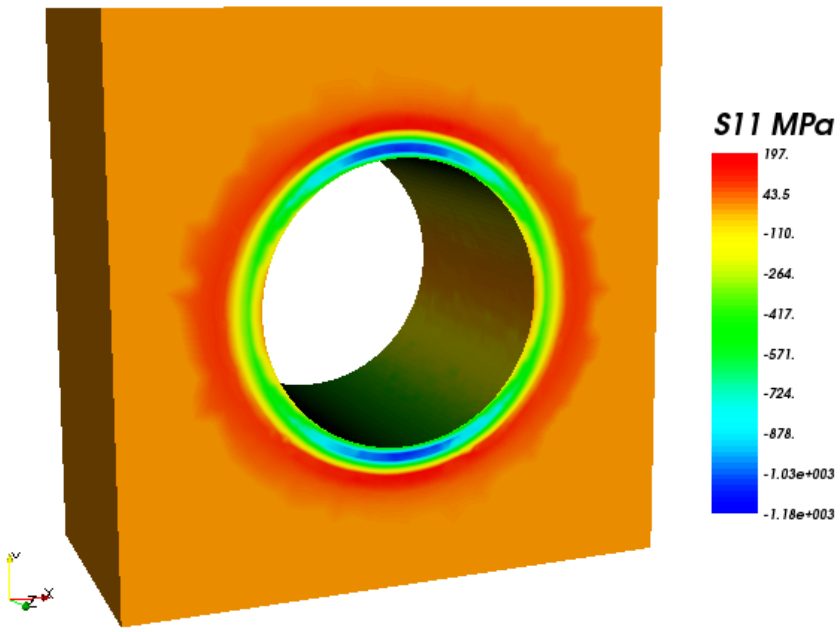

(a)

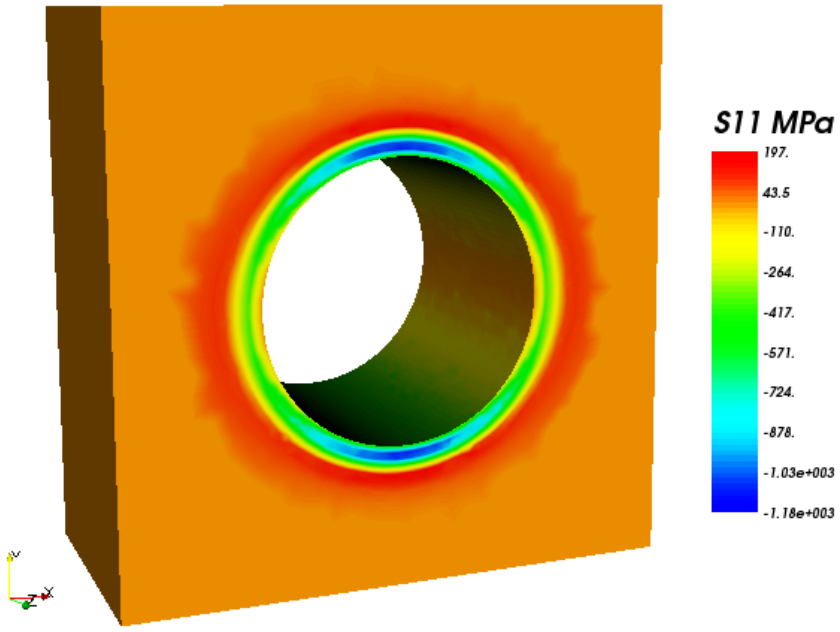

(b)

Figure 6.17: Mapped stresses in the x direction by using: **(a)** Method A; **(b)** Method B

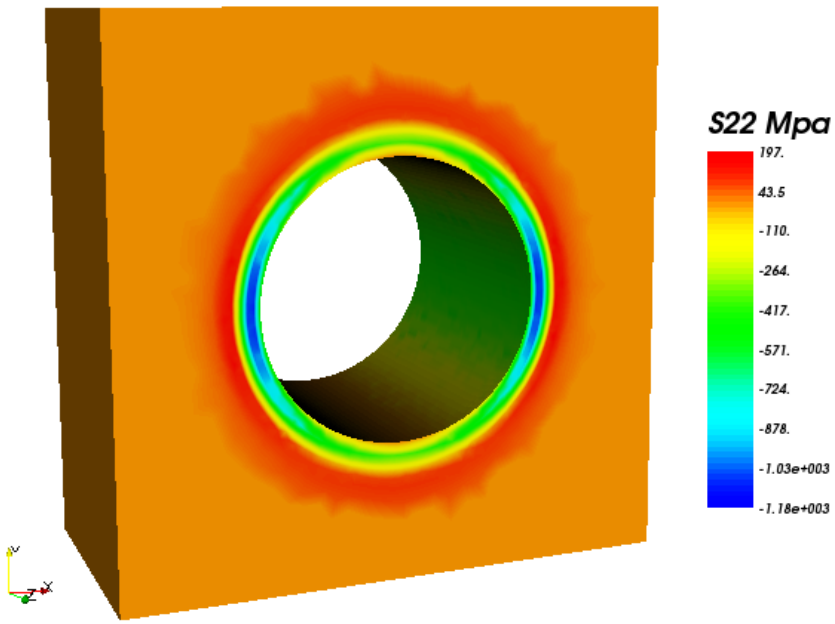

(a)

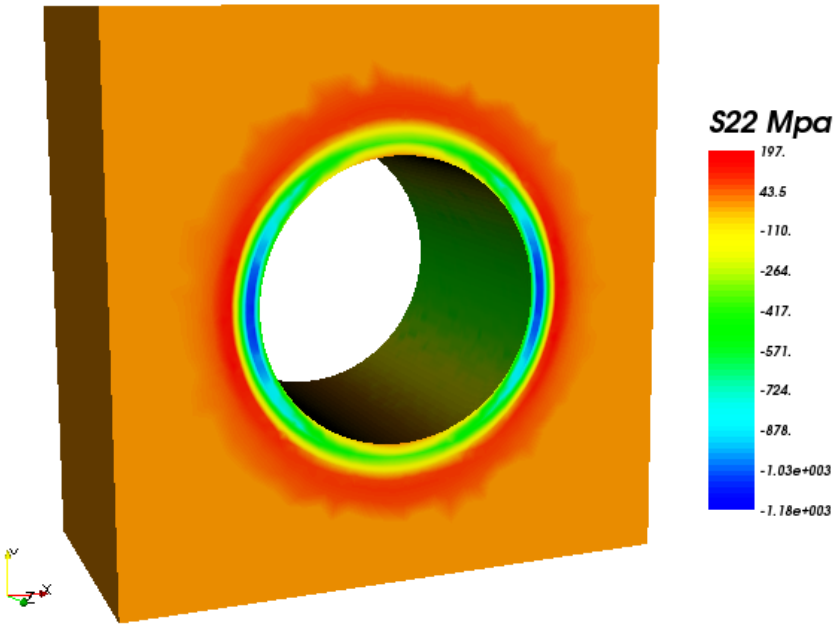

(b)

Figure 6.18: Mapped stresses in the y direction by using: **(a)** Method A; **(b)** Method B

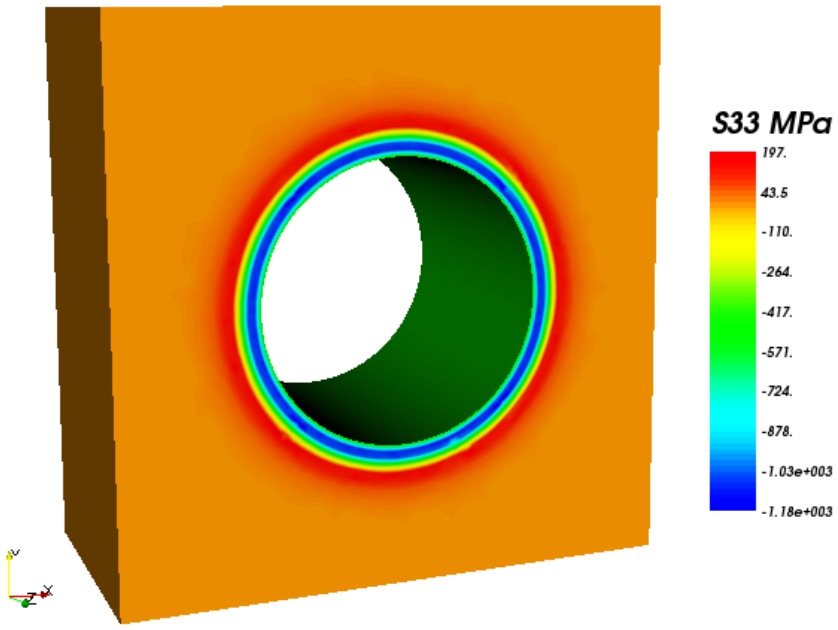

(a)

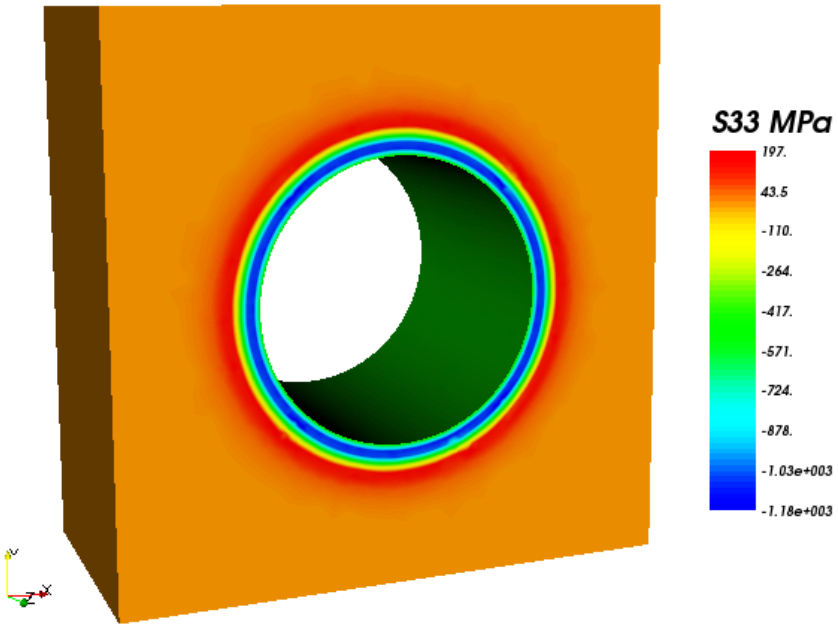

(b)

Figure 6.19: Mapped stresses in the z direction by using: **(a)** Method A; **(b)** Method B

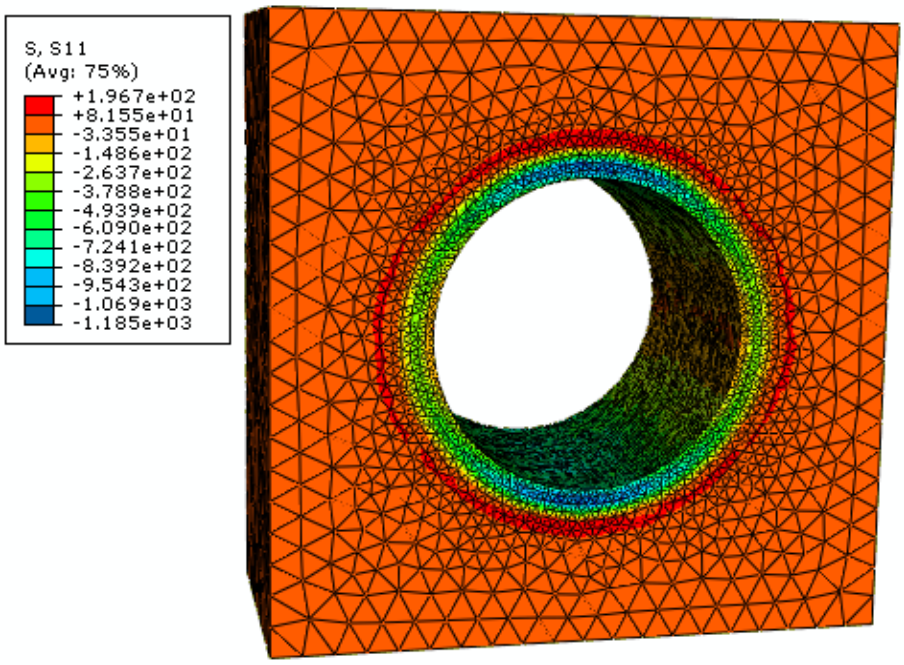

(a)

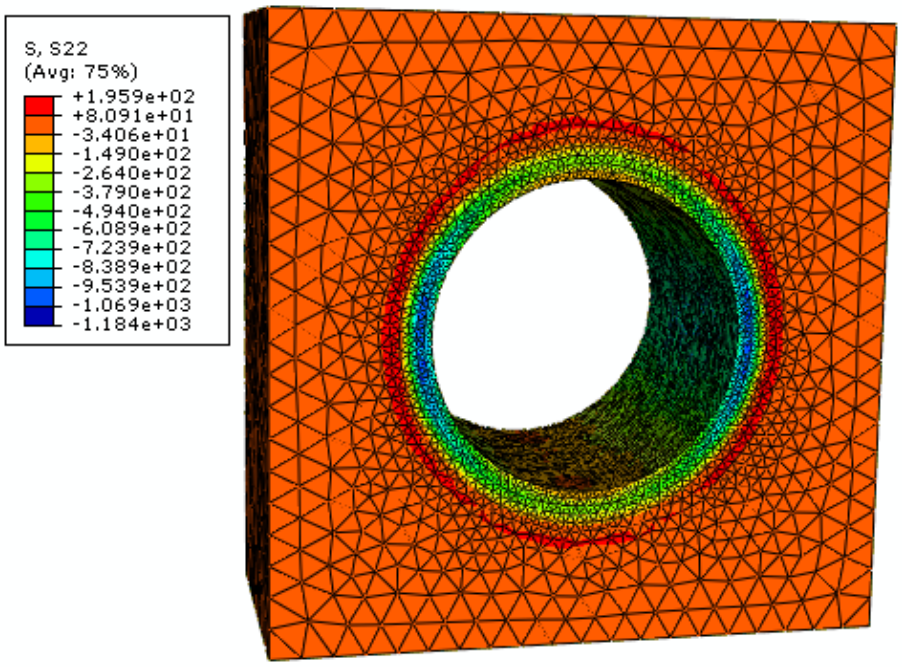

Figure 6.20: (b)

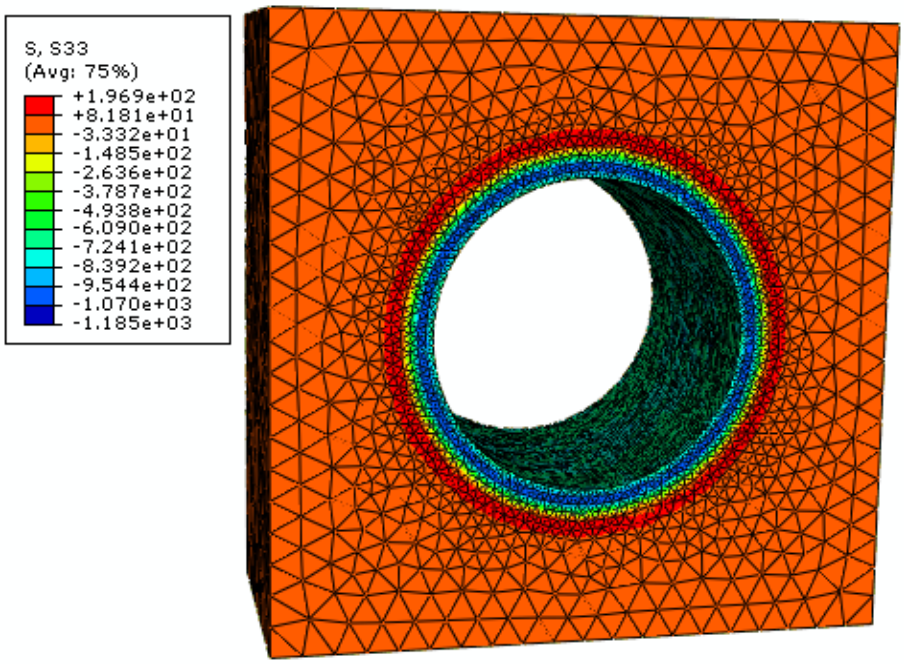

(c)

Figure 6.20: Mapped stresses and implemented in ABAQUS in the: **(a)** x direction; **(b)** y direction; **(c)** z direction

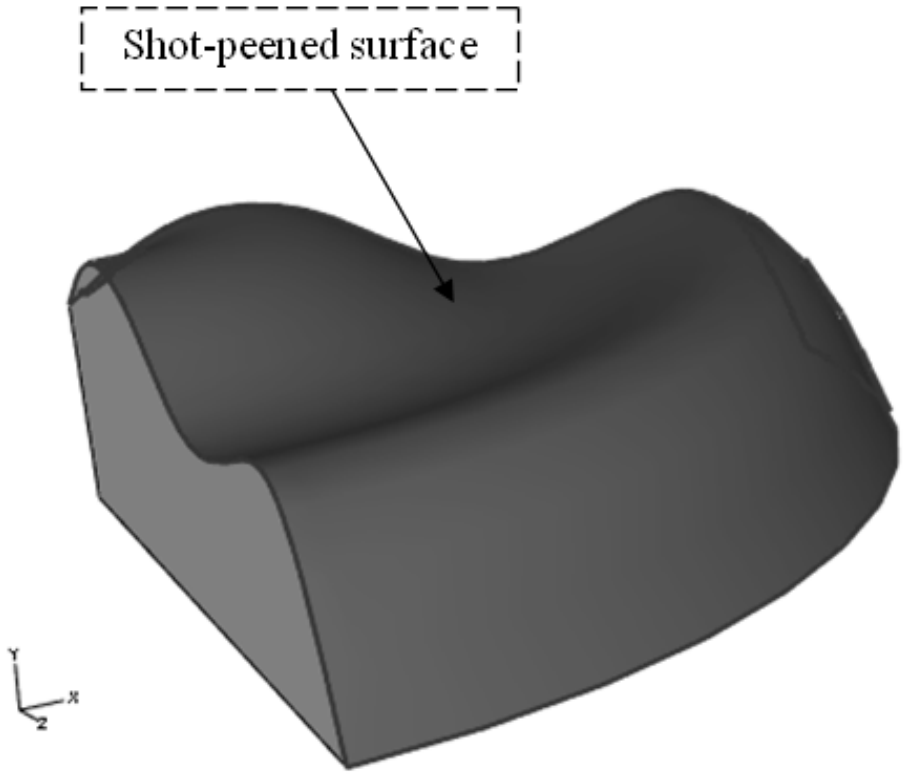

Figure 6.21: Geometry of a complex surface created by a revolved spline curve to 90 degrees

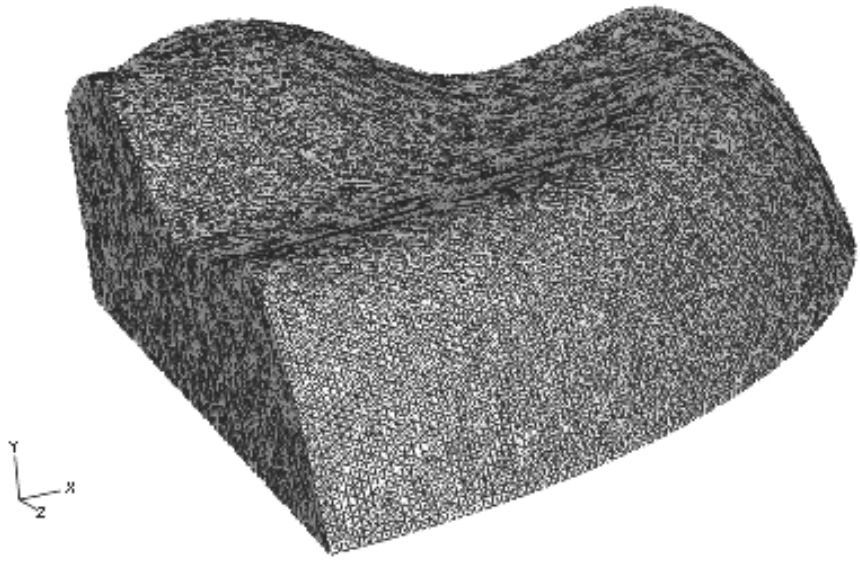

Figure 6.22: Mesh with four nodes linear tetrahedron elements for the model from Figure 6.21

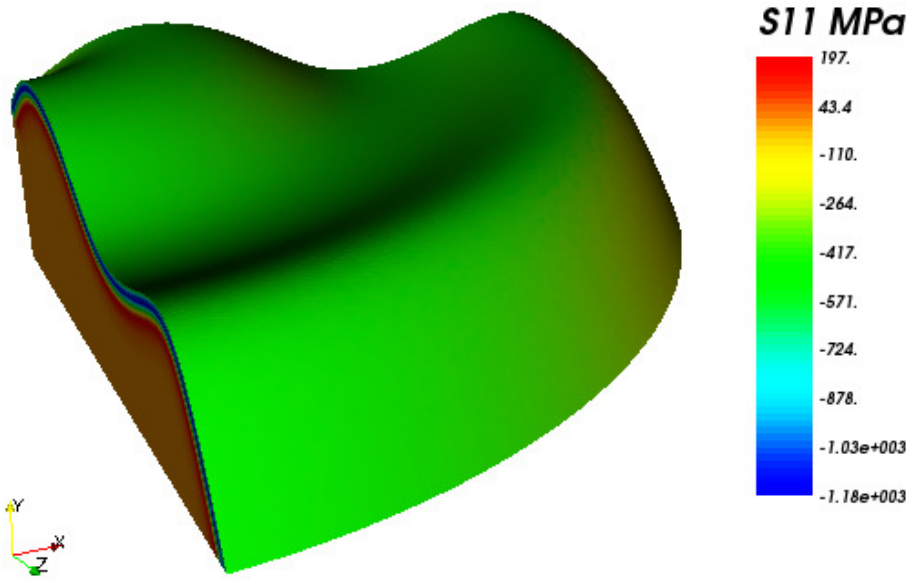

Figure 6.23: (a)

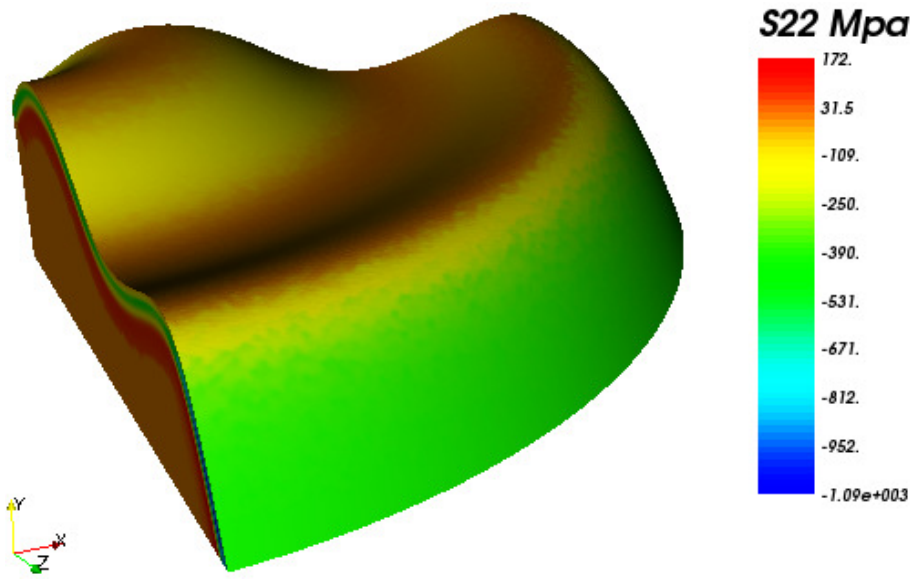

(b)

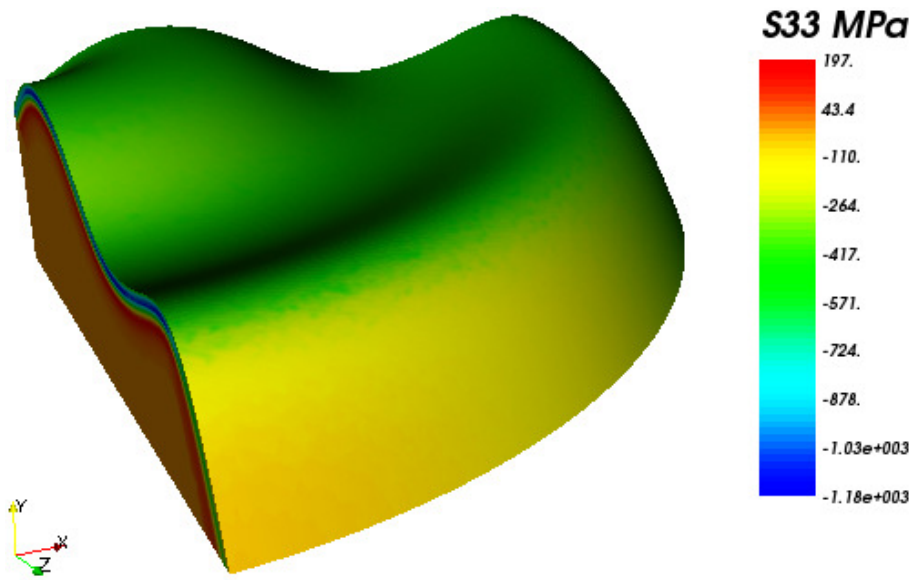

(c)

Figure 6.23: Mapped stresses into the model form Figure 6.21 in the: **(a)** x direction; **(b)** y direction; **(c)** z direction

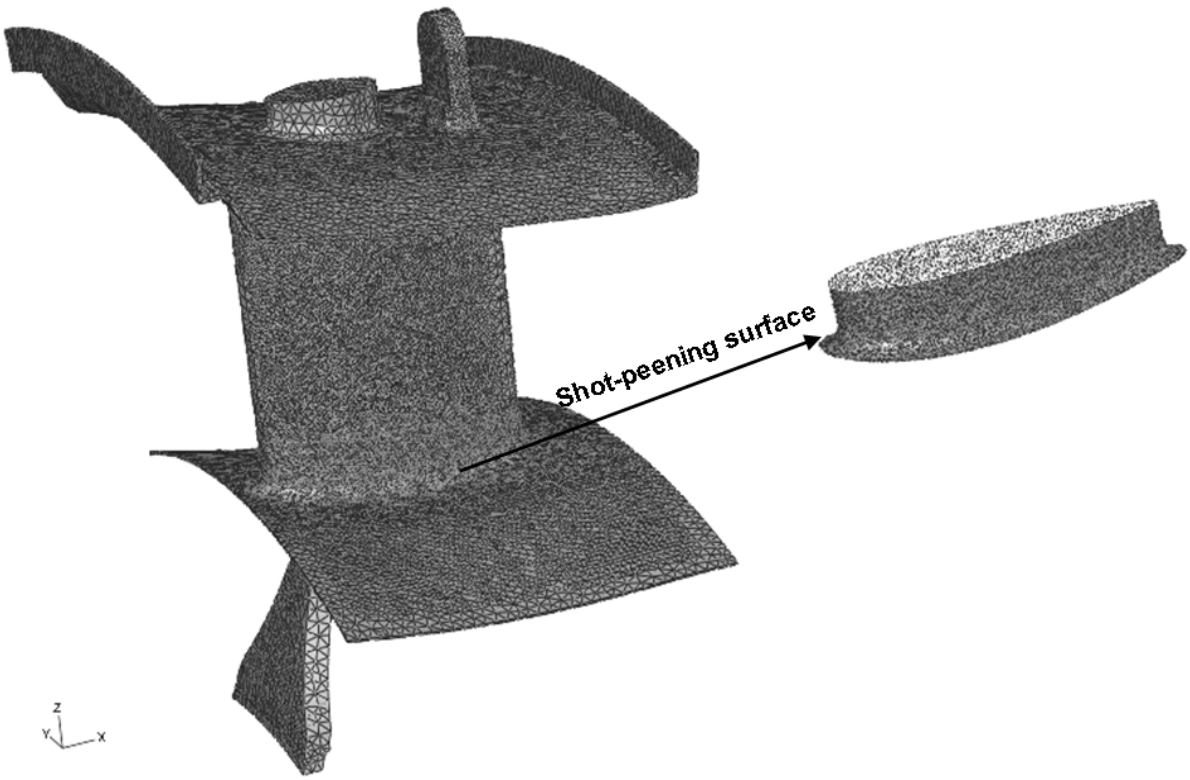

Figure 6.24: Mesh of an aero-engine vane subjected to shot-peening

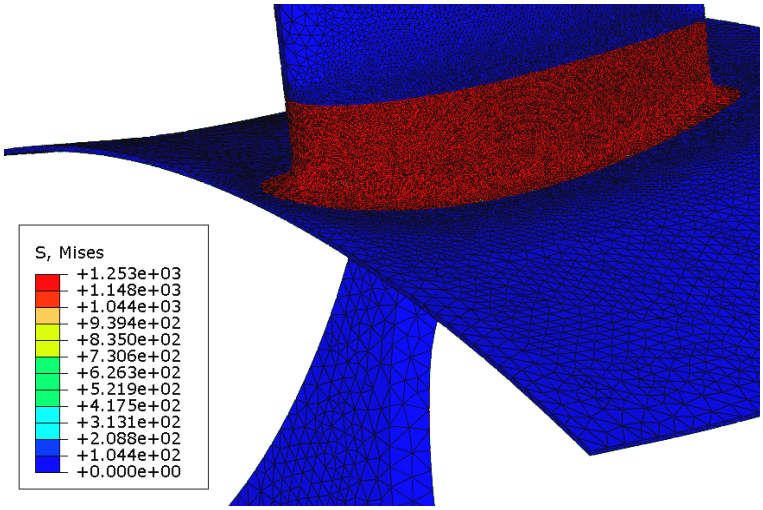

Figure 6.25: (a)

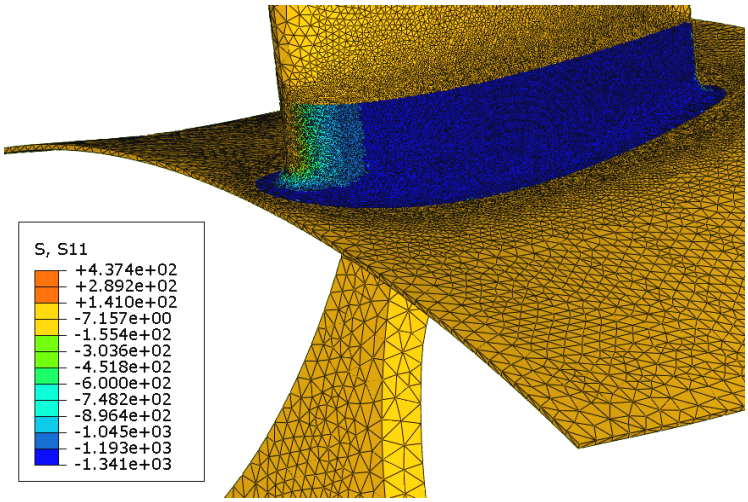

(b)

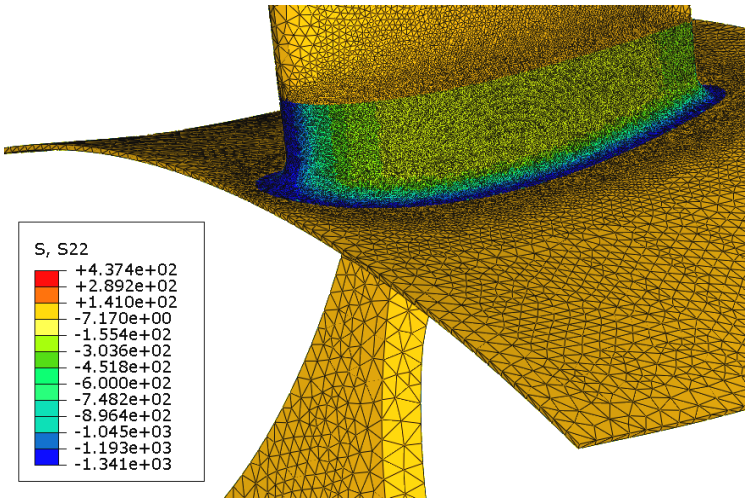

(c)

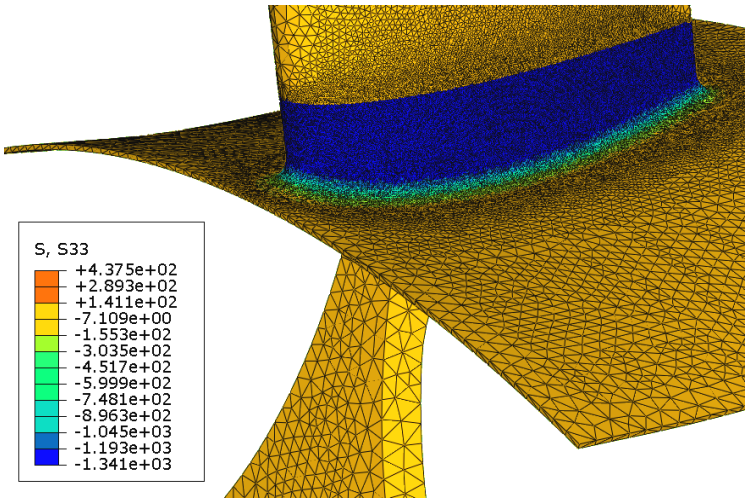

(d)

Figure 6.25: Mapped stresses beneath the shot-peening surface of the aero-engine vane: **(a)** Von Mises stresses; **(b)** Stress in the x direction; **(c)** Stress in the y direction; **(d)** Stress in the z direction

CHAPTER 7

FE DATA MAPPING BETWEEN DIFFERENT FE MESHES

This chapter reviews four interpolation techniques used for mapping FE data between different 2D and 3D meshes. The mathematical models and the algorithms for the nearest point method, the distance method using field of points, the distance method using elements and the method using the element shape function are described in detail. Comparison between all four interpolation techniques is performed for 2D and 3D FE models where the results are reviewed and discussed.

7.1 Introduction

A number of packages for FEA have been developed for linear and nonlinear structural analysis, fluid flow, solid-fluid interaction, heat conduction, flow through porous media, and coupled physical problems. Each finite element package (FEP) has its advantages in different fields. Producing high quality final products in a manufacturing chain requires involvement of many manufacturing processes. Simulating each process requires a close investigation for the most appropriate FEP for the corresponding process. This means that for simulating a chain of manufacturing processes the use of different FEPs can be required. The creation of residual stresses after each simulated process requires stress transfer among FEPs for accurate tracking of the progress of the residual stresses in the chain, which means that stresses have to be mapped from one FEP to another. This issue raises the need of creating software for transferring stresses among different FEPs and mapping data between deferent meshes with different element types and densities. Four interpolation techniques are presented in this chapter for data mapping between deferent meshes. A computer program called FEDES is developed by the author in order to cover the above mentioned issues which are described in detail in chapter 8. The interpolation techniques are implemented within FEDES. Results for 2D and 3D models are performed and compared by using the four interpolation techniques.

7.2 Interpolation techniques

Four interpolation techniques are implemented in FEDES – nearest point method (NPM), distance method using field of points (DMUFP), distance method using elements (DMUE) and method using the element shape function (MUESF).

7.2.1 Method 1: Nearest point method

This is the simplest method for interpolating data between two meshes with different element densities and types. Practically, it can be used for mapping data from refined to coarse meshes where it can provide accurate results and fast calculations. The opposite variant can also be achieved but it can provide results with lower accuracy. Figure 7.1 shows a perforated plate with two different meshes. All nodes in mesh 1 contain result data (stresses, strains, displacements, state variables, etc.). The goal is to map data into all nodes in mesh 2 from mesh 1. The nearest point method takes each node form mesh 2 and searches for the closest node in mesh 1. When the closest node from mesh 1 is located then the corresponding node form mesh 2 imports the data from the closest node from mesh 1. For example (see Figure 7.2), for a given node M from mesh 2 the nearest point method looks for the closest node in mesh 1 which in this case is node N. Node M from mesh 2 imports the entire data from node N from mesh 1. The distances between node M and nodes N_i can be given by.

$$d_i = \sqrt{\left(N_i(x) - M(x)\right)^2 + \left(N_i(y) - M(y)\right)^2 + \left(N_i(z) - M(z)\right)^2}, i = 1,2,...,n \quad (7.1)$$

where:

n	number of nodes in mesh 1
$M(x)$	x coordinate of node M
$M(y)$	y coordinate of node M
$M(z)$	z coordinate of node M
$N_i(x)$	x coordinates of node N_i
$N_i(y)$	y coordinates of node N_i

$N_i(z)$ z coordinates of node N_i

d_i distances between node N_i and node M

Figure 7.3 shows the algorithm for locating the nearest node to node M and assigning data to it. The interpolation technique works with integration points in the same way as nodal points. The coordinates of the integration points are required in that case.

7.2.2 Method 2: Distance method using field of points

This interpolation can be used for mapping data from refined to coarse meshes with different element densities and types and the other way around. This method performs the interpolation by using a field of nodes. As described earlier, Figure 7.1 shows two meshes, i.e. mesh 1 where all nodes contain result data and mesh 2 where the nodes are without data. This method is used to interpolate data from mesh 1 to mesh 2, as in method 1. The location of node M is transferred from mesh 2 to mesh 1 (see Figure 7.4). Node M in mesh 1 is used as an origin of new coordinate system with axis x_1, y_1 where x_1 is parallel to the x-axis and y_1 to the y-axis. This coordinate system is defined by four quadrants in 2D models and eight quadrants in 3D models. The nearest nodes to node M for each quadrant are located. It can be seen from Figure 7.4 that the nearest node to node M in the first quadrant is node N_1, in the second quadrant node N_2, in the third quadrant node N_3 and in the forth quadrant node N_4. A total of eight nodes must be located for 3D models because there are eight quadrants. This method can be used for both integration and nodal points. Figure 7.5 shows the algorithm for defining the nearest nodes in each quadrant to node M from mesh 1. Table 7.1 shows the criteria for locating the nearest node in each quadrant. After locating the closest nodes in each quadrant from which data is taken, the distances between node M and N_1, N_2, N_3 and N_4 for 2D models can be given by:

$$d_i = \sqrt{\left(N_i(x) - M(x)\right)^2 + \left(N_i(y) - M(y)\right)^2}, i = 1,2,3,4 \qquad (7.2)$$

where:

$N_i(x)$ x coordinates of nodes N_1, N_2, N_3 and N_4

$N_i(y)$ y coordinates of nodes N_1, N_2, N_3 and N_4

d_i distances between node N_i and node M

The next step defines the proportional distance coefficients for each distance.

$$k_i = \frac{\sum_{n=1}^{4} d_n}{d_i}, i = 1,2,3,4 \tag{7.3}$$

where: k_i represents the proportional distance coefficients

The mapped data at node M can be given by:

$$D_M = D_{N_1} \frac{k_1}{\sum_{n=1}^{4} k_n} + D_{N_2} \frac{k_2}{\sum_{n=1}^{4} k_n} + D_{N_3} \frac{k_3}{\sum_{n=1}^{4} k_n} + D_{N_4} \frac{k_4}{\sum_{n=1}^{4} k_n} \tag{7.4}$$

where: D_M is the mapped data (stress, strain, displacement, etc.) at node M and D_{N_i} is the data at nodes N_i

Equation (7.4) can be presented in the following form:

$$D_M = \sum_{i=1}^{4} \frac{\frac{d_i}{\sum_{n=1}^{4} d_n}}{\sum_{k=1}^{4} \frac{d_k}{\sum_{n=1}^{4} d_n}} D_{Ni} \tag{7.5}$$

The distances between node M and nodes N_i for 3D models can be calculated from Equation (7.2) where $n = 1,...,8$.

7.2.3 Method 3: Distance method using elements

As in the previous two interpolation techniques, this method can be used for interpolating between different element types and densities. The perforated plate is

used for explaining the interpolation technique. Mapping form mesh 1 to mesh 2 (see Figure 7.1) is performed by using this interpolation technique. As an example, node M is taken from mesh 2 and data is mapped into it from mesh 1(see Figure 7.6). The location of node M is transferred from mesh 2 to mesh 1. If node M is located on a line between two elements then node M is assigned to the smaller element by size. The other case is when node M is located on a node of mesh 1 then node M takes the entire data from that node. After defining the nodes from which data can be taken then the distance method can be used. Equation (7.2) can be used for defining the distances between node M and nodes N_i , Equation (7.3) for defining the proportional distance coefficients and Equations (7.4) and (7.5) for defining the data in node M. The example in Figure 7.6 shows a 2D quadrilateral element with four nodes. Figure 7.7 shows the algorithm for defining the element in mesh 1 to which node M belongs. The algorithm calculates the distances from node M to all nodes of the element and then calculates the average distance, as follows:

$$d_{average} = \frac{\sum_{j=1}^{n} dj}{n} \tag{7.6}$$

By calculating the $d_{average}$ for all elements from the model, node M will belong to the element with $\min(d_{average})$. After locating the element to which node M belongs and the distance from node M to the element nodes, the proportional distance coefficient can be calculated as in Equations (7.3) and (7.4)

7.2.4 Method 4: Method using the element shape function

This method is also applicable for mapping data between meshes with different element densities and types. It can be used with high accuracy for mapping data from coarse to refined meshes and vice versa. Figure 7.1 is again used as an example for interpolating data from mesh 1 to mesh 2. The method using the element shape function uses the sequence of operations shown in Figure 7.8. The same element search technique is used as the one explained in Section 7.2.3. Figure 7.9 shows the algorithm for locating the elements to which the nodes belong. Figure 7.10 shows an exception when this method is used. It can be seen that node M belongs to element one but the average distance value between node M and nodes of the element,

calculated by Equation (7.6), is smaller for element two. This means that node M will belong to element two.

The FEM uses different element types. Each element shape can be described by its shape function. In the FEM, the shape function is used to interpolate displacements, temperatures and etc. from the nodal to the integration points. The shape function can be used for transferring any data (displacements, strains, stresses, temperature, state variables, etc.) from the nodal points to any points within the element. Mapping data to node M can be given by:

$$D_M = \sum_{i=1}^{n} N_i D_i \tag{7.7}$$

where N_i is the shape function in node i, D_M is a FE data at node M, D_i is a data (stress, strain, displacement, temperature, etc.) at node i

Assuming that node M is located inside a 2D triangular element then Equation (7.7) for triangular elements is given by:

$$D_M = (1-g-h)D_1 + gD_2 + hD_3 \tag{7.8}$$

The local coordinates g and h are obtained by solving a system of linear equations as explained in Appendix 1 section A1.1. The function for obtaining data for node M located inside 3D tetrahedron elements can be given by:

$$D_M = (1-g-h-r)D_1 + gD_2 + hD_3 + rD_4 \tag{7.9}$$

The local coordinates g, h and r are obtained by solving a system of linear equations as explained in Appendix 1 section A1.2. The function for obtaining data for node M located inside 2D quadrilateral elements can be given by:

$$D_M = \frac{1}{4}\left((1-g)(1-h)D_1 + (1+g)(1-h)D_2 + (1+g)(1+h)D_3 + (1-g)(1+h)D_4\right) \tag{7.10}$$

The local coordinates g and h are obtained by solving a system of non-linear equations as shown in Appendix 1 section A1.3. The function for obtaining data for node M located inside 3D hexahedron elements can be given by:

$$D_M = \frac{1}{8}\begin{pmatrix} (1-g)(1-h)(1-r)D_1 + (1+g)(1-h)(1-r)D_2 + \\ +(1+g)(1+h)(1-r)D_3 + (1-g)(1+h)(1-r)D_4 + \\ +(1-g)(1-h)(1+r)D_5 + (1+g)(1-h)(1+r)D_6 + \\ +(1+g)(1+h)(1+r)D_7 + (1-g)(1+h)(1+r)D_8 \end{pmatrix} \tag{7.11}$$

The local coordinates g, h and r are obtained by solving a system of non-linear equations as demonstrated in Appendix 1 section A1.4. The function for obtaining data for node M located inside 3D wedge elements can be given by:

$$D_M = \frac{1}{2}\begin{pmatrix} (1-g-h)(1-r)D_1 + g(1-r)D_2 + +h(1-r)D_3 + \\ +(1-g-h)(1+r)D_4 + g(1+r)D_5 + h(1+r)D_6 + \end{pmatrix} \tag{7.12}$$

The local coordinates g, h and r are obtained by solving a system of non-linear equations as shown in Appendix 1 section A1.5.

7.3 Results for 2D and 3D models

The four interpolation techniques are applied to 2D and 3D models. A plate, with width and height of 100 mm, perforated in the centre with a cylinder of radios 20 mm, is used as an example for the 2D model, as shown in Figure 7.11. A distributed load of 100 MPa is applied on surface S_1 and zero displacements in the x and y directions are applied to all nodes on surface S_2 (see Figure 7.11). Figure 7.12(a) shows a mesh with 718 four node linear quadrilateral elements and Figure 7.12(b) a mesh with 11,776 three node linear triangular elements. Both meshes are used for obtaining results from the FEA. An elastic material is used with an elastic modulus of 200 GPA and a Poisson's ratio of 0.3. The simulation is performed in ABAQUS and the stresses in the y direction are shown in Figure 7.13(a) for mesh A and Figure 7.13(b) for mesh B. The purpose of the simulation is to provide data which is used for mapping. Two mapping variants are investigated.

- Variant 1 - Mapping the stresses in the y direction obtained from mesh A from Figure 7.13(a) into mesh B from Figure 7.12(b)
- Variant 2 - Mapping the stresses in the y direction obtained from mesh B from Figure 7.13(b) into mesh A from Figure 7.12(a)

Figure 7.14 shows the mapped stresses for variant 1 by using the four interpolation techniques. By comparing the results from the results from Figure 7.13(a) with the

results obtained after the mapping using the four interpolation techniques in Figure 7.14, it can be seen that the minimum and the maximum stresses are the same. Method 1 (see Figure 7.14(a)) shows poor stress distribution. Method 2 (see Figure 7.14(b)) and the method 3 (see Figure 7.14(c)) show acceptable stress distribution. Method 4 (see Figure 7.14(d)) shows almost identical stress distribution. Figure 7.15 shows the mapped stresses for variant 2. It can be seen that the minimum and the maximum stresses are the same by using all interpolation techniques. The stress distribution is similar for all interpolation techniques. It can be concluded that the method using the element shape function shows good results when mapping data from coarse to refined meshes and vice versa. Method 2 and method 3 show acceptable results when mapping from coarse to refined meshes and good results when mapping from refined to coarse meshes. Method 1 is recommended to be used only for mapping from very refined to coarse meshes. It requires less computational time compared to method 4. Method 2 uses only nodes from the model and can be used for mapping data from meshless method into FEM.

All four interpolation techniques are applied to 3D elements. Based on the results obtained for the 2D mapping, method 4, as the most accurate interpolation technique, is used to demonstrate the capability of mapping results between wedge, hexahedron and tetrahedron elements for 3D meshes. A disk geometry is shown in Figure 7.16. Three meshes with wedge, hexahedron and tetrahedron elements are used, as shown in Figure 7.17. Figure 7.18 shows the applied load and the boundary conditions. The aim is to obtain FE results and to perform the mapping between different 3D meshes. Figure 7.19 shows the stresses in the y direction obtained for the three meshes from Figure 7.17. Three mapping variants are used:

- Variant 1 – mapping the stresses in the y direction obtained by mesh A with hexahedron elements from Figure 7.19(a) into mesh B with tetrahedron elements from Figure 7.17(b). The mapped stresses are shown in Figure 7.20(a). Comparing Figure 7.19(a) and Figure 7.20(a), it can be seen that the stress distribution and the maximum stresses are similar. There is a difference of less than 1% between the minimum mapped stresses.
- Variant 2 – mapping the stresses in the y direction obtained by mesh B with tetrahedron elements from Figure 7.19(b) into mesh C with wedge elements

from Figure 7.17(c). The mapped stresses are shown in Figure 7.20(b). The stress distribution and the minimum stresses are similar. There is a difference of less than 0.06 % between the maximum stresses.

- Variant 3 – mapping the stresses in the y direction obtained by mesh C with wedge elements from Figure 7.19(c) into mesh A with hexahedron elements from Figure 7.17(a). The mapped stresses are shown in Figure 7.20(c). The stress distribution is similar. There is a difference of around 4% between the minimum and less than 3% between the maximum stresses.

7.4 Conclusions

Four interpolation techniques for mapping FE data between 2D and 3D meshes with different element types and densities were demonstrated. The four methods are capable for mapping FE data between different FE meshes and different element types. The method using the element shape function showed the highest accuracy. Method 2 and method 3 showed acceptable results. Method 1 showed poor results when mapping from coarse to refined meshes. All four techniques showed similar results when the mapping was performed from refined to coarse meshes. However, for very large models, method 1 is computationally efficient. Method 2 can be used for mapping data from models using MM to FEM.

Table 7.1: Defining the quadrant in which node N_j is located

k	Expression	Description
0	**$(N_j(x) = M(x))$ and $(N_j(y) = M(y))$ and $(N_j(z) = M(z))$**	Node M coincide with node N
1	**$(N_j(x) \leq M(x))$ and $(N_j(y) \leq M(y))$ and $(N_j(z) \leq M(z))$**	Node M is located in first quadrant
2	**$(N_j(x) > M(x))$ and $(N_j(y) < M(y))$ and $(N_j(z) < M(z))$**	Node M is located in second quadrant
3	**$(N_j(x) \geq M(x))$ and $(N_j(y) \leq M(y))$ and $(N_j(z) \geq M(z))$**	Node M is located in third quadrant
4	**$(N_j(x) < M(x))$ and $(N_j(y) < M(y))$ and $(N_j(z) > M(z))$**	Node M is located in fourth quadrant
5	**$(N_j(x) \leq M(x))$ and $(N_j(y) \geq M(y))$ and $(N_j(z) \leq M(z))$**	Node M is located in fifth quadrant
6	**$(N_j(x) > M(x))$ and $(N_j(y) > M(y))$ and $(N_j(z) < M(z))$**	Node M is located in sixth quadrant
7	**$(N_j(x) \geq M(x))$ and $(N_j(y) \geq M(y))$ and $(N_j(z) \geq M(z))$**	Node M is located in seventh quadrant
8	**$(N_j(x) < M(x))$ and $(N_j(y) > M(y))$ and $(N_j(z) > M(z))$**	Node M is located in eighth quadrant

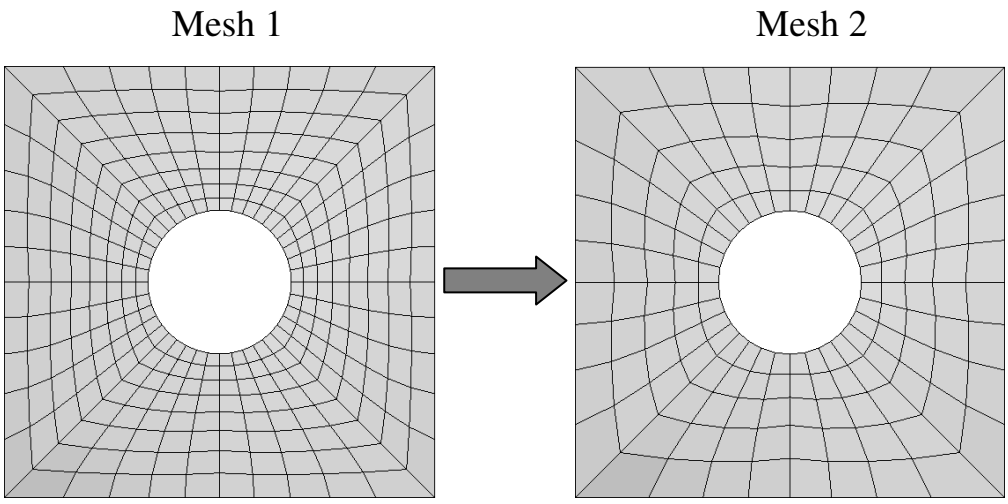

Figure7.1: Perforated plate presented in two meshes. Mesh 1 contains result data and Mesh 2 is empty.

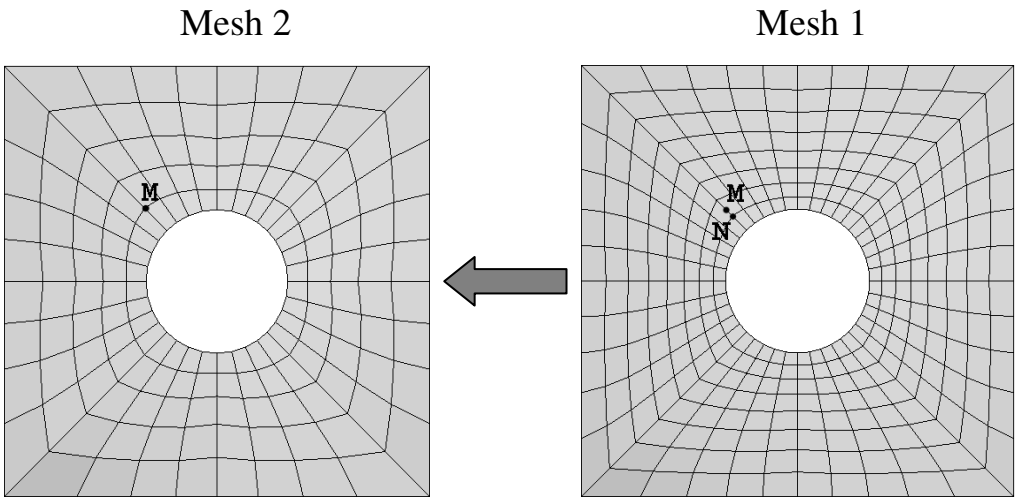

Figure 7.2: Perforated plate presented in two meshes. Mesh 2 with node M and Mesh 1 with transferred node M and closest to it node N

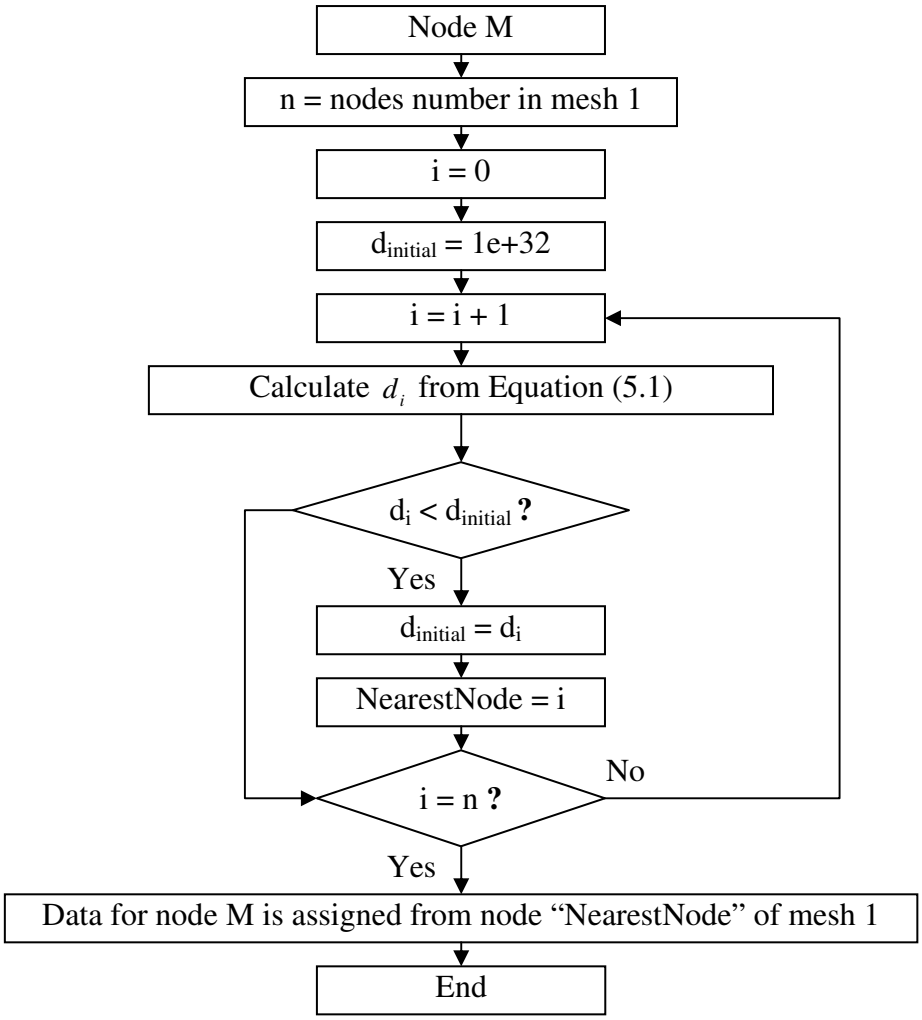

Figure 7.3: Algorithm for locating the nearest point from mesh 1 to node M and assigning data to it

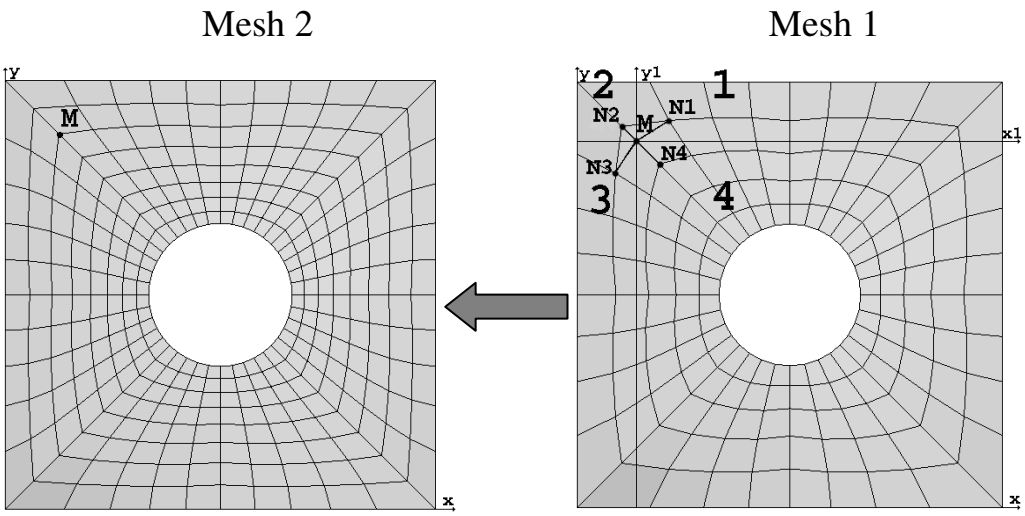

Figure 7.4: Perforated plate presented in two meshes. Mesh 2 with node M and Mesh 1 with transferred node M which is origin of new coordinate system with axis x_1 and y_1

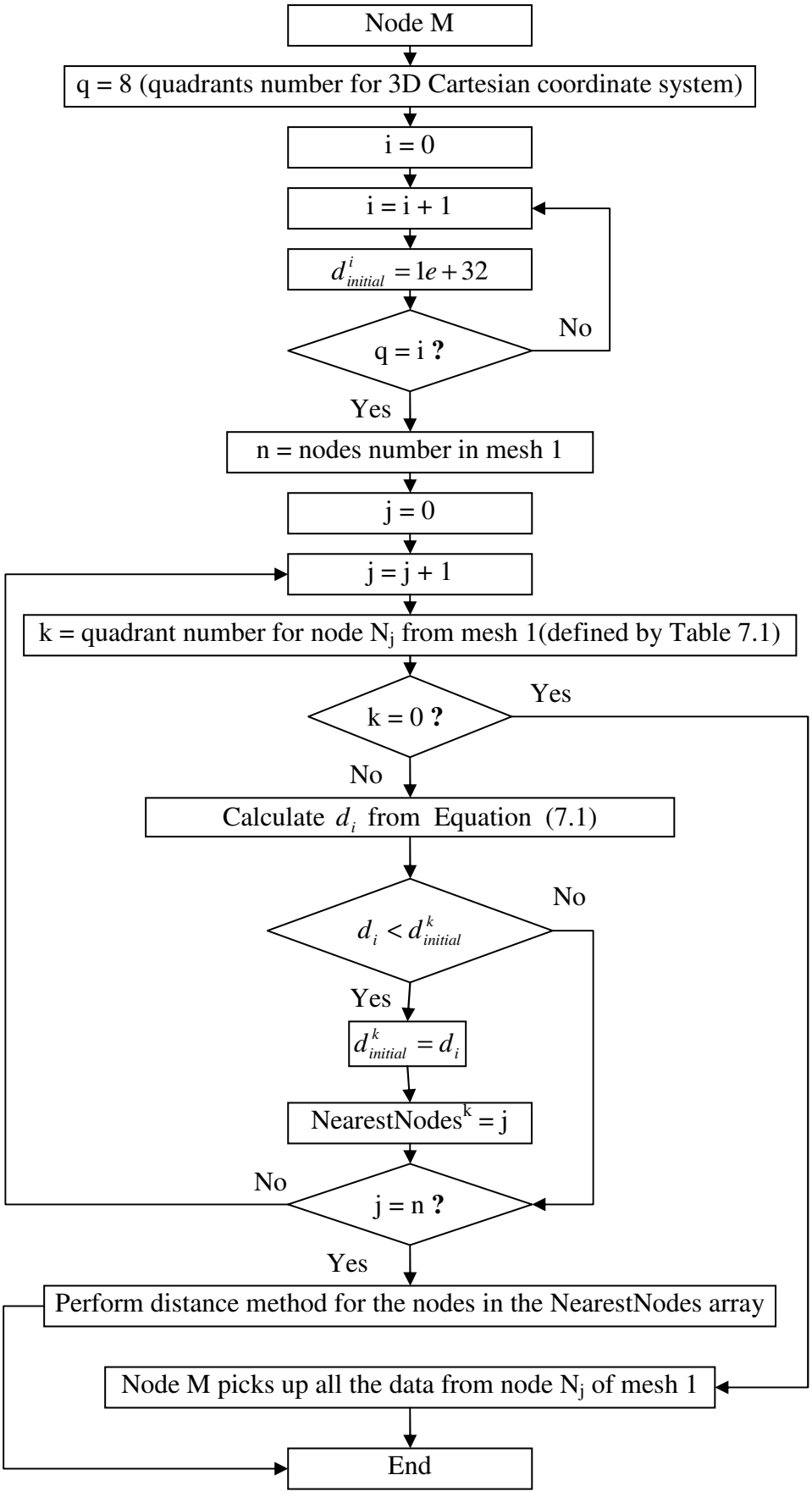

Figure 7.5: Algorithm for defining the nearest nodes to node M in each quadrant from mesh 1

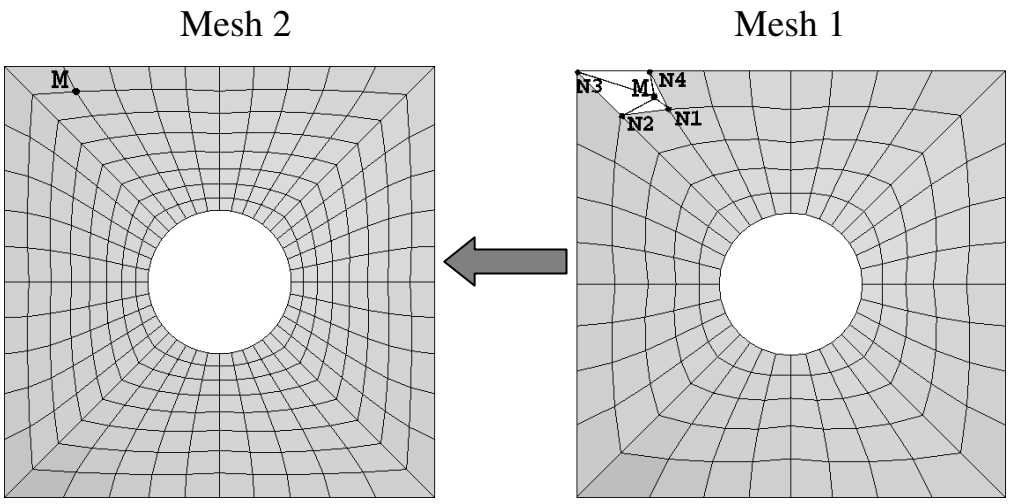

Figure 7.6: Performed plate presented in two meshes. Mesh 2 with node M and Mesh 1 with transferred node M and located element to which node M belongs

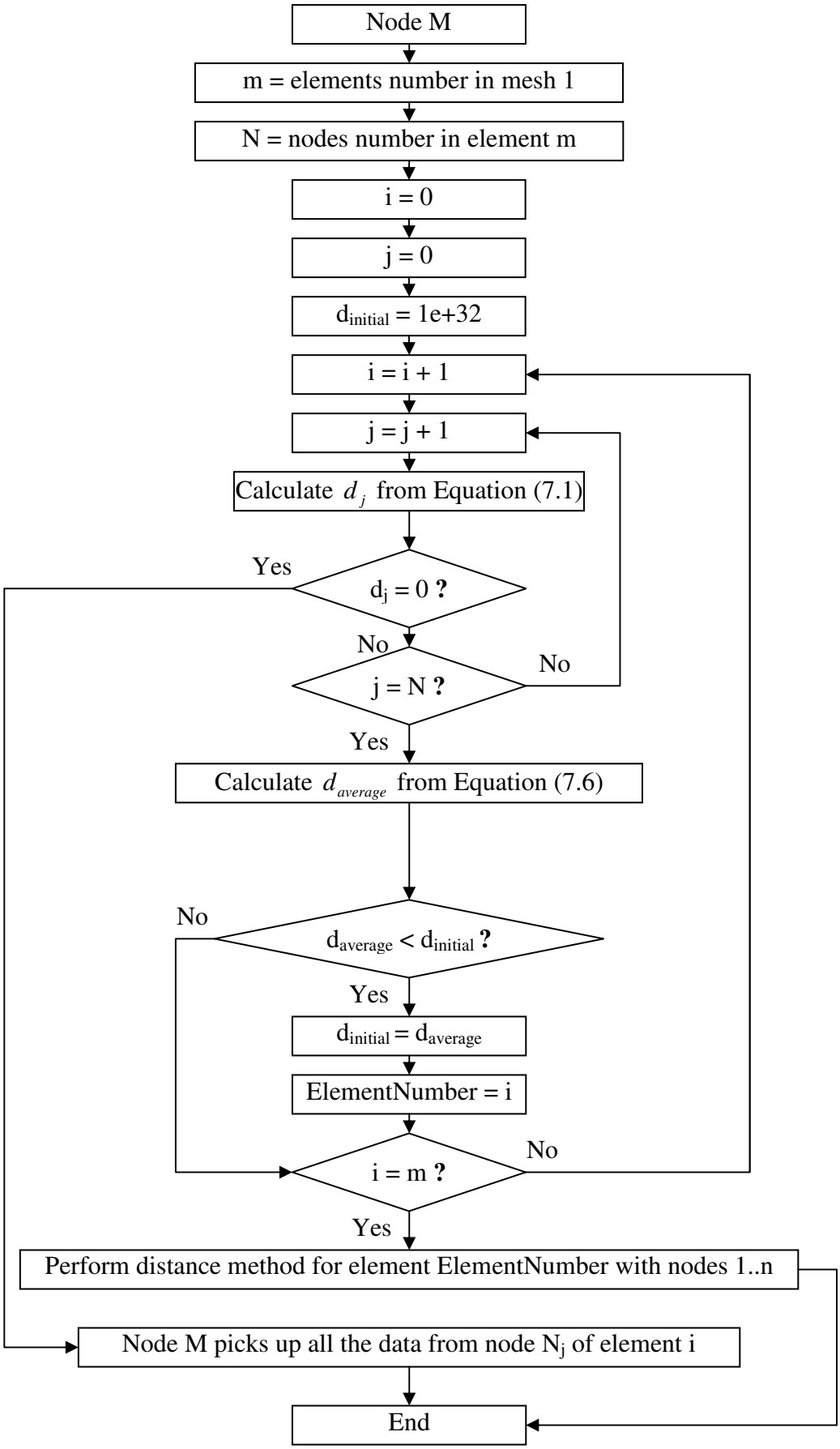

Figure 7.7: Algorithm for defining the element in mesh 1 to which node M belongs

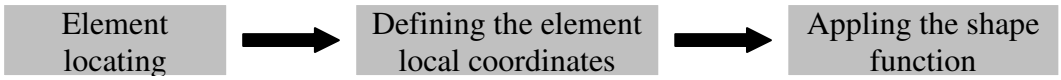

Figure 7.8: Sequence of operations for performing the method using the element shape function

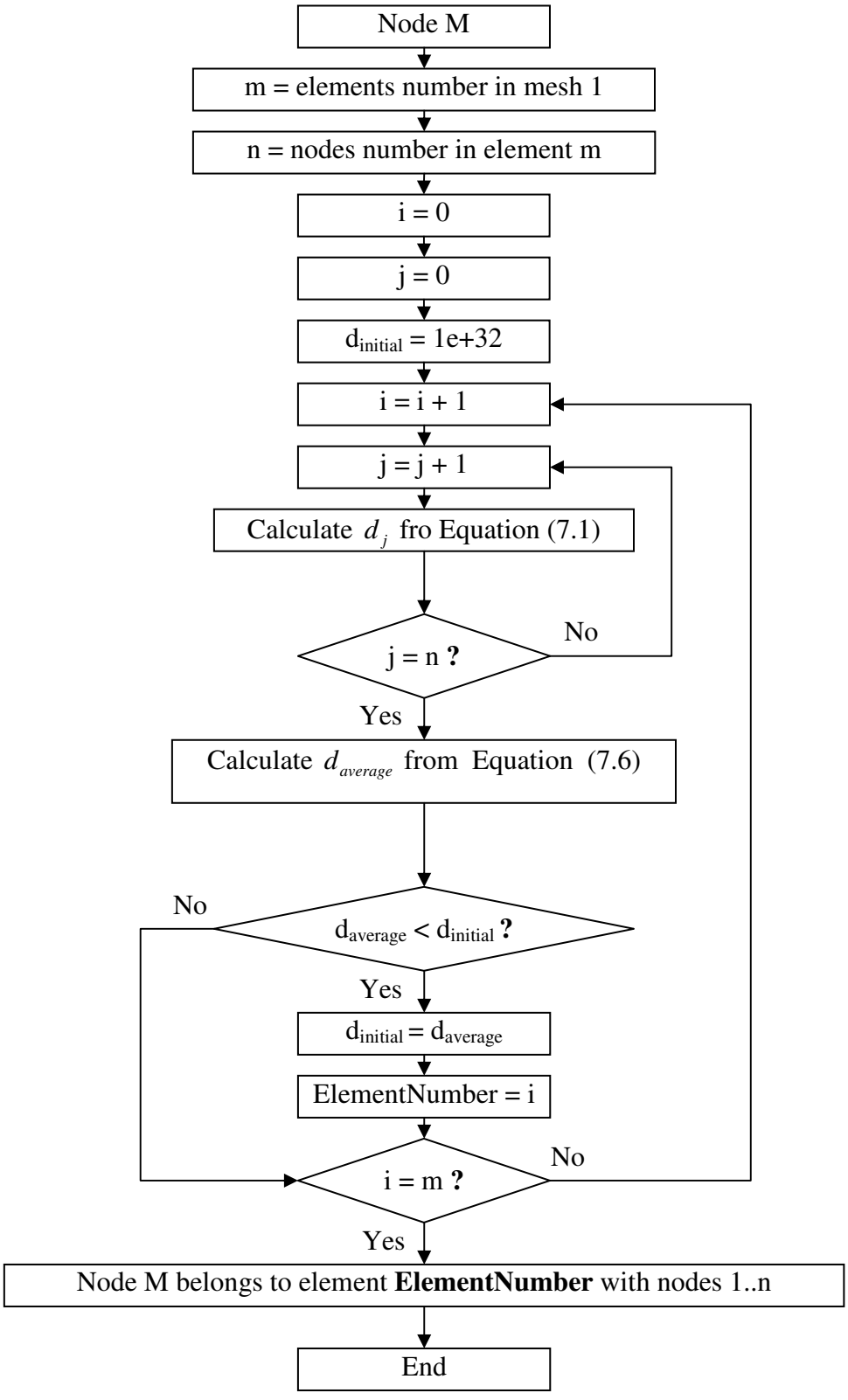

Figure 7.9: Algorithm for defining the element in mesh 1 to which node M belongs

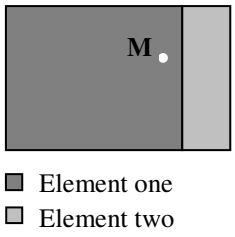

Figure 7.10: Exception for locating an element

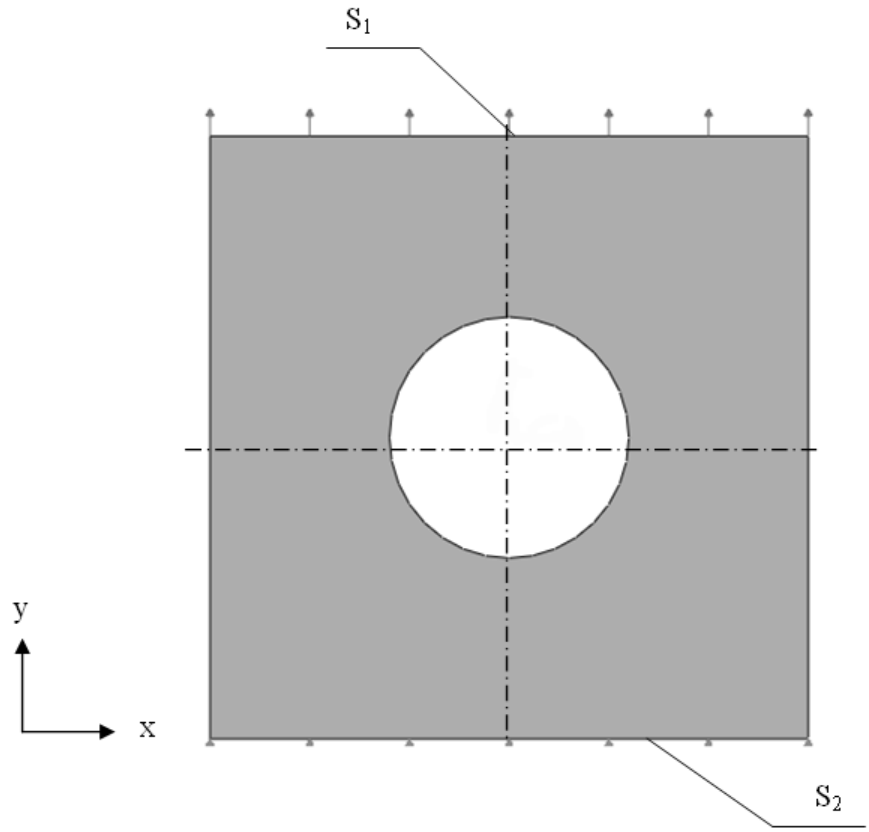

Figure 7.11: Geometry, loads and boundary conditions of a quadratic plate, with width and height of 100 mm, perforated in the centre with a cylinder with radios of 20 mm

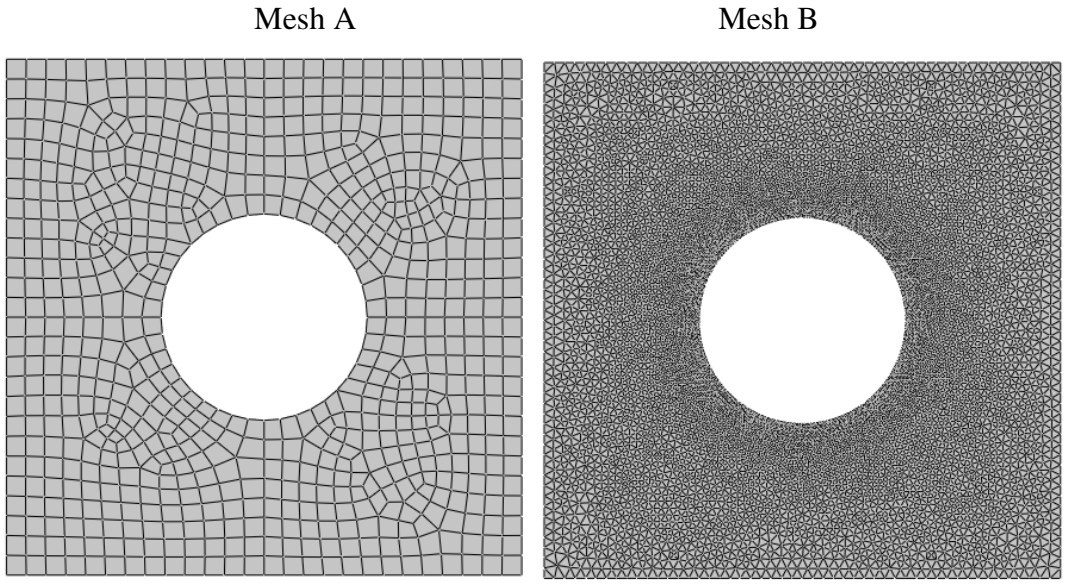

Figure 7.12: Meshes used for the model from Figure 7.11: **(a)** mesh with 718 four nodes linear quadrilateral elements; **(b)** mesh with 11,776 three nodes linear triangular elements

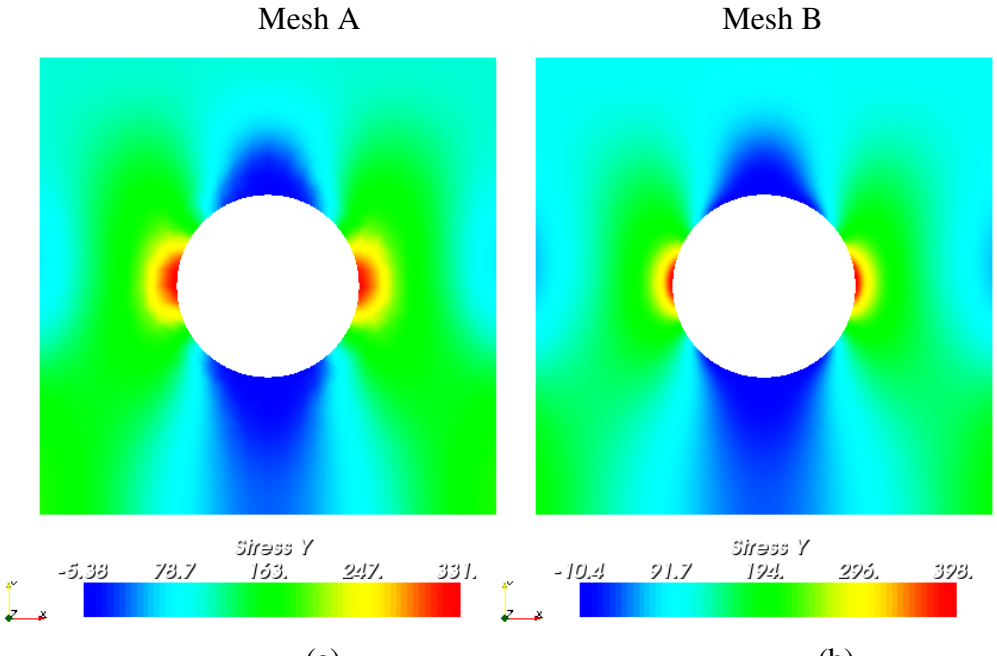

Figure 7.13: Stresses in the y direction obtained for the model from Figure 7.11.: **(a)** stresses obtained by using mesh A from Figure 7.12(a); **(b)** stresses obtained by using mesh B from Figure 7.12(b)

Variant 1

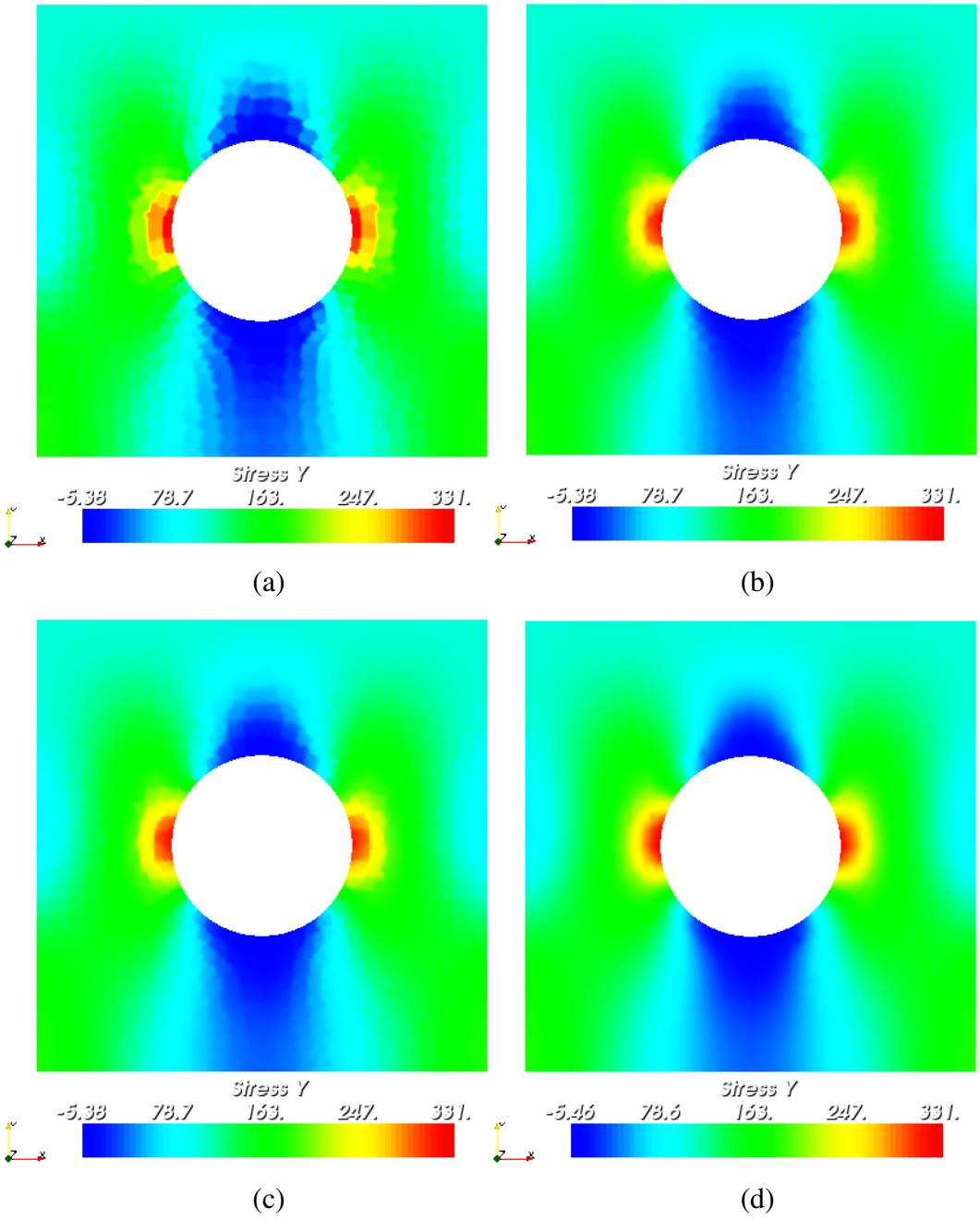

Figure 7.14: Mapped stresses in the y direction, obtained by mapping from mesh A from Figure 7.13(a) into mesh B from Figure 7.12(b) by using: **(a)** method 1; **(b)** method 2; **(c)** method 3; **(d)** method 4

Variant 2

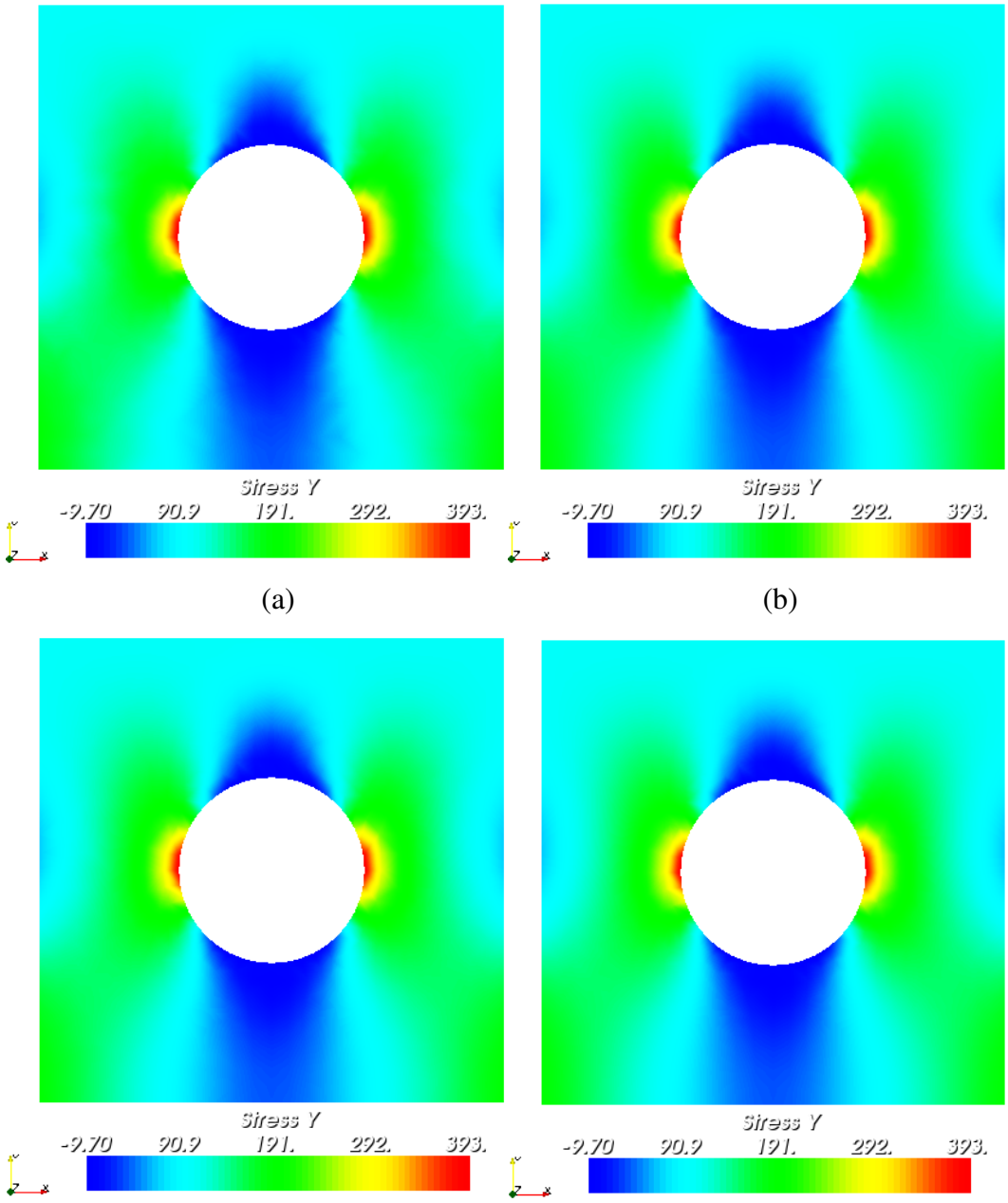

Figure 7.15: Mapped stresses in the y direction, obtained by mapping from mesh B from Figure 7.13(b) into mesh A from Figure 7.12(a) by using: **(a)** method 1; **(b)** method 2; **(c)** method 3; **(d)** method 4

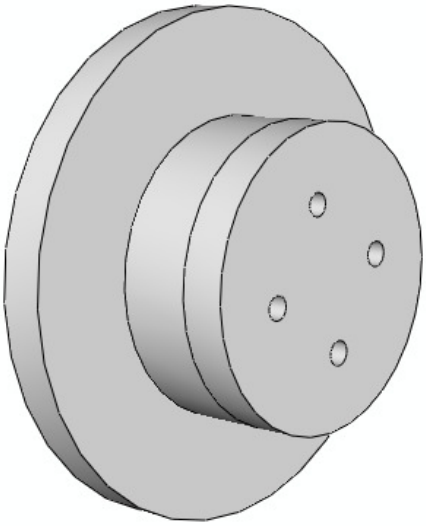

Figure 7.16: Geometry of a disk

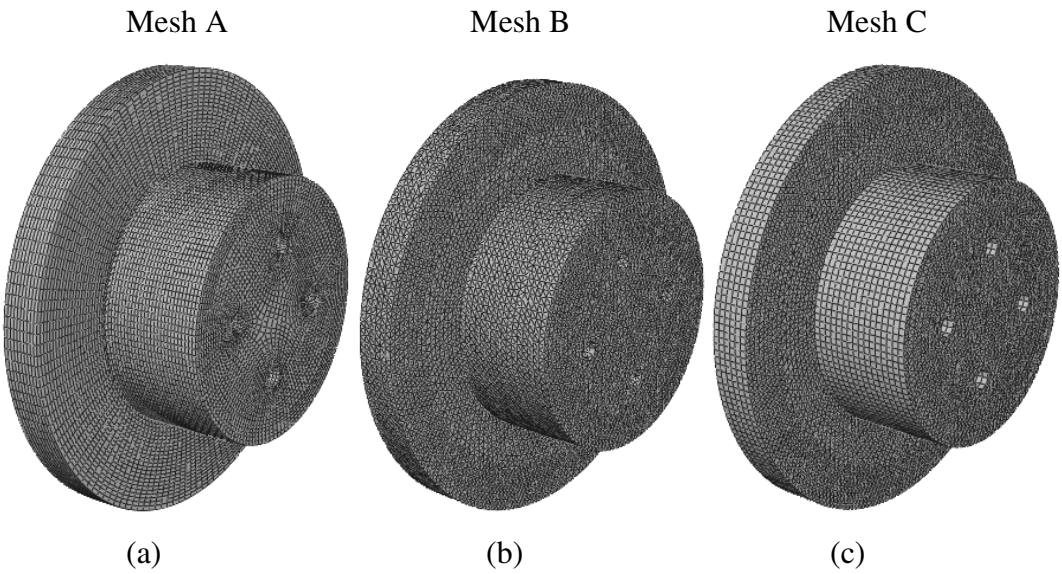

Figure 7.17: Meshes used for the model from Figure 7.16: **(a)** mesh with 77,505 eight nodes linear hexahedron elements; **(b)** mesh with 206,216 four nodes linear tetrahedron elements; **(c)** mesh with 61,247 six nodes linear wedge elements

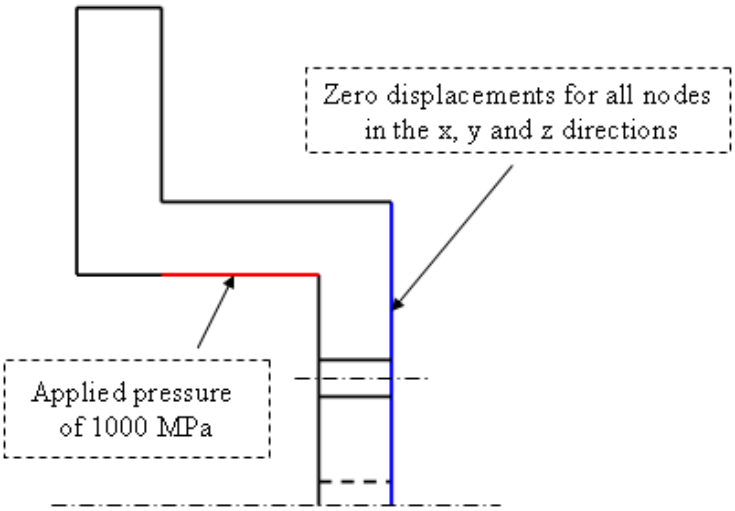

Figure 7.18: Loads and boundary conditions applied to the disk

Mesh A

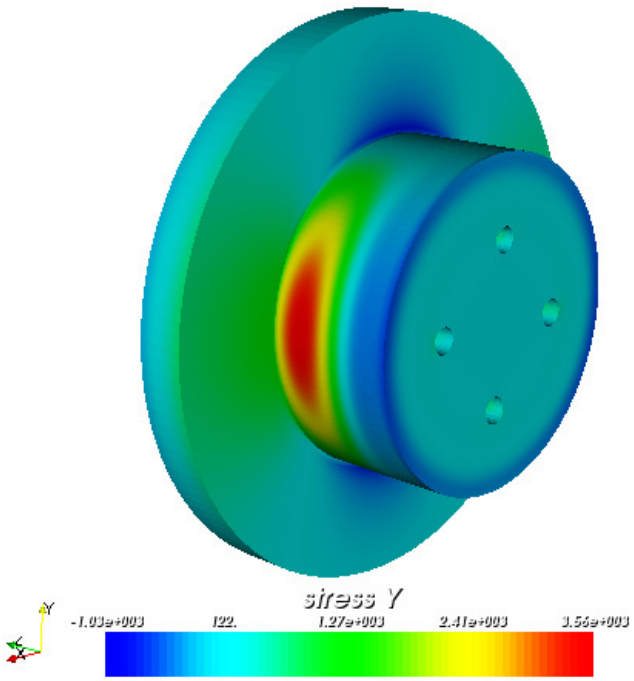

Figure 7.19: (a)

Mesh B

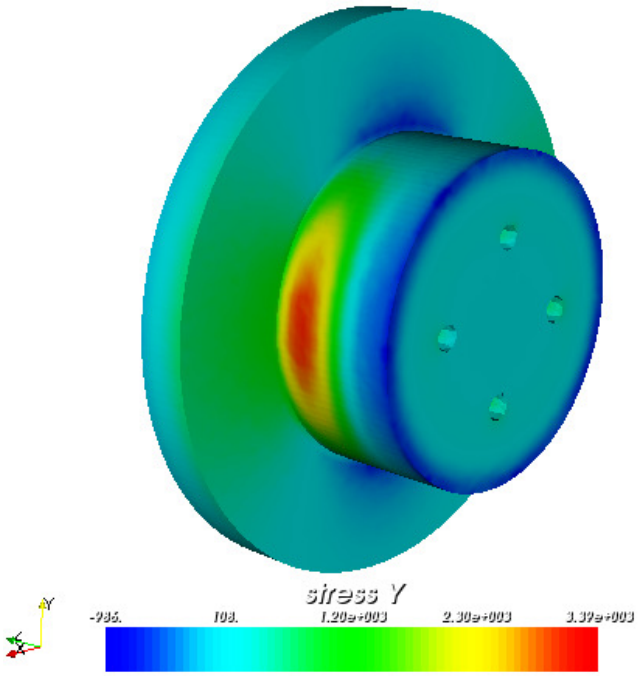

(b)

Mesh C

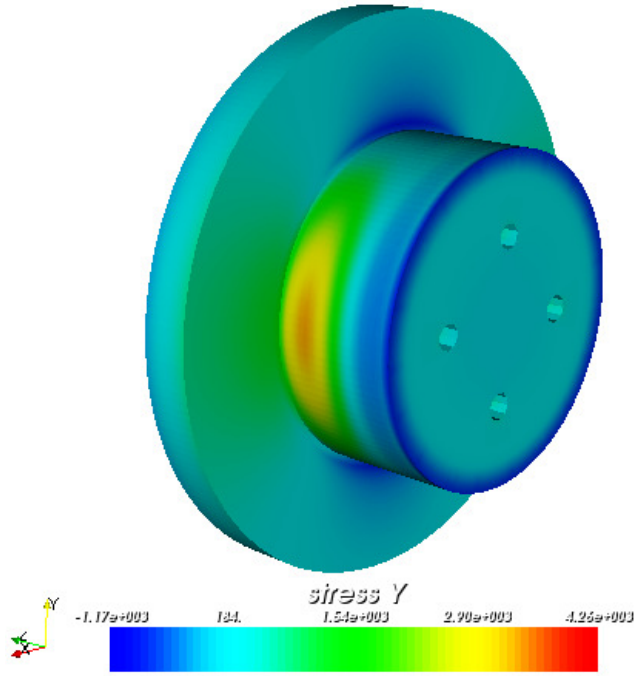

(c)

Figure 7.19: Stresses in the y direction obtained for the model from Figure 7.16: **(a)** results obtained by using Mesh A from Figure 7.17(a); **(b)** results obtained by using Mesh B from Figure 7.17(b); **(c)** results obtained by using Mesh C from Figure 7.17(c)

Variant 1

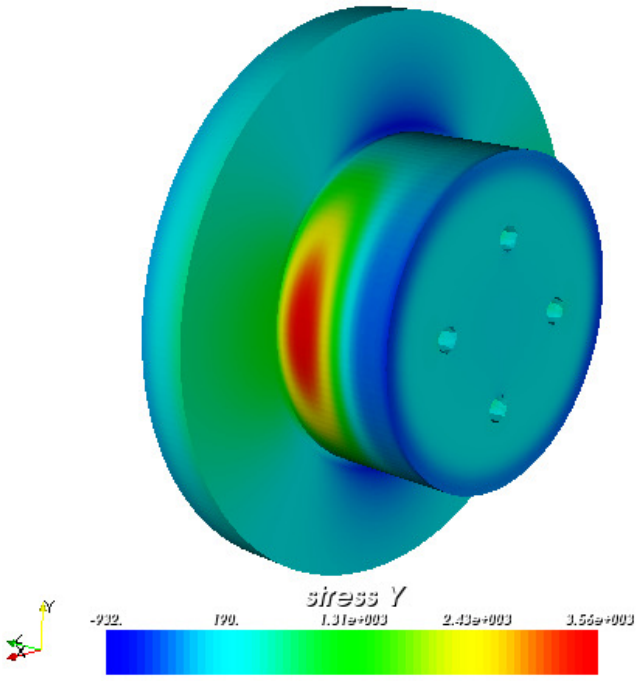

(a)

Variant 2

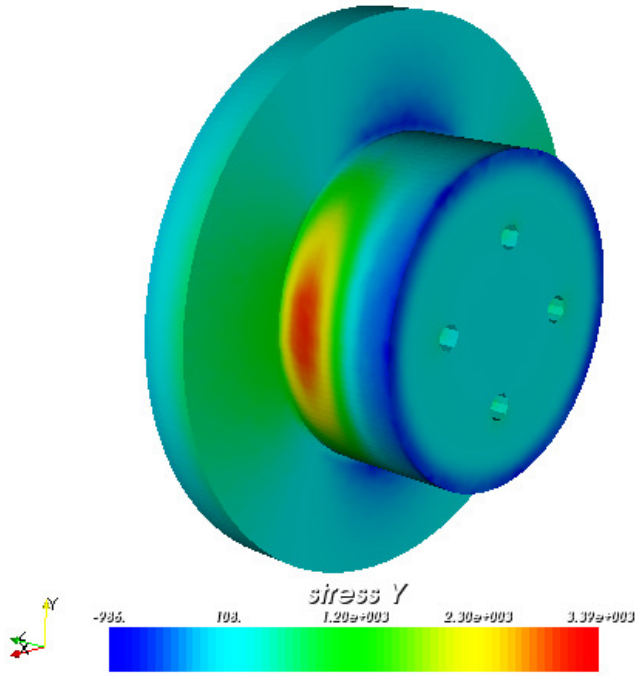

Figure 7.20: (b)

Variant 3

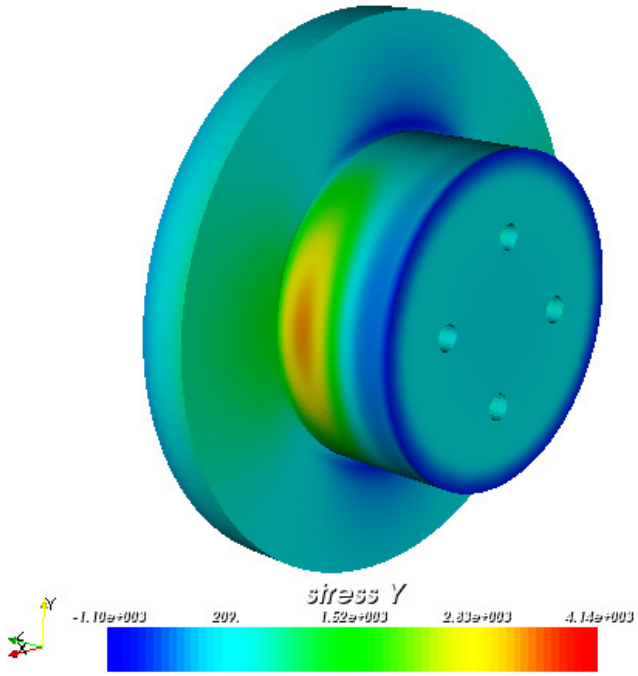

(c)

Figure 7.20: Mapped stresses in the y direction: **(a)** Variant 1 - mapped stresses in the y direction from the results from mesh A with hexahedron elements into mesh B with tetrahedron elements; **(b)** Variant 2 - mapped stresses in the y direction from the results from mesh B with tetrahedron elements into mesh C with wedge elements; **(c)** Variant 3 - mapped stresses in the y direction from the results from mesh C with wedge elements into mesh A with hexahedron elements

CHAPTER 8

SIMULATION OF MANUFACTURING CHAINS BY USING THE FINITE ELEMENT DATA EXCHANGE SYSTEM (FEDES)

FEDES is created in order to transfer FE data (stresses, strains, displacements, state variables, etc.) between different FE solvers. Six FE solvers are implemented in FEDES (ABAQUS, ANSYS, MARC, DEFORM, VULCAN and MORFEO). The four mapping techniques from Chapters 7 and the mapping technique from micro-to-macro FE models from Chapter 6 are incorporated in FEDES which allows the data transfer between meshes with different element types and densities. The design, structure and the capabilities of FEDES are described in detail. Results from the data transfer and mapping between different FE simulations are shown. Two manufacturing chain simulations are performed using FEDES. Manufacturing processes, such as casting, forging and heat treatment are used for the chain simulation of a simple model with parallelepiped geometry. The second manufacturing chain simulation is performed on an aero-engine vane component which includes the following manufacturing processes: metal deposition, welding, heat treatment, macro machining and shot-peening.

8.1 Introduction

As mentioned before, a number of FEPs have been developed for many engineering applications. Each FEP has its advantages in different fields which makes it the first option among the modellers and the analysts. Producing quality final products in the manufacturing requires involvement of many manufacturing processes. For simulating a chain of processes, many different FEPs can be used. The creation of residual stresses, plastic deformations, distortions, etc., after each simulated process requires data transfer among different FEPs for tracking the residual stresses and the

distortions after each process in the chain. This issue raises the need for creating a software code for transferring and mapping FE data among different FEPs.

8.2 FEDES design and structure

FEDES is created in Delphi [99-101]. Delphi is a set of object-oriented extensions to the standard Pascal language. Pascal is a high-level, compiled language that supports structured and object-oriented design. Its benefits include easy-to-read code, quick compilation, and the use of multiple unit files for modular programming. FEDES is created by using Delphi's Visual Component Library (VCL) for Windows platform applications. The main purpose of FEDES is to transfer data among different FEPs using meshes with different element types and densities. FEDES contains four basic modules (main, reading, writing and interpolation modules) linked together (see Figure 8.1). The main module contains Graphic User Interface (GUI) components from the Delphi's VCL. Subroutines from the reading, writing and interpolation modules are included in the main module. The reading module contains subroutines for reading the FE data from the input and the output files of the FEPs. The writing module contains subroutines for writing FE data in different output formats needed for transferring the data into the FEPs, visualization, storage and data transfer purposes. The interpolation module contains subroutines for performing the mapping between non-matching meshes and micro-to-macro models by using the interpolation techniques described in Chapters 6 and 7. Many other modules from VCL libraries are included, such as array manipulation modules, string manipulation modules, file manipulation modules, etc. Packed together, these modules form FEDES. FEDES requires very little Random Access Memory (RAM) and provides a very fast performance.

8.3 FEDES capabilities

FEDES can read and write FE data among ABAQUS, ANSYS, MARC, DEFORM, VULCAN and MORFEO and perform mapping between different meshes (see Figure 8.2). FEDES can output two neutral formats. XML structured format is used for storage and visualization purposes. This format can be visualized with the open

source code ParaView [102]. The second neutral format is created to link FEDES with external mapping tools. It is important to know that, when FEDES is used for data transfer and mapping, the FEPs need to output the displacements, stresses, strains, state variables, etc. at the nodal points in order to perform the mapping techniques from Chapter 7. When the mapping is performed by external mapping tool then the FEPs need to output the displacements at the nodal points and the stresses, strains, state variables, etc. at the integration points.

8.3.1 Main features

FEDES is organised in control tabs and menus, as shown in Figure 8.3. There is a menu bar on the top of the FEDES window. Control tabs are located beneath the menu bar and each control tab has GUI components assigned to it. There are six control tabs with the names ABAQUS, ANSYS, MARK, DEFORM, VULCAN and MORFEO. Each control tab contains GUI components connected to the subroutines from the different modules. A group of radio buttons allow selecting the FEP from which data can be read for model one and model two. A group of control panels allow amending the input and output files. A progress bar indicated the progress of the read data after pressing the button “Read data”. Depending on the contained data from the input and the output files for the corresponding FEPs, the user can choose which FE data to map from the section “Variables to be mapped”. An interpolation technique can be chosen from the group of radio buttons named “Interpolation technique” for interpolating the chosen FE data. A scale factor (SF) can be used in order to increase or decrease the value of the mapped data globally at all nodes, e.g. for changing units. Some FEPs offer more than one variant for importing the initial conditions. As an example, the stresses and the equivalent plastic strains can be imported in ABAQUS by using user defined subroutines or by including them into the input file. Therefore different file formats can be saved from the save buttons located at the bottom of the GUI form.

The data transfer module for creating, reading and linking the neutral format with the FEPs can be selected from menu Tools→Data Transfer. Figure 8.4 shows the screen-shot of the data transfer module.

8.3.2 FEPs formats

The formats for the FEPs were obtained from the industrial partners of the VERDI EU Consortium. VERDI is a research project within the European sixth framework program where six major aero engine and component manufacturers, together with six universities and three research institutes have joined their expertise and resources to reach beyond the current state-of-the-art in manufacturing process simulation.

A simple beam benchmark was performed within the project for obtaining the formats for the corresponding FEP. The geometry of the beam benchmark is shown in Figure 8.5 where the width W = 5 mm, the height H = 5 mm and the length L = 20 mm. The coordinate system is fixed at point A(0,0,0) and the geometry is located in Quadrant I (+x,+y,+z). The mesh is generated by defining the element type and density by the VERDI partners. Elastic material properties are used, module of elasticity E = 200 GPa and Poisson's ratio $\nu = 0.3$. Figure 8.6 shows the boundary and the loading conditions applied to the beam model. The distance d = 5 mm. All nodes on surface S_1 are constrained in x, y and z directions. A distributed load (pressure) of +1000 MPa is applied on surface S_2. Apart from the output formats, the VERDI partners provided information about how the displacements, stresses, strains, state variables, etc. are imported into the corresponding FEP. Based on this information, the FEDES was developed. Tables 8.1-8.4 show the current capabilities of reading and importing FE data from and to the FEPs. Full documentation for the formats and how to use FEDES can be found in the FEDES User's Manual [103] which is embedded in FEDES as a help module (see Figure 8.7).

8.3.3 Error handling

Figure 8.8 shows the error report module in FEDES. The first line shows the selected interpolation technique and the mapping performed between the two models calculated in the corresponding FEPs. Three error calculations (minimum, maximum and average) for the direct stresses (S_1, S_{22} and S_{33}) and the Von Misses stresses are implemented in the error report module. The three error calculations can be given by:

- Minimum error

$$error_{\min} = \frac{\left|\sigma_{\min 2} - \sigma_{\min 1}\right|}{\sigma_{\min 2}} 100 \ (\%) \tag{8.1}$$

where $\sigma_{\min 2}$ is the minimum stress value in model 2 and $\sigma_{\min 1}$ is the minimum stress value in model 1

- Maximum error

$$error_{\max} = \frac{\left|\sigma_{\max 2} - \sigma_{\max 1}\right|}{\sigma_{\max 2}} 100 \ [\%] \tag{8.2}$$

- Average error

$$error_{average} = \frac{\left|\sigma_{average2} - \sigma_{average1}\right|}{\sigma_{average2}} 100 \ [\%] \tag{8.3}$$

$$\sigma_{average} = \frac{\sum_{i=1}^{N} \sigma_i}{N} \tag{8.4}$$

where $\sigma_{average2}$ is the average stress value in model 2, $\sigma_{average1}$ is the average stress value in model 1, σ is the stress value and N is the number of the nodes.

Equations (8.1-8.3) are applicable when the mapping is performed to the nodal FE data, such as displacements and temperature. The element data (stresses, strains, state variables, etc.) are mapped at the integration points. An additional error can be introduced due to extrapolating the element data from the integration points to the nodal. Figure 8.9 show two meshes, mesh with one element (Mesh 2) and mesh with 25 elements (Mesh 1). Assuming that mesh 1 is populated with data at the nodal points and data needs to be mapped to mesh 2 at the integration point I_1. The mapping techniques in FEDES will determine that the integration point I_1 belongs to the relevant element from mesh 1 and will perform the interpolation. After mapping the data to the integration point I_1, the corresponding solver will extrapolate these data to the nodal points and the error in such cases is the summation of the mapping error and the extrapolation error. FEDES allows another option for performing the mapping. Instead of locating the position of the integration point I_1, first the mapping is performed to the nodal points N_1,N_2,N_3 and N_4 and then a second

mapping is perform in order to obtain data for the integration point I_1 from nodes N_{1-4} by using some of the interpolation techniques from Chapter 7.

8.4 Manufacturing chain simulation of parallelepiped

The main goal in this section is to demonstrate the simulation of a manufacturing chain. Three manufacturing processes (casting, forging and heat treatment) are used in this manufacturing chain. The parallelepiped geometry from Chapter 3 with Inconel 718 material properties is used for performing the chain simulation. Figure 8.10 shows the sequence of the chain simulation. All processes (casting, forging and heat treatment) are simulated in ABAQUS, but as explained, they can be simulated in any of the FEPs supported by FEDES.

8.4.1 Casting simulation

The results from the parallelepiped casting simulation from Chapter 3 are used. The model is run and the nodal displacements, stresses and equivalent plastic strains are output in an ASCII file format where FEDES is used to read these data and pass them to the next process in the chain by using the data transfer and mapping capabilities of FEDES. The deformed shape, mesh, residual Von Mises stresses and the equivalent strains can be seen in Figure 8.11.

8.4.2 Forging simulation

The displacements, stresses and the equivalent plastic strains from the casting model are mapped and transferred by FEDES into the forging model as initial conditions, as shown in Figure 8.12. The mapping is performed from hexahedron to hexahedron elements where the forging mesh is more refined than the casting mesh. The forging is performed in two steps, as explained in Chapter 3. Dynamic analysis is performed where a punch with sphere geometry is moved into the billet with parallelepiped geometry to depth of 2 mm. The second step is performed in a static analysis and the final shape, residual Von Misses and the equivalent plastic strains are obtained, as shown in Figure 8.13.

8.4.3 Heat treatment simulation

The heat treatment is simulated in three steps. Increasing the temperature to 800 ºC (furnace ambient temperature), holding it for 3 hours and cooling down to room temperature. The deformed shape, residual Von Mises stresses and the equivalent plastic strains from the forging model are mapped to the heat treatment model by using FEDES as initial conditions, as shown in Figure 8.14. The mapping is performed form hexahedron to wedge elements. The first step when the temperature is increased to 800 ºC is performed in two analyses. Thermal analysis is performed in order to obtain the temperature history for the model. The model is put in a furnace with 800 ºC. The initial temperature of the model is 20 ºC and it is heated up to 800 ºC by applying a radiation to all surfaces of the model. A mechanical analysis by taking the temperature history from the thermal analysis is performed. The deformed shape, residual Von Mises stresses and the equivalent plastic strains after this step are shown in Figure 8.15. Creep is applied during the holding step where the stress relieving is observed. The Norton creep law for the secondary creep is applied.

$$\dot{\varepsilon} = \frac{d\varepsilon}{dt} = A\sigma^n \tag{8.5}$$

The following constants are used: $n = 10.82459$ and $A = 4.330103 \times 10^{-95}$ (stresses in Pa and time in hours)

The deformed shape, residual Von Mises and the equivalent plastic strains after this step are shown in Figure 8.16. Coupled temperature-displacement analysis is performed during the cooling processes from 800 ºC to room temperature. The cooling is achieved by convection of 10 W/m^{2}ºC applied to all surfaces of the model. Due to different element types in ABAQUS, the results from the creep analysis could not be imported into the coupled temperature-displacement analysis within ABAQUS. Therefore FEDES is used to transfer the deformed shape, residual stresses and the equivalent plastic strain from the creep analysis to the coupled temperature-displacement analysis. The deformed shape, residual Von Mises and the equivalent plastic strains after this step are shown in Figure 8.17.

8.5 Manufacturing chain simulation of an aero-engine vane

This section shows a simulation of a manufacturing chain of an aero-engine vane performed within the VERDI project. Five manufacturing chains are included in the chain. First, metal deposition is performed followed by welding, heat treatment, macro machining and shot-peening. The same geometry is used for all processes except for the shot-peening where the machined material is removed. Figure 8.18 shows the five different meshes used in each process, the total displacements and the Von Misses stresses from all simulations. Tetrahedron elements are used for the meshes of all processes except the machining where mixture of wedge and tetrahedron elements are used. The metal deposition simulation is performed in VULCAN, the welding in ANSYS, the heat treatment in ABAQUS, the machining in ANSYS and the shot-peening in ABAQUS. The stresses and the displacements from the machining and the stresses from the shot-peening are mapped to a mesh which is used for predicting the fatigue life in ANSYS. The shot-peening process is simulated on a simple micro scale geometry and the stresses are mapped to the model by using the micro to macro mapping techniques from Chapter 6.

8.6 Conclusions

FEDES was developed and its structure and capabilities has been described. FEDES has been used to simulate two chains of manufacturing processes. Three manufacturing processes (casting, forging and heat treatment) have been simulated in the first chain where FEDES has been used for FE data mapping and transferring between different FE meshes. The deformed shape, residual stresses and the equivalent plastic strains have been transferred and mapped between the models. Five manufacturing processes (metal deposition, welding, heat treatment, machining and shot-peening) have been simulated in the second chain in different FE codes and different meshes. The simulations have been performed on aero-engine vane component in order to demonstrate the applicability of FEDES to an industrial manufacturing simulation.

Table 8.1: FEDES capabilities to read FE data from FEPs when the displacements are output at the nodal points and the stresses, total strains, plastic strains, equivalent plastic strains and the state variables are output at the integration points and the external mapping tool is used with the neutral file

FEP	Node Coordinates	Element Connectivity	Displacements	Stresses	Total Strains	Plastic Strains	Equivalent Plastic Strains	State Variables
ABAQUS	Yes	Yes	Yes	Yes	Yes	Yes	Yes	-
ANSYS	Yes	Yes	Yes	Yes	Yes	-	-	-
DEFORM	Yes	Yes	Yes	Yes	Yes	-	Yes	-
MARC	Yes	Yes	Yes	Yes	-	-	Yes	Yes
MORFEO	Yes	Yes	Yes	Yes	Yes	-	Yes	-
VULCAN	Yes	Yes	Yes	Yes	Yes	-	-	-

Table 8.2: FEDES capabilities of importing FE data as initial conditions to FEPs when the displacements are output at the nodal points and the stresses, total strains, plastic strains, equivalent plastic strains and the state variables are output at the integration points

FEP	Displacements	Stresses	Total Strains	Plastic Strains	Equivalent Plastic Strains	State Variables
ABAQUS	Yes	Yes	-	Yes	Yes	-
ANSYS	Yes	Yes	-	-	-	-
DEFORM	Yes	Yes	-	-	Yes	-
MARC	Yes	Yes	-	-	Yes	Yes
MORFEO	Yes	Yes	-	-	Yes	-
VULCAN	-	-	-	-	-	-

Table 8.3: FEDES capabilities to read FE data from FEPs when the displacements, stresses, total strains, plastic strains, equivalent plastic strains and the state variables are output at the nodal points and the mapping techniques from Chapter 7 are used

FEP	Node Coordinates	Element Connectivity	Displacements	Stresses	Total Strains	Plastic Strains	Equivalent Plastic Strains	State Variables
ABAQUS	Yes	Yes	Yes	Yes	Yes	Yes	Yes	-
ANSYS	Yes	Yes	Yes	Yes	Yes	-	-	-
DEFORM	Yes	Yes	Yes	Yes	Yes	-	Yes	-
MARC	Yes	Yes	Yes	Yes	-	-	-	-
MORFEO	Yes	Yes	Yes	Yes	Yes	-	Yes	-
VULCAN	Yes	Yes	Yes	Yes	Yes	-	-	-

Table 8.4: FEDES capabilities of importing FE data as initial conditions to FEPs when the displacements, stresses, total strains, plastic strains, equivalent plastic strains and the state variables are output at the nodal points and the mapping techniques from Chapter 7 are used

FEP	Displacements	Stresses	Total Strains	Plastic Strains	Equivalent Plastic Strains	State Variables
ABAQUS	Yes	Yes	-	Yes	Yes	-
ANSYS	Yes	Yes	-	-	-	-
DEFORM	Yes	Yes	-	-	Yes	-
MARC	Yes	Yes	-	-	-	-
MORFEO	Yes	Yes	-	-	Yes	-
VULCAN	-	-	-	-	-	-

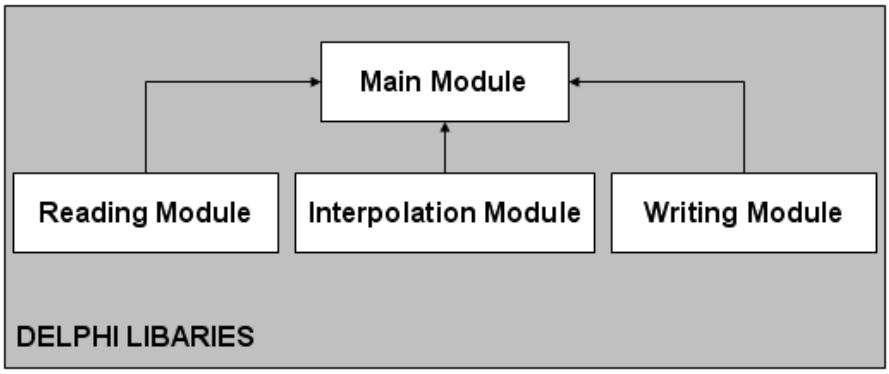

Figure 8.1: FEDES design structure

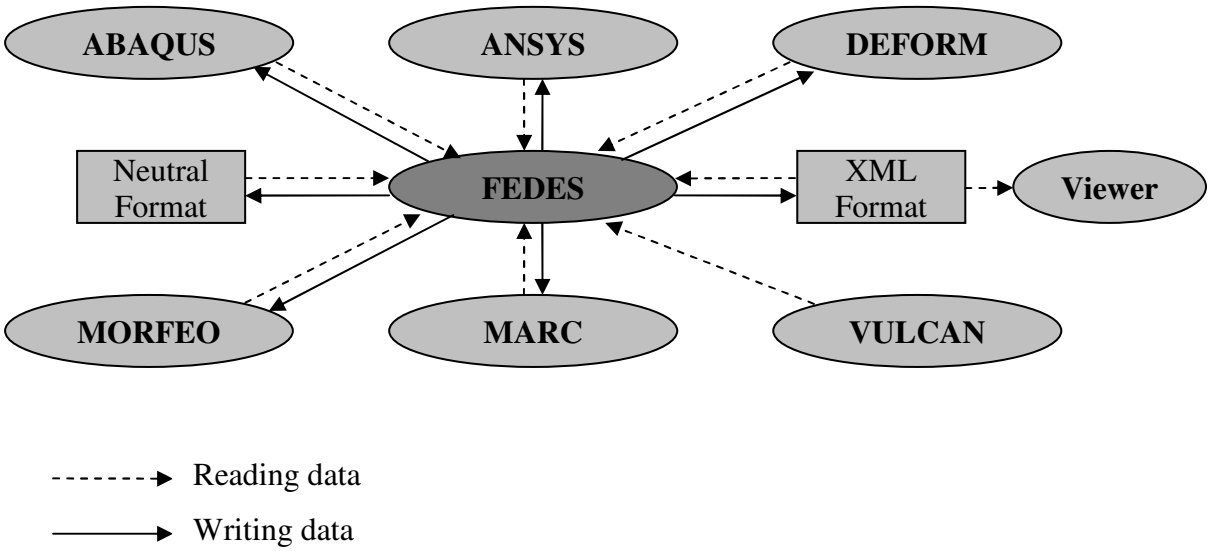

Figure 8.2: FEDES data transfer capabilities

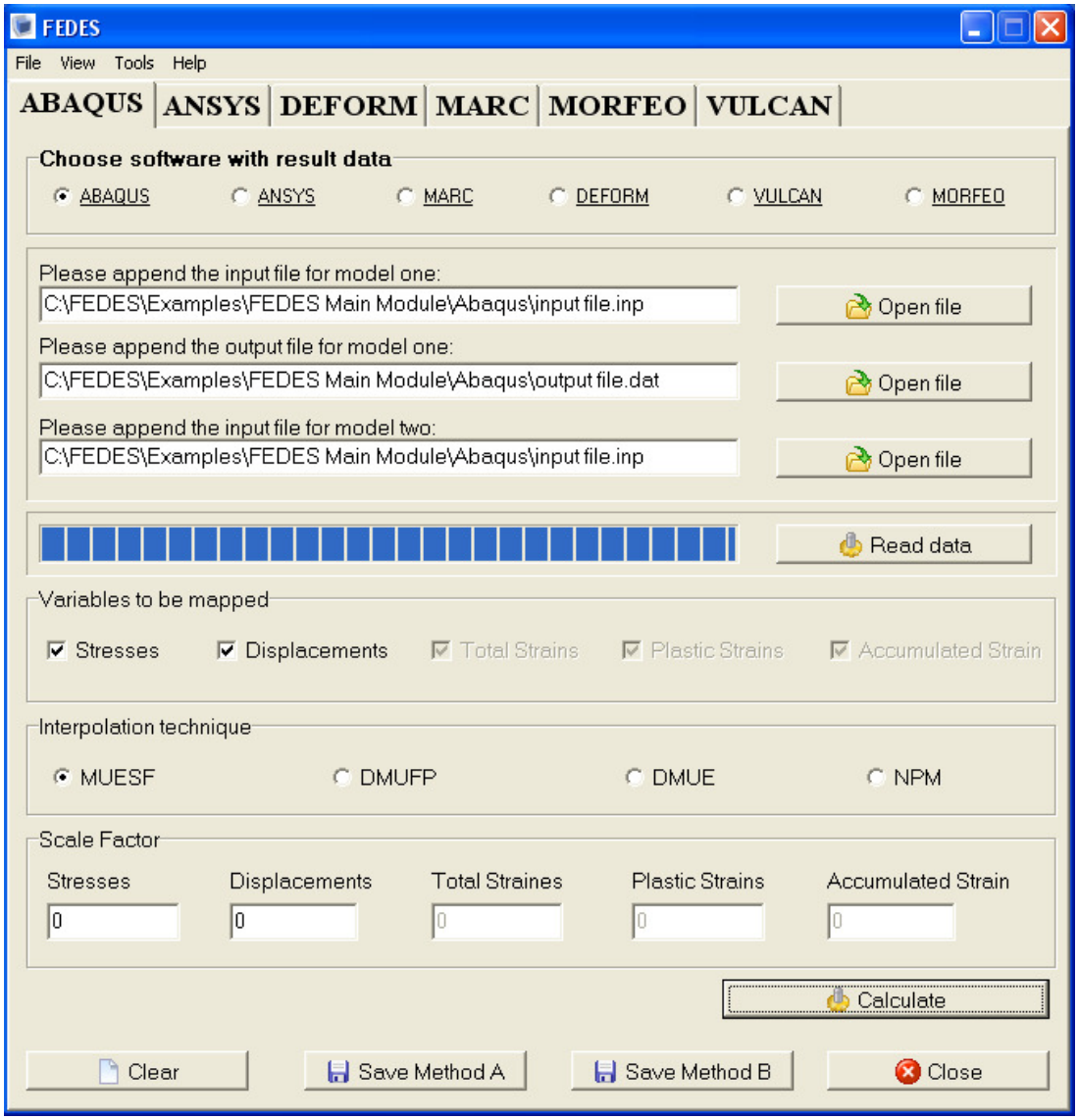

Figure 8.3: FEDES's Graphic User Interface

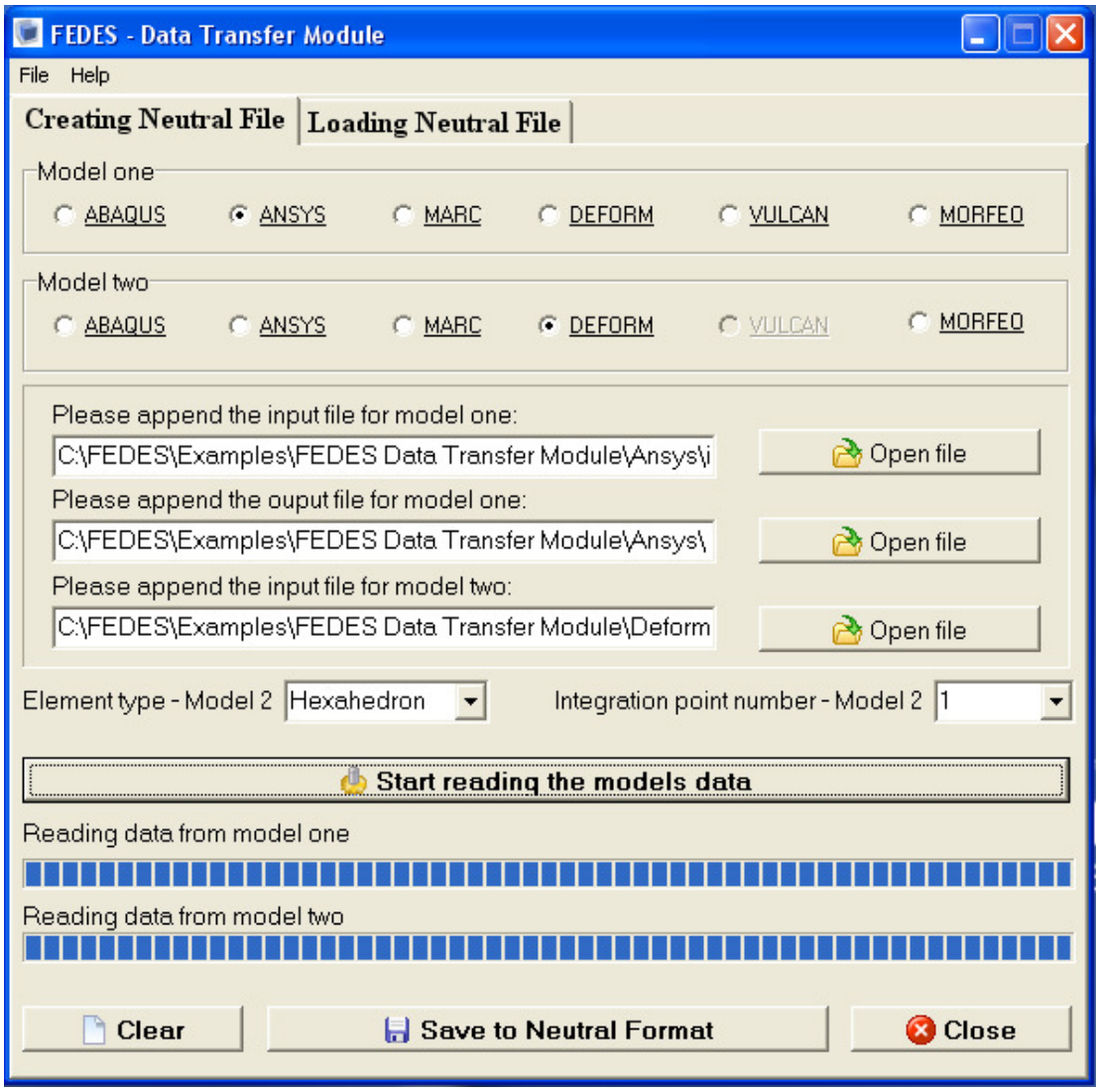

Figure 8.4: GUI of the data transfer module used for creating, reading and linking the neutral files with FEPs

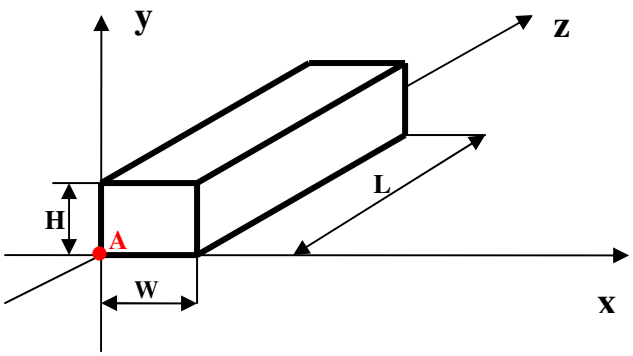

Figure 8.5: Geometry of the beam benchmark

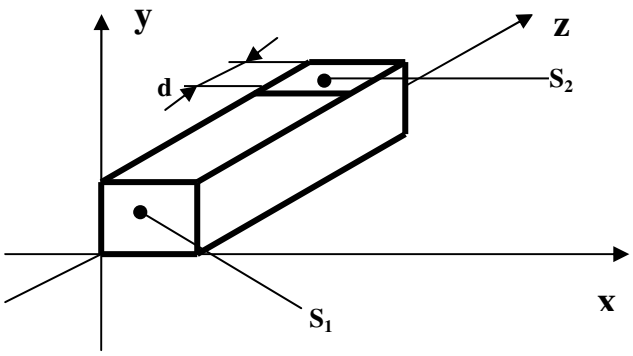

Figure 8.6: Beam boundary conditions and loading. Zero displacements applied to all nodes of surface S_1 in the x, y and z directions. Applied pressure of 1000 MPa on surface S_2

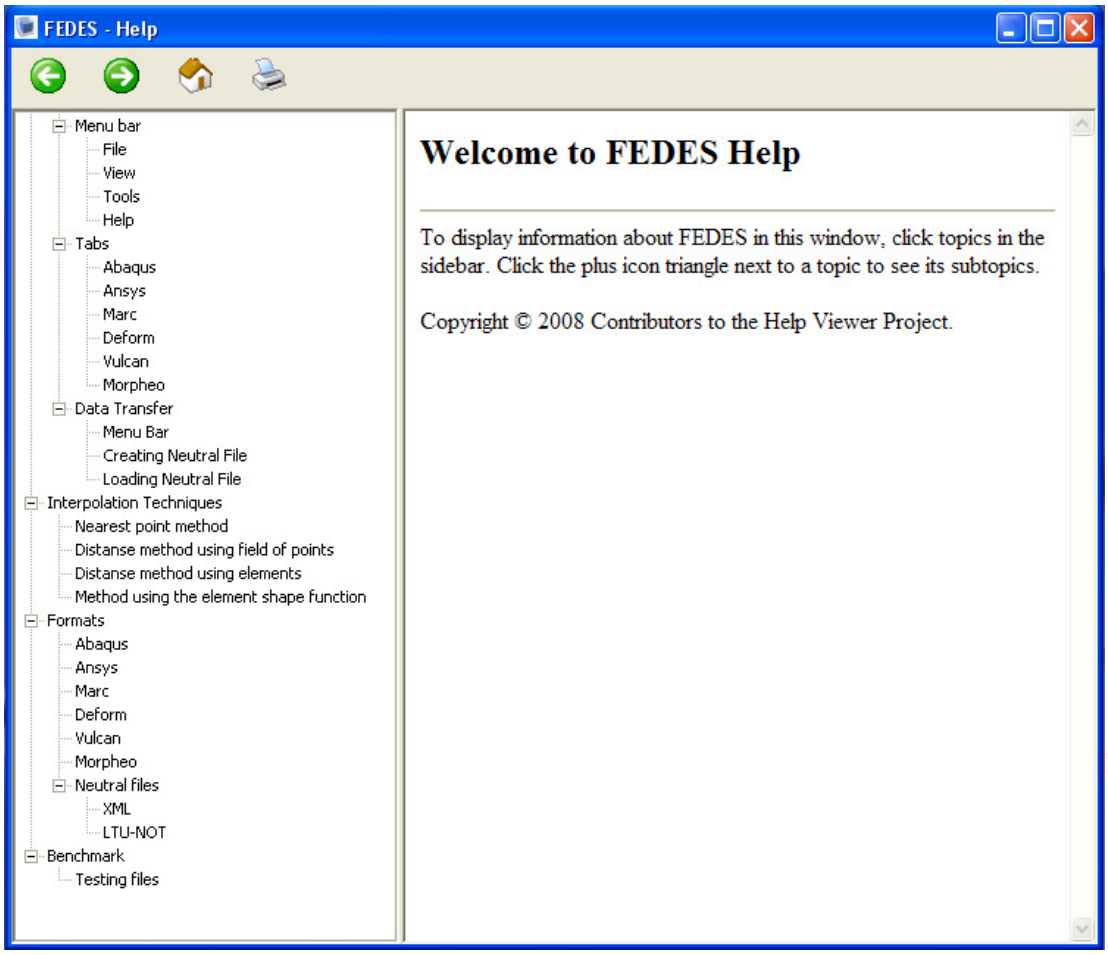

Figure 8.7: GUI of the FEDES help manual

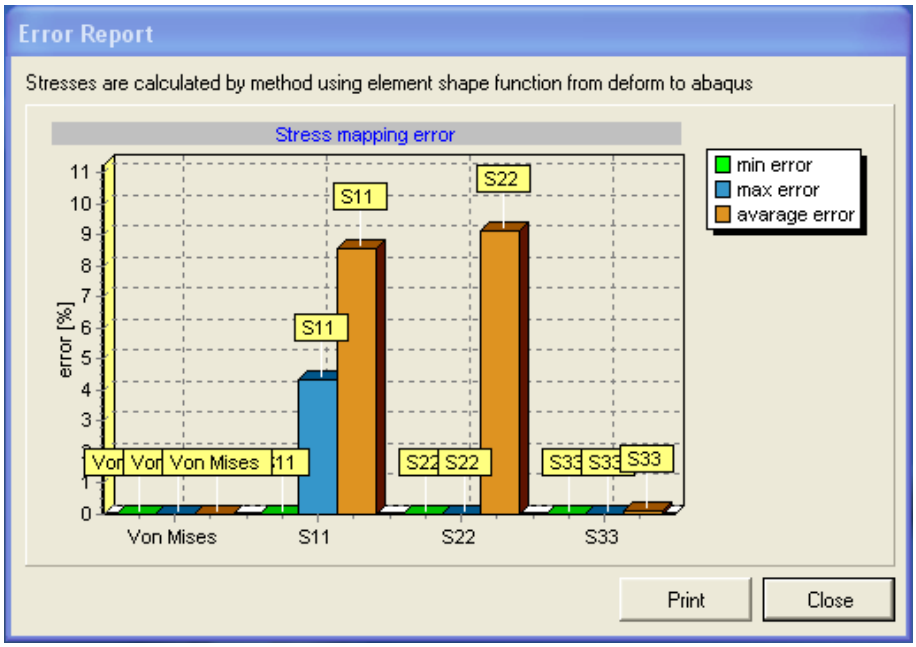

Figure 8.8: GUI of the FEDES error report module

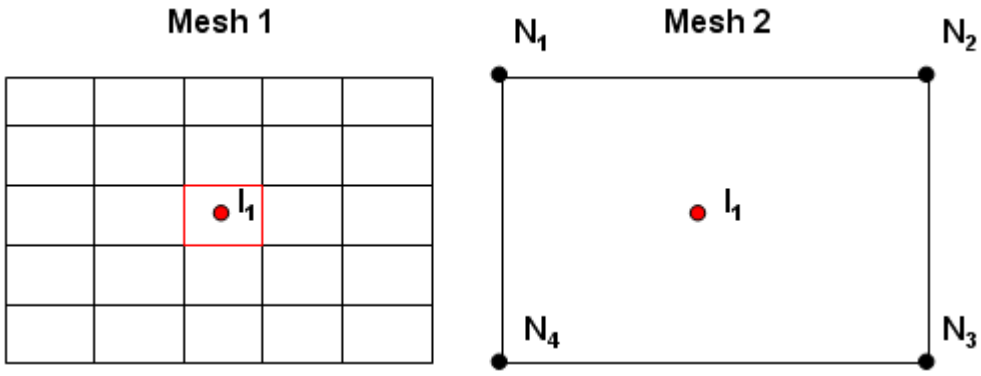

Figure 8.9: Two incompatible meshes. Mesh 1 has 25 elements while mesh 2 has 1 element with one integration point I_1

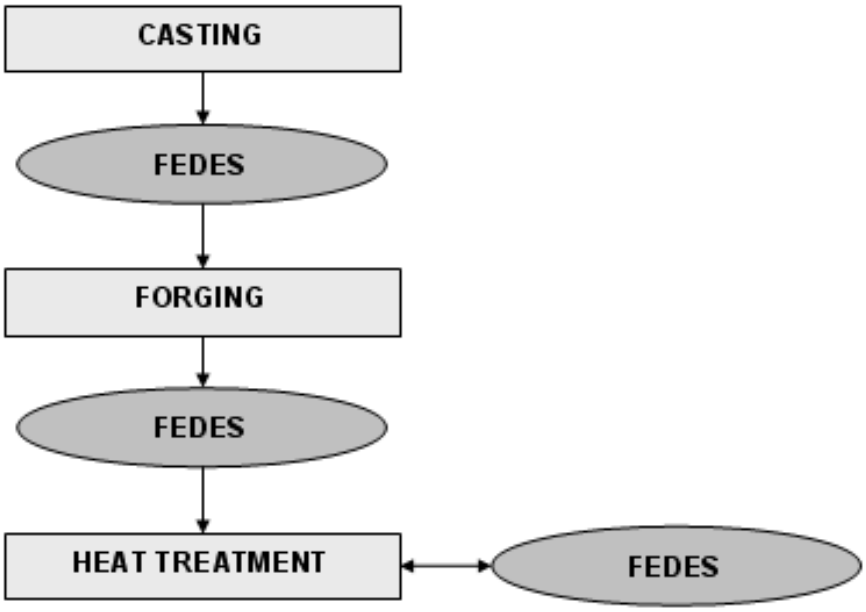

Figure 8.10: Sequence of manufacturing chain simulation of parallelepiped

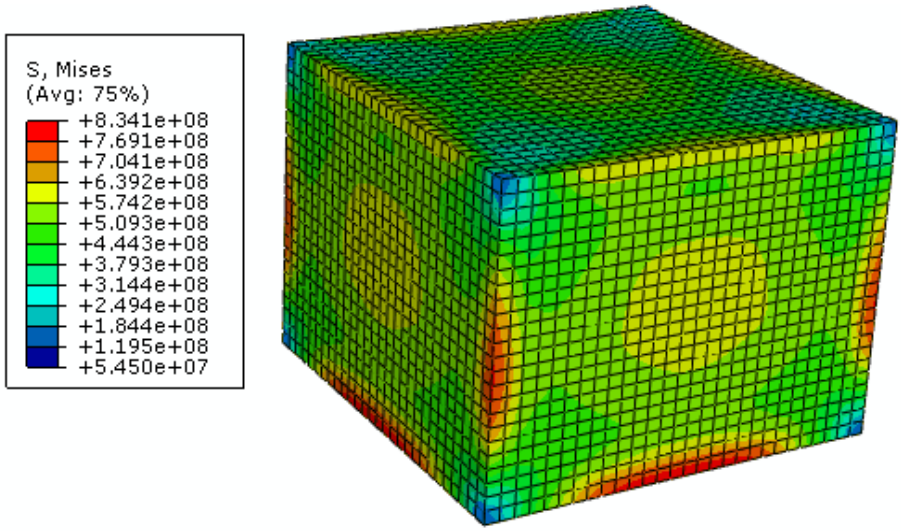

(a)

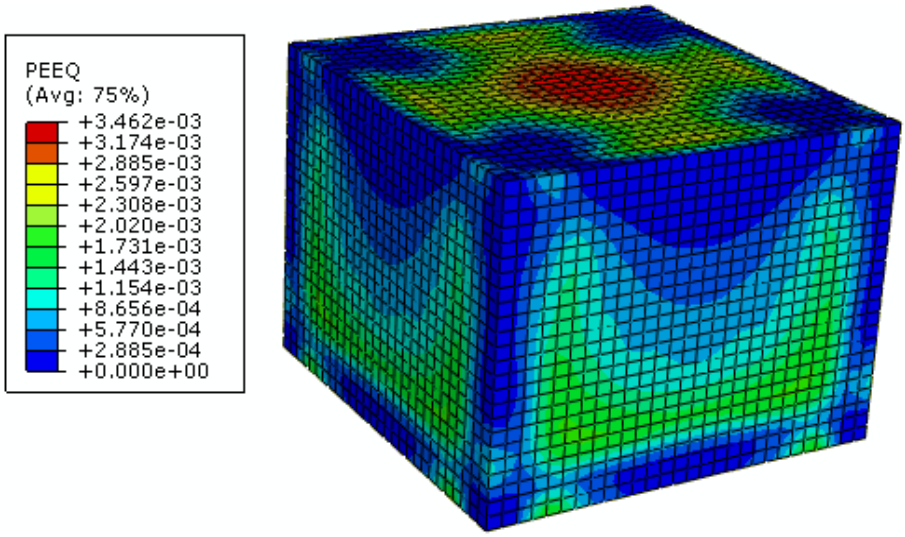

(b)

Figure 8.11: FE results obtained from the casting simulation from Chapter 3: **(a)** residual Von Mises stresses; **(b)** equivalent plastic strains

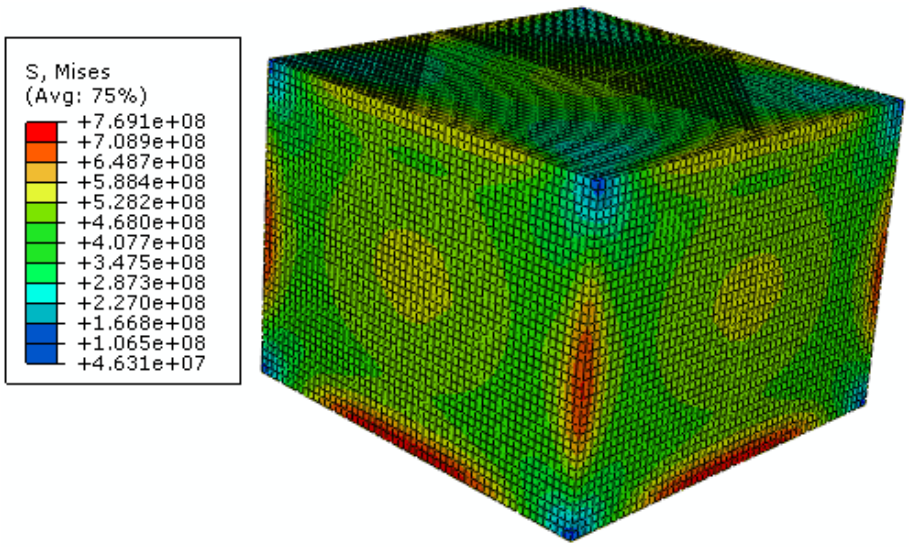

(a)

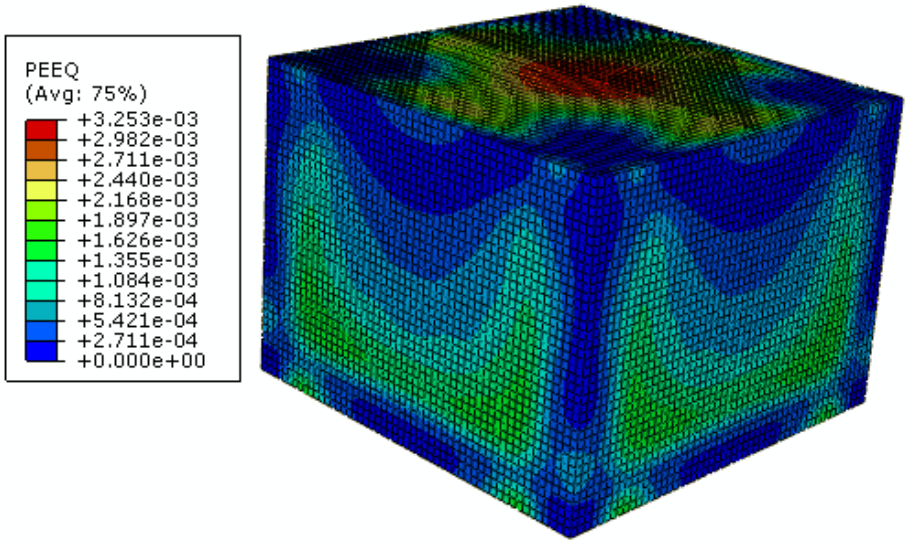

(b)

Figure 8.12: Mapped FE results from the casting into the forging model as an initial condition: **(a)** residual Von Mises stresses; **(b)** equivalent plastic strains

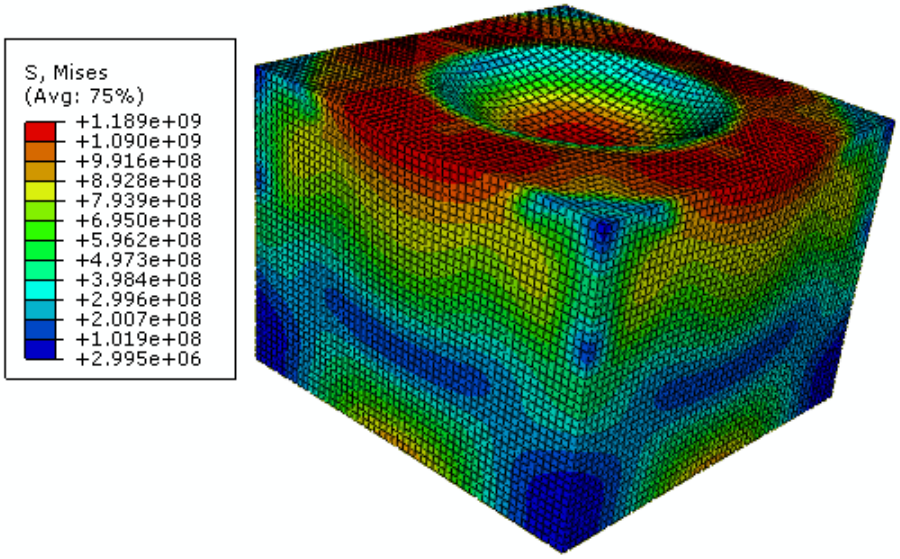

(a)

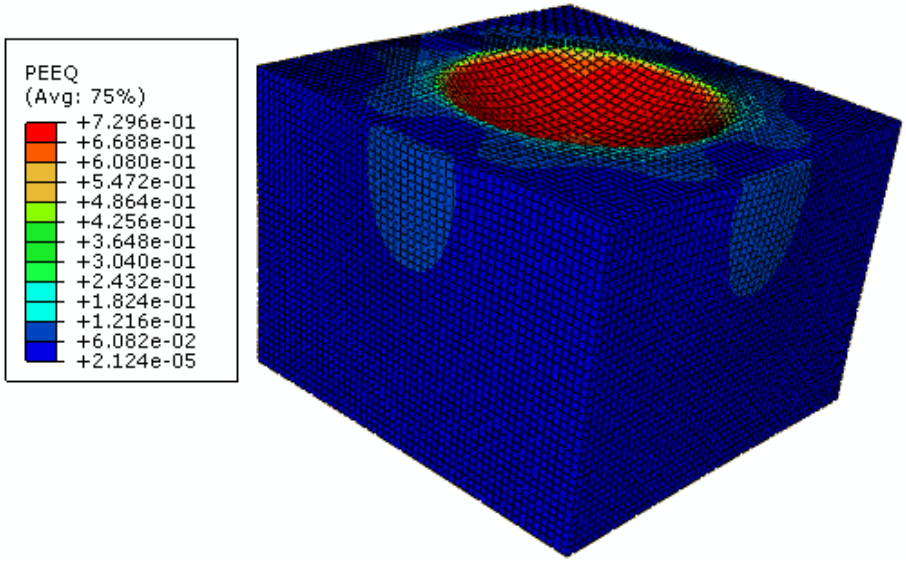

(b)

Figure 8.13: FE results obtained from the forging simulation: **(a)** residual Von Mises stresses; **(b)** equivalent plastic strains

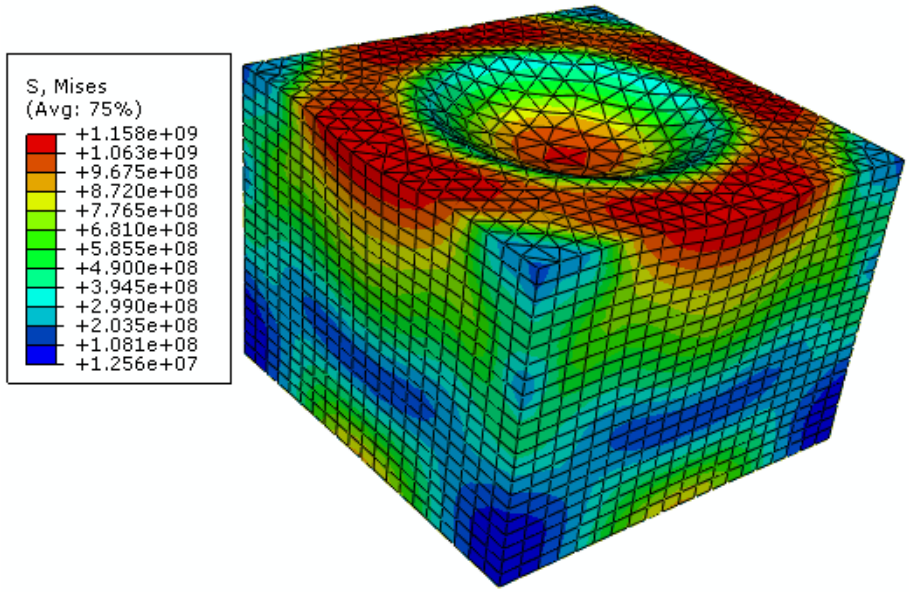

(a)

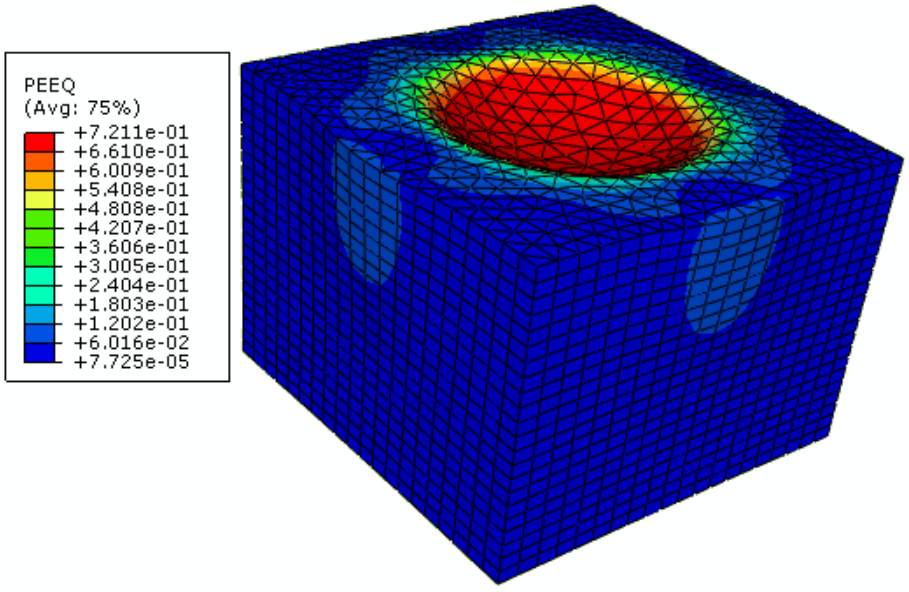

(b)

Figure 8.14: Mapped FE results from the forging into the heat treatment model as an initial condition: **(a)** residual Von Mises stresses; **(b)** equivalent plastic strains

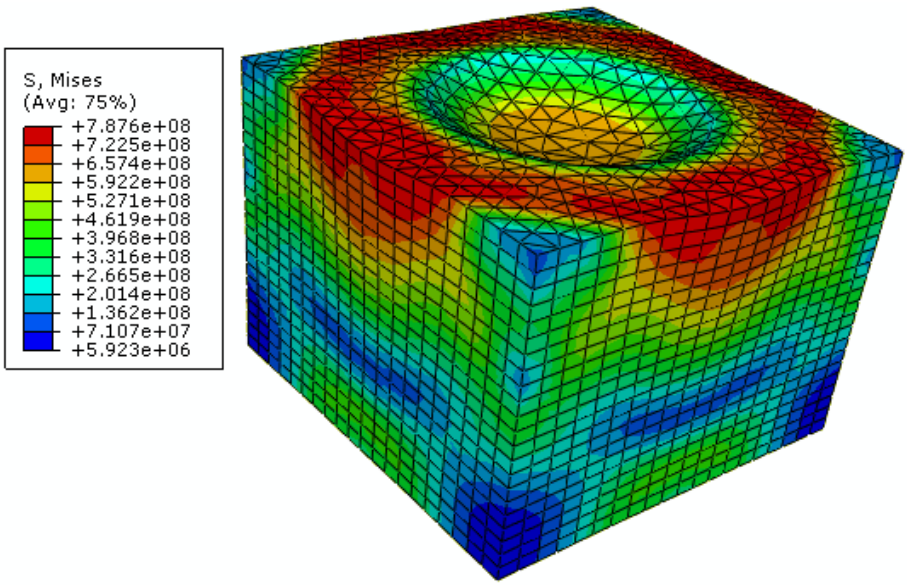

(a)

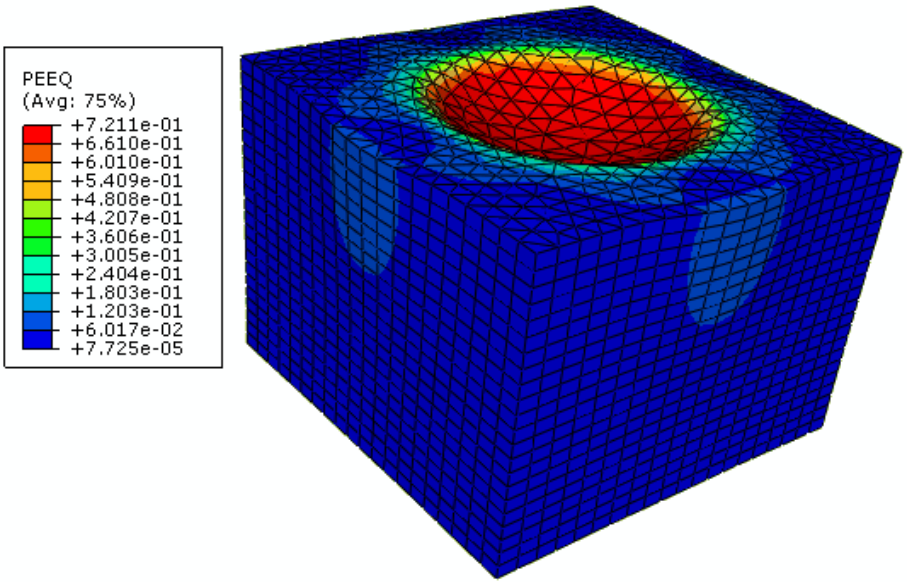

(b)

Figure 8.15: FE results obtained from the first step of the heat treatment simulation when the model is heated up to 800ºC: **(a)** residual Von Mises stresses; **(b)** equivalent plastic strains

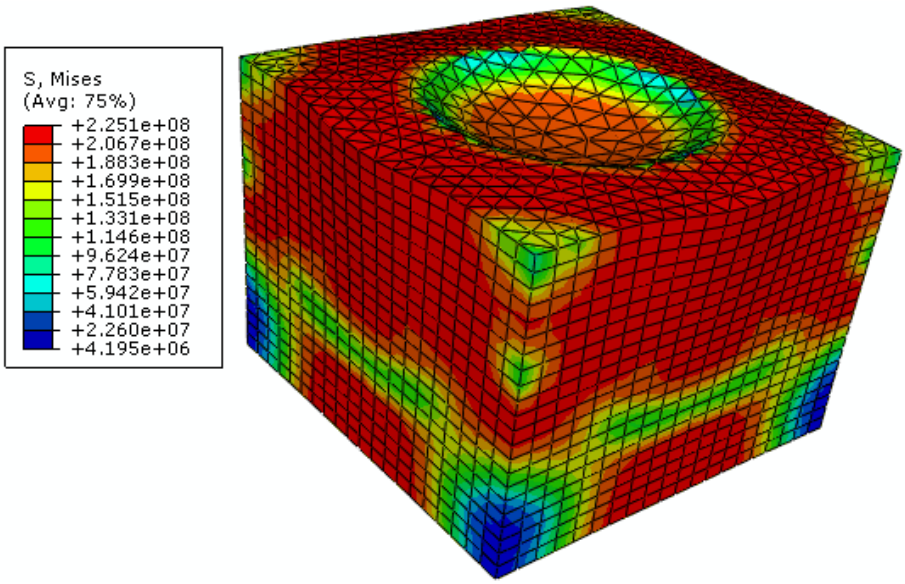

(a)

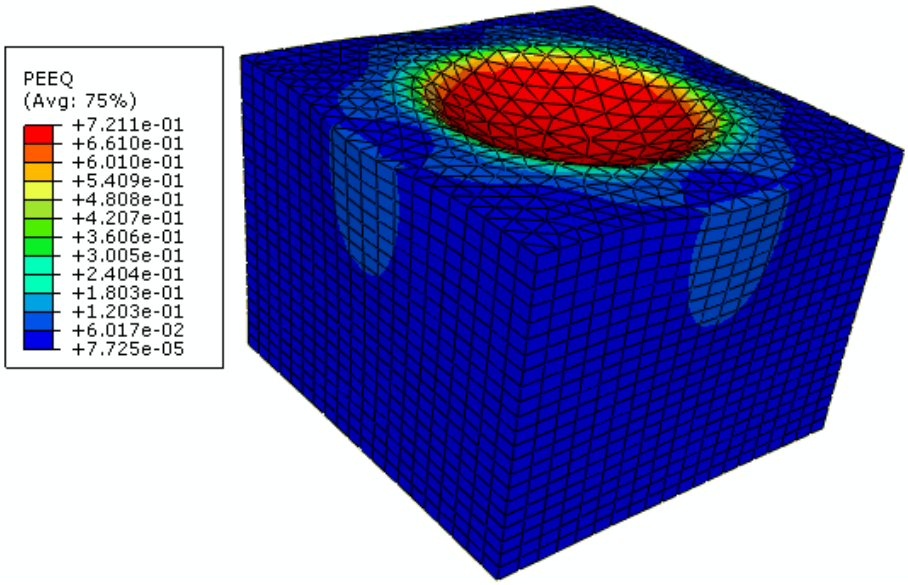

(b)

Figure 8.16: FE results obtained from the second step of the heat treatment simulation when the model is held to 800ºC and creep analysis is performed: **(a)** residual Von Mises stresses; **(b)** equivalent plastic strains

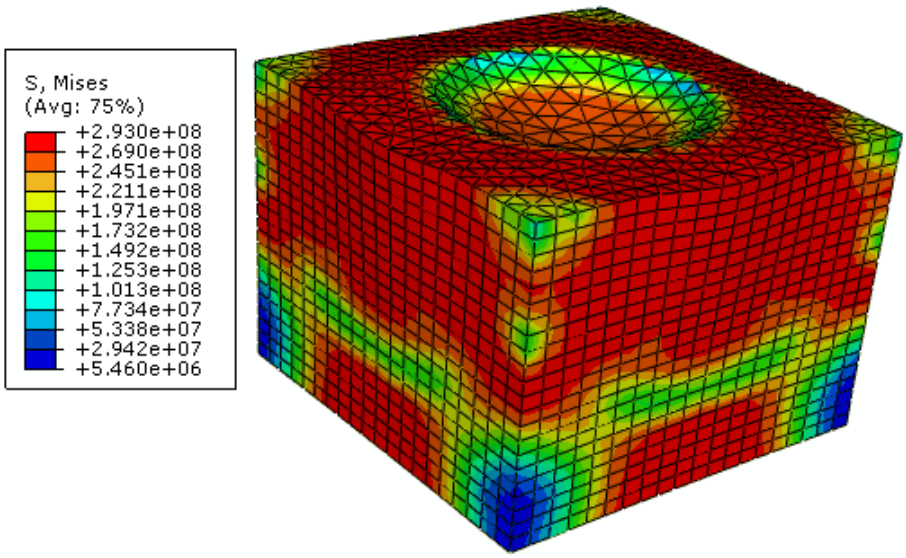

(a)

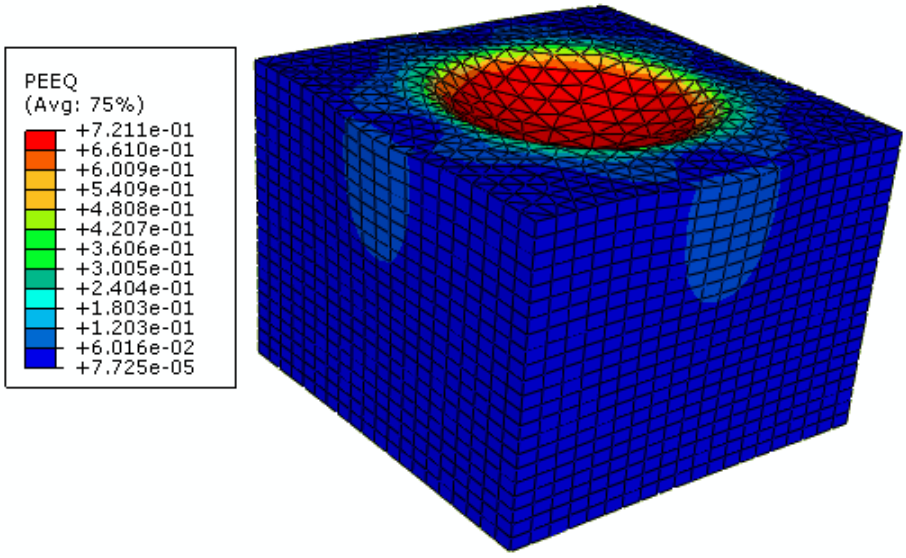

(b)

Figure 8.17: FE results obtained from the first step of the heat treatment simulation when the model is cooled down from 800ºC to room temperature: **(a)** residual Von Mises stresses; **(b)** equivalent plastic strains

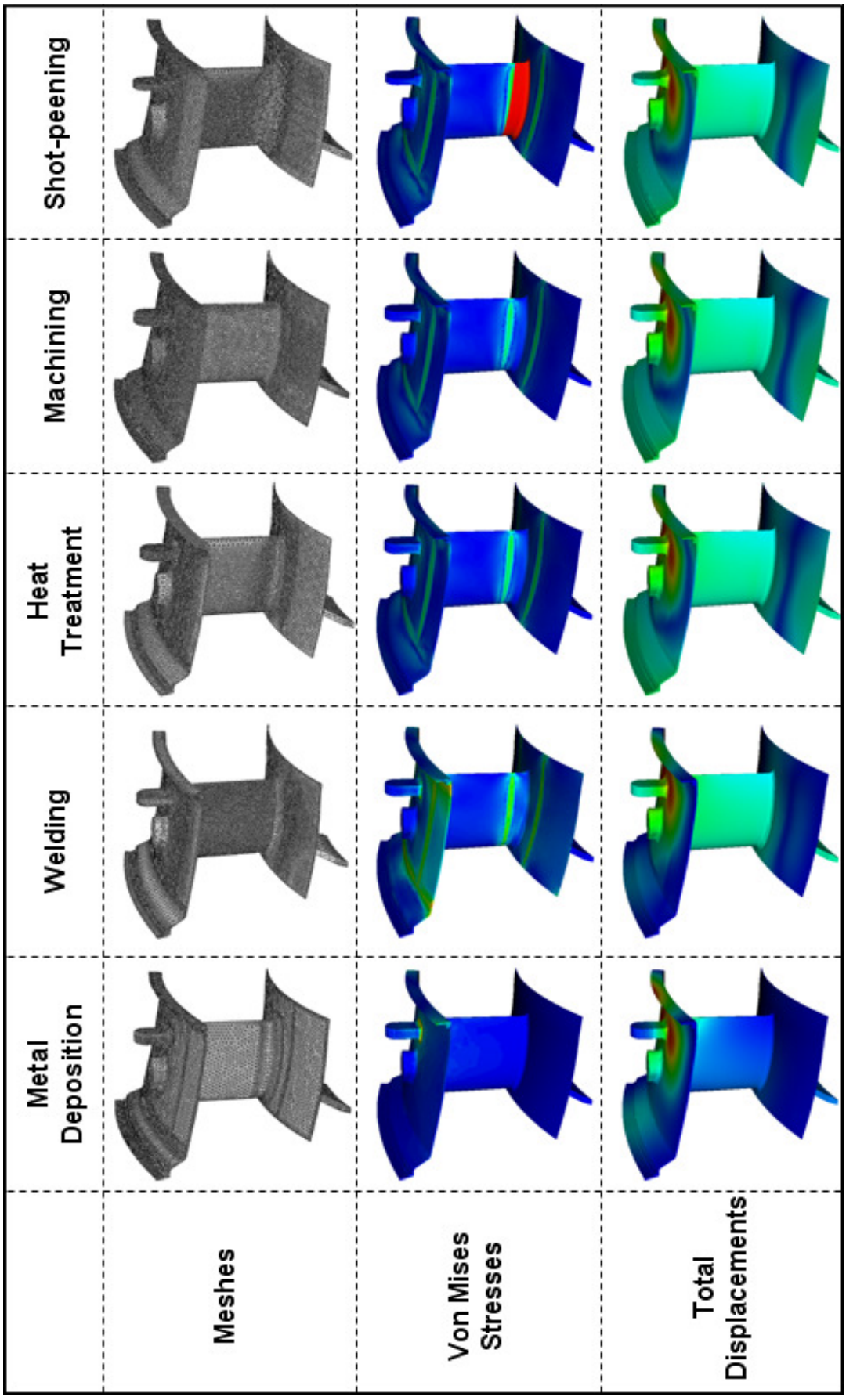

Figure 8.18: Simulation of manufacturing chain of an aero-engine vane component

CHAPTER 9

EFFECT OF MICRO STRESSES FROM MACHINING AND SHOT-PEENING PROCESSES ON THE COMPONENT FATIGUE LIFE

This chapter investigates the effect of the micro machining and the shot-peening residual stresses on the fatigue life. A broached specimen under three point bending is modelled as a 2D plane stress model by using the FEM. Inconel 718 mechanical and fatigue material properties at 600 ºC are used. Micro machining and shot-peening residual stresses are mapped around the notched area of the model and their influence on the fatigue life experiencing high cycle fatigue (HCF) and the low cycle fatigue (LCF) is investigated. It has been observed that the shot-peening significantly increases the life at HCF compared to the LCF.

9.1 Introduction

Mechanical failures have caused many injuries and much financial loss. The material fatigue is one of the phenomena which causes failure of the materials. For producing a final component in industry, many manufacturing processes are involved where each manufacturing process can affect the life of the component.

Depending on the loading conditions, components can exhibit either HCF or LCF. The HCF is characterised mainly with elastic deformations while at LCF large plastic deformations are observed. A range of experimental tests are performed by many researchers to obtain the fatigue material properties at HCF and LCF. Kobayashi et al. [104] have performed an axial load-controlled fatigue test at 600 ºC on forged Inconel 718 material. A sinusoidal wave shape with frequency of 10 Hz has been applied for obtaining a stress-life data, known as S-N curve, for up to 10^7 cycles. Connolley et al. [105] have performed three point fatigue tests at 600 ºC

under load control with a trapezoidal loading waveform at 0.25 Hz. Notches have been machined in specimens of Inconel 718 by a broaching process. Two batches of single-edge U-notch specimens, labelled batch A and batch B, have been extracted from two Inconel 718 turbine disc forgings produced from the same cast of material. Batch A is only machined, while batch B is machined and polished by standard polishing procedure. The U-shape specimen geometry is shown in Figure 9.1. The strain-life data for each batch have been fitted to the Coffin-Manson relationship [106-107]:

$$\frac{\Delta\varepsilon}{2} = \left(\frac{\sigma_f'}{E}\right)(2N_f)^{\lambda_1} + \varepsilon_f'(2N_f)^{\lambda_2} \tag{9.1}$$

where:

$\Delta\varepsilon$	strain range
σ_f'	fatigue strength coefficient
E	elastic modulus
N_f	number of cycles to failure
ε_f'	fatigue ductility coefficient (material-dependent)
λ_1, λ_2	material dependent constants

The aim of this study is to investigate the effect of the micro machining and shot-peening stresses on the fatigue life of Inconel 718 notched specimen, loaded under three-point bending and undergoing HCF and LCF by using the FEM. The stress-life data [104] has been fitted to the Basquin equation for predicting the life at HCF, the strain-life curve fitted into Coffin-Manson equation has been used to predict the fatigue life at LCF, and the mathematical algorithms from Chapter 6 for mapping micro residual stress to macro 2D FE models have been used.

9.2 FE model

The specimen from Figure 9.1 is modelled in ABAQUS as a 2D plane stress model by using only half of the specimen due to the symmetry. Figure 9.2 shows the model with applied loading and boundary conditions. In three point bending tests, the

specimen is placed on two fixed rollers and loaded at the middle. The fixed roller, in the FE model, is represented as a rigid body with reference point RP. The rigid body has a circular geometry with radius of 2.5 mm. Zero displacements in the x and y direction, and zero rotation in x-y plane are applied at the reference point RP which constraints the rigid body. Frictionless contact is applied between surface S_2 and S_3. All nodes from surface S_1 are constrained in the x direction and a concentrated force F is applied at the middle of the specimen.

Cyclic loading is applied as shown in Figure 9.3. Seventy cycles are performed with load ratios between F_{min} and F_{max} of 0.1. Each cycle includes loading followed by unloading. The applied loads for F_{max} are in the range between 100-150 N at the HCF and 650-700 N at the LCF.

The model is meshed with four node linear quadrilateral elements with full integration, as shown in Figure 9.4. The number of the elements is 8,540. Refined mesh is used around the notched area for producing accurate mapping and final results.

9.3 Initial stress conditions

Three FE models are investigated with different initial stress conditions at the HCF and the LCF. No initial stress conditions are applied to the first model. Typical micro machining residual stresses obtained experimentally for Inconel 718 have in-depth stresses as shown in Figure 9.5. The micro machining stresses are mapped to the second model. Shot-peening residual stresses for Inconel 718 obtained by Zimmermann et al. [108], as shown in Figure 9.6, are mapped to the third model.

Figure 9.7 shows the Von Mises, the direct and the shear stresses after mapping the residual stresses from the micro machining process around the notched area. It can be seen an uniform distribution of the Von Mises stresses, which demonstrates the accuracy of the mapping. The mapped direct stresses show a maximum tensile stress of 980 MPa which is identical to the maximum tensile stresses from Figure 9.5. The residual stresses from the shot-peening process are mapped and shown in Figure 9.8.

Again, it can be seen the uniform Von Mises stress distribution after mapping. The maximum compressive stresses from Figure 9.6 and the mapped maximum compressive direct stresses arrive at the same value of 1233 MPa.

9.4 Material properties

Inconel 718 mechanical material properties at temperature of 600 ºC are used, as shown in Table 9.1. It is assumed that all three models have the same material properties. The change of the mechanical properties after shot-peening and machining processes has not been taken into account.

For performing the HCF, only an elastic material model is used. Figure 9.9 shows representative stress-life data [104] fitted to the Basquin equation [109].

$$\sigma_a = \sigma_f' (2N_f)^b \tag{9.2}$$

where:

σ_a stress amplitude

b fatigue strength exponent

After fitting, Equation (9.2) can be given by:

$$\sigma_a = 2084.93781733487(2N_f)^{-0.097485085188} \tag{9.3}$$

A plastic material model with non-linear combined kinematic/isotropic hardening is used for performing the LCF. The non-linear combined isotropic/kinematic hardening can be used for modelling phenomena, such as ratcheting, relaxation of the mean stress, and cyclic hardening, that are typical of materials subjected to cyclic loading [58]. This model is based on the work of Lemaitre and Chaboche [110] where the size of the yield surface is defined as a function of equivalent plastic strain, temperature and field variables.

The strain-life data is fitted in Equation (9.1) and the constants are obtained [105]. Equation (9.1) for batch A and batch B can be given by:

Batch A:

$$\frac{\Delta\varepsilon}{2} = \left(\frac{580}{168000}\right)\left(2N_f\right)^{-0.01} + 0.339702\left(2N_f\right)^{-0.71371} \tag{9.4}$$

Batch B:

$$\frac{\Delta\varepsilon}{2} = \left(\frac{580}{168000}\right)\left(2N_f\right)^{-0.01} + 0.445076\left(2N_f\right)^{-0.74398} \tag{9.5}$$

9.5 Results and discussion

Two deferent loading ranges are applied to the three models. A concentrated force F_{max} in the range 100-150 N is applied where the material exhibits elastic behaviour and the life at the HCF is predicted based on the stress-life approach. A concentrated force F_{max} in the range 650-700 N is applied where large plastic deformations occur and the life at the LCF is predicted based on the strain-life approach.

9.5.1 High cycle fatigue

A cyclic load with F_{max} in the range 100-150 N is applied. Figure 9.10 shows the location of the peak stress amplitude at load F_{max} of 100 N. It can be seen that for the models with none and micro machining initial stresses the location of the peak stress amplitude is at the same node A, while for the model with the shot-peening initial stresses, the peak stress amplitude is inside the material at Node B.

Figure 9.11 shows a constant stress amplitude at F_{max} of 100 N for the all seventy cycles due to the elastic shakedown. It is observed that the maximum principle stresses has the same magnitude as the direct stresses in the x direction σ_{11}. It can be seen that the model with the shot-peening initial stresses shows lowest stress amplitude while the model with micro machining initial stresses shows stress amplitude higher than the yield stress. This means that the tensile machining stresses result in plastic behaviour at low loads which leads to a shorter life of the component. Figure 9.12 shows the stress amplitude in the x direction (σ^a_{11}), obtained at F_{max} of 100 N, versus the distance from node A to 1mm depth of surface S_1 (see

Figure 9.2). It can be noticed that the stress amplitudes for the models with initial machining and shot-peening stresses have the same trend as the stresses from Figures 9.5 and 9.6. The compressive shot-peening stresses have decreased while the machining tensile stresses have increased. The stress amplitude is obtained for three loading conditions at F_{max} of 100, 125 and 150 N, as shown in Figure 9.13. As expected, the stress amplitude at different loads exhibits linear behaviour due to the elastic material model used in the FE model. It can be noticed that the gradient, for the model with shot-peening initial stresses, is smaller than the model with non initial stresses.

The fatigue life is predicted by substituting the stress amplitudes obtained at different loads into Equation (9.3) and solving the equation numerically by using the Newton-Raphson method [111]. Comparison of the model with none and shot-peening initial stresses is shown in Figure 9.14. It can be seen that the compressive initial stresses from the shot-peening increase the fatigue life. Figure 9.15 shows the proportion between the fatigue life predicted with shot-peening and none initial stresses at different loads. It can be seen that the shot-peening has significant effect on the fatigue life at higher loads at the HCF.

9.5.2 Low cycle fatigue

Cyclic load with F_{max} in the range 650-700 N is applied. Figure 9.16 shows the location of the peak maximum principal plastic strains at F_{max} of 650 N during loading and unloading. It can be seen that for the models with none and micro machining initial stress the peak maximum principal plastic strains occur at the same location (node A), while the location of the peak maximum principal plastic strains, for the model with the shot-peening initial stresses, is inside the material at Node B.

Figure 9.17 shows the stress-strain cycles for the direct stresses and plastic strains, obtained at F_{max} of 650 N, for the three models for 70 cycles. The stress-strain cycles are plotted at the nodes with the peak maximum principal plastic strains where crack initiation is more likely to occur (see Figure 9.16). It can be seen that the cycles show a ratcheting behaviour followed by stabilizing.

The mean stress relaxation in the x direction (σ^m_{11}) for all models, in the y direction (σ^m_{22}) for the model with shot-peening initial stresses and the maximum principal mean stresses can be seen in Figure 9.18. The models with none and machined initial stresses arrive at the similar values. It can be noticed that the direct mean stresses tend to zero. The stabilised ratcheting can be seen in Figure 9.19 where the mean plastic strains tend to become constant. As expected, the mean plastic strains for the model with the machining initial stresses are highest due to the initial mapped tensile stresses and the model with the shot-peening initial stresses are lowest due to the initial mapped compressive stresses.

Similar plastic strain ranges for the model with none and machining initial stresses can be seen in Figure 9.20, while the shot-peening strain range shows much lower values. For predicting the fatigue life, it is important to determine the hot-spots (points at which the failure occurs). Figure 9.21 shows the maximum principal plastic strains, at the seventieth cycle, from node A through the thickness of the material, for the three models during loading and unloading. It can be seen that for the model with shot-peening initial stresses, node B has the highest peek maximum principal plastic strains and it is more likely that crack initiations will take place at that point. Figure 9.22 shows the maximum principal plastic strain range variation with the distance. Figure 9.23 shows the proportion between the maximum principal plastic strains at Node B and node A at F_{max} of 650, 675 and 700 N for the model with shot-peening initial stresses. It can be seen that by increasing the load the maximum principal plastic strains at both nodes become closer.

Figure 9.24 shows the maximum principal plastic strain ranges, obtained at the seventieth cycle, at F_{max} of 650, 675 and 700 N. The fatigue life is predicted by substituting the maximum principal plastic strain ranges, obtained from the stabilized cycles, into Equation (9.4) and solving the equation numerically by using the Newton-Raphson method. When the maximum principal plastic strain range at node B is used for predicting the fatigue life of the model with shot-peening initial stresses, the predicted life is grater than 10^{15} cycles. Figure 9.25 compares the predicted fatigue life for the three models by using the maximum principal plastic strain ranges at Node A. The shot-peening compressive stresses improved the fatigue life by 0.8% at F_{max} of 650 N and 0.3 % at 700 N at node A.

9.6 Conclusions

It has been observed that the hot-spot at HCF and LCF, for the models with none and micro machining initial stresses, has been located on the surface of the notched area, while for the model with shot-peening initial stresses the hot-spot has been located inside the material.

The shot-peening compressive stresses improved significantly the life at HCF, more than 1.2 times, when the specimen has been loaded with F_{max} = 100 N and more than 2.3 times at load F_{max} = 150 N, compared to the model with no initial stresses. The micro machining tensile stresses resulted in the onset of plastic behaviour at low loads which leads to decreasing the fatigue life.

The three models with none, micro machining and shot-peening initial stresses arrived at similar life predictions at LCF. The shot-peening compressive stresses improved the fatigue life by 0.8% at F_{max} = 650 N and 0.3 % at F_{max} = 700 N when the hot-spot has been selected at the surface of the notched. It has been observed that the micro machining tensile stresses increased the mean plastic stains while the compressive shot-peening stresses decreased the mean plastic strains.

Table 9.1: Material properties of Inconel 718 at 600 ºC [68, 69, 104, 105]

Elastic Modulus (GPa)	168
Poisson ratio (-)	0.29
Yield Stress (MPa)	956
Ultimate Stress (MPa)	1058
Elongation (%)	21

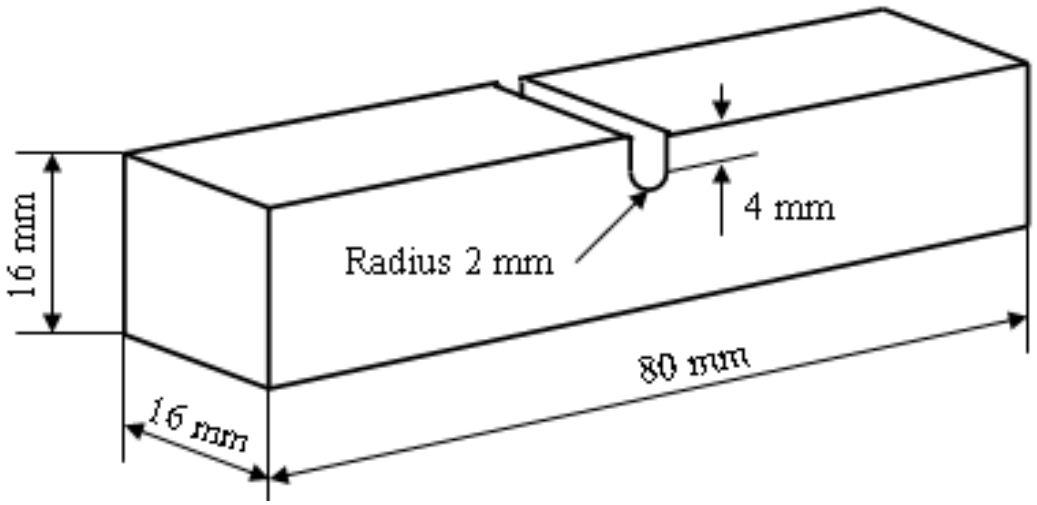

Figure 9.1: Geometry of U-notch specimen

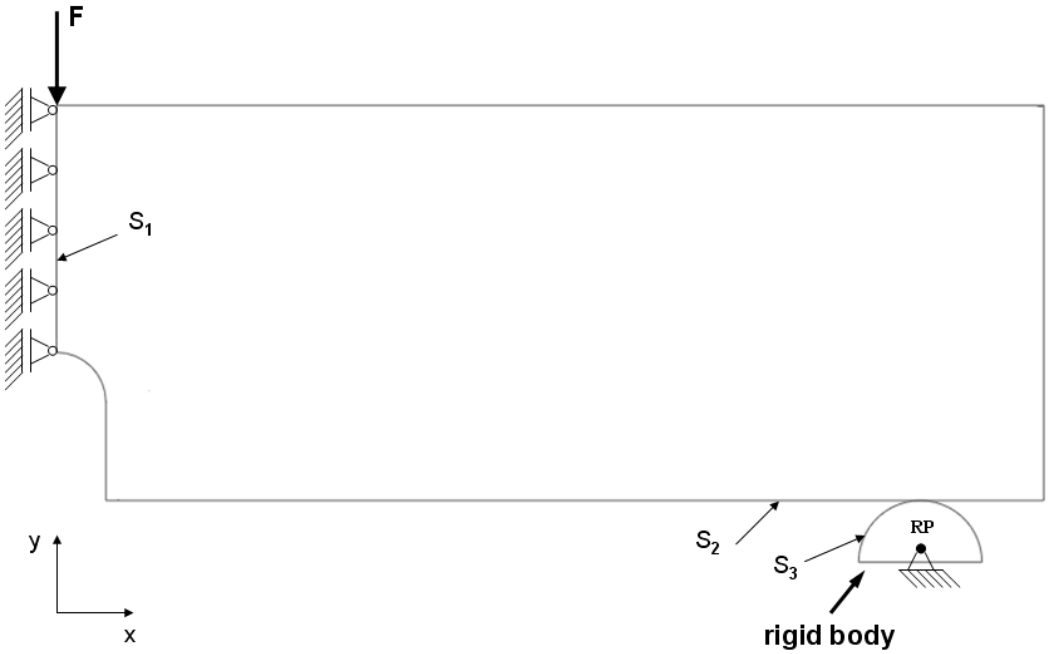

Figure 9.2: FE model for the U-notch specimen

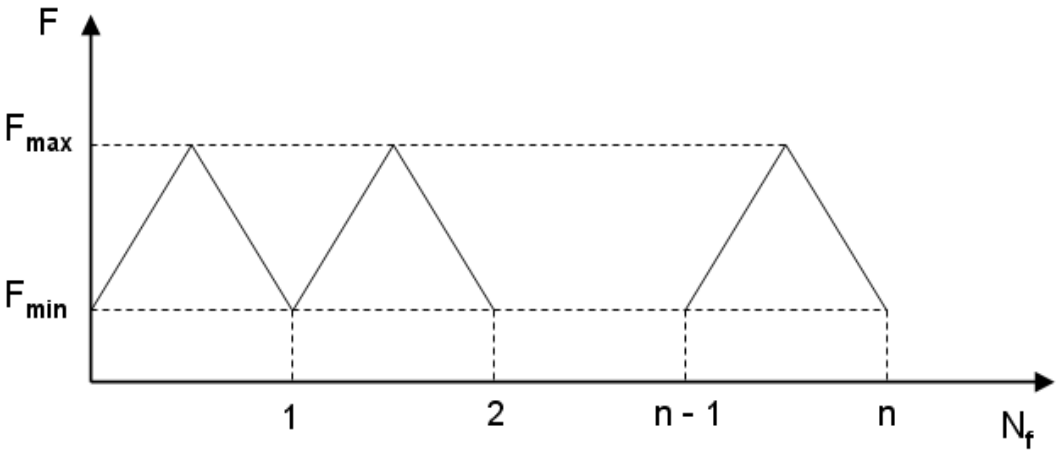

Figure 9.3: Cyclic loading applied to the FE model

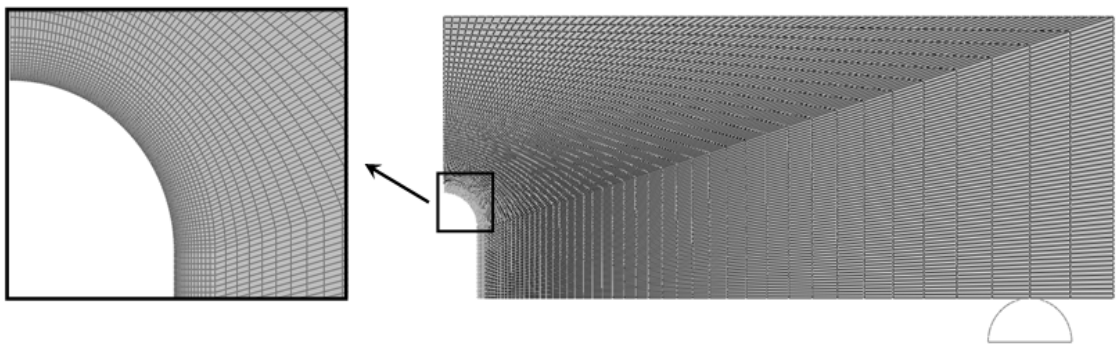

Figure 9.4: FE mesh with 8,540 four node linear quadrilateral elements

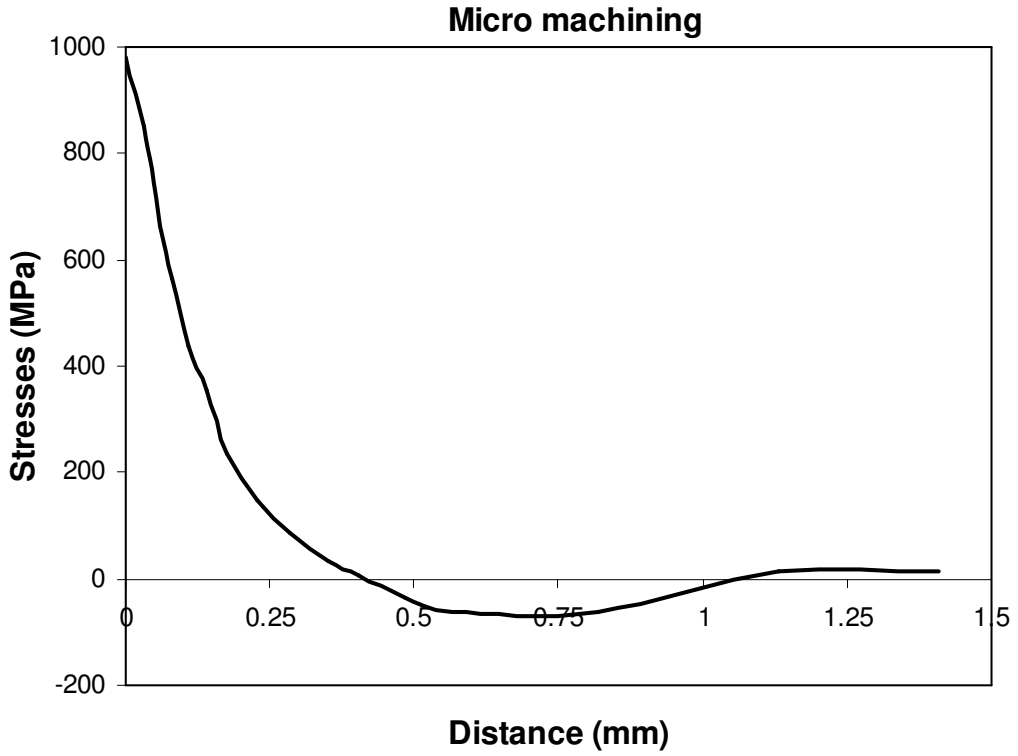

Figure 9.5: Typical micro stresses in depth from micro machining process

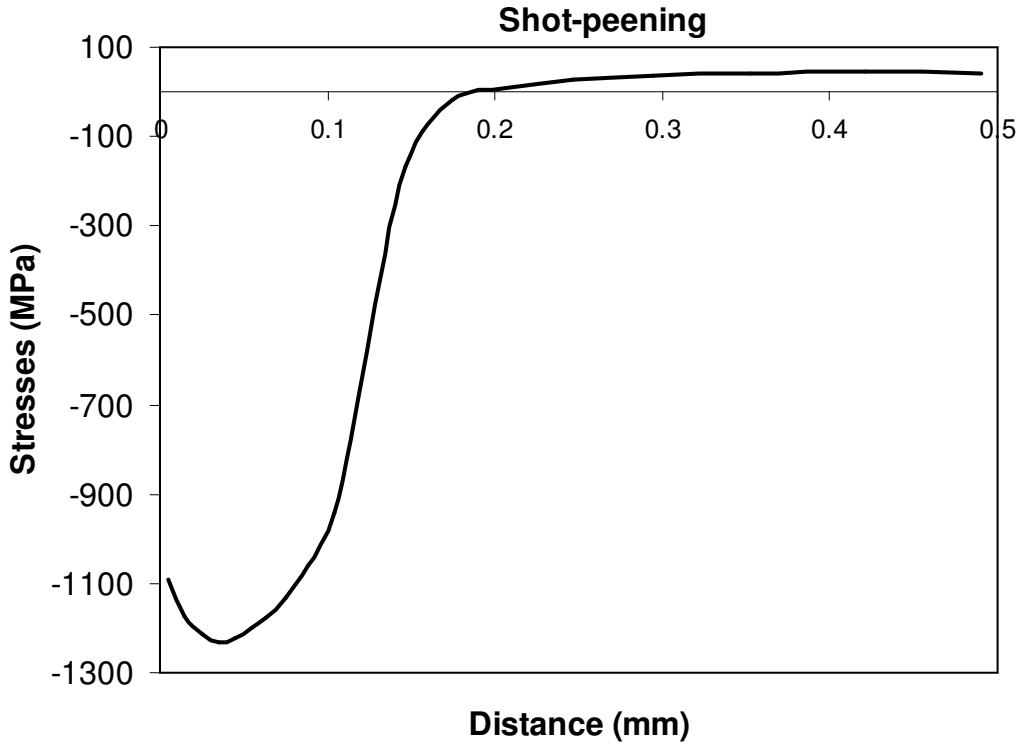

Figure 9.6: Micro stresses in depth from shot-peening process [108]

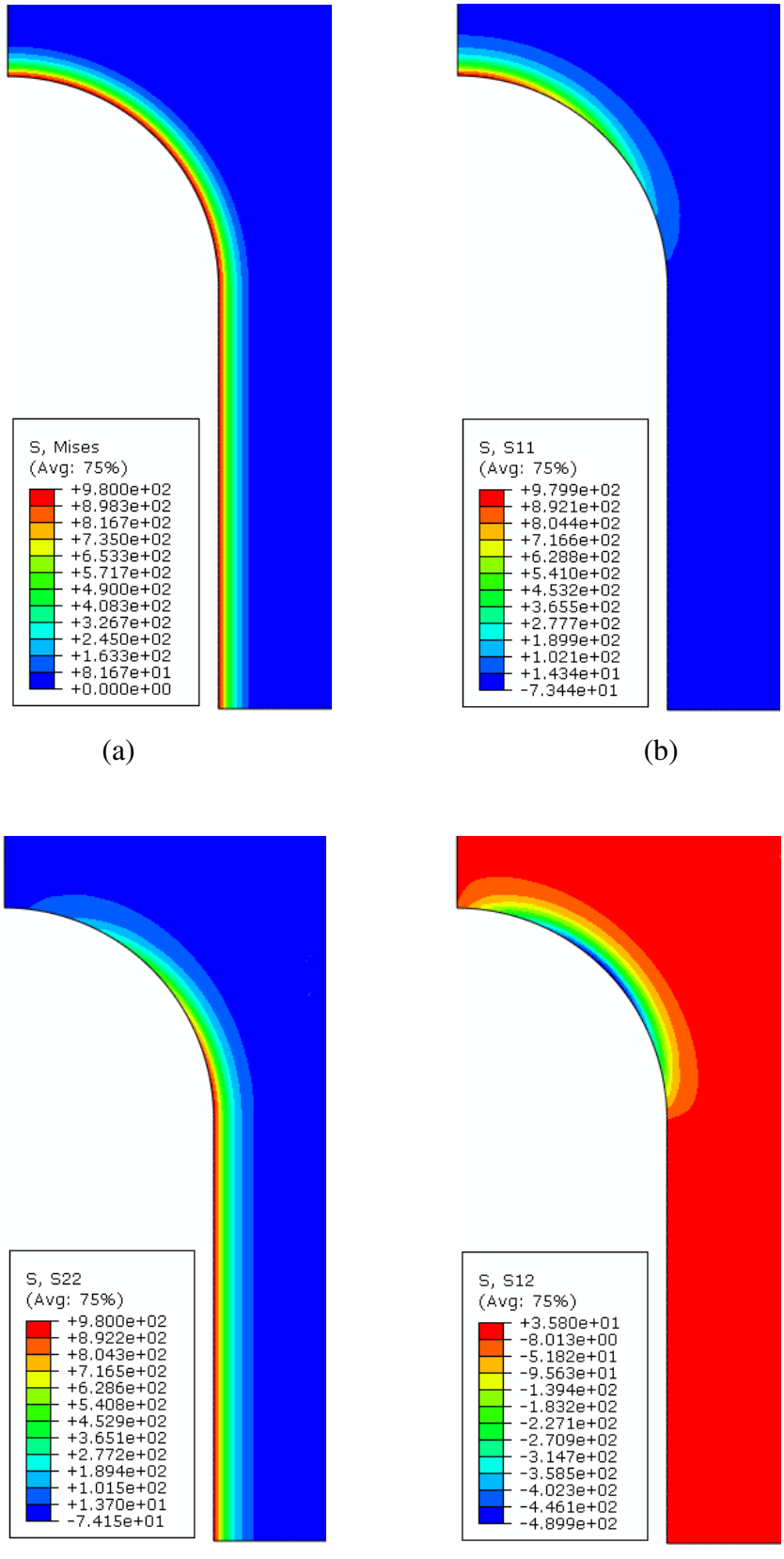

Figure 9.7: Mapped micro machining stresses beneath the notched surface: **(a)** Von Mises stresses; **(b)** Stresses in the x direction; **(c)** Stresses in the y direction; **(d)** Shear stresses in x-y plane

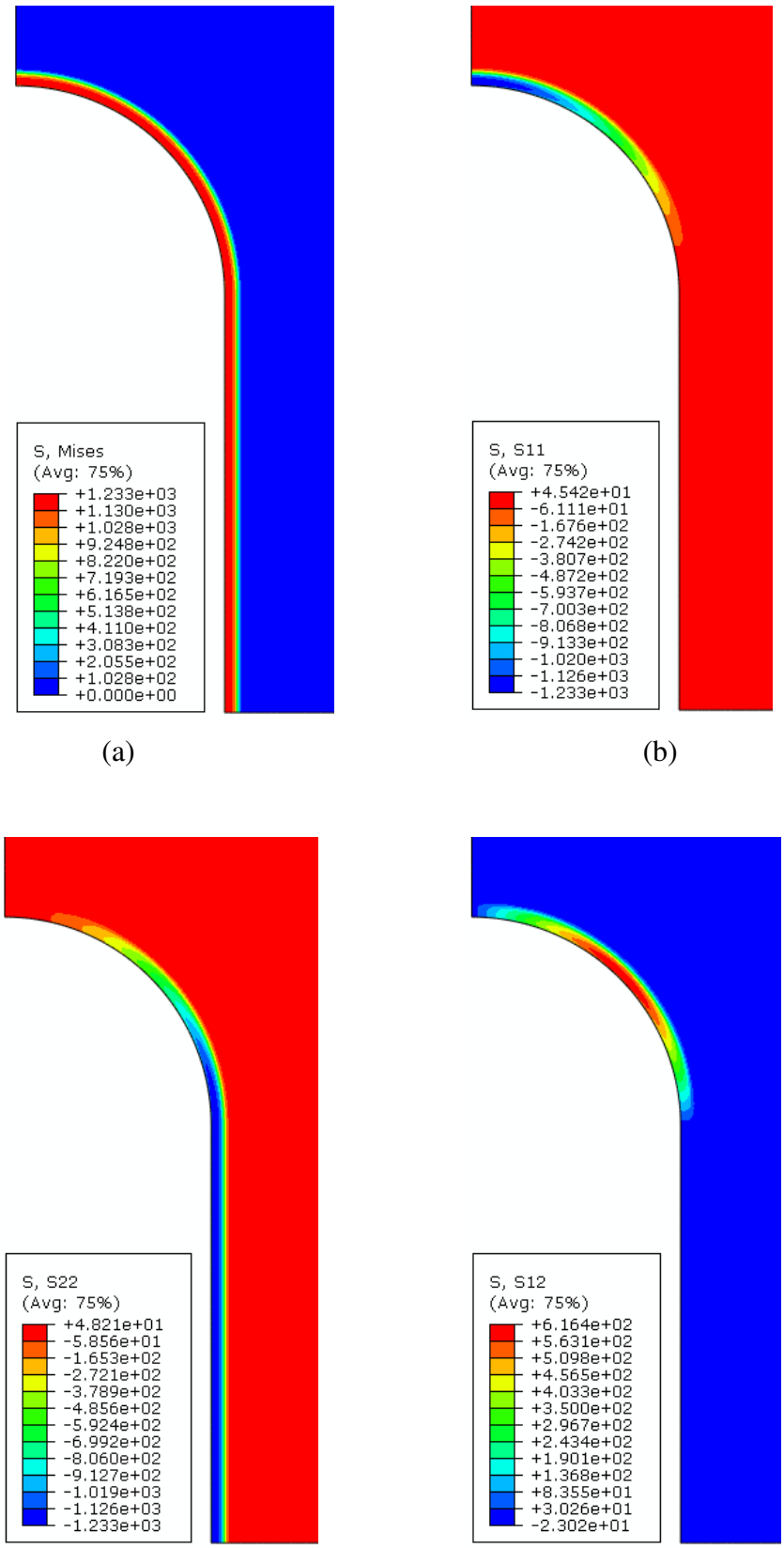

Figure 9.8: Mapped shot-peening stresses beneath the notched surface: **(a)** Von Mises stresses; **(b)** Stresses in the x direction; **(c)** Stresses in the y direction; **(d)** Shear stresses in x-y plane

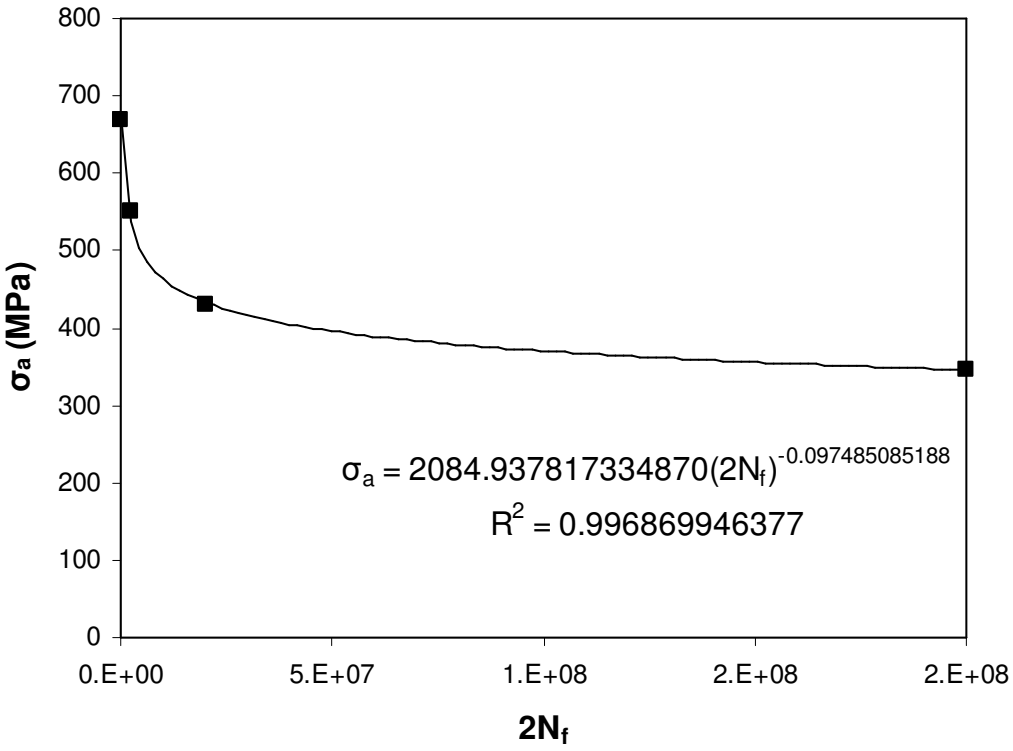

Figure 9.9: Representative stress-life data [104] fitted to the Basquin equation

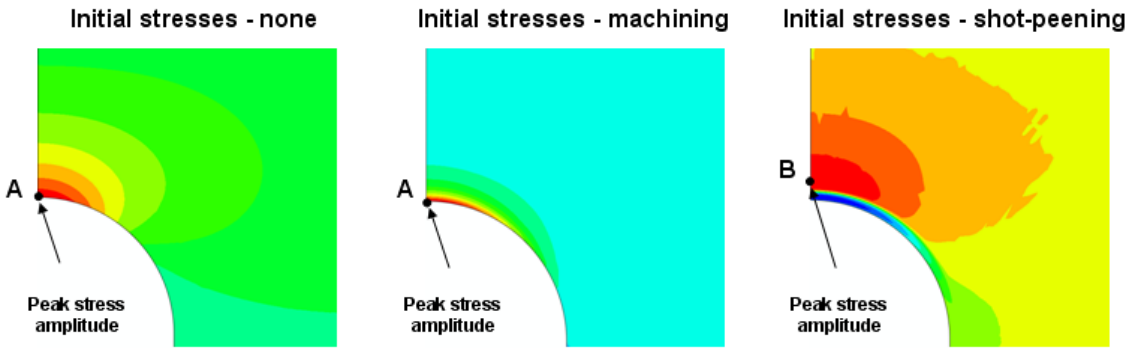

Figure 9.10: Location of the peak stress amplitude at load F_{max} of 100 N

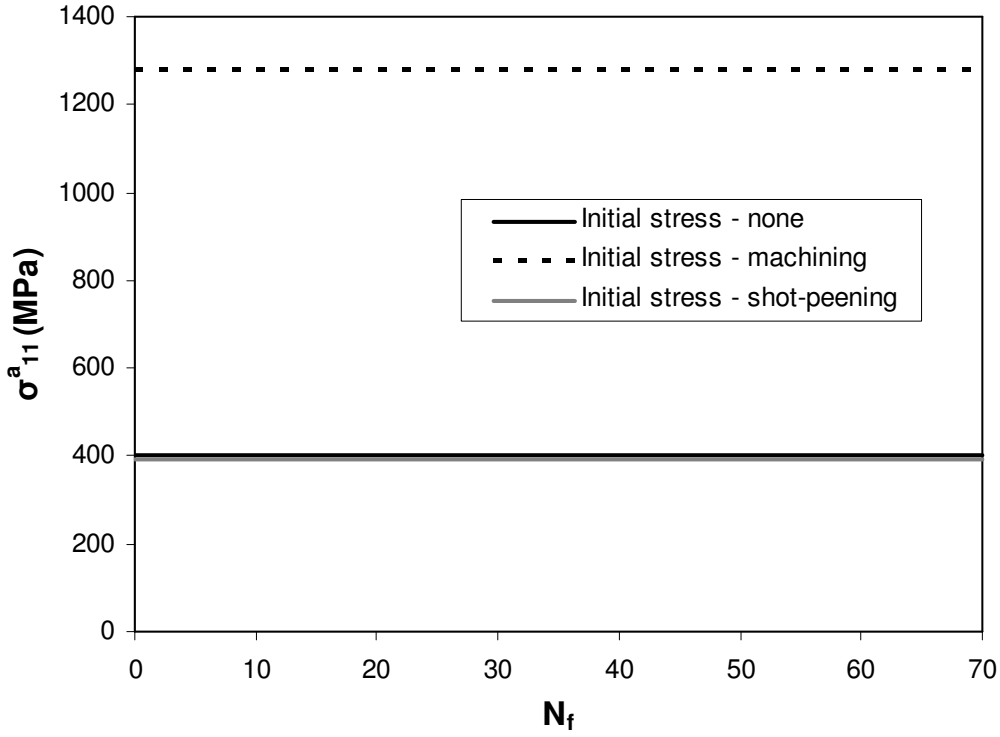

Figure 9.11: Stress amplitude obtained for seventy cycles at F_{max} of 100 N

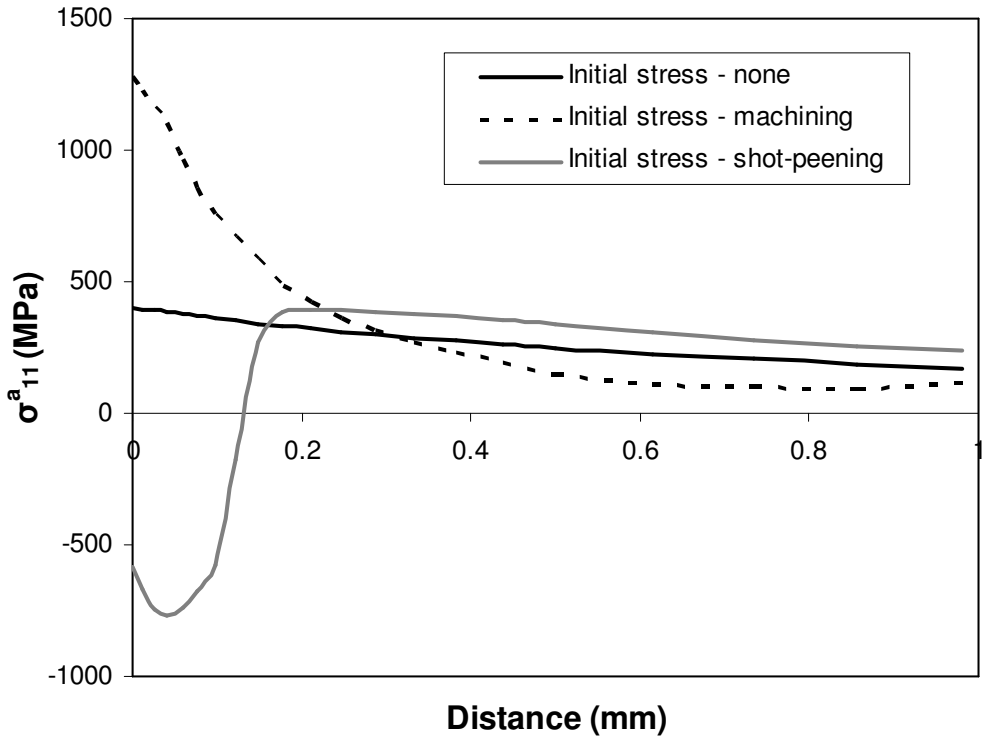

Figure 9.12: Stress amplitude in the x direction, obtained at F_{max} of 100 N, from node A to 1mm depth of surface S_1

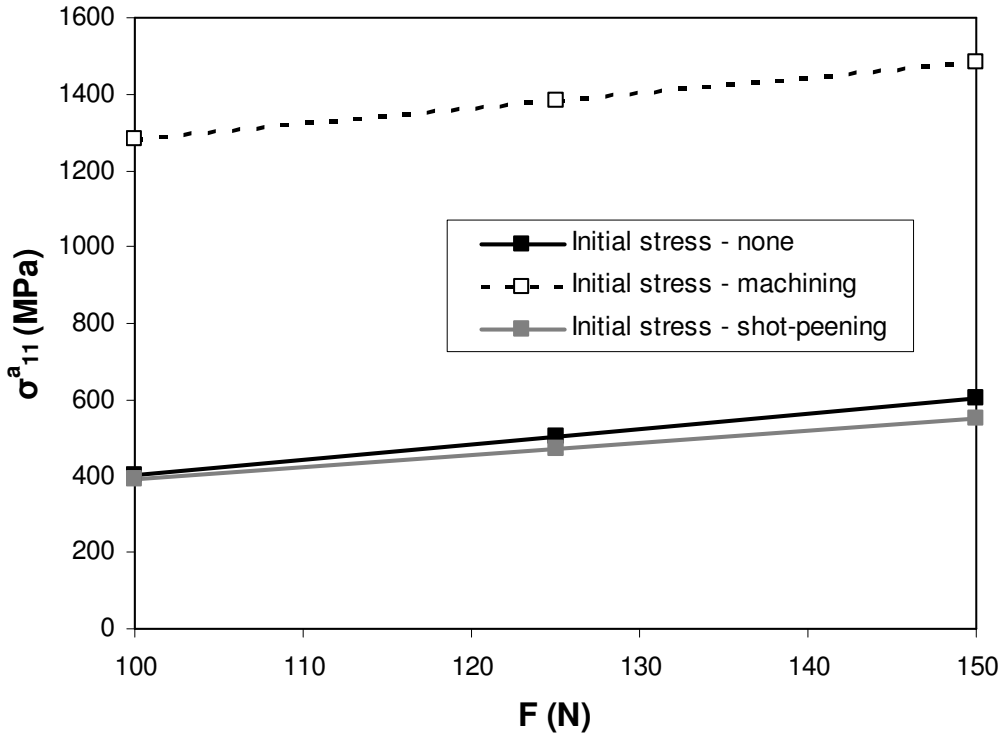

Figure 9.13: Stress amplitude in the x direction obtained at F_{max} of 100, 125 and 150 N

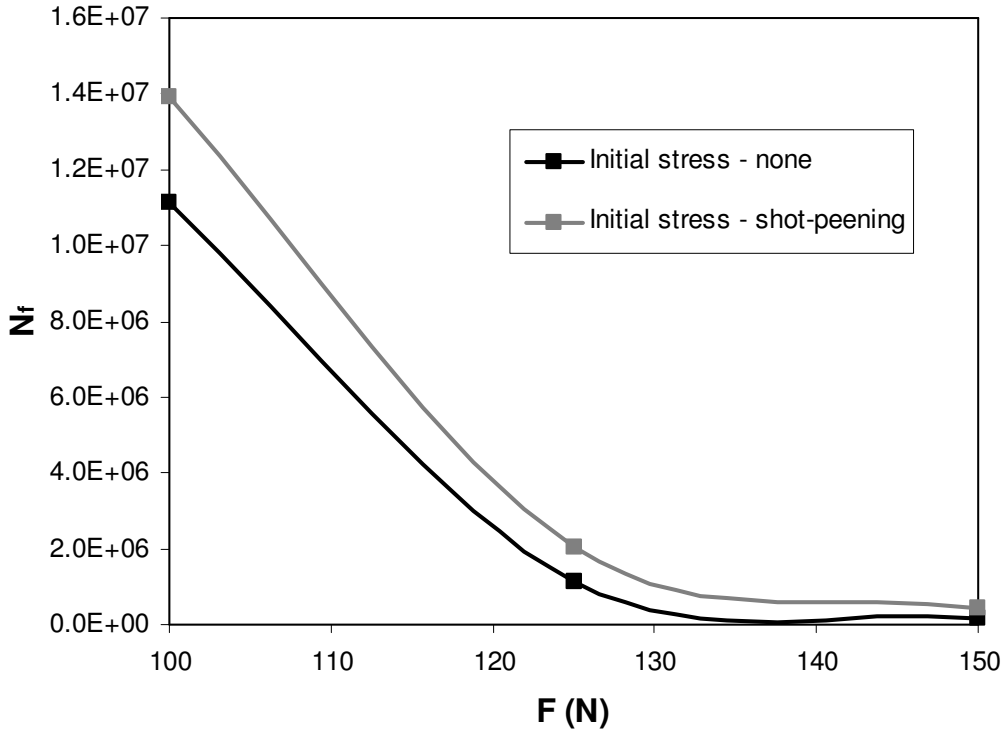

Figure 9.14: Predicted life at HCF at F_{max} of 100, 125 and 150 N

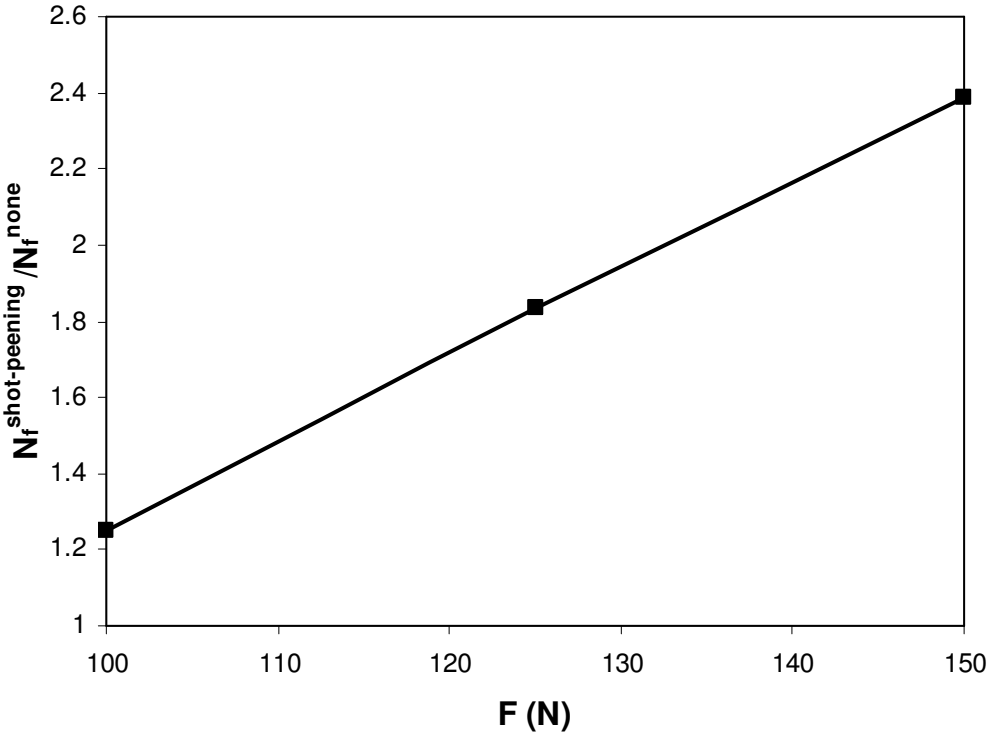

Figure 9.15: Proportion between the life predicted with shot-peening and with none initial stresses at HCF at F_{max} of 100, 125 and 150 N

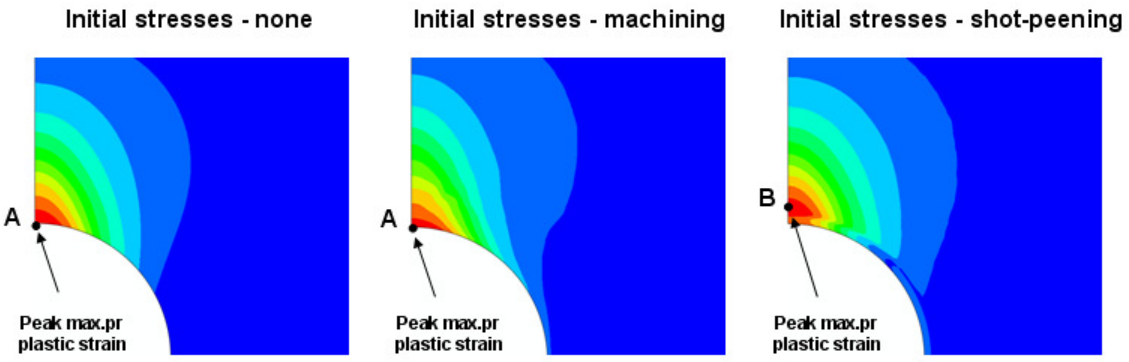

Figure 9.16: Location of the peak maximum principal plastic strains at F_{max} of 650 N during loading and unloading

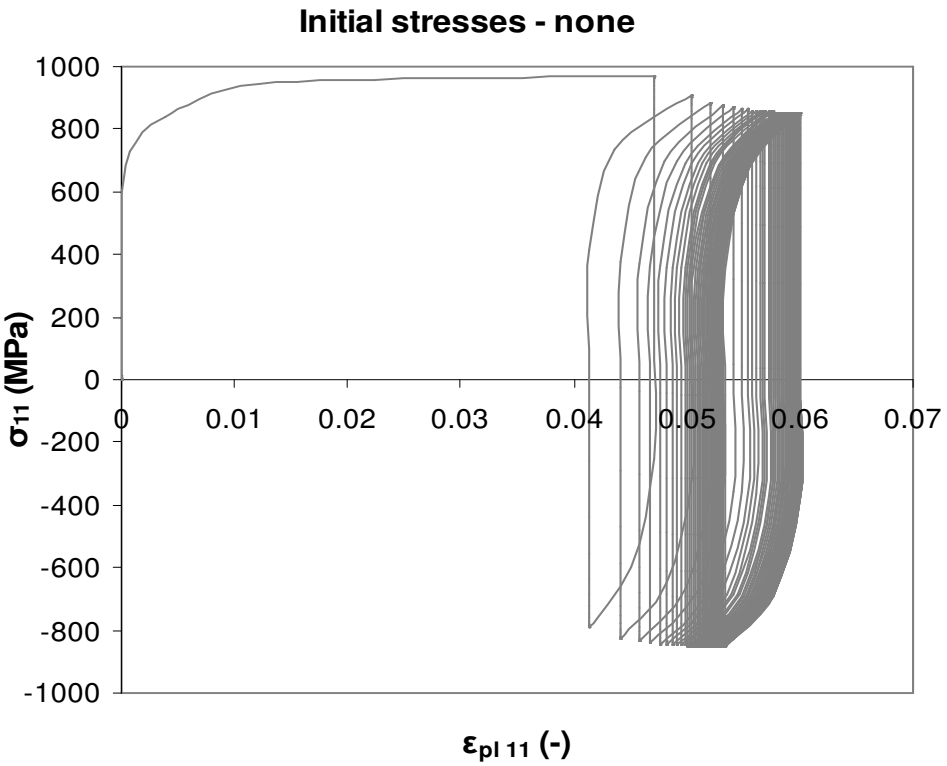

(a)

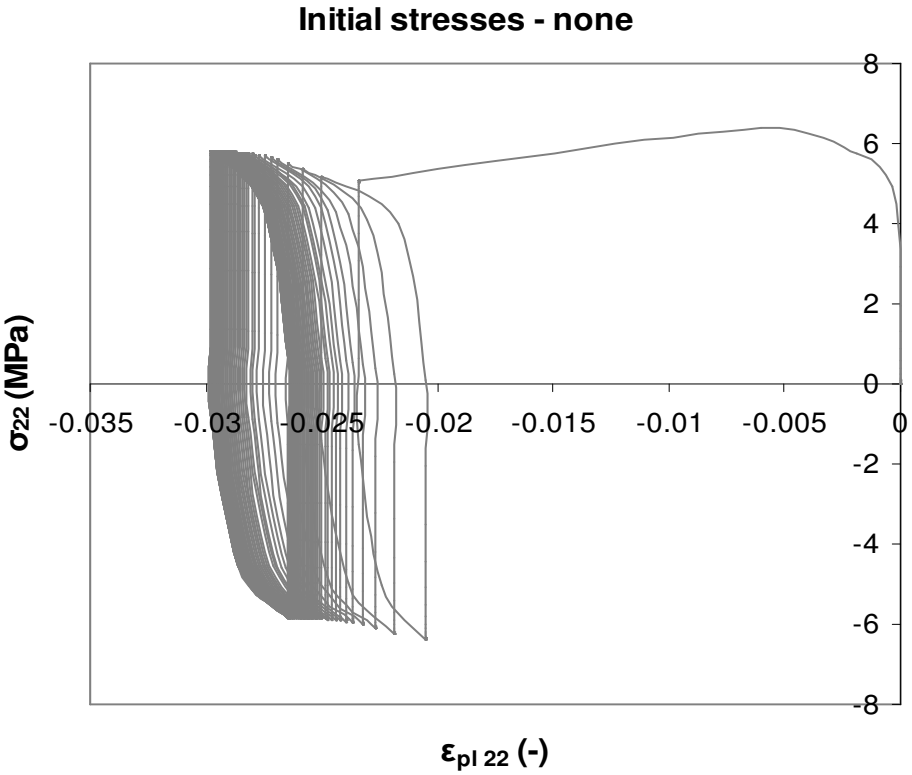

Figure 9.17: (b)

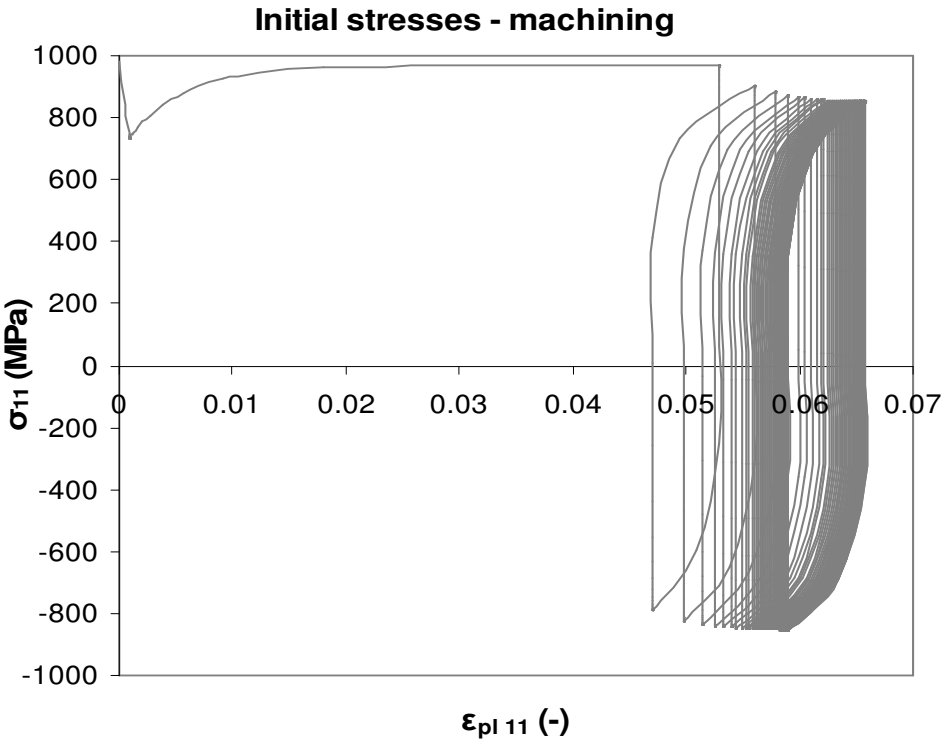

(c)

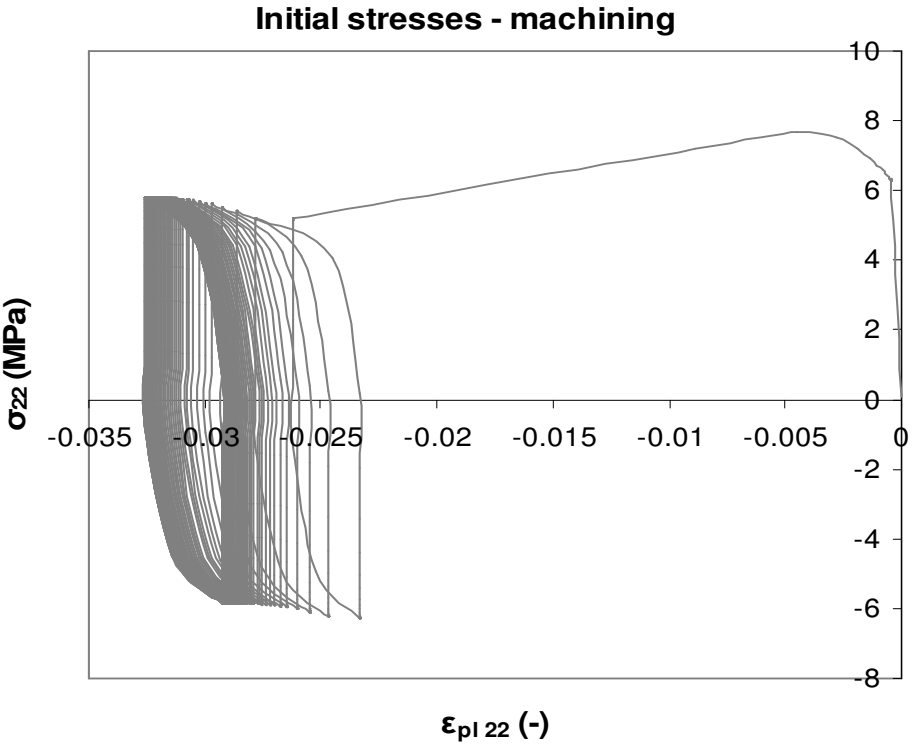

Figure 9.17: (d)

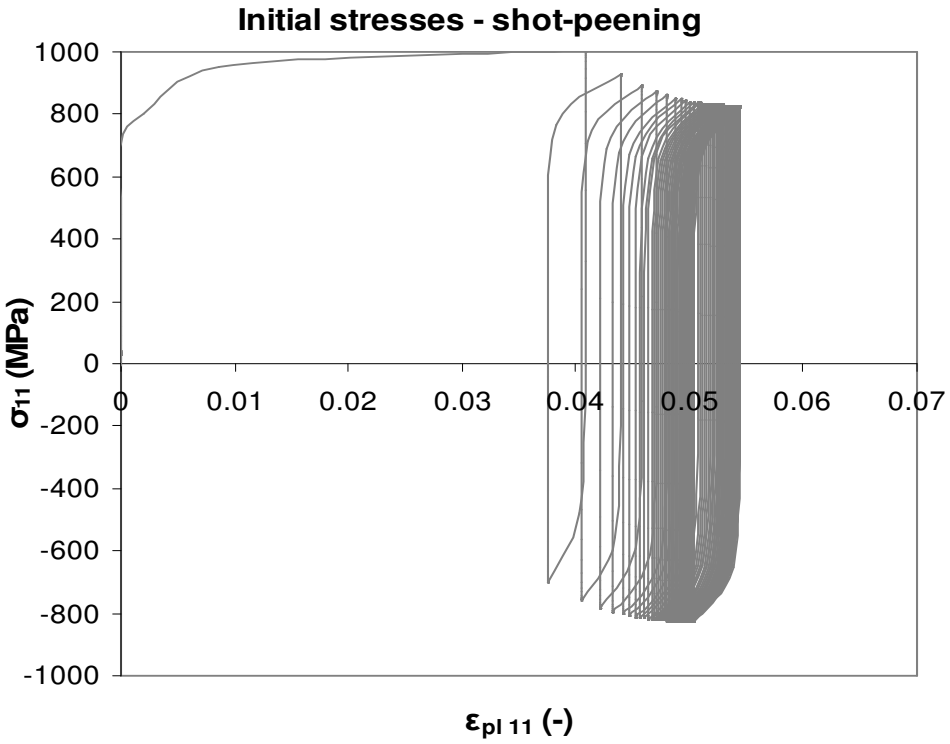

(e)

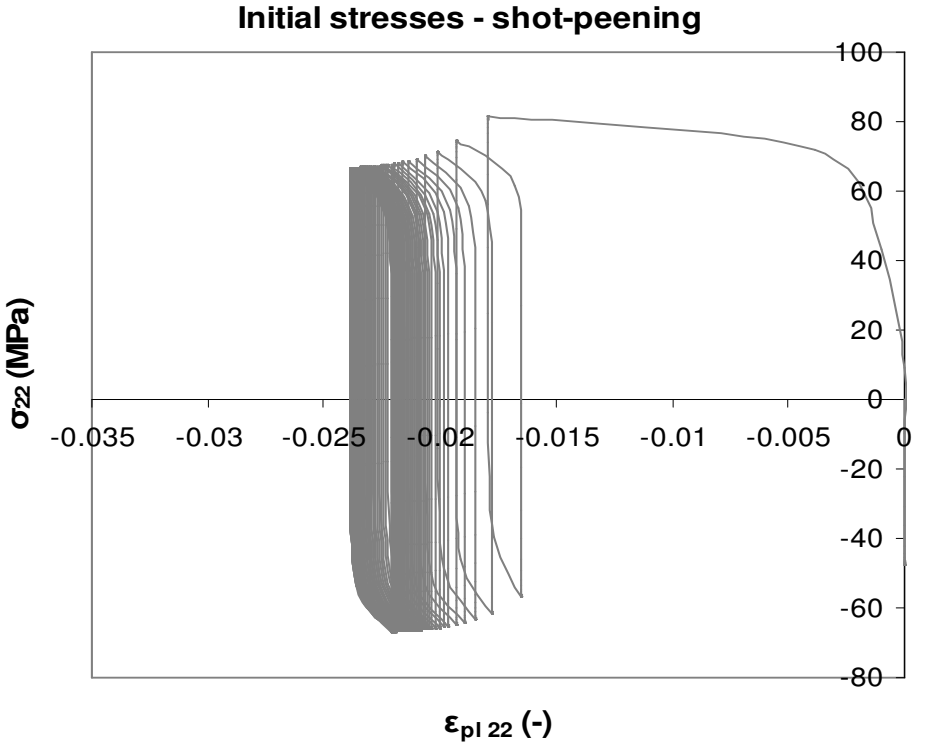

(f)

Figure 9.17: Stress-strain cycles at F_{max} of 650 N at the nodes with peak maximum principal plastic strain for the three models: **(a, b)** none initial stresses; **(c, d)** machining initial stresses; **(e, f)** shot-peening initial stresses

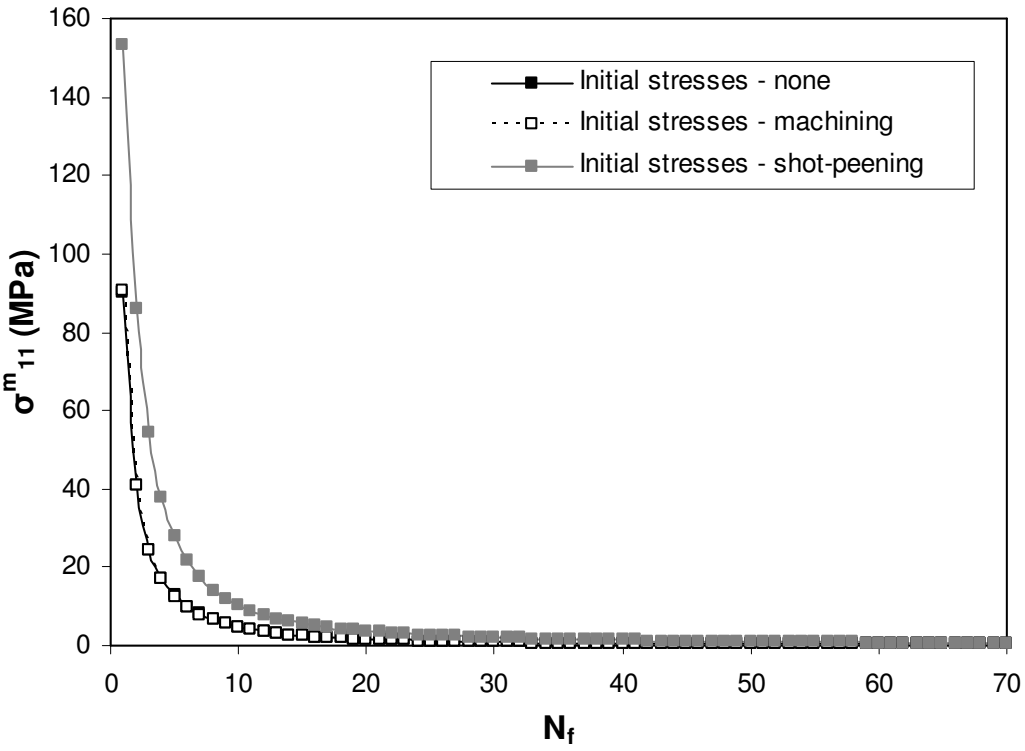

(a)

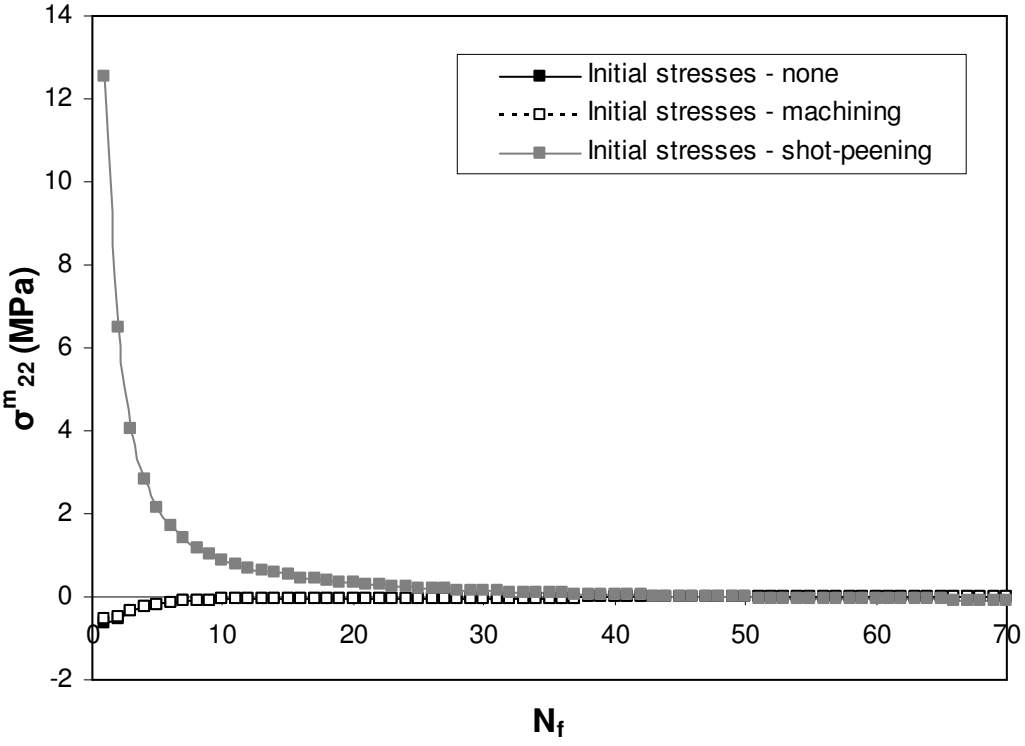

Figure 9.18: (b)

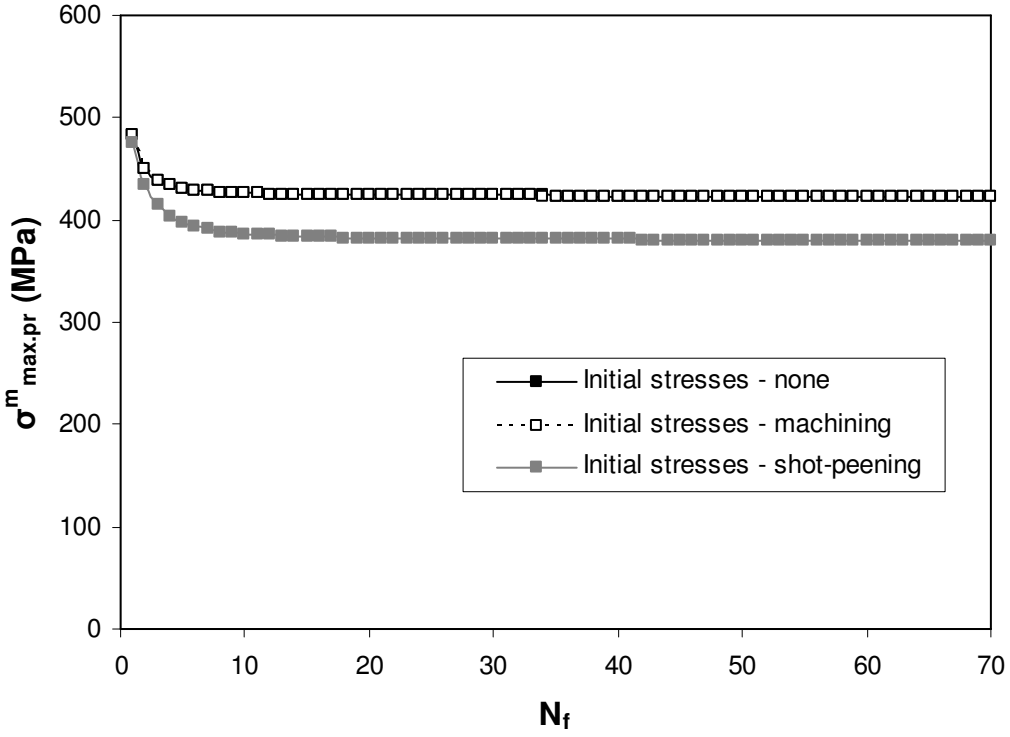

(c)

Figure 9.18: Mean stresses obtained for seventy cycles at F_{max} of 650 N at the nodes with peak maximum principal plastic strain: **(a)** Stresses in the x direction; **(b)** Stresses in the y direction; **(c)** Maximum principal stresses

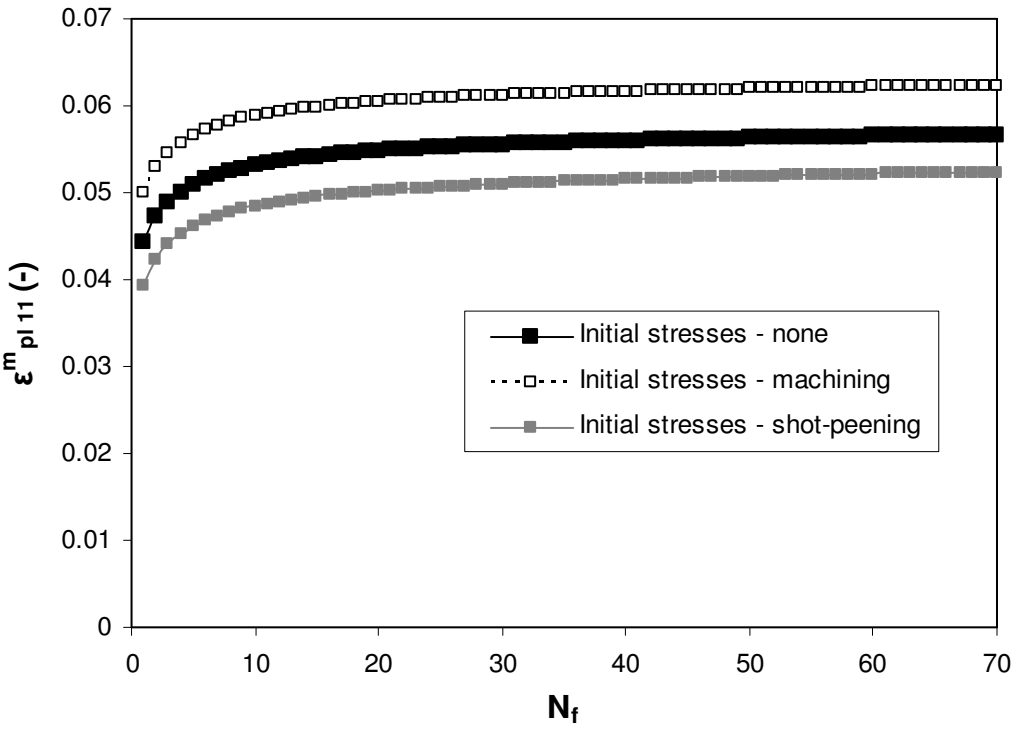

Figure 9.19: (a)

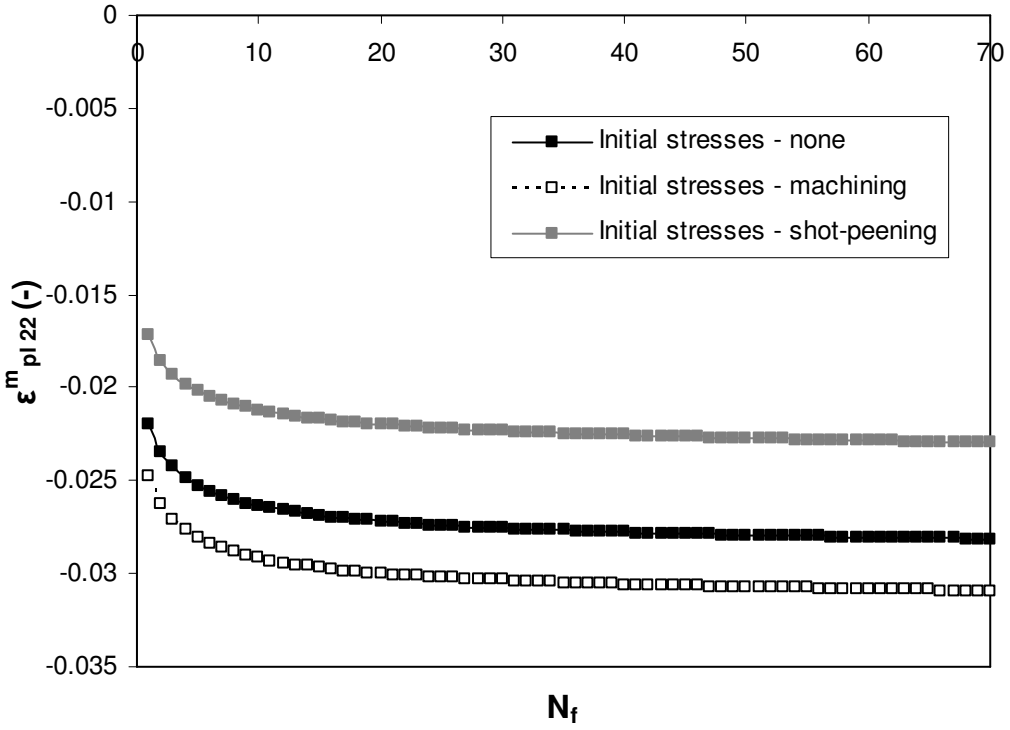

(b)

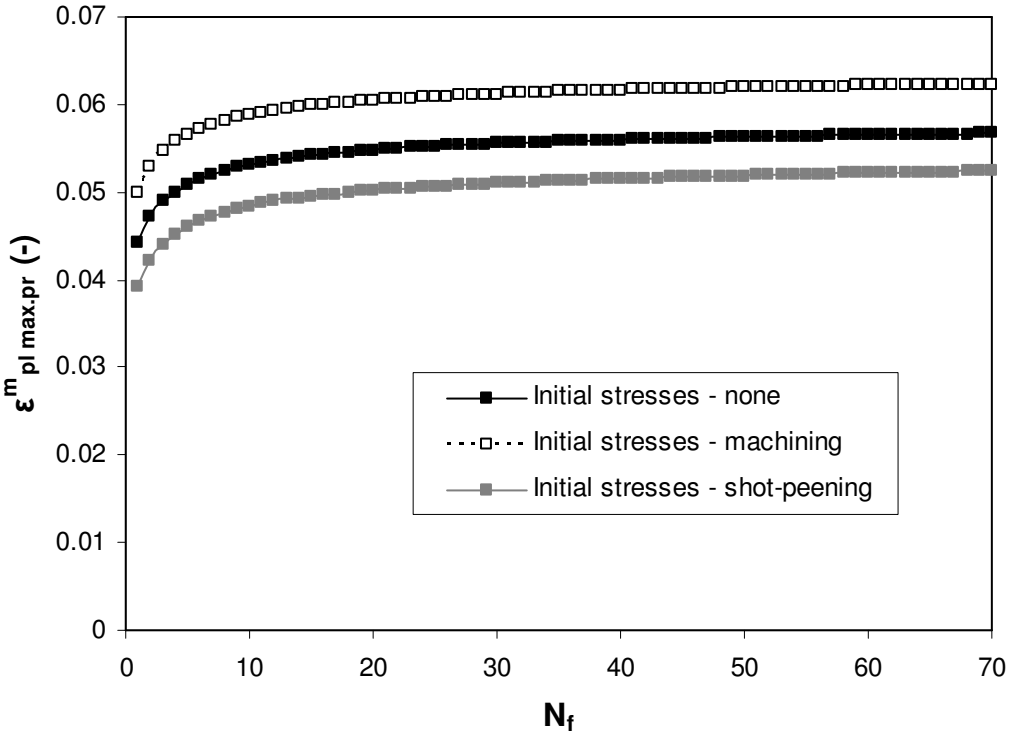

(c)

Figure 9.19: Mean plastic strains obtained for seventy cycles at F_{max} of 650 N at the nodes with peak maximum principal plastic strain: **(a)** Plastic strains in the x direction; **(b)** Plastic strains in the y direction; **(c)** Maximum principal plastic strains

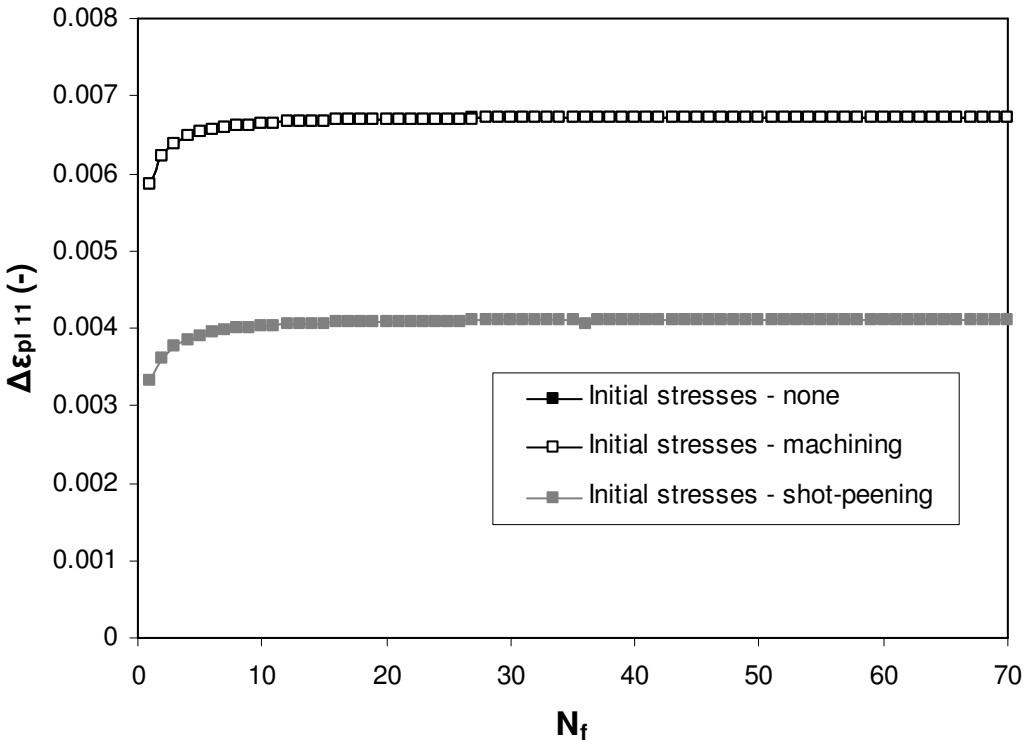

(a)

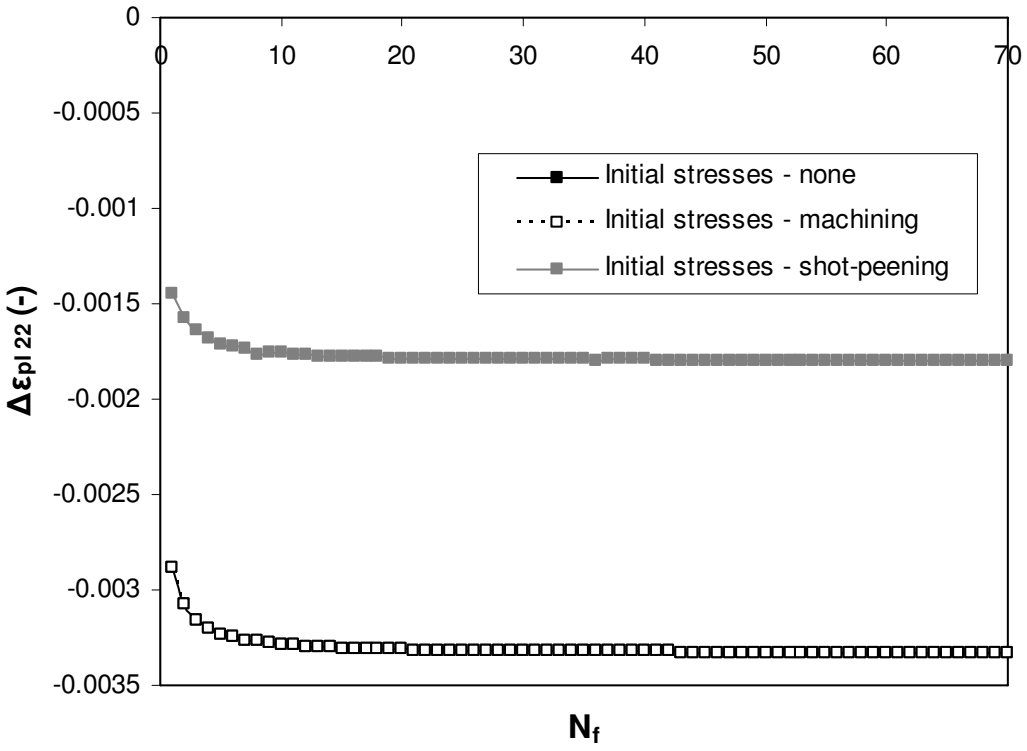

Figure 9.20: (b)

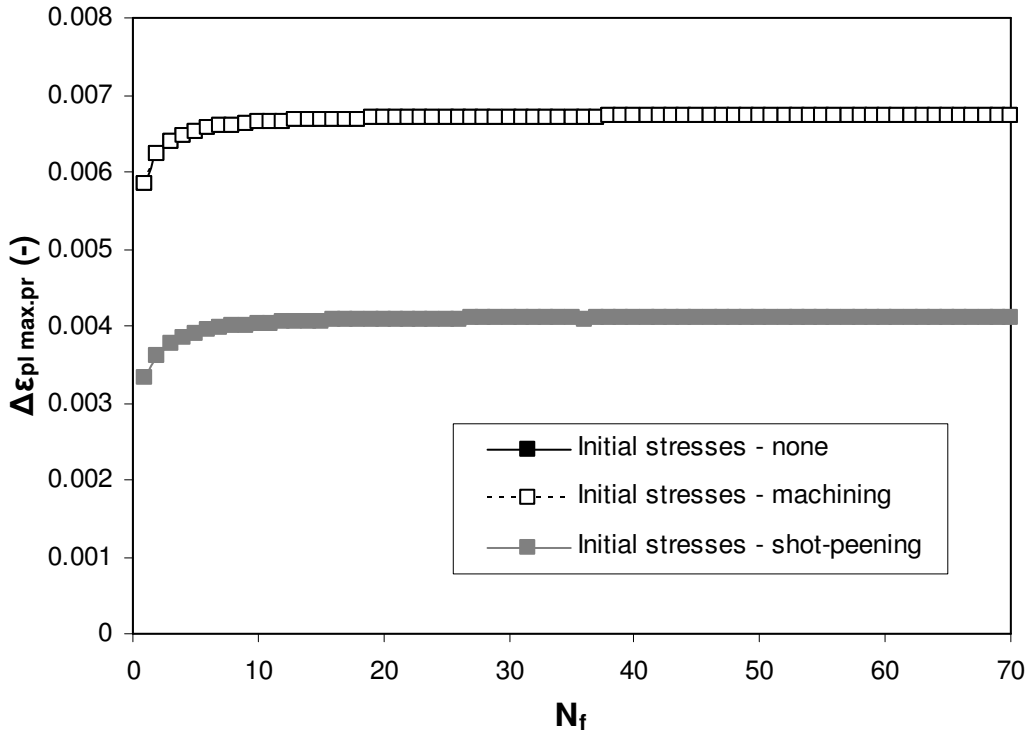

(c)

Figure 9.20: Plastic strain ranges obtained for seventy cycles at F_{max} of 650 N at the nodes with peak maximum principal plastic strain: **(a)** Plastic strain range in the x direction; **(b)** Plastic strain range in the y direction; **(c)** Maximum principal plastic strain range

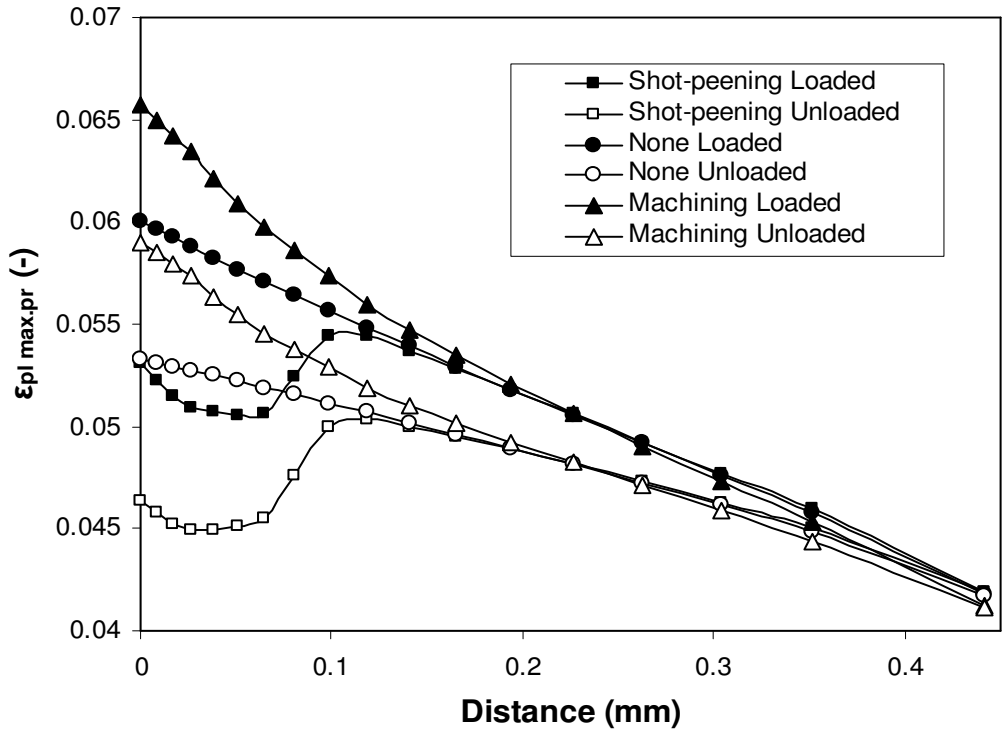

Figure 9.21: Maximum principal plastic strains obtained at the seventieth cycle, for F_{max} of 650 N versus the distance from node A through the thickness during loading and unloading

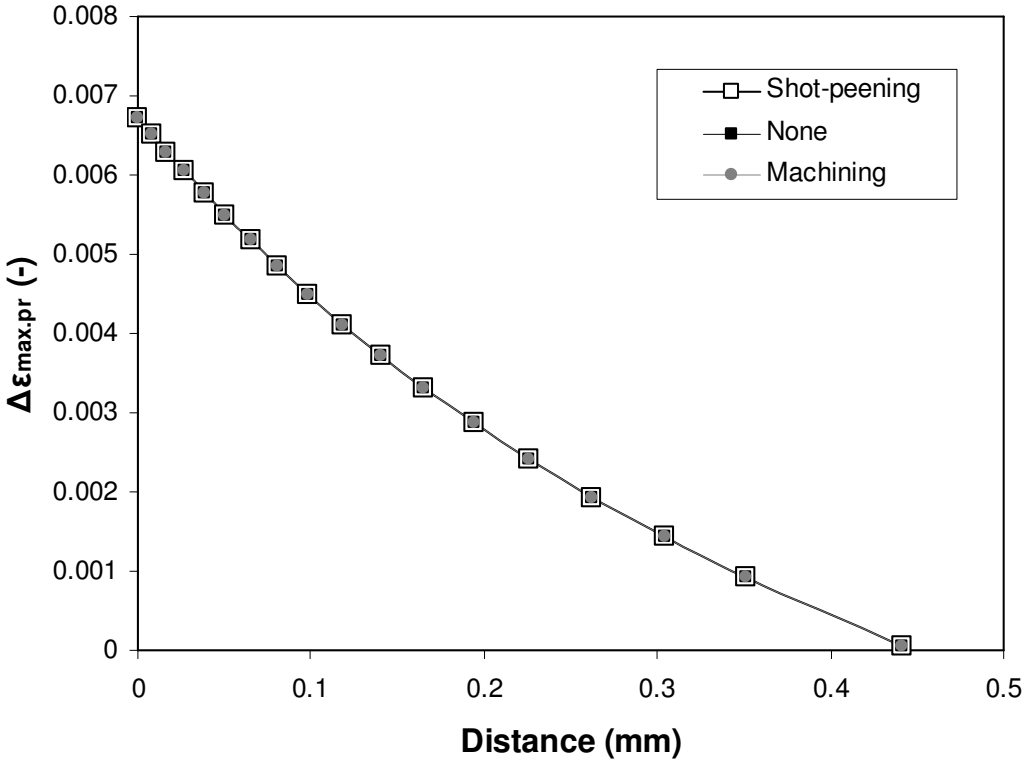

Figure 9.22: Maximum principal plastic strain ranges obtained at the seventieth cycle, at F_{max} of 650 N versus the distance from node A through the thickness

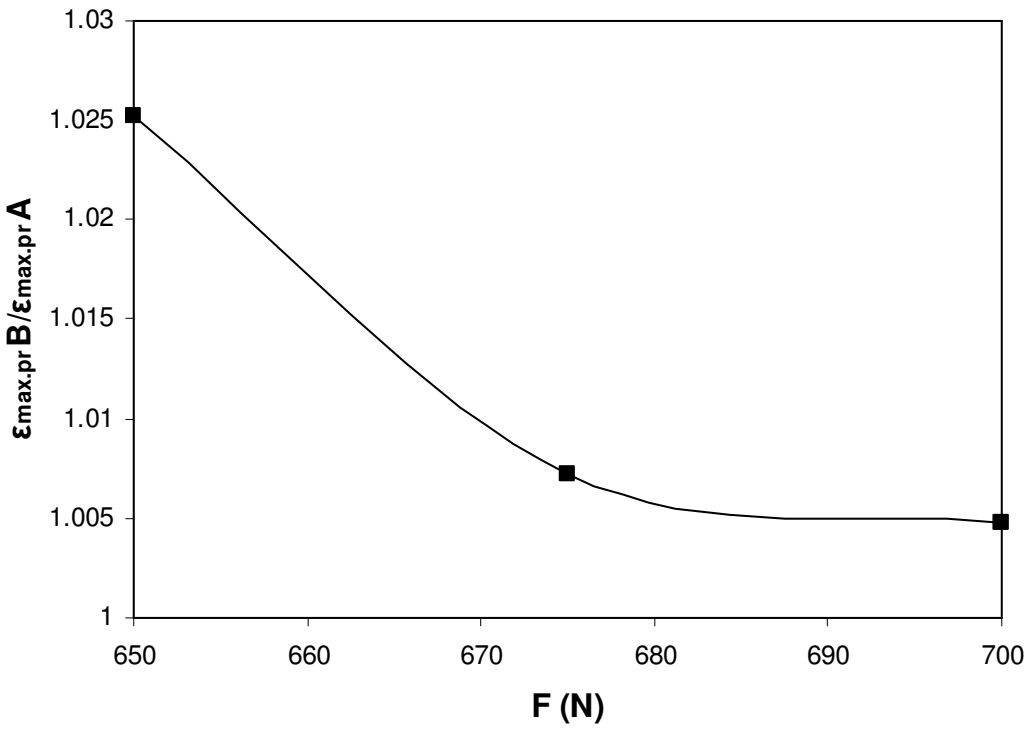

Figure 9.23: Proportion between the maximum principal plastic strains at Node B and node A at F_{max} of 650, 675 and 700 N for the model with shot-peening initial stresses

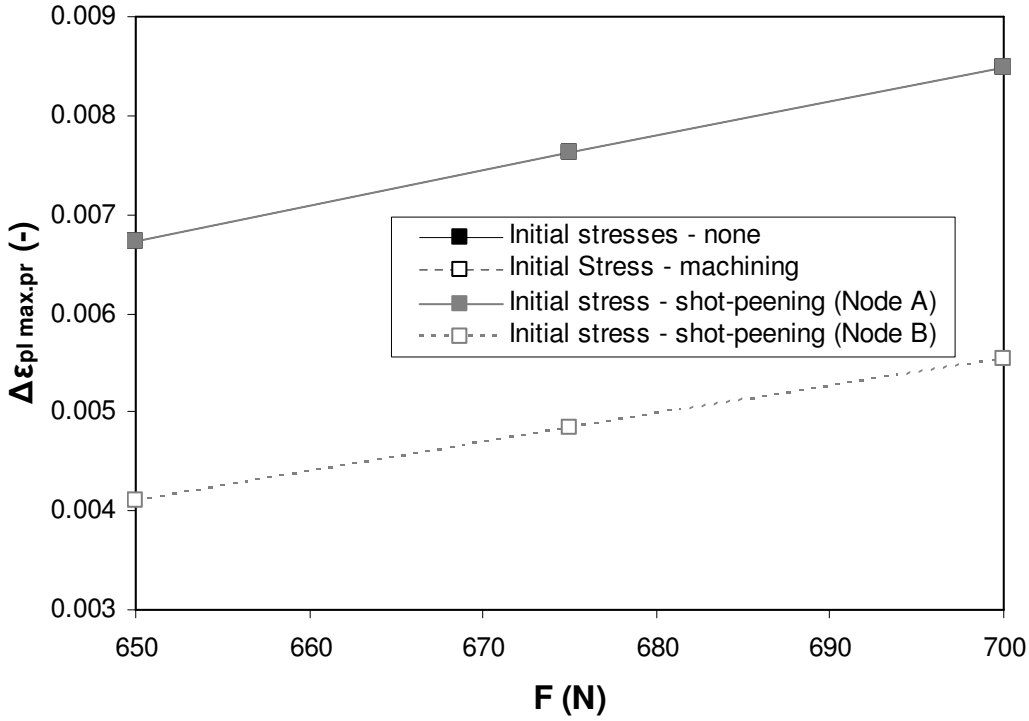

Figure 9.24: Maximum principal plastic strain ranges, obtained at the seventieth cycle, at F_{max} of 650, 675 and 700 N

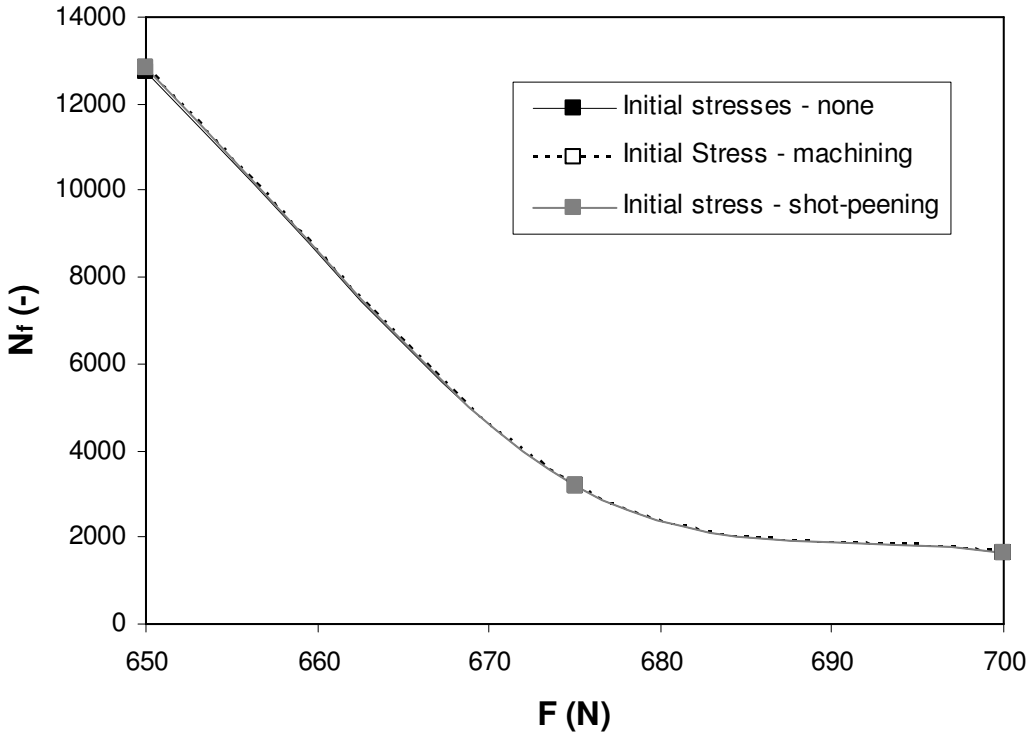

Figure 9.25: Predicted fatigue life at LCF at F_{max} of 650, 675 and 700 N

CHAPTER 10

GENERAL CONCLUSIONS AND RECOMMENDATIONS FOR FUTURE WORK

This chapter contains a review of the main conclusions of this work. Finally, this chapter provides ideas for possible ways to extend the research field presented in this thesis.

10.1 General conclusions

A forging simulation was performed in static and dynamic analyses when the punch was moved into a billet. The inertia calculations were investigated in a dynamic analysis and re-meshing was used. The elastic spring-back was performed in a static analysis by importing the results from the static and the dynamic analyses where the punch was moved into the billet. It can be concluded that for the forging model, the inertia did not have a significant influence on the final results for the used material properties. The model using re-meshing showed similar results as the models without re-meshing which means that the re-meshing algorithms in ABAQUS are reliable and can be used for models where very large plastic deformations are expected. It can be concluded that for simulating a forging process when the punch is moved into the billet, it is suitable to use dynamic analyses with explicit code and re-meshing when very large plastic deformations are expected. The elastic spring-back was calculated in a static analysis where the residual stress state was obtained after releasing the elastic strains from the model.

A casting process was simulated using the FEM. The main goal was to obtain the residual stresses and to implement the gap conductance criterion into the FEA. A parallelepiped geometry surrounded with the mould was used for the simulation. The gap conductance was investigated and implemented in ABAQUS by using the user defined GAPCON subroutine. A mould filling technique was implemented in a

thermal analysis by activating a contact pairs between the mould and the ingot. A solidification criterion was performed based on the temperature observation of the ingot. After the initiation of the solidification, the temperature from the thermal analysis was imported into the coupled temperature-displacement analysis where the final gap formation and the residual stresses were obtained. The gap conductance model was implemented into the complex BCV component of the aero-engine.

Residual stresses for the investment casting simulation of the BCV, subjected to equiaxed cooling, have been obtained in two commercial FE codes (ABAQUS and ProCAST). The temperature and the residual stresses have been compared in both FE codes. The results showed than both codes are suitable for carrying out a casting simulation. Some differences were observed in the residual stress calculations between both codes. However, the calculated peak stresses have the same location and magnitude in both codes. The mould filling effect on the residual stresses has been investigated. The results have shown than for a filling time of 1.63 seconds, the mould filling effect has not significantly affected the residual stresses for the used material properties.

Thermal and mechanical FEAs of a HPTB have been performed where the temperature and the residual stresses at withdrawal velocities of 0.6 and 0.06 mm/s have been obtained. It has been observed that for a withdrawal velocity of 0.6 mm/s, the temperature of the ingot in the baffle zone of the Bridgman furnace was in a liquid stage which is undesirable. Also, temperature differences in the cross sections have been observed which lead to creation of stray grains. The temperature at six nodes of the ingot for a withdrawal velocity of 0.06 mm/s has been also investigated. It has been observed that the temperature of the ingot in the baffle zone of the Bridgman furnace is in a solid stage which indicates the desired dendrites growth in the direction of withdrawal. Some nodes in the lower (thick) part of the HPTB have been found in the mushy stage. This indicated that a lower withdrawal velocity needs to be applied in that area. Also, an equal temperature for a withdrawal velocity of 0.06 mm/s in the cross sections has been observed which avoids creation of stray grains. Higher residual stresses have been determined in the lower (thick) part of the HPTB for a withdrawal velocity of 0.6 compared to 0.06 mm/s. The residual stresses in the rest of the HPTB have been found within a close range for both

withdrawal velocities. The peak stresses have been observed in the sharp corners of the HPTB.

The shot-peening process is widely used in industry for improving the life of components by replacing the surface tensile stresses with compressive stresses. Shot-peening was simulated using the FEM by performing a single shot with velocities in the range 5 – 100 m/s. The residual stresses and the spring-back recovery were investigated. It was shown that by increasing the shot velocity the springback recovery increases. Mapping algorithm and techniques were developed in order to map stresses obtained from processes simulated on a micro scale, such as shot-peening, machining, roller-burnishing, etc into new macro 2D and 3D FE models. The mapping techniques were applied to a perforated parallelepiped, a geometry with a complex surface and a simplified aero-engine vane by using the residual stresses obtained from the shot-peening simulation. The mapping techniques were successfully implemented in ABAQUS where the stresses from the shot-peening were mapped.

The manufacturing processes can be simulated using different FEPs and meshes. Four interpolation techniques for mapping FE data between 2D and 3D meshes with different element types and densities were developed and demonstrated. The four techniques are capable of mapping FE data between different FE meshes. The method using the element shape function showed the highest accuracy. The distance method using field of points and the distance method using elements showed acceptable results. The nearest point method showed poor results when mapping from coarse to refined meshes. All four techniques showed similar results when the mapping was performed from refined to coarse meshes. However, for very large models, the nearest point method is computationally efficient. The distance method using field of points can be used for mapping data from models using meshless method to FEM.

A new finite element data exchange system (FEDES) was developed and its structure and capabilities has been described. FEDES has been used to simulate two chains of manufacturing processes. Three manufacturing processes (casting, forging and heat treatment) have been simulated in the first chain and FEDES has been used

for FE data mapping and transferring between different FE meshes. The deformed shape, residual stresses and the equivalent plastic strains have been transferred and mapped between the models. Five manufacturing processes (metal deposition, welding, heat treatment, machining and shot-peening) have been simulated in the second chain in different FE codes and meshes. The simulations have been successfully performed on aero-engine vane component.

The effects of the micro stresses from machining and shot-peening were investigated on the fatigue life of a U-notch beam subjected to three point bending. It has been observed that the hot-spots at HCF and LCF, for the models with none and micro machining initial stresses, were located on the surface of the notched area, while for the model with shot-peening initial stresses the hot-spot was located inside the material. The shot-peening compressive stresses significantly improved the life at HCF, more than 1.2 times, when the specimen has been loaded with F_{max} = 100 N and more than 2.3 times at load F_{max} = 150 N, compared to the model with none initial stresses. The micro machining tensile stresses resulted in plastic behaviour at low loads which leads to decreasing the fatigue life. The three models with none, micro machining and shot-peening initial stresses arrived at similar life predictions at LCF. The shot-peening compressive stresses improved the fatigue life with 0.8% at F_{max} = 650 N and 0.3 % at F_{max} = 700 N when the hot-spot has been selected at the surface of the notched. It has been observed that the micro machining tensile stresses increased the mean plastic stains while the compressive shot-peening stresses decreased the mean plastic strains.

10.2 Recommendations for future work

As discussed, the casting processes create high residual stresses in the components. Further research can be performed to investigate different cooling regimes for decreasing the residual stresses. It has been assumed that the feeding system of the investment casting of the BCV has no influence on the simulation. Further research can be carried out to predict the residual stresses by including the feeding system into the FEA for simulating the BCV or other industrial components. Optimizations

for obtaining quality HPTB by controlling the withdrawal velocity can be made in the FEA by implementing algorithms in user defined subroutines.

FEDES can be extended to support a wider range of FE data for the existing FEPs. More FEPs can be added to FEDES which can make it an attractive and useful system in industry and research organizations. The calculation speed of the mapping techniques can be optimized for performing faster calculations. More mapping techniques can be developed and embedded in FEDES, e.g. the shape function can be formed by a field of points, as in the meshless methods, and Lagrange interpolation can be used. This can allow transferring and mapping data between solvers using FEM and meshless method. The micro-to-macro mapping techniques can be extended to the meshless method and BEM. All these improvements can take FEDES on a commercial level.

Improving the fatigue life of the component can be performed by optimization of the manufacturing chains. This can be achieved by performing a number of loops by changing the geometry or some of the parameters for the corresponding manufacturing process. For example, for increasing the life of the core vane from Section 8.5 the shot-peening can be applied at the areas with high tensile stress concentration. Such engineering decisions can be investigated to accurately predict and extend the life of the components.

REFERENCES

[1] C.C. Aydıner, E. Üstündag, Residual stresses in a bulk metallic glass cylinder induced by thermal tempering, Mechanics of Materials 37 (2005) 201–212

[2] C.C. Aydıner, E. Üstündag, B. Clausen, J.C. Hanan, R.A. Winholtz, M.A.M. Bourke, A. Peker, Residual stresses in a bulk metallic glass–stainless steel composite, Materials Science and Engineering A 399 (2005) 107–113

[3] A. Diószegi , I.L. Svensson, On the problems of thermal analysis of solidification, Materials Science and Engineering A 413–414 (2005) 474–479

[4] M.Y. He, M. Kiser, B. Wu, F.W. Zok, Influence of thermal expansion mismatch on residual stresses and flow response of microballoon composites, Mechanics of Materials 23 (1996) 133-146

[5] J. Sengupta, S.L. Cockcroft, D.M. Maijer, A. Larouche, Quantification of temperature, stress, and strain fields during the start-up phase of direct chill casting process by using a 3D fully coupled thermal and stress model for AA5182 ingots, Materials Science and Engineering A 397 (2005) 157–177

[6] B.G. Kim, S.L. Dong, S.D. Park, Effects of thermal processing on thermal expansion coefficient of a 50 vol.% SiCp/Al composite, Materials Chemistry and Physics 72 (2001) 42–47

[7] B. C. Lui, J. W. Kang, S. M. Xiong, A study on the numerical simulation of thermal stress during the solidification of shaped castings, Science and Technology of Advance Materials 2 (2001) 157-164

[8] H. Farhangi, S. Norouzi, M. Nili-Ahmadabadi, Effects of casting process variables on the residual stress in Ni-base superalloys, Journal of Materials Processing Technology 153–154 (2004) 209–212

[9] A.E. Ragab, Sensitivity analysis of casting distortion and residual stress prediction through simulation modelling and experimental verification, Thesis (2003) Ohio State University

[10] O.N. Grigoriev, A.V. Karoteev, E.N. Maiboroda, I,L. Berezhinsky, B.K. Serdega, D.Yu. Ostrovoi, V.G. Piskumov, Structure, nonlinear stress–strain state and strength of ceramic multilayered composites, Composites: Part B xx (2006) 1-12

[11] D. Metzger, K. Jarrett New, J. Dantzing, A sand surface element for efficient modeling of residual stress in castings, Apllied Mathematikal Modelling 25 (2001) 825-842

[12] X.L. Yang, H.B. Dong, W. Wang, P.D. Lee, Microscale simulation of stray grain formation in investment cast turbine blades, Material Science and Engineering A 386 (2004) 129–139

[13] A. Kermanpur, M. Mehrara, N. Varahram and P. Davami, Improvement of grain structure and mechanical properties of a land bases gas turbine blade directionally solidified with liquid metal cooling process, 2008 Institute of Materials, Minerals and Mining Published by Maney on behalf of the Institute DOI 10.1179/174328407X239109

[14] N. D'Souza, M. Newell, K. Devendra, P.A. Jennings, M.G. Ardakani, B.A. Shollock, Formation of low angle boundaries in Ni-based supperalloys, Material Science and Engineering A 413-414 (2005) 567–750

[15] N. Hofmann, S. Olive, G. Laschet, F. Hediger, J. Wolf and P.R. Sahm, Numerical optimization of process control variables for the Bridgman casting process, Modelling Simul. Mater. Sci. Eng. 5 (1997) 23-34

[16] H. Esaka, K. Shinozuka, M. Tamura, Analysis of single crystal casting process taking into account the shape of pigtail, Material Science and Engineering A 413-414 (2005) 151–155

[17] P. Carter, D.C. Cox, C.A. Gandin, R.C. Reed, Process modelling of grain selection during the solidification of single crystal superalloy castings, Materials Science and Engineering A 280 (2000) 233-246

[18] H. Saari, J. Beddoess, D.Y. Seo, L. Zhao, Development of directionally solidified γ-TiAl structure, Intermetallics 13 (2005) 937-943

[19] D.Z. Li, J. Campbell, Y.Y. Li, Filling system for investment cast Ni-base turbine blades, Journal of Materials Processing Technology 148 (2004) 310-316

[20] J.F. Wang, R.H. Wagoner, W.D. Carden, D.K. Matlock, F. Barlat, Creep and anelasticity in the springback of aluminium, International Journal of Plasticity 20 (2004) 2209–2232

[21] G. Gantar, K. Kuzman, M. Makarovič, An industrial example of FE supported development of a new product, Journal of Materials Processing Technology 150 (2004) 163–169

[22] M.P. Mungi, S.D. Rasane, P.M. Dixit, Residual stresses in cold axisymmetric forging, Journal of Materials Processing Technology 142 (2003) 256–266

[23] D.A. Tanner and J.S. Robinson, Residual Stress Prediction and Determination in 7010 Aluminium Alloy Forgings, Experimental Mechanics Vol. 40, No. 1, March 2000

[24] A. Giuliani, G. Albertini, A. Manescu, Residual stress analysis on tensile MMC specimens after loading/unloading tests in several conditions, Physica B 350 (2004) e499–e501

[25] M.K. Lee, G.H. Kim, K.H. Kim, W.W. Kim, Control of surface hardnesses, hardening depths, and residual stresses of low carbon 12Cr steel by flame hardening, Surface and Coatings Technology 184 (2004) 239–246

[26] J.S. Robinson and D.A. Tanner, Residual stress development and relief in high strength aluminium alloys using standard and retrogression thermal treatments, 2003 Io M Communication Ltd

[27] G.P. Dolan, J.S. Robinson, Residual stress reduction in 7175-T73, 6061-T6 and 2017A-T4 aluminium alloys using quench factor analysis, Journal of Materials Processing Technology 153–154 (2004) 346–351

[28] S. Serajzadeh, Thermo-Mechanical Modeling of Hot Forging Process, Vol. 126, 2006

[29] H. Hsieh, J. Lin, Study of the buckling mechanism in laser tube forming, Optics & Laser Technology 37 (2005) 402–409

[30] C.Y. Gao, P. Lours, G. Bernhart, Thermomechanical stress analysis of superplastic forming tools, Journal of Materials Processing Technology 169 (2005) 281–291

[31] A. Giuliani, G. Albertini, F. Fiori, E. Girardin, Residual stress analysis on AA6061+22%Al 2O3p simple shape demonstrators of a wheel hub, Physica B 350 (2004) e495–e498

[32] D.A. Tanner, J.S. Robinson, Modelling stress reduction techniques of cold compression and stretching in wrought aluminium alloy products, Finite Elements in Analysis and Design 39 (2003) 369–386

[33] M.B. Prime, M.A. Newborn, and J.A. Balog, Quenching and .Cold Work Residual Stresses in Aluminium Hand Forgings: Contour Method

Measurement and FEM Prediction, Materials Science Forum Vols. 426-432 (2003) pp. 435-440

[34] J. Kosanov, J.G. Lenard , J. Uhrig, B. Wallfarth, The effect of lubricant additives on the coefficient of friction in the flat-die test, Materials Science and Engineering A 427 (2006) 274–281

[35] D.Y. Jang, J.H. Liou, Study of stress development in axi-symmetric products processed by radial forging using a 3-D non-linear finite-element method, Journal of Materials Processing Technology 74 (1998) 74–82

[36] W.M. Quach, J.G. Teng, K.F. Chung, Residual stresses in steel sheets due to coiling and uncoiling: a closed-form analytical solution, Engineering Structures 26 (2004) 1249–1259

[37] W.M. Quach, J.G. Teng, K.F. Chung, Finite element predictions of residual stresses in press-braked thin-walled steel sections, Engineering Structures (2006)

[38] P. Fogarassy, A. Manescu, N. Markocsan, F. Rustichelli, Residual stress analysis in near net-shape formed specimens obtained by thermal spraying, Physica B 350 (2004) e537–e539

[39] J.R. Cho, Y.S. Joo, H.S. Jeong, The Al-powder forging process: its finite element analysis, Journal of Material Process Technology 111 (2001) 204-209

[40] F.P. Bowden and D. Tabor, The Friction and Lubrication of Solids, Oxford University Press, London, 1950, pp. 20-32.

[41] L.C. Thomas, Heat Transfer Secon Edition, Capstone Publishing Corporation, 1999

[42] E.L. Olsen, S.V. Garimella and C.V. Madhusudana, Modeling of Constriction Resistance in Coated Joints, AIAA Journal of Thermophysics and Heat Transfer, Vol. 16, 2002, pp. 207-216.

[43] M. G. Cooper, B. B. Mikic and M. M. Yovanovich, Thermal Contact Conductance, int. J. Heat Mass Transfer. Vol. 12, pp. 279400. Pergamoon Press 19699.

[44] C.V. Madhusudana, Thermal conductance of cylindrical joints, International Journal of Heat and Mass Transfer 42 (1999) 1273-1287

[45] J.J. Fuller and E.E. Marotta, Thermal Contact Conductance of Metal/Polymer Joints: An Analytical and Experimental Investigation, Journal of Thermophysics and Heat Transfer, (2001) Vol. 15, No. 2, pp. 228-238.

[46] J.H. Lee, H.S. Kim, C.W. Won, B. Cantor, Effect of the gap distance on the cooling behaviour and the microstructure of indirect squeeze cast and gravity die cast 5083 wrought Al alloy, Materials Science and Engineering A338 (2002) 182-190

[47] S.M.S. Wahid, C.V. Madhusudana, Thermal contact conductance: effect of overloading and load cycling, International Journal of Heat and Mass Transfer 46 (2003) 4139–4143

[48] S.M.S. Wahid, C.V. Madhusudana, E. Leonardi, Solid spot conductance at low contact pressure, Experimental Thermal and Fluid Science 28 (2004) 489–494

[49] V. Singhal, P.J. Litke, A.F. Black, S.V. Garimella, An experimentally validated thermo-mechanical model for the prediction of thermal contact conductance, International Journal of Heat and Mass Transfer 48 (2005) 5446–5459

[50] R. Xu, H. Feng, L. Zhao, L. Xu, Experimental investigation of thermal contact conductance at low temperature based on fractal description, International Communications in Heat and Mass Transfer 33 (2006) 811–818

[51] J.L.M. Fernandes, P.A.F.Martins, All-hexahedral remeshing for the finite element analysis of metal forming processes, Finite Elements in Analysis and Design 43 (2007) 666-679

[52] D. Dureisseix, H. Bavestrello, Information transfer between incompatible finite element meshes: Applicatio to coupled thermo-viscoelasticity, Computer Methods in Applied Mechanics and Engineering 195 (2006) 6523-6541

[53] Y. Luo, A nearest-nodes finite element method with local multivariate Lagrange interpolation, Finite Elements in Analysis and Design 44 (2008) 797-803

[54] S. Hyun, L. Lindgren, Simulating a chain of manufacturing processes using a geometry-based finite element code with adaptive meshing, Finite Elements in Analysis and Design 40 (2004) 511-528

[55] M. Pietrzyk, L. Madej, S. Weglarczyk, Tool for optimal design of manufacturing chain based on metal forming, CIRP Annals – Manufacturing Technology 57 (2008) 309-312

[56] H. Jahansson, P. Astrom, K. Orsborn, A system for information management in simulation of manufacturing processes, Advances in Engineering Software 35 (2004) 725-733

[57] ABAQUS Analysis User's Manuel, Hibbitt, Karlsson & Sorensen, Inc., Pawtucket, Rhode Island, 6.5-1 edition, 2004

[58] ABAQUS Theory Manuel, Hibbitt, Karlsson & Sorensen, Inc., Pawtucket, Rhode Island, 6.5-1 edition, 2004

[59] ABAQUS/CAE User's Manuel, Hibbitt, Karlsson & Sorensen, Inc., Pawtucket, Rhode Island, 6.5-1 edition, 2004

[60] E.M. Kennard, Kinetic Theory of Gases, McGrow – Hill, New York, 1938

[61] G. Dour, M. Dargusch, C. Davidson, Recommendations and guidelines for the performance of accurate heat transfer measurements in rapid forming processes, International Journal of Heat and Mass Transfer 49 (2006) 1773-1789

[62] A.H. Yaghi, T.H. Hyde, A.A. Becker, J.A. Williams, W. Sun, Residual stress simulation in welded sections of P91 pipes, Journal of Materials Processing Technology 167 (2005) 480–487

[63] M. Anderson, R. Patwa and Y.C. Shin, Laser-assisted machining of Inconel 718 with an economic analysis, International Journal of Machine Tools & Manufacture 46 (2006) 1879–1891

[64] R.A. Overfelt and R. E. Taylor: Thermal Conductivity 23, edited K.E. Wilkes, R.B. Dinwiddie and R.S. Graves (Technomic, Basle, 1996) pp 538-549

[65] J.B. Henderson and A. Strobel.: Thermal conductivity 23 edited K E Wilkes, R.B. Dunwiddie and R.S. Graves (Technomic, Basle, 1996) pp 530-537

[66] M.A. Arafin, M. Medraj, D.P. Turner and P. Bocher, Transient liquid phase bonding of Inconel 718 and Inconel 625 with BNi-2: Modeling and experimental investigations, Materials Science and Engineering A 447 (2007) 125–133

[67] M.S. Lewandowski and R.A. Overfelt, High temperature deformation behaviour of solid and semi-solid alloy 718, PII: S1359-6454(99) 00252-9

[68] G. Appa Rao, M. Srinivas, D.S. Sarma, Effect of oxygen content of powder on microstructure and mechanical properties of hot isostatically pressed superalloy Inconel 718, Materials Science and Engineering A 435–436 (2006) 84–99

[69] M. Preuss, P.J. Withers, G.J. Baxter, A comparison of inertia friction welds in thee nickel base superalloys, Materials Science and Engineering A 437 (2006) 8–45

[70] D. Kim, J. Kim, J. Sa, Y. Lee, C. Park, S. Moon, Stress rupture characteristics of Inconel 718 alloy for ramjet combustor, Materials Science and Engineering A 483–484 (2008) 262–265

[71] A. Thomas, M. El-Wahabi, J.M. Cabrera, J.M. Prado, High temperature deformation of Inconel 718, Journal of Materials Processing Technology 177 (2006) 469–472

[72] www.hightempmetals.com

[73] R.C. Reed, The Superalloys Fundamentals and Applications, Cambridge University Press, 2006

[74] M. Rappaz and Ph. Thévoz, Acta Metall 35 (1987), p. 2929.

[75] C.Y. Wang and C. Beckermann, Metall Trans A 24 (1993), p. 2787.

[76] C.Y. Wang and C. Beckermann, Mater Sci Eng A 171 (1993), p. 199

[77] O. Grong, A.K. Dahle, M.I. Onsøien and L. Arnberg, Acta Mater 46 (1998), p. 5045.

[78] O. Nielsen, B. Appolaire, H. Combeau and A. Mo, Metall Mater Trans A 32 (2001), p. 2049

[79] ESI Group, ProCast 2007.0 User's Manual, ESI Group, 2007

[80] A. Meneghini, L. Tomesani, Chill material and size effects on HTC evolution in sand casting of aluminum alloys, Journal of Materials Processing Technology 162–163 (2005) 534–539

[81] S. Alaruri, L. Bianchini, A. Brewington, Effective spectral emissivity measurements of superalloys and YSZ thermal barrier coating at high temperatures using a 1.6 μm single wavelength pyrometer, Optics and Lasers in Engineering 30 (1998) 77-91

[82] P. Spittle, Gas turbine technology, 2003 IOP Publishing Ltd

[83] A.J. Elliott and T.M. Pollock, Thermal Analysis of the Bridgman and Liquid Metal-Cooled Directional Solidification Investment Casting Processes, Metallurgical and materials transactions Volume 38A April 2007—871

[84] D. Siebörger, H. Knake, U. Glatzel, Temperature dependence of the elastic moduli of the nickel-base superalloy CMSX-4 and its isolated phases, Material Science and Engineering A 298 (2001) 26-33

[85] B. Baufeld, M. Bartsch, M. Heinzelmann, Advanced thermal gradient mechanical fatigue testing of CMSX-4 with an oxidation protection coating, International Journal of Fatigue 30 (2008) 219-225

[86] J. Carrigan, M.G. Launsbach, J.R. Mihalisin, Nickel base superalloy and single crystal castings, Patent Application Publication US 2004/0213693 A1

[87] K.C. MILLS, Y.M. YOUSSEF and Z. LI, The Effect of Aluminium Content on Thermophysical Properties of Ni-based Superalloys, ISIJ International, Vol. 46 (2006), No. 1, pp. 50-57

[88] H. Tanaka, S. Sawai, K. Morimoto and K. Hisano, Mesurement of spectral emmissivity and thermal conductivity of zirconia by thermal radiation calorimetry, Journal of Thermal Analysis and Calorimetry, Vol. 64 (2001) 867-872

[89] H. Shinno, M. Kitajima and M. Okada, Thermal stress analysis of high heat flux materials, Journal of Nuclear Materials 155-157 (1988) 290-294, North Holland Amsterdam

[90] H. Hashizume, K. Miya, Thermomechanical behaviour of the first wall subjected to plasma disruption, Fusion Engineering and Design, 5 (2) 141-154 (1987)

[91] T. Hong, J.Y. Ooi, B. Shaw, A numerical simulation to relate the shot peening parameters to the induced residual stresses, Engineering Failure Analysis 15 (2008) 1097–1110

[92] T. Hong, J.Y. Ooi, B. Shaw, A numerical study of the residual stress pattern from single shot impacting on a metallic component, Advances in Engineering Software 39 (2008) 743–756

[93] J. Edberg, L. Lindgren, K. Mori Shot peening simulated by two different finite element formulations. In: Shen S, Dawson E, editors. Simulation of materials processing: theory, methods and applications –NUMIFORM95; 1995. p. 425–30

[94] K. Schiffner and C.D. Helling, Simulation of residual stresses by shot peening, Comput Struct 72 (1999), pp. 329–340

[95] S. Baragetti, Three-dimensional finite element procedures for shot peening residual stress field prediction, Int J Comput Appl Technol 14 (2001), pp. 51–63

[96] S.A. Meguid, G. Shagal, J.C. Stranart and J. Daly, Three-dimensional dynamic finite element analysis of shot-peening induced residual stresses, Finite Elem Anal Des 31 (1999), pp. 179–191

[97] Y. Harada, K. Fukauara and S. Kohamada, Effects of microshot peening on surface characteristics of high-speed tool steel, journal of materials processing technology 201 (2008) 319–324

[98] E.O. Ezugwu, J. Bonney, D.A. Fadare, W.F. Sales, Machining of nickel-base, Inconel 718, alloy with ceramic tools under finishing conditions with various coolant supply pressures, Journal of Materials Processing Technology 162–163 (2005) 609–614

[99] M. Cantu, Mastering Delphi 6, SYBEX, Inc. 2001

[100] P. Kimmel, Building Delphi 6 Applications, 2001 Osborne/McGraw-Hill

[101] X. Pacheco, Delphi for .NET, 2004 SAMS

[102] www.paraview.org

[103] S.M. Afazov, FEDES User's Manual, University of Nottingham - 2008

[104] K. Kobayashi, K. Yamaguchi, M. Hayakawa, M. Kimura, High-temperature fatigue properties of austenitic superalloys 718, A286 and 304L,International Journal of Fatigue 30 (2008) 1978–1984

[105] T. Connolley, M.J. Starink and P.A.S. Reed, Effect of broaching on high-temperature fatigue behaviour in notched specimens of Inconel 718, Metallurgical and materials transactions 35A (2004) 771

[106] L.F. Coffin and J.F. Tavernelli, Trans. AIME 215 (1959), pp. 794–807.

[107] S.S. Manson, Mach. Des. 21 (1960), pp. 139–144.

[108] M. Zimmermann, V. Schulze, H. U. Baron & D. Löhe (2008), A Novel 3D Finite Element Simulation Model for the Prediction of the Residual Stress State after Shot Peening, in 'Proc. of the 10th Int. Conf. on Shot Peening'.

[109] O.H. Basquin, The exponential law of endurance test, Proc ASTM 10 (1910), pp. 625–630.

[110] J. Lemaitre, and J.-L. Chaboche, Mechanics of Solid Materials, Cambridge University Press, 1990.

[111] T.J. Ypma, Historical development of the Newton-Raphson method, SIAM Review 37 (4), 531–551, 1995.

[112] O. C. Zienkiewicz, R. L. Taylor and J. Z. Zhu, The Finite Element Method: Its Basis and Fundamentals, 6th edition, Oxford: Elsevier Butterworth-Heinemann, 2005.

[113] R.I. Stephens, A. Fatemi, Robert R. Stephens, Henry O. Fuchs, Metal fatigue in engineering, AJohn Wiley & Sons, Inc. 2001

APPENDIX ONE

DEFINING THE LOCAL COORDINATES OF THE ELEMENT SHAPE FUNCTION FOR 2-D AND 3-D LINEAR ELEMENTS

A1.1 Triangular elements

Figure A1.1 shows a three node triangular element with local coordinates (g and h) and node M.

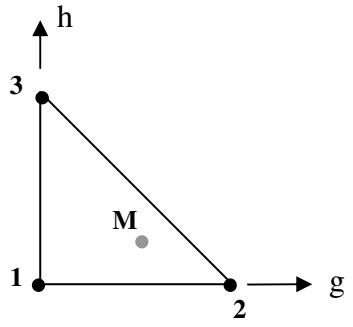

Figure A1.1: Three node triangular element and node M

where g and h are the local coordinates for the element, they span a range from 0 to 1and must satisfy the following equation:

$$g + h \leq 1 \tag{A1.1}$$

The local coordinates can be obtained by solving a system of equations:

$$\begin{vmatrix} x_M = (1-g-h)x_1 + gx_2 + hx_3 \\ y_M = (1-g-h)y_1 + gy_2 + hy_3 \end{vmatrix} \tag{A1.2}$$

The system of Equations (A1.2) after algebraic manipulation can be given by:

$$\begin{vmatrix} x_M - x_1 = g(x_2 - x_1) + h(x_3 - x_1) \\ y_M - y_1 = g(y_2 - y_1) + h(y_3 - y_1) \end{vmatrix} \tag{A1.3}$$

Using linear algebra, the system of linear equations (A1.3) can be given by:

$$\begin{bmatrix} x_M - x_1 \\ y_M - y_1 \end{bmatrix} = \begin{bmatrix} x_2 - x_1 & x_3 - x_1 \\ y_2 - y_1 & y_3 - y_1 \end{bmatrix} \times \begin{bmatrix} g \\ h \end{bmatrix} \tag{A1.4}$$

The local coordinates g and h can be given by:

$$g = \begin{vmatrix} x_M - x_1 & x_3 - x_1 \\ y_M - y_1 & y_3 - y_1 \end{vmatrix} / Det = ((x_M - x_1)(y_3 - y_1) - (x_3 - x_1)(y_M - y_1)) / Det \quad \text{(A1.5)}$$

$$h = \begin{vmatrix} x_2 - x_1 & x_M - x_1 \\ y_2 - y_1 & y_M - y_1 \end{vmatrix} / Det = ((x_2 - x_1)(y_M - y_1) - (x_M - x_1)(y_2 - y_1)) / Det \quad \text{(A1.6)}$$

where:

$$Det = \begin{vmatrix} x_2 - x_1 & x_3 - x_1 \\ y_2 - y_1 & y_3 - y_1 \end{vmatrix} = (x_2 - x_1)(y_3 - y_1) - (x_3 - x_1)(y_2 - y_1) \quad \text{(A1.7)}$$

If Det is equal to zero, it means that the element volume is zero.

A1.2 Tetrahedron elements

Figure A1.2 shows a four node tetrahedron element with local coordinates (g , h and r) and node M.

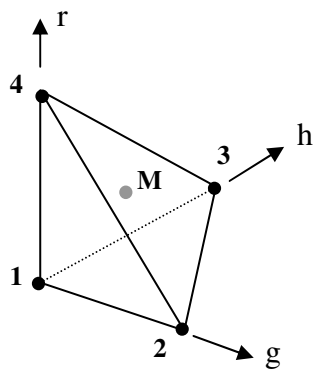

Figure A1.2: Four node hexahedron element and node M

where g , h and r are the local coordinates for the element, they span a range from 0 to 1and must satisfy the Equation (A1.8):

$$g + h + r \leq 1 \quad \text{(A1.8)}$$

The local coordinates can be obtained by solving a system of equations (A1.9)

$$\begin{vmatrix} x_M = (1 - g - h - r)x_1 + gx_2 + hx_3 + rx_4 \\ y_M = (1 - g - h - r)y_1 + gy_2 + hy_3 + ry_4 \\ z_M = (1 - g - h - r)z_1 + gz_2 + hz_3 + rz_4 \end{vmatrix} \quad \text{(A1.9)}$$

The system of equations (A1.9), after an algebraic manipulation, can be given by:

$$\begin{cases} x_M - x_1 = g(x_2 - x_1) + h(x_3 - x_1) + r(x_4 - x_1) \\ y_M - y_1 = g(y_2 - y_1) + h(y_3 - y_1) + r(y_4 - y_1) \\ z_M - z_1 = g(z_2 - z_1) + h(z_3 - z_1) + r(z_4 - z_1) \end{cases} \tag{A1.10}$$

Using linear algebra, the system of linear equations (A1.10) can be given by:

$$\begin{bmatrix} x_M - x_1 \\ y_M - y_1 \\ z_M - z_1 \end{bmatrix} = \begin{bmatrix} x_2 - x_1 & x_3 - x_1 & x_4 - x_1 \\ y_2 - y_1 & y_3 - y_1 & y_4 - y_1 \\ z_2 - z_1 & z_3 - z_1 & z_4 - z_1 \end{bmatrix} \times \begin{bmatrix} g \\ h \\ r \end{bmatrix} \tag{A1.11}$$

The local coordinate g is given by:

$$g = \begin{vmatrix} x_M - x_1 & x_3 - x_1 & x_4 - x_1 \\ y_M - y_1 & y_3 - y_1 & y_4 - y_1 \\ z_M - z_1 & z_3 - z_1 & z_4 - z_1 \end{vmatrix} / Det \tag{A1.12}$$

or

$$g = \begin{pmatrix} (x_M - x_1)(y_3 - y_1)(z_4 - z_1) - (x_M - x_1)(y_4 - y_1)(z_3 - z_1) - \\ -(y_M - y_1)(x_3 - x_1)(z_4 - z_1) + (y_M - y_1)(x_4 - x_1)(z_3 - z_1) + \\ +(z_M - z_1)(x_3 - x_1)(y_4 - y_1) - (z_M - z_1)(x_4 - x_1)(y_3 - y_1) \end{pmatrix} / Det \tag{A1.13}$$

The local coordinate h is given by:

$$h = \begin{vmatrix} x_2 - x_1 & x_M - x_1 & x_4 - x_1 \\ y_2 - y_1 & y_M - y_1 & y_4 - y_1 \\ z_2 - z_1 & z_M - z_1 & z_4 - z_1 \end{vmatrix} / Det \tag{A1.14}$$

or

$$h = \begin{pmatrix} (x_2 - x_1)(y_M - y_1)(z_4 - z_1) - (x_2 - x_1)(y_4 - y_1)(z_M - z_1) - \\ -(y_2 - y_1)(x_M - x_1)(z_4 - z_1) + (y_2 - y_1)(x_4 - x_1)(z_M - z_1) + \\ +(z_2 - z_1)(x_M - x_1)(y_4 - y_1) - (z_2 - z_1)(x_4 - x_1)(y_M - y_1) \end{pmatrix} / Det \tag{A1.15}$$

The local coordinate r is given by:

$$r = \begin{vmatrix} x_2 - x_1 & x_3 - x_1 & x_M - x_1 \\ y_2 - y_1 & y_3 - y_1 & y_M - y_1 \\ z_2 - z_1 & z_3 - z_1 & z_M - z_1 \end{vmatrix} / Det \tag{A1.16}$$

or

$$r = \begin{pmatrix} (x_2 - x_1)(y_3 - y_1)(z_M - z_1) - (x_2 - x_1)(y_M - y_1)(z_3 - z_1) - \\ -(y_2 - y_1)(x_3 - x_1)(z_M - z_1) + (y_2 - y_1)(x_M - x_1)(z_3 - z_1) + \\ +(z_2 - z_1)(x_3 - x_1)(y_M - y_1) - (z_2 - z_1)(x_M - x_1)(y_3 - y_1) \end{pmatrix} / Det \tag{A1.17}$$

The determinant Det can be defined as:

$$Det = \begin{vmatrix} x_2 - x_1 & x_3 - x_1 & x_4 - x_1 \\ y_2 - y_1 & y_3 - y_1 & y_4 - y_1 \\ z_2 - z_1 & z_3 - z_1 & z_4 - z_1 \end{vmatrix} \tag{A1.18}$$

or

$$\begin{aligned} Det = {} & (x_2 - x_1)(y_3 - y_1)(z_4 - z_1) - (x_2 - x_1)(y_4 - y_1)(z_3 - z_1) - \\ & - (y_2 - y_1)(x_3 - x_1)(z_4 - z_1) + (y_2 - y_1)(x_4 - x_1)(z_3 - z_1) + \\ & + (z_2 - z_1)(x_3 - x_1)(y_4 - y_1) - (z_2 - z_1)(x_4 - x_1)(y_3 - y_1) \end{aligned} \tag{A1.19}$$

If Det is equal to zero, it means that the element volume is zero.

A1.3 Quadrilateral elements

Figure A1.3 shows a four node quadrilateral element with local coordinates (g and h) and node M.

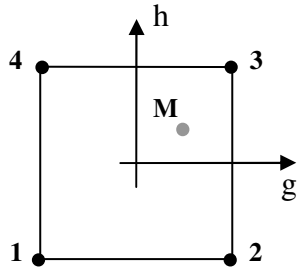

Figure A1.3: Four node quadrilateral element and node M

The local coordinates (g and h) span a range from -1 to +1.

$$g \in [-1,+1] \tag{A1.20}$$

$$h \in [-1,+1] \tag{A1.21}$$

For defining the local coordinates the system of bi-linear equations must be solved:

$$\begin{vmatrix} x_M = \frac{1}{4}\left((1-g)(1-h)x_1 + (1+g)(1-h)x_2 + (1+g)(1+h)x_3 + (1-g)(1+h)x_4\right) \\ y_M = \frac{1}{4}\left((1-g)(1-h)y_1 + (1+g)(1-h)y_2 + (1+g)(1+h)y_3 + (1-g)(1+h)y_4\right) \end{vmatrix}$$

(A1.22)

Equation (A1.22) can be given in the following form:

$$\begin{cases} f_1 = (1-g)(1-h)x_1 + (1+g)(1-h)x_2 + (1+g)(1+h)x_3 + (1-g)(1+h)x_4 - 4x_M = 0 \\ f_2 = (1-g)(1-h)y_1 + (1+g)(1-h)y_2 + (1+g)(1+h)y_3 + (1-g)(1+h)y_4 - 4y_M = 0 \end{cases} \tag{A1.23}$$

The system of equations (A1.23) is solved by using the Newton-Raphson method for solving a system of non-linear equations. This is an iterative method which requires an initial guess close to the solution.

Initial guess values for the local coordinates (g and h) are chosen to be zero. These values are in the middle of the g and h range (see Equations A1.20 and A1.21).

$$g = 0 \tag{A1.24}$$

$$h = 0 \tag{A1.25}$$

Defining the Jacobian matrix (J) for the system of equations (A1.23)

$$J = \begin{bmatrix} \dfrac{\partial f_1}{\partial g} & \dfrac{\partial f_1}{\partial h} \\ \dfrac{\partial f_2}{\partial g} & \dfrac{\partial f_2}{\partial h} \end{bmatrix} \tag{A1.26}$$

or

$$J = \begin{bmatrix} (1-h)(x_2 - x_1) + (1+h)(x_3 - x_4) & (1-g)(x_4 - x_1) + (1+g)(x_3 - x_2) \\ (1-h)(y_2 - y_1) + (1+h)(y_3 - y_4) & (1-g)(y_4 - y_1) + (1+g)(y_3 - y_2) \end{bmatrix} \tag{A1.27}$$

Defining a matrix (M) from the system of equations (A1.23) as a function of the local coordinates g and h for the corresponding iteration ($g = 0$ and $h = 0$ for the initial iteration)

$$M = \begin{bmatrix} f_1(g,h) \\ f_2(g,h) \end{bmatrix} \tag{A1.28}$$

or

$$M = \begin{bmatrix} (1-g)(1-h)x_1 + (1+g)(1-h)x_2 + (1+g)(1+h)x_3 + (1-g)(1+h)x_4 - 4x_M \\ (1-g)(1-h)y_1 + (1+g)(1-h)y_2 + (1+g)(1+h)y_3 + (1-g)(1+h)y_4 - 4y_M \end{bmatrix} \tag{A1.29}$$

Solving the system of linear equations:

$$J \times p = -M \tag{A1.30}$$

where:

$$p = \begin{bmatrix} p_1 \\ p_2 \end{bmatrix} \tag{A1.31}$$

The system of linear Equations (A1.30) is solved as Equation (A1.2). See also Equations A1.3-A1.7.

After solving the system of linear equations (A1.30), the local coordinate values are defined as follow:

$$g = g + p_1 \tag{A1.32}$$

$$h = h + p_2 \tag{A1.33}$$

The iterations are repeated until the following convergence criterion is satisfied.

$$|f_1| + |f_2| \cong 0 \tag{A1.34}$$

The following convergence criterion is applied in the code:

$$|f_1| + |f_2| < 1 \times 10^{-5} \tag{A1.35}$$

Between one and two iterations are required for solving the system of equations (A1.22), using the convergence criterion from equation (A1.35) and the chosen initial guess.

A1.4 Hexahedron elements

Figure A1.4 shows an eight node hexahedron element with local coordinates (g , h and r) and node M.

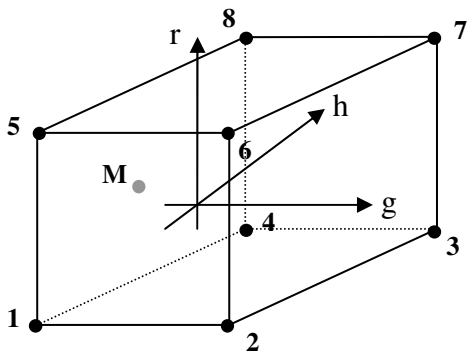

Figure A1.4: Eight node hexahedron element and node M

The local coordinates (g , h and r) span a range from -1 to +1. For defining the local coordinates the following system of tri-linear equations must be solved:

$$\left|\begin{array}{l} x_M = \frac{1}{8}\left(\begin{array}{l}(1-g)(1-h)(1-r)x_1+(1+g)(1-h)(1-r)x_2+\\+(1+g)(1+h)(1-r)x_3+(1-g)(1+h)(1-r)x_4+\\+(1-g)(1-h)(1+r)x_5+(1+g)(1-h)(1+r)x_6+\\+(1+g)(1+h)(1+r)x_7+(1-g)(1+h)(1+r)x_8\end{array}\right) \\ y_M = \frac{1}{8}\left(\begin{array}{l}(1-g)(1-h)(1-r)y_1+(1+g)(1-h)(1-r)y_2+\\+(1+g)(1+h)(1-r)y_3+(1-g)(1+h)(1-r)y_4+\\+(1-g)(1-h)(1+r)y_5+(1+g)(1-h)(1+r)y_6+\\+(1+g)(1+h)(1+r)y_7+(1-g)(1+h)(1+r)y_8\end{array}\right) \\ z_M = \frac{1}{8}\left(\begin{array}{l}(1-g)(1-h)(1-r)z_1+(1+g)(1-h)(1-r)z_2+\\+(1+g)(1+h)(1-r)z_3+(1-g)(1+h)(1-r)z_4+\\+(1-g)(1-h)(1+r)z_5+(1+g)(1-h)(1+r)z_6+\\+(1+g)(1+h)(1+r)z_7+(1-g)(1+h)(1+r)z_8\end{array}\right) \end{array}\right. \qquad \text{(A1.36)}$$

Equation (A1.36) can be given in the following form:

$$\left|\begin{array}{l} f_1 = \left(\begin{array}{l}(1-g)(1-h)(1-r)x_1+(1+g)(1-h)(1-r)x_2+\\+(1+g)(1+h)(1-r)x_3+(1-g)(1+h)(1-r)x_4+\\+(1-g)(1-h)(1+r)x_5+(1+g)(1-h)(1+r)x_6+\\+(1+g)(1+h)(1+r)x_7+(1-g)(1+h)(1+r)x_8-8x_M\end{array}\right)=0 \\ f_2 = \left(\begin{array}{l}(1-g)(1-h)(1-r)y_1+(1+g)(1-h)(1-r)y_2+\\+(1+g)(1+h)(1-r)y_3+(1-g)(1+h)(1-r)y_4+\\+(1-g)(1-h)(1+r)y_5+(1+g)(1-h)(1+r)y_6+\\+(1+g)(1+h)(1+r)y_7+(1-g)(1+h)(1+r)y_8-8y_M\end{array}\right)=0 \\ f_3 = \left(\begin{array}{l}(1-g)(1-h)(1-r)z_1+(1+g)(1-h)(1-r)z_2+\\+(1+g)(1+h)(1-r)z_3+(1-g)(1+h)(1-r)z_4+\\+(1-g)(1-h)(1+r)z_5+(1+g)(1-h)(1+r)z_6+\\+(1+g)(1+h)(1+r)z_7+(1-g)(1+h)(1+r)z_8-8z_M\end{array}\right)=0 \end{array}\right. \qquad \text{(A1.37)}$$

The system of equations (A1.37) is solved by using the Newton-Raphson method, as for the quadrilateral elements. The initial guess values for the local coordinates (g , h and r) are chosen to be zero.

Defining the Jacobian matrix (J) for the system of equations (A1.37):

$$J = \begin{bmatrix} \frac{\partial f_1}{\partial g} & \frac{\partial f_1}{\partial h} & \frac{\partial f_1}{\partial r} \\ \frac{\partial f_2}{\partial g} & \frac{\partial f_2}{\partial h} & \frac{\partial f_2}{\partial r} \\ \frac{\partial f_3}{\partial g} & \frac{\partial f_3}{\partial h} & \frac{\partial f_3}{\partial r} \end{bmatrix} \tag{A1.38}$$

where:

$$\begin{aligned}
\frac{\partial f_1}{\partial g} &= \begin{pmatrix} -(1-h)(1-r)x_1 + (1-h)(1-r)x_2 + (1+h)(1-r)x_3 - (1+h)(1-r)x_4 - \\ -(1-h)(1+r)x_5 + (1-h)(1+r)x_6 + (1+h)(1+r)x_7 - (1+h)(1+r)x_8 \end{pmatrix} \\
\frac{\partial f_1}{\partial h} &= \begin{pmatrix} -(1-g)(1-r)x_1 - (1+g)(1-r)x_2 + (1+g)(1-r)x_3 + (1-g)(1-r)x_4 - \\ -(1-g)(1+r)x_5 - (1+g)(1+r)x_6 + (1+g)(1+r)x_7 + (1-g)(1+r)x_8 \end{pmatrix} \\
\frac{\partial f_1}{\partial r} &= \begin{pmatrix} -(1-g)(1-h)x_1 - (1+g)(1-h)x_2 - (1+g)(1+h)x_3 - (1-g)(1+h)x_4 + \\ +(1-g)(1-h)x_5 + (1+g)(1-h)x_6 + (1+g)(1+h)x_7 + (1-g)(1+h)x_8 \end{pmatrix} \\
\frac{\partial f_2}{\partial g} &= \begin{pmatrix} -(1-h)(1-r)y_1 + (1-h)(1-r)y_2 + (1+h)(1-r)y_3 - (1+h)(1-r)y_4 - \\ -(1-h)(1+r)y_5 + (1-h)(1+r)y_6 + (1+h)(1+r)y_7 - (1+h)(1+r)y_8 \end{pmatrix} \\
\frac{\partial f_2}{\partial h} &= \begin{pmatrix} -(1-g)(1-r)y_1 - (1+g)(1-r)y_2 + (1+g)(1-r)y_3 + (1-g)(1-r)y_4 - \\ -(1-g)(1+r)y_5 - (1+g)(1+r)y_6 + (1+g)(1+r)y_7 + (1-g)(1+r)y_8 \end{pmatrix} \\
\frac{\partial f_2}{\partial r} &= \begin{pmatrix} -(1-g)(1-h)y_1 - (1+g)(1-h)y_2 - (1+g)(1+h)y_3 - (1-g)(1+h)y_4 + \\ +(1-g)(1-h)y_5 + (1+g)(1-h)y_6 + (1+g)(1+h)y_7 + (1-g)(1+h)y_8 \end{pmatrix} \\
\frac{\partial f_3}{\partial g} &= \begin{pmatrix} -(1-h)(1-r)z_1 + (1-h)(1-r)z_2 + (1+h)(1-r)z_3 - (1+h)(1-r)z_4 - \\ -(1-h)(1+r)z_5 + (1-h)(1+r)z_6 + (1+h)(1+r)z_7 - (1+h)(1+r)z_8 \end{pmatrix} \\
\frac{\partial f_3}{\partial h} &= \begin{pmatrix} -(1-g)(1-r)z_1 - (1+g)(1-r)z_2 + (1+g)(1-r)z_3 + (1-g)(1-r)z_4 - \\ -(1-g)(1+r)z_5 - (1+g)(1+r)z_6 + (1+g)(1+r)z_7 + (1-g)(1+r)z_8 \end{pmatrix} \\
\frac{\partial f_3}{\partial r} &= \begin{pmatrix} -(1-g)(1-h)z_1 - (1+g)(1-h)z_2 - (1+g)(1+h)z_3 - (1-g)(1+h)z_4 + \\ +(1-g)(1-h)z_5 + (1+g)(1-h)z_6 + (1+g)(1+h)z_7 + (1-g)(1+h)z_8 \end{pmatrix}
\end{aligned} \tag{A1.39}$$

Defining a matrix (M) from the system of equations (A1.37) as a function of the local coordinates g, h, and r for the corresponding iteration ($g=0$, $h=0$ and $r=0$ for the initial iteration):

$$M = \begin{bmatrix} f_1(g,h,r) \\ f_2(g,h,r) \\ f_3(g,h,r) \end{bmatrix} \tag{A1.40}$$

Solving the system of linear equations:

$$J \times p = -M \tag{A1.41}$$

where:

$$p = \begin{bmatrix} p_1 \\ p_2 \\ p_3 \end{bmatrix} \tag{A1.42}$$

The system of linear equations (A1.41) is solved as Equation (A1.9). See also Equations A1.10-A1.19.

After solving the system of equations (A1.41) the local coordinate values are defined as follow:

$$g = g + p_1 \tag{A1.43}$$

$$h = h + p_2 \tag{A1.44}$$

$$r = r + p_3 \tag{A1.45}$$

The iterations are repeated until the following convergence criterion is satisfied.

$$|f_1| + |f_2| + |f_3| \cong 0 \tag{A1.46}$$

The following convergence criterion is applied in the code:

$$|f_1| + |f_2| + |f_3| < 1 \times 10^{-5} \tag{A1.47}$$

One or two iterations are needed for solving the system of equations (A1.36), using the convergence criterion from equation (A1.47) and the chosen initial guess.

A1.5 Wedge elements

Figure A1.5 shows a six node wedge element with local coordinates (g , h and r) and node M.

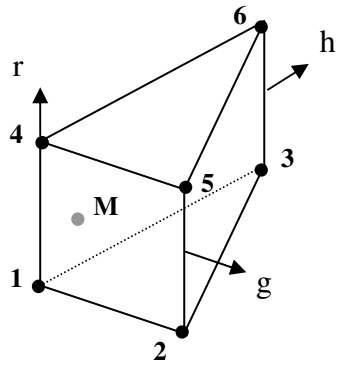

Figure A1.5: Six node wedge element and node M

The local coordinates (g, h and r) span the following ranges:

$$g \in [0,+1] \tag{A1.48}$$

$$h \in [0,+1] \tag{A1.49}$$

$$z \in [-1,+1] \tag{A1.50}$$

The local coordinates must satisfy Equation A1.8.

For defining the local coordinates the following system of equations must be solved:

$$\left|\begin{array}{l} x_M = \frac{1}{2}\left(\begin{array}{l}(1-g-h)(1-r)x_1 + g(1-r)x_2 + h(1-r)x_3 + \\ +(1-g-h)(1+r)x_4 + g(1+r)x_5 + h(1+r)x_6\end{array}\right) \\ y_M = \frac{1}{2}\left(\begin{array}{l}(1-g-h)(1-r)y_1 + g(1-r)y_2 + h(1-r)y_3 + \\ +(1-g-h)(1+r)y_4 + g(1+r)y_5 + h(1+r)y_6\end{array}\right) \\ z_M = \frac{1}{2}\left(\begin{array}{l}(1-g-h)(1-r)z_1 + g(1-r)z_2 + h(1-r)z_3 + \\ +(1-g-h)(1+r)z_4 + g(1+r)z_5 + h(1+r)z_6\end{array}\right) \end{array}\right. \tag{A1.51}$$

Equation (A1.52) can be given by:

$$\left|\begin{array}{l} f_1 = \left(\begin{array}{l}(1-g-h)(1-r)x_1 + g(1-r)x_2 + h(1-r)x_3 + \\ +(1-g-h)(1+r)x_4 + g(1+r)x_5 + h(1+r)x_6 - 2x_M\end{array}\right) = 0 \\ f_2 = \left(\begin{array}{l}(1-g-h)(1-r)y_1 + g(1-r)y_2 + h(1-r)y_3 + \\ +(1-g-h)(1+r)y_4 + g(1+r)y_5 + h(1+r)y_6 - 2y_M\end{array}\right) = 0 \\ f_3 = \left(\begin{array}{l}(1-g-h)(1-r)z_1 + g(1-r)z_2 + h(1-r)z_3 + \\ +(1-g-h)(1+r)z_4 + g(1+r)z_5 + h(1+r)z_6 - 2z_M\end{array}\right) = 0 \end{array}\right. \tag{A1.52}$$

The system of equations (A1.51) is solved by using the Newton-Raphson method, as in the previous cases. The initial guess values for the local coordinates (g , h and r) are chosen as follows: $g = 0.5$; $h = 0.5$; $r = 0$

The Jacobian matrix (J) from Equation A1.38 is defined by the following derivatives:

$$\frac{\partial f_1}{\partial g} = -(1-r)x_1 + (1-r)x_2 - (1+r)x_4 + (1+r)x_5$$

$$\frac{\partial f_1}{\partial h} = -(1-r)x_1 + (1-r)x_3 - (1+r)x_4 + (1+r)x_6$$

$$\frac{\partial f_1}{\partial r} = -(1-g-h)x_1 - gx_2 - hx_3 + (1-g-h)x_4 + gx_5 + hx_6$$

$$\frac{\partial f_1}{\partial g} = -(1-r)y_1 + (1-r)y_2 - (1+r)y_4 + (1+r)y_5$$

$$\frac{\partial f_1}{\partial h} = -(1-r)\,y_1 + (1-r)\,y_3 - (1+r)\,y_4 + (1+r)\,y_6$$
$$\frac{\partial f_1}{\partial r} = -(1-g-h)\,y_1 - g y_2 - h y_3 + (1-g-h)\,y_4 + g y_5 + h y_6$$
$$\frac{\partial f_1}{\partial g} = -(1-r)\,z_1 + (1-r)\,z_2 - (1+r)\,z_4 + (1+r)\,z_5$$
$$\frac{\partial f_1}{\partial h} = -(1-r)\,z_1 + (1-r)\,z_3 - (1+r)\,z_4 + (1+r)\,z_6$$
$$\frac{\partial f_1}{\partial r} = -(1-g-h)\,z_1 - g z_2 - h z_3 + (1-g-h)\,z_4 + g z_5 + h z_6$$

(A1.54)

Matrix M from Equation A1.40 is defined as a function of the local coordinates g, h, and r, for the corresponding iteration ($g = 0.5$, $h = 0.5$ and $r = 0$ for the first iteration). Equations from A1.41 to A1.47 are applied for the wedge elements in the same way as for the hexahedron elements for determining the local coordinates.